The Deep Space Network Progress Report 42-40

May and June 1977

National Aeronautics and Space Administration

Jet Propulsion Laboratory
California Institute of Technology
Pasadena, California 91103

The Deep Space Network Progress Report 42-40

May and June 1977

August 15, 1977

National Aeronautics and
Space Administration

Jet Propulsion Laboratory
California Institute of Technology
Pasadena, California 91103

Prepared Under Contract No NAS 7-100
National Aeronautics and Space Administration

Preface

Beginning with Volume XX, the Deep Space Network Progress Report changed from the Technical Report 32- series to the Progress Report 42- series. The volume number continues the sequence of the preceding issues. Thus, Progress Report 42-20 is the twentieth volume of the Deep Space Network series, and is an uninterrupted follow-on to Technical Report 32-1526, Volume XIX.

This report presents DSN progress in flight project support, tracking and data acquisition (TDA) research and technology, network engineering, hardware and software implementation, and operations. Each issue presents material in some, but not all, of the following categories in the order indicated.

Description of the DSN

Mission Support
- Ongoing Planetary/Interplanetary Flight Projects
- Advanced Flight Projects

Radio Astronomy

Special Projects

Supporting Research and Technology
- Tracking and Ground-Based Navigation
- Communications–Spacecraft/Ground
- Station Control and Operations Technology
- Network Control and Data Processing

Network and Facility Engineering and Implementation
- Network
- Network Operations Control Center
- Ground Communications
- Deep Space Stations
- Quality Assurance

Operations
- Network Operations
- Network Operations Control Center
- Ground Communications
- Deep Space Stations

Program Planning
- TDA Planning

In each issue, the part entitled "Description of the DSN" describes the functions and facilities of the DSN and may report the current configuration of one of the five DSN systems (Tracking, Telemetry, Command, Monitor & Control, and Test & Training).

The work described in this report series is either performed or managed by the Tracking and Data Acquisition organization of JPL for NASA.

Contents

DESCRIPTION OF THE DSN

MISSION SUPPORT

Ongoing Planetary/Interplanetary Flight Projects

SUPPORTING RESEARCH AND TECHNOLOGY

Tracking and Ground-Based Navigation

Communications — Spacecraft/Ground

Network Control and Data Processing

NETWORK AND FACILITY ENGINEERING AND IMPLEMENTATION

Network

Deep Space Stations

OPERATIONS

Network Operations

PROGRAM PLANNING

TDA Planning

Network Functions and Facilities

N. A. Renzetti
Office of Tracking and Data Acquisition

The objectives, functions, and organization of the Deep Space Network are summarized; deep space station, ground communication, and network operations control capabilities are described.

The Deep Space Network (DSN), established by the National Aeronautics and Space Administration (NASA) Office of Tracking and Data Acquisition under the system management and technical direction of the Jet Propulsion Laboratory (JPL), is designed for two-way communications with unmanned spacecraft traveling approximately 16,000 km (10,000 miles) from Earth to the farthest planets of our solar system. It has provided tracking and data acquisition support for the following NASA deep space exploration projects: Ranger, Surveyor, Mariner Venus 1962, Mariner Mars 1964, Mariner Venus 1967, Mariner Mars 1969, Mariner Mars 1971, and Mariner Venus Mercury 1973, for which JPL has been responsible for the project management, the development of the spacecraft, and the conduct of mission operations; Lunar Orbiter, for which the Langley Research Center carried out the project management, spacecraft development, and conduct of mission operations; Pioneer, for which Ames Research Center carried out the project management, spacecraft development, and conduct of mission operations; and Apollo, for which the Lyndon B. Johnson Space Center was the project center and the Deep Space Network supplemented the Manned Space Flight Network (MSFN), which was managed by the Goddard Space Flight Center (GSFC). It is providing tracking and data acquisition support for Helios, a joint U.S./West German project; and Viking, for which Langley Research Center provides the project management, the Lander spacecraft, and conducts mission operations, and for which JPL also provides the Orbiter spacecraft.

The Deep Space Network is one of two NASA networks. The other, the Spaceflight Tracking and Data Network, is under the system management and technical direction of the Goddard Space Flight Center. Its function is to support manned and unmanned Earth-orbiting satellites. The Deep Space Network supports lunar, planetary, and interplanetary flight projects.

From its inception, NASA has had the objective of conducting scientific investigations throughout the solar sys-

tem. It was recognized that in order to meet this objective, significant supporting research and advanced technology development must be conducted in order to provide deep space telecommunications for science data return in a cost effective manner. Therefore, the Network is continually evolved to keep pace with the state of the art of telecommunications and data handling. It was also recognized early that close coordination would be needed between the requirements of the flight projects for data return and the capabilities needed in the Network. This close collaboration was effected by the appointment of a Tracking and Data Systems Manager as part of the flight project team from the initiation of the project to the end of the mission. By this process, requirements were identified early enough to provide funding and implementation in time for use by the flight project in its flight phase.

As of July 1972, NASA undertook a change in the interface between the Network and the flight projects. Prior to that time, since 1 January 1964, in addition to consisting of the Deep Space Stations and the Ground Communications Facility, the Network had also included the mission control and computing facilities and provided the equipment in the mission support areas for the conduct of mission operations. The latter facilities were housed in a building at JPL known as the Space Flight Operations Facility (SFOF). The interface change was to accommodate a hardware interface between the support of the network operations control functions and those of the mission control and computing functions. This resulted in the flight projects assuming the cognizance of the large general-purpose digital computers which were used for both network processing and mission data processing. They also assumed cognizance of all of the equipment in the flight operations facility for display and communications necessary for the conduct of mission operations. The Network then undertook the development of hardware and computer software necessary to do its network operations control and monitor functions in separate computers. This activity has been known as the Network Control System Implementation Project. A characteristic of the new interface is that the Network provides direct data flow to and from the stations; namely, metric data, science and engineering telemetry, and such network monitor data as are useful to the flight project. This is done via appropriate ground communication equipment to mission operations centers, wherever they may be.

The principal deliverables to the users of the Network are carried out by data system configurations as follows:

- The DSN Tracking System generates radio metric data; i.e., angles, one- and two-way doppler and range, and transmits raw data to Mission Control.
- The DSN Telemetry System receives, decodes, records, and retransmits engineering and scientific data generated in the spacecraft to Mission Control.
- The DSN Command System accepts coded signals from Mission Control via the Ground Communications Facility and transmits them to the spacecraft in order to initiate spacecraft functions in flight.

The data system configurations supporting testing, training, and network operations control functions are as follows:

- The DSN Monitor and Control System instruments, transmits, records, and displays those parameters of the DSN necessary to verify configuration and validate the Network. It provides operational direction and configuration control of the Network, and provides primary interface with flight project Mission Control personnel.
- The DSN Test and Training System generates and controls simulated data to support development, test, training and fault isolation within the DSN. It participates in mission simulation with flight projects.

The capabilities needed to carry out the above functions have evolved in three technical areas:

(1) The Deep Space Stations, which are distributed around Earth and which, prior to 1964, formed part of the Deep Space Instrumentation Facility. The technology involved in equipping these stations is strongly related to the state of the art of telecommunications and flight-ground design considerations, and is almost completely multimission in character.

(2) The Ground Communications Facility provides the capability required for the transmission, reception, and monitoring of Earth-based, point-to-point communications between the stations and the Network Operations Control Center at JPL, Pasadena, and to the mission operations centers, wherever they may be. Four communications disciplines are provided: teletype, voice, high-speed, and wideband. The Ground Communications Facility uses the capabilities provided by common carriers throughout the world, engineered into an integrated system by Goddard Space Flight Center, and controlled from the communications Center located in the Space Flight Operations Facility (Building 230) at JPL.

(3) The Network Operations Control Center is the functional entity for centralized operational control of the Network and interfaces with the users. It has two separable functional elements; namely, Network Operations Control and Network Data Processing. The functions of the Network Operations Control are:

- Control and coordination of Network support to meet commitments to Network users.
- Utilization of the Network data processing computing capability to generate all standards and limits required for Network operations.
- Utilization of Network data processing computing capability to analyze and validate the performance of all Network systems.

The personnel who carry out the above functions are located in the Space Flight Operations Facility, where mission operations functions are carried out by certain flight projects. Network personnel are directed by an Operations Control Chief. The functions of the Network Data Processing are:

- Processing of data used by Network Operations Control for control and analysis of the Network.
- Display in the Network Operations Control Area of data processed in the Network Data Processing Area.
- Interface with communications circuits for input to and output from the Network Data Processing Area.
- Data logging and production of the intermediate data records.

The personnel who carry out these functions are located approximately 200 meters from the Space Flight Operations Facility. The equipment consists of minicomputers for real-time data system monitoring, two XDS Sigma 5s, display, magnetic tape recorders, and appropriate interface equipment with the ground data communications.

DSN Tracking System—Mark III-77

W. D. Chaney
TDA Engineering

This article provides a description of the DSN Tracking System – Mark III-77 currently in use for multimission support. Tracking functions performed by the Deep Space Stations, Ground Communications Facility, and Network Operations Control Center are given. Changes that were made to the subsystems of the DSN Tracking System – Mark III-75 to implement the DSN Tracking System – Mark III-77 are briefly described.

I. Introduction

The DSN Tracking System is a multiple-mission system that generates radio metric data for use by Projects for spacecraft navigation. The radio metric data types are as follows:

(1) S-band doppler

(2) S/X-band doppler

(3) S-band range

(4) S/X-band range

(5) Angles

The DSN Tracking System, while multimission, must be upgraded to meet the more stringent requirements of outer planet navigation. The previous designation of the DSN Tracking System was Mark III-75 (Ref. 1) and was used for Viking, Pioneer and Helios Project support. This article describes the upgrade of the DSN Tracking System from the Mark III-75 to the Mark III-77 for additional support of the Voyager and Pioneer Venus 1978 Projects.

II. Key Characteristics

The key characteristics of the new Mark III-77 DSN Tracking System are as follows:

(1) S/X-band doppler and range data generation using precision hydrogen maser frequency standards.

(2) Simultaneous two station doppler for use in the determination of unmodelled spacecraft acceleration.

(3) Near simultaneous two station range data for the improvement of navigation accuracies during low declination angle tracks.

(4) Data time tagged to the 10-nanosecond level relative to the DSN master clock.

(5) Calibration data for the RF transmission media.

(6) Precision control of Block IV receiver and exciter frequencies for very narrow band tracking.

(7) Generation of tracking predictions for spacecraft acquisition by DSN tracking operations.

(8) Real-time validation of the DSN Tracking System performance.

(9) Real-time reporting of the DSN Tracking System status to DSN Operations Control.

(10) Generation of a Tracking Intermediate Data Record (future).

III. DSN Tracking System Functions

The Mark III-77 DSN Tracking System consists of the Deep Space Stations (DSS), Ground Communications Facility (GCF), and Network Operations Control Center (NOCC). The general functions performed in each are presented in Fig. 1.

A. DSS Functions and Modifications

The DSS functions, the subsystems required to perform those functions, and external interfaces are presented in Fig. 2. Modifications that were made in each subsystem in progressing from the Mark III-75 to the Mark III-77 are given below. Simplified Mark III-77 block diagrams depicting the subsystems and assemblies within the 26-m and 64-m antenna DSSs are presented in Figs. 2, 3 and 4.

1. **Frequency and Timing Subsystem.** Hydrogen maser frequency standards are being added to the 64-m subnet (DSSs 14, 43, and 63). These frequency standards will improve the DSS frequency stability by approximately two orders of magnitude which will extend precision range and doppler capability to beyond 20 AU. Hydrogen maser stability is also available at the conjoint 26-m DSSs (DSSs 42 and 61).

2. **Microwave Subsystem.** An acquisition aid with approximately 16-degree beamwidth has been added at DSS 12 for the initial pass acquisition of the Voyager spacecraft.

3. **Technical Facilities Subsystems.** A Meteorological Monitor Assembly has been added, which measures and records ground temperature, pressure, relative humidity, and ionosphere data. The ionosphere data are measured from tracking the polarization angle of a linearly polarized stationary satellite. These data are recorded on magnetic tape and transmitted via high-speed data lines on a post-pass basis using the Original Data Record (ODR) recall software.

4. **DSS Tracking Subsystem.** A major upgrade of the Tracking Subsystem is in progress. The previous Tracking Data Handling Subsystem has been replaced by the Metric Data Assembly (see Section IV, this article, for details). The Ranging Demodulator Assembly(s) was reassigned from the Receiver-Exciter Subsystem to the Tracking Subsystem. The Planetary Ranging Assembly is being modified for near sun line-of-sight angle operation in order to improve radio science data.

B. GCF Functions and Modifications

The GCF functions, the subsystems to perform these functions, and the external interfaces are given in Fig. 5. Modifications to the High-Speed Data Subsystem were the addition of the Communications Formatter Assembly at the DSN stations and the generation of a centralized Original Data Record (ODR) at the station containing the data available for HSD transmission for all DSN systems.

Future addition to the GCF will be the modification of the Data Records Processor Subsystem for the generation of a tracking Intermediate Data Record (IDR). The IDR will contain data as received from the DSN stations. Missing data will be recalled from the station ODR as necessary to meet Project commitments.

C. NOCC Functions and Modifications

The NOCC functions, the subsystems to perform these functions, and the external interfaces are shown in Fig. 6. Modifications to each assembly are described below.

1. **Predictions.** The Fast Phi Factor Generation Program (FPGP) was added to the prediction assembly. The FPGP provides a simplified station independent interface to the Project, wherein the Project supplies a Probe Ephemeris Tape that contains trajectory data for several months rather than several days.

2. **Display.** A single digital TV channel will be made available to the Projects to provide displays of DSN radio metric data performance (future).

3. **Real-Time Monitor (RTM).** The RTM has been modified in order to supply volume real-time Tracking System performance data in the Network Operations Control Area.

IV. DSS Tracking Subsystem

The DSS Tracking Subsystem (DTK), a part of the DSN Tracking System, performs the following three main functions:

(1) Generation of radio metric data

(2) Transmission of radio metric data

(3) Validation of the DSN Tracking System

The generation of radio metric data consists of those functions necessary to acquire doppler, range, angle, and RF transmission media calibration data. The transmission of radio metric data consists of those functions necessary to format and transmit the information to the user. The validation of the Tracking System consists of those functions necessary to verify the performance of the subsystem in the generation and transmission of the data.

DSS Tracking Subsystem functions and interfaces are presented in Fig. 7.

V. DTK Key Characteristics

The key characteristics of the DTK are as follows:

(1) Automatic configuration of the DSS Tracking Su system.

(2) Generation of range codes.

(3) Full use of the Ground Communications High-Speed Data Subsystem (HSS) for the transmission of DSN Tracking System radio metric data between the DSS and the Mission Control and Computing Center (MCCC) and/or Network Operations Control Center (NOCC).

(4) Simultaneous sampling of doppler from three spacecraft carriers at rates up to 10 per second.

(5) Simultaneous S/X-band ranging from one spacecraft.

(6) Automatic validation of DSS performance in generating radio metric data.

(7) Automatic generation of the temporary DSS tracking Original Data Record with selective recall data interlaced with the real-time data.

VI. Functional Operation

DTK functions and primary intersubsystem data flow are presented in Fig. 8. Predictions, system configuration, and data mode messages are received from the NOCC via the Ground Communications HSS and are stored by the DTK for use when requested by Network Operations. The predictions are used to provide frequencies for digital programming and control of the DSS Receiver-Exciter Subsystem (RCV) frequencies, and to provide angles for control of antenna pointing. The system configuration messages and data mode messages are used to configure, control, and validate the DTK.

Planetary range code is generated and transmitted to the RCV for modulation of the uplink carrier. Time-delayed range code is supplied to the Range Demodulator Assembly (RDA) where range correlation is determined. Range correlation is then used in conjunction with clock and RF carrier doppler in the acquisition and tracking of range and differenced range versus integrated doppler (DRVID). Doppler data generated by the RCV doppler extractor are counted by the doppler counters for up to three RF carriers.

Angles, doppler, range, and DRVID data plus status, configuration, data mode, and reference frequencies data are sampled, then formatted and transmitted via the Ground Communications HSS. Supplementary data, i.e., ground weather data, ionospheric data, and polarizer data, are sampled and inserted in the HSS data stream. A temporary ODR of all data taken in real time is maintained for selective recall to the NOCC or MCCC.

Reference

1. Chaney, W. D., "DSN Tracking System – Mark III-75," in *The Deep Space Network Progress Report 42-32*, pp. 4-13, Jet Propulsion Laboratory, Pasadena, Calif., Apr. 15, 1976.

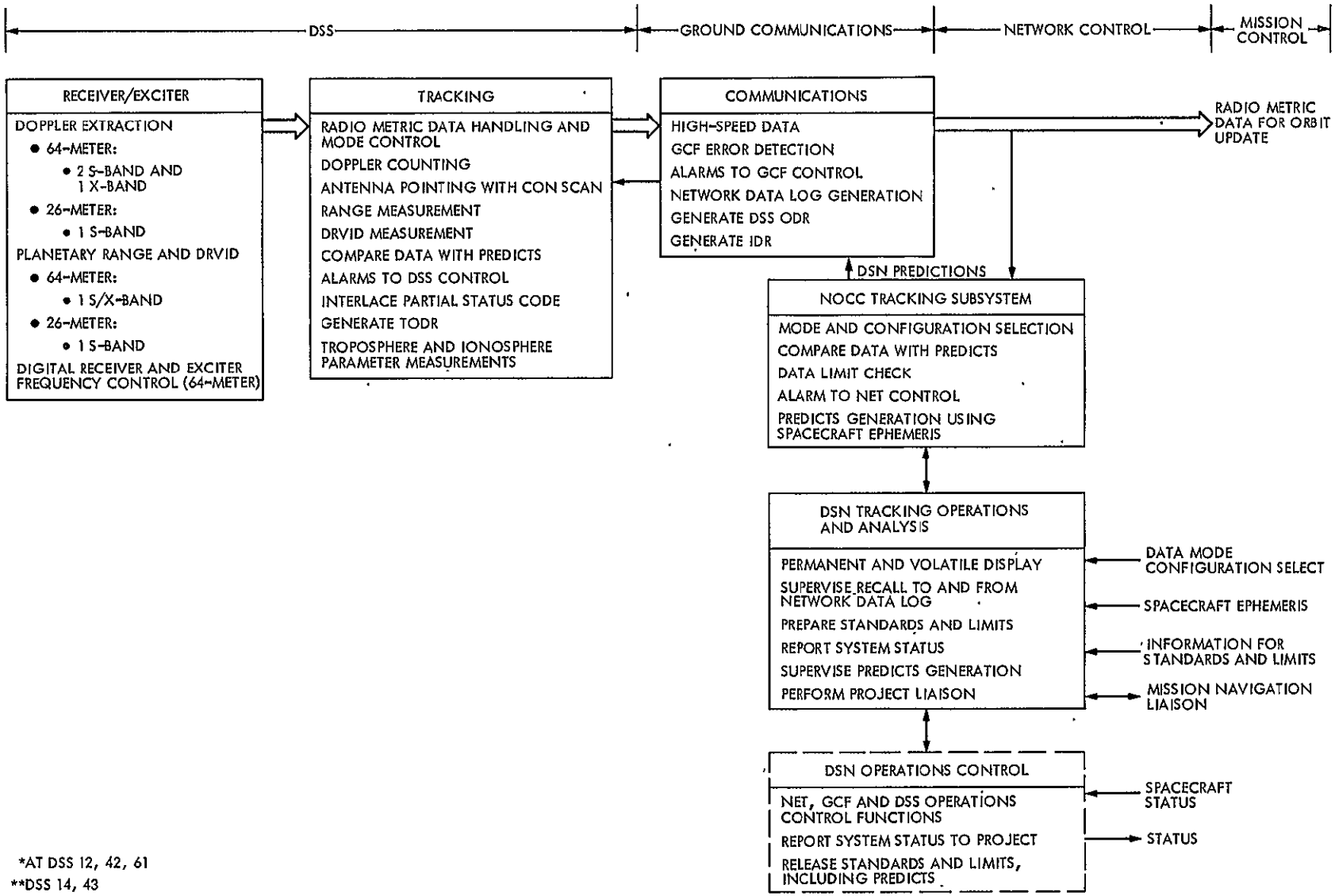

Fig. 1. Mark III-77 DSN Tracking System

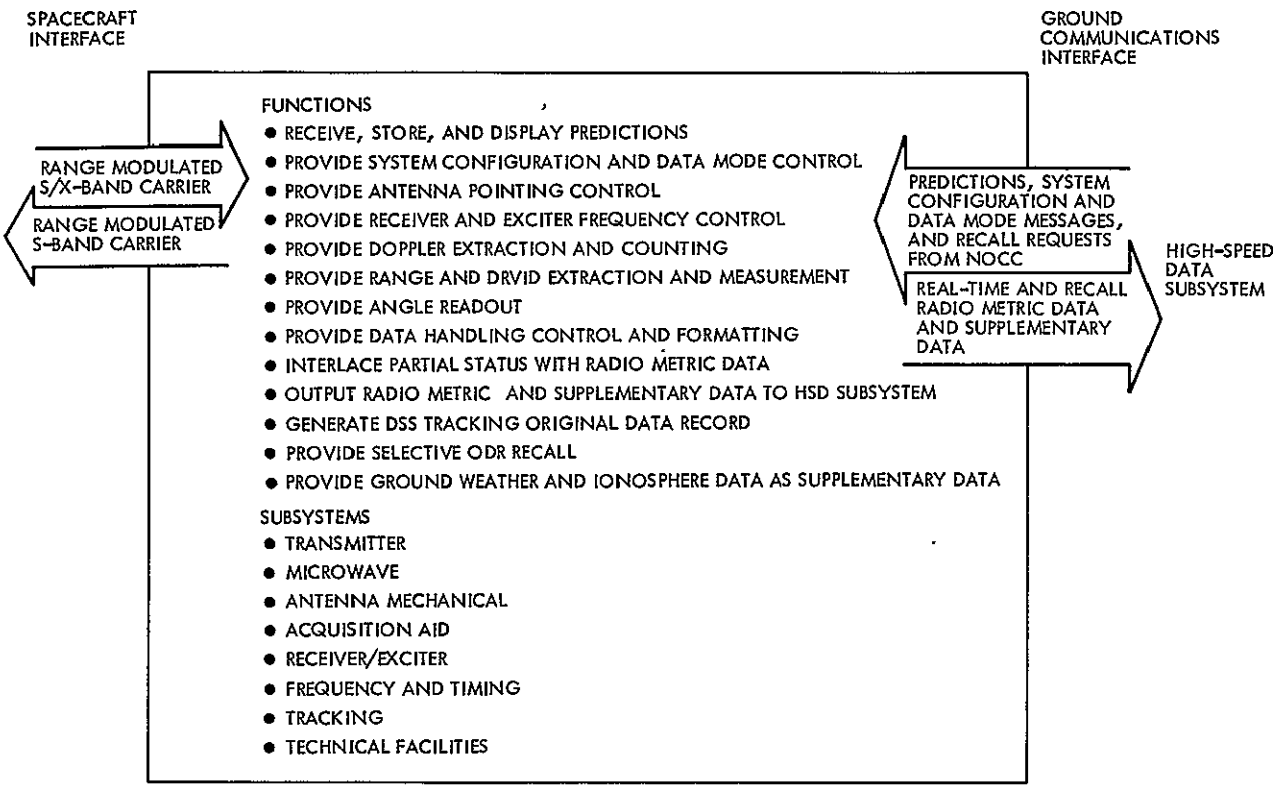

Fig. 2. DSS tracking functional requirements

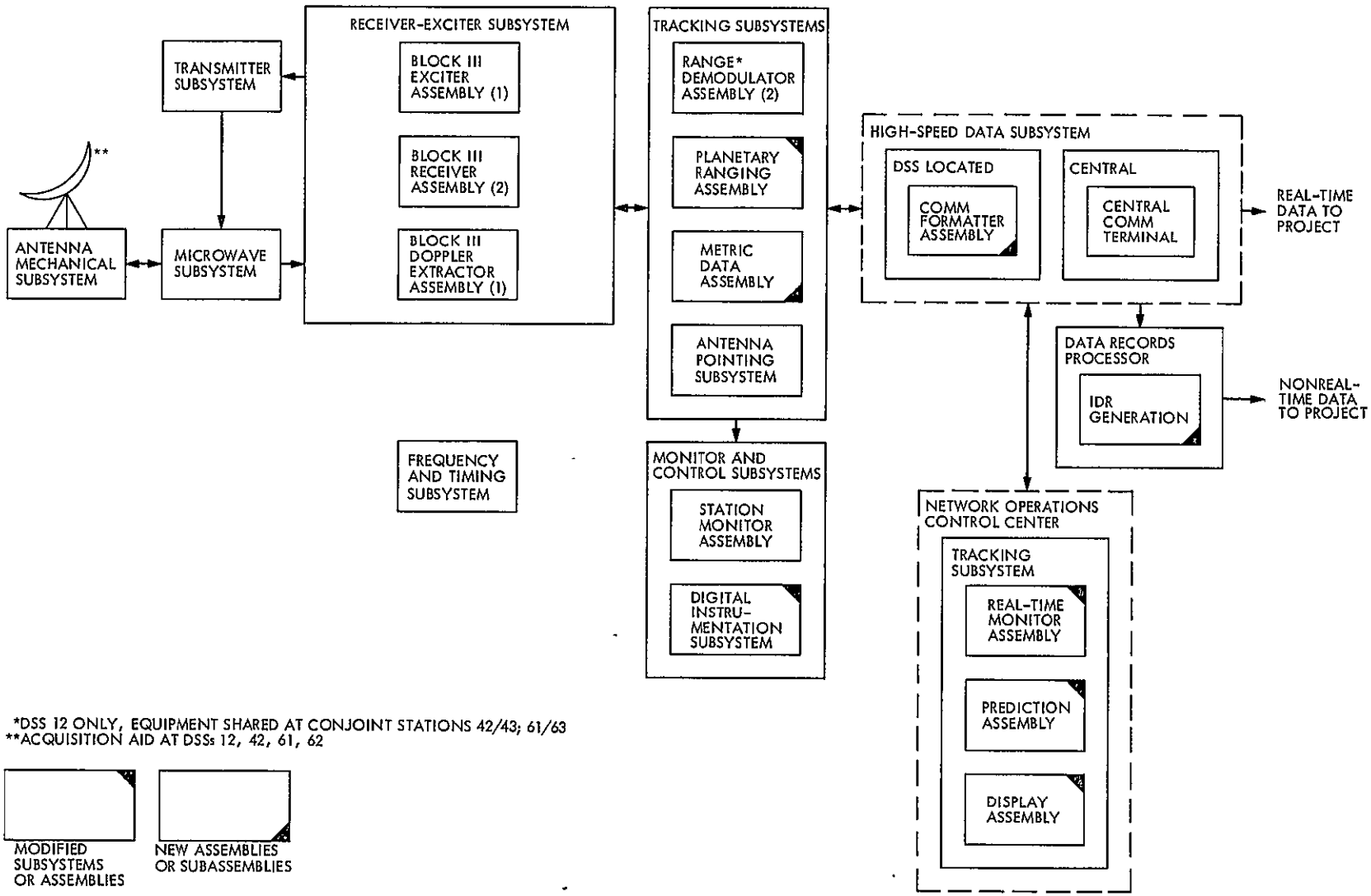

Fig. 3. DSN Tracking System—Mark III-77 26-m simplified block diagram

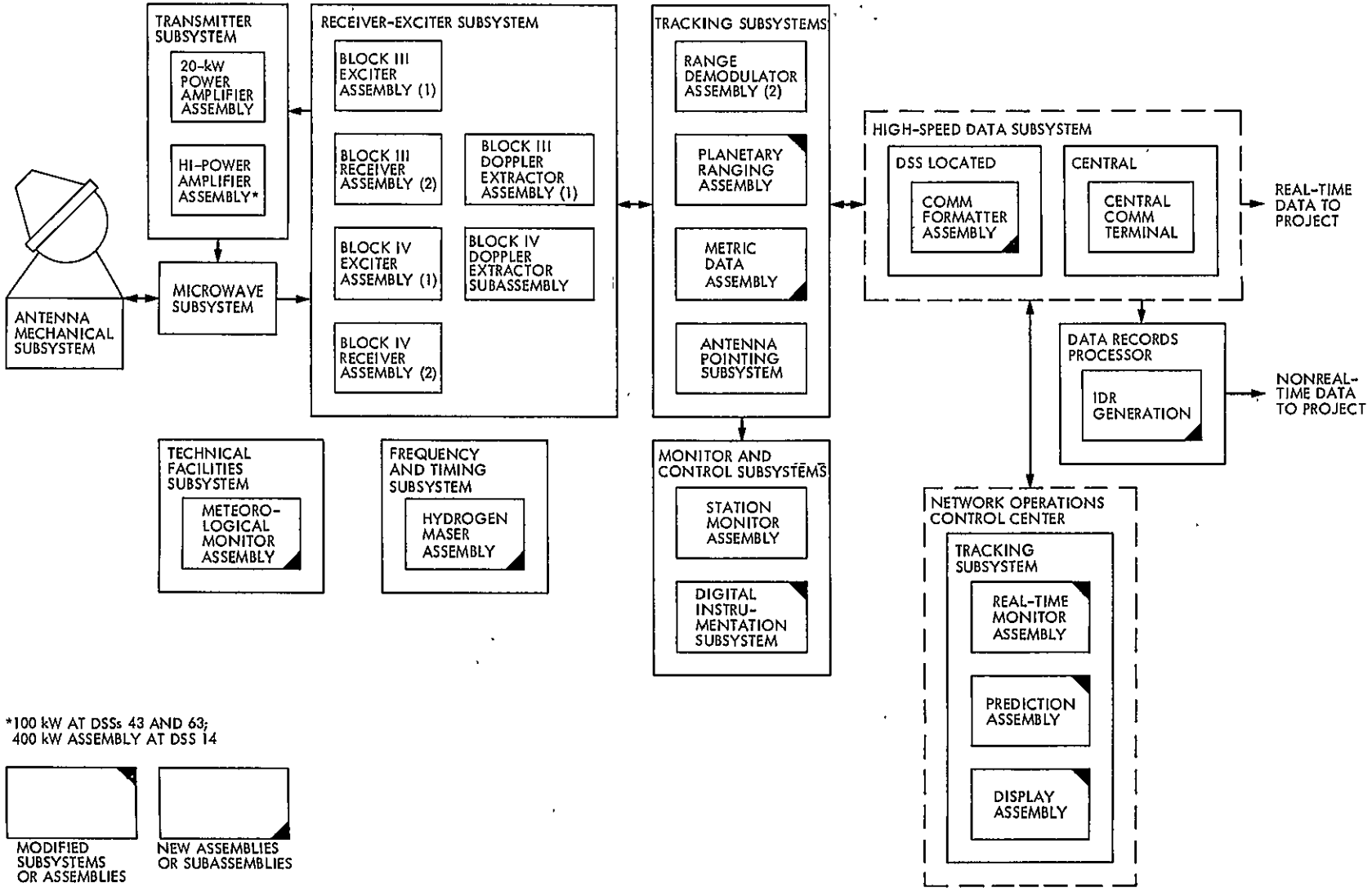

Fig. 4. DSN Tracking System—Mark III-77 64-m simplified block diagram

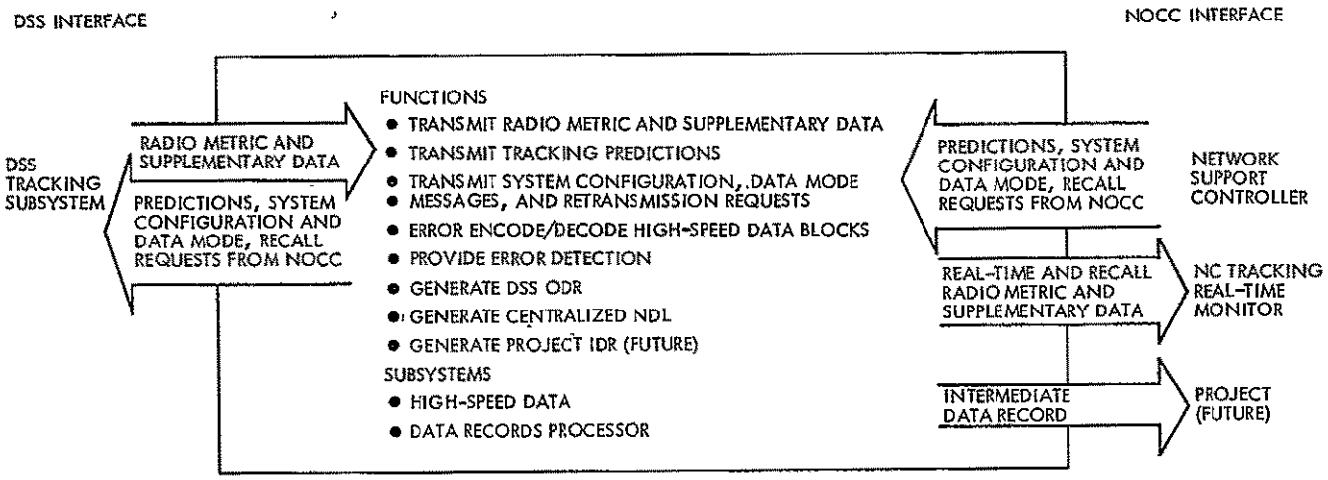

Fig. 5. Ground communications functional requirements

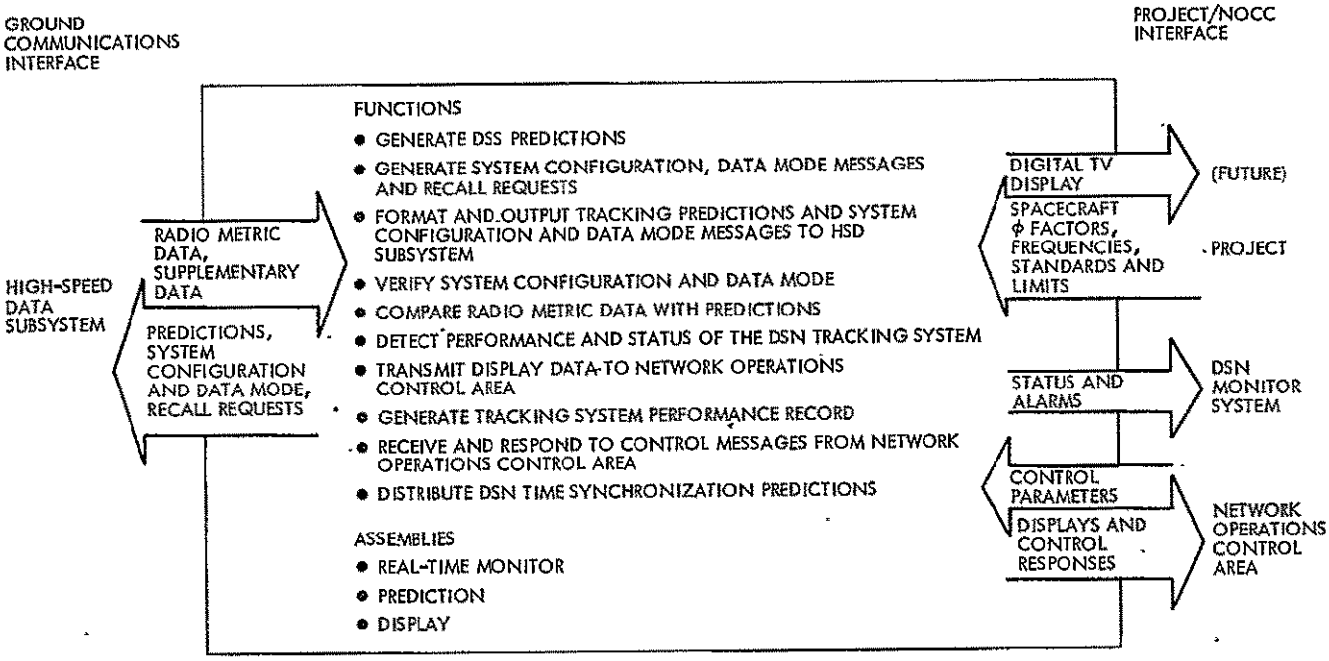

Fig. 6. NOCC tracking subsystem functional requirements

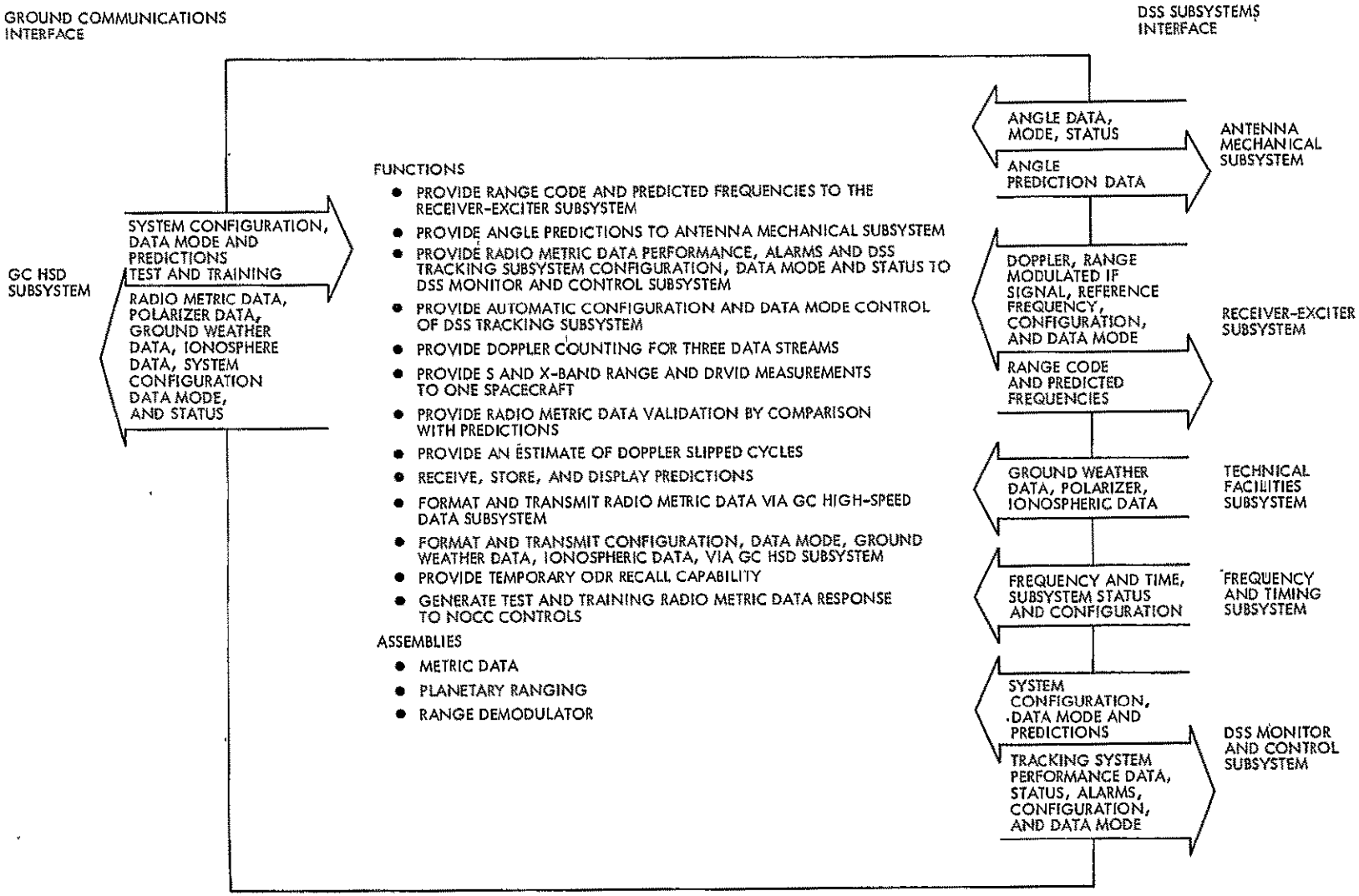

Fig. 7. DSS Tracking Subsystem functional requirements

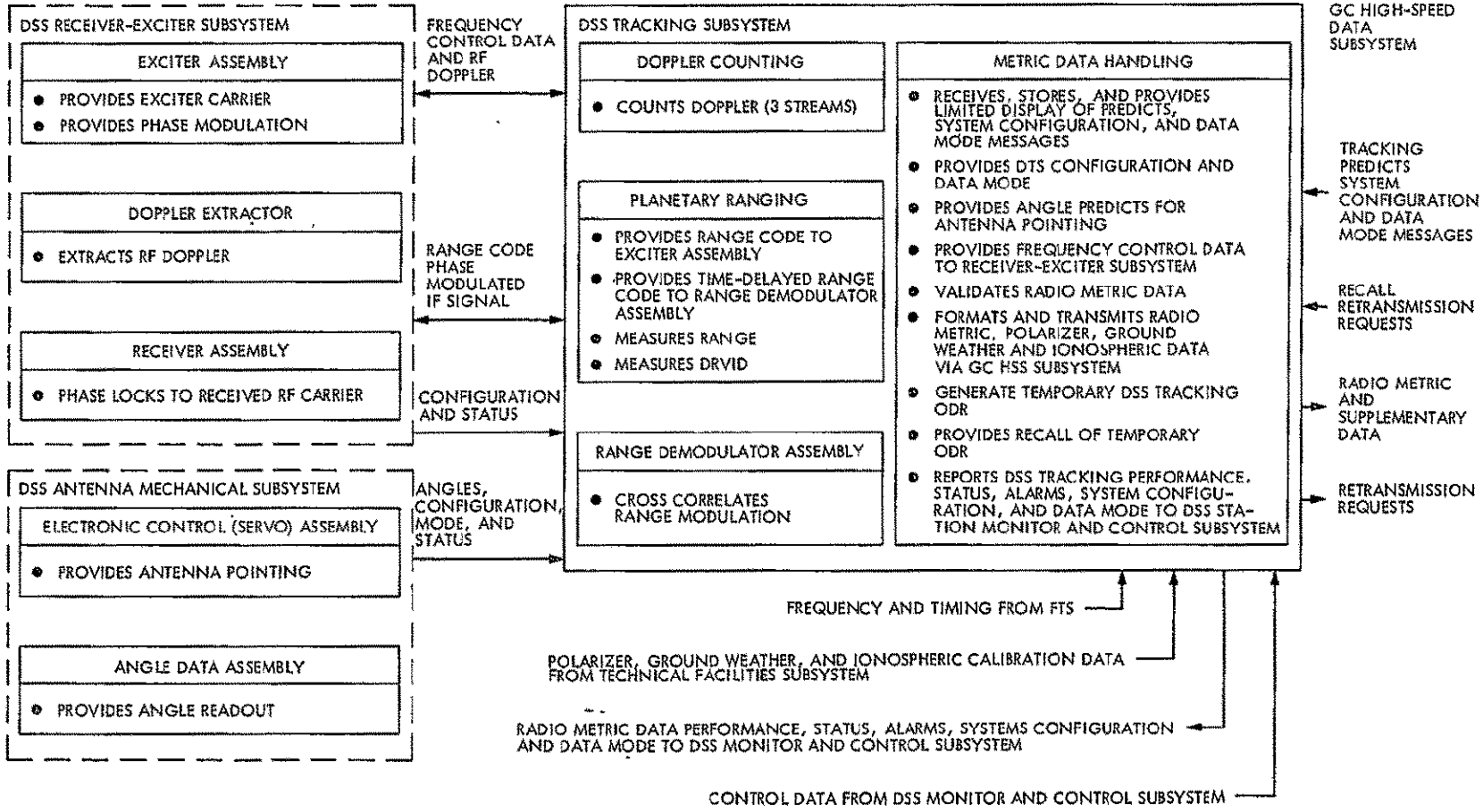

Fig. 8. DSS Tracking Subsystem functions and data flow

D3

Pioneer Venus 1978 Mission Support

R. B. Miller
TDA Mission Support Office

The DSN Master Schedule for preparations for the Pioneer Venus 1978 Mission is updated and the current support status for the mission described.

I. Introduction

The DSN Major Milestone Schedule for Pioneer Venus was originally presented in Ref. 1, and the portion of the schedule dealing with the Differential Long Baseline Interferometry (DLBI) experiment was updated in Ref. 2. The following article brings those schedules and the DSN support status for Pioneer Venus up to date as of June 3, 1977.

In general, at the time of writing of this article, the DSN implementation required for support of Pioneer Venus is in the fabrication stage with essentially all detail design work completed.

II. DSN Major Milestone Schedule for the Orbiter and Multiprobe

The following status information relates to Fig. 1, one of the three schedules accompanying this article. Although no officially signed Support Instrumentation Requirements Document (SIRD) for Pioneer Venus has been received, a preliminary unsigned version of the NASA Support Plan (NSP) was released in mid-April 1977 in order to desseminate current DSN plans and agreements with the Pioneer Project. The unsigned NSP is consistent with DSN implementation and budgetary plans.

The first stage of DSN spacecraft compatibility testing was completed in what is called the weak signal level tests which were conducted at CTA 21 using breadboard spacecraft RF subsystems and a Project-provided telemetry emulator. The tests were in general successful with no problems discovered in the RF area; however, a spacecraft encoder problem was isolated. The encoder problem involved resetting the state of the encoder seven bits later than the end of the fixed sync word in the telemetry frame. The extra bits included the higher-order bits of the subcomm ID word, which is an indexing counter, and therefore the reset was at such a point that the encoder was never reset to a known state. Hughes Aircraft personnel participating in the testing were able to rewire the telemetry emulator in order to put the reset in the proper location. It was subsequently determined that the encoder in the telemetry emulator was identical to that in the Orbiter and Bus spacecraft. Having made special analog recordings of output from an actual probe, Hughes Aircraft brought a recorder to CTA 21 and successfully demonstrated that the encoders on the Probes were indeed correct.

A major objective of the Weak Signal Level Compatibility Testing was the demonstration of coded data telemetry thresholds. Although it was thought at the time of the tests that predicted telemetry thresholds were either met or exceeded in the test conditions for each bit rate, subsequent analysis of the

test data showed that the minimum thresholds, in terms of energy per bit to noise ratio, may have been between 1-1/2 to 3 dB above theoretical values. At this time, it is not known whether the losses experienced were due to the test configurations or some problem with CTA 21 equipment/software. The latter is currently the prime suspect. The plan is now to do self-testing of the DSN equipment within CTA 21 to determine measured values of the telemetry threshold for sequentially decoded data.

The Mark III/DSN Data Subsystems Project has been proceeding generally satisfactorily. DSS 14 may return to operations (here defined as starting the support of mission-dependent testing) on the order of one week late compared to plan because of unanticipated problems in the installation and associated systems performance testing. It will be necessary to extend the downtime schedule of the two conjoint stations (DSS 42-43 and DSS 61-63) two or three weeks because of the experience at DSS 14 coupled with a re-evaluation of the work required at those stations. It is not anticipated that these slips in the MDS Project will have any impact on Pioneer Venus since the completion date for each station is well ahead of Pioneer Venus need dates. The telemetry and command software for Pioneer Venus was available for supporting the Weak Signal Level Compatibility Tests and has subsequently completed formal transfer to operations minus the dual sequentially decoding capability. That means that the telemetry and command software required for support of the launch and the entire Orbiter Mission is already in the hands of operations. Dual sequentially decoding capability is only required for Multiprobe entry and will be utilized to handle the four probes' telemetry data at a single station simultaneously. This is a change from the original plan, which was to produce a Symbol Synchronizer Assembly recording of symbols for two streams out of the four in real-time because of the restriction of having only two Telemetry Processor Assemblies per station. The implementing organization felt that it would be possible to take advantage of the 5-times-faster decoding capability of the TPA compared to the old Digital Data Assembly in order to handle two low-rate streams simultaneously with no significant loss of performance.

A recent addition to Pioneer Venus requirements is the radio metric Intermediate Data Record. Implementation by the DSN of error-detection correction for high-speed data transmission required implementation of new high-speed data formats which involve a 22-bit error code. It was negotiated with Ames Research Center from the beginning that the entire Pioneer Venus Mission would be flown with the new high-speed data formats to avoid a required change in high-speed data formats during the mission. Subsequent to this agreement, it was discovered that there was an incompatibility between the agreed dates for converting to the 22-bit error code high-speed data formats for Pioneer Venus and the Mission Computing and Control Center (MCCC) schedule for converting to the new format. Although MCCC is not involved in the telemetry and command processing for Pioneer Venus, it is involved in the existing Navigation interface, where radio metric data currently flows through the MCCC 360/75 computer before passing to the Navigation 1108 computers. MCCC does not intend to implement the new high-speed data formats in the 360/75 but rather intends to wait until the implementation of the minicomputers which replace the 360/75 real-time functions. This is planned for May or later in 1978 and also involves a new radio metric interface by which the DSN provides radio metric data directly to the Navigation Team in the form of Intermediate Data Records produced by the Ground Communications Facility of the Deep Space Network.

Pioneer Venus Orbiter launch is in May 1978 and clearly the MCCC May schedule for accommodating 22-bit error code high-speed data formats is incompatible with the Pioneer Venus requirement to have those formats fully operational by February 1, 1978, and available for support of testing by October 1, 1977. This problem was solved by negotiating an earlier date for the availability of the new direct DSN Navigation interface. It is now planned to have both the 22-bit error code high-speed data formats and the radio metric Intermediate Data Record capability available for support of engineering-level tests by October 1, 1977, and fully operational for all Pioneers (including 6 through 11) by February 1, 1978.

Pioneer Venus Orbiter will utilize a new occultation support subsystem at the tracking stations. This subsystem will involve the use of computer-controlled programmable oscillators driving the first LO in the open-loop receivers, which will enable operating the open-loop receivers at a much narrower bandwidth than for previous missions. This narrower bandwidth output from the open-loop receivers (the design goal is for 1-kHz bandwidth at S-band) will be digitized in real-time and recorded on computer-compatible tapes using a dedicated MODCOMP minicomputer. The programmable oscillators will be driven using predicts, which include a prediction of the atmospheric effects of Venus. It is intended that the computer-compatible recordings will be replayed in non-real-time over high-speed data lines back to JPL for production of an Intermediate Data Record for radio science as a deliverable to the experimenters. A backup capability will be provided for shipping the tapes to JPL for direct tape conversion to the IDR format. Detail design is essentially complete on both the hardware and software of this subassembly.

Integration contractor support was desired for the implementation of the occultation support subsystem, and initial problems in negotiating the contract with the vendor, due to

excessive costs, in the first part of calendar 1977 were resolved by delaying some hardware until FY'78 and pulling some of the work back in-house. Secondary requirements for support of the radio science experiments (excluding the DLBI experiment) are the only significant open area in the requirements vs commitments between the DSN and the Pioneer Project. The most serious open area is the question of providing a wider bandwidth backup to the new occultation support subsystem because of experimenter concerns with this new method of supporting occultations and also because as much as the first month of occultations may be visible from only a single DSS. There are other secondary issues such as what data would be available and where the experimenters could view it in real-time during the mission. Many of these issues are being handled on a multimission basis because of similar requirements for the Voyager mission.

As for Near-Earth support for Pioneer Venus, a major decision was reached in deciding that Vanguard support, because of cost vs benefit for the Pioneer Venus launches, has been designated as a desirable but not mandatory requirement, and the Vanguard support has been deleted by the Office of Tracking and Data Acquisition. The deletion of Vanguard has caused the Project to require real-time telemetry and command capability from the STDN station on Ascension Island. The details of the command capability are currently under direct negotiation between Goddard and the Project. The telemetry will be provided via MIL-71 for formatting. The Command System will most likely consist of prerecorded cassette tapes located at Ascension with voice instructions from the Project for their use.

III. Multiprobe Telemetry Recovery Status

Figure 2 portrays the progress for preparing for the Multiprobe telemetry recovery. The extra open- and closed-loop receivers required are well on plan at the current time. The new analog recorders for the precarrier detection telemetry recovery are on plan, and testing to date indicates that the $\leq$1.5 dB additional loss specification on the precarrier detection recording will be easily met. During the first part of CY'77, some question was raised as to whether the purchase of brand-new Honeywell 96 recorders to meet this requirement was the most cost-effective approach for NASA, and a possible approach of utilizing existing available recorders and borrowing additional recorders from the JPL Loan Pool was investigated. The available recorders' performance compared to Honeywell 96's for this particular application was shown to involve potential additional losses, particularly with mixing of different types of recorders for record and playback, and therefore it was decided that the Honeywell 96's were the proper approach for support of Pioneer Venus. A new requirement related to the precarrier detection recordings is for providing a capability to play the recordings backwards and record the backward symbol output of the Symbol Synchronizer Assembly (SSA). Preliminary testing indicates that such a reverse playback will be feasible with the Honeywell 96 recorders with no appreciable additional loss. This requirement will require some special software for the Telemetry Processor Assembly in order to make the computer-compatible recordings of the output of the SSA. The purpose of this requirement is to attempt to recover the data that will be lost every time the DSN has to reacquire a particular Probe signal.

DSN acquisition involves the sequential acquisition of the receiver, Subcarrier Demodulator Assembly (SDA), Symbol Synchronizer Assembly, and the sequential decoder within the Telemetry Processor Assembly before usable data is produced. This sequential acquisition will take a minimum of two to three minutes (and potentially much longer) every time a receiver is out of lock and has to be reacquired. With the backward playback capability, it should be possible to go several minutes after each receiver out-of-lock and start playing data backwards so the sequential acquisitions of the receiver, SDA, and SSA are completed during a time of good forward data, and then data can be maintained in-lock up to the time of receiver acquisition. The Project will have to provide a capability for decoding the backward symbol stream recordings.

The Multiprobe entry simulator is proceeding well on plan and should provide an excellent capability for operator training for the Multiprobe Mission entry event. For more details on this device, consult Ref. 3.

The functional design of the Signal Presence Indicator (renamed the Spectral Signal Indicator) has been completed. The concept calls for procurement of three commercial 300-kHz bandwidth capability spectrum analyzers per station. A switching matrix will be provided which will enable hooking up any one of the analyzers with any one of the four open-loop receivers or to the output of the DLBI receiver or to a read-after-write of the DLBI recorder. The system will also include a microcontroller and two low-speed printers as well as CRT displays. It is intended that the microcontroller will enable preloading all of the different synthesizer settings both in the open- and closed-loop receivers so that the cursor on the spectrum analyzer can be used to locate the signal of interest and the microcontroller will do all the computations necessary to convert that detected signal into the proper frequency input for a closed-loop receiver operator. The microcontroller may also incorporate an acquisition-aiding feature such as an automatic narrower bandwidth scan of the 300-kHz region of interest.

As far as achieving total readiness for the Multiprobe entry event, the basic plan is to have established the Multiprobe

entry configuration by March 1978 to be followed by two months of procedure development utilizing the complete configurations at DSS 14 and 43. This procedure development is expected to involve utilizing both JPL and station expertise. A procedure verification period will then follow between the Orbiter launch and the Multiprobe launch where although operational proficiency will not be expected, the entry sequence will be exercised in order to verify the validity of the operational concept and procedures. Multiprobe entry testing and training for the purpose of developing operational proficiency will then commence after the Multiprobe launch up to the time of Multiprobe entry.

IV. DLBI Wind Measurement Status

Figure 3 updates the schedule contained in Ref. 2. Only significant changes in plans from that reported in Ref. 2 will be described below. The DSN receiver and calibrator work has been proceeding well and according to plan. STDN detailed receiver design involved the use of modules identical to those of the DSN receiver. The STDN therefore negotiated for the DSN to procure or fabricate the common modules, and funds were transferred from Goddard to JPL for that purpose. It is planned to provide the first set of DSN modules to Goddard on July 1 and the remaining sets on August 1, 1977. It is still intended to do a DSN-STDN equipment integration test utilizing the STDN station at Goldstone from mid-November to mid-December 1977.

Significant changes in the recorder were required because of cost problems which developed in negotiating the contract with the vendor for the operational units. The cost problems were solved by eliminating the microcontroller from the recorders, eliminating some desired multimission capabilities including the deletion of one bit A-to-D required for VLBI purposes, and the delay of one transport each for DSS 14 and 43 to FY'78. The result will be more complexity for the operators, but there has been no loss of the required fundamental capabilities for the Pioneer Venus DLBI Wind Experiment. Delay of one transport each for DSS 14 and 43 to about April 1978 will mean that initial testing will not have redundant recorders available in case of equipment failure.

The bandwidth reduction hardware and software is proceeding satisfactorily and again cost problems had to be solved in the first part of 1977 due to excessive costs proposals from the integration contractor. These cost problems were solved by renegotiation of certain details of the contract and by pulling some of the work back in-house. Detailed format of the deliverable computer-compatible recording out of the bandwidth reduction assembly is now under negotiation between the experimenter and JPL.

It is still intended to start total system checkout from end to end by tracking of ALSEP packages as each station comes on line, starting in February 1978.

There will be a major review of the end-to-end DLBI experiment and equipment in August at the Massachusetts Institute of Technology, with the Review Board comprised of the Project Manager and certain recognized experts across the country who are not directly involved with the experiment.

References

1. Miller, R. B., "Pioneer Venus 1978 Mission Support," in *The Deep Space Network Progress Report 42-32*, pp. 25-30, Jet Propulsion Laboratory, Pasadena, California, April 15, 1976.
2. Miller, R. B., "Pioneer Venus 1978 Mission Support," in *The Deep Space Network Progress Report 42-36*, pp. 22-27, Jet Propulsion Laboratory, Pasadena, California, December 15, 1976.
3. Friedenberg, S. E., "Pioneer Venus 1978 Multiprobe Spacecraft Simulator," in *The Deep Space Network Progress Report 42-38*, pp. 148-151, Jet Propulsion Laboratory, Pasadena, California, April 15, 1977.

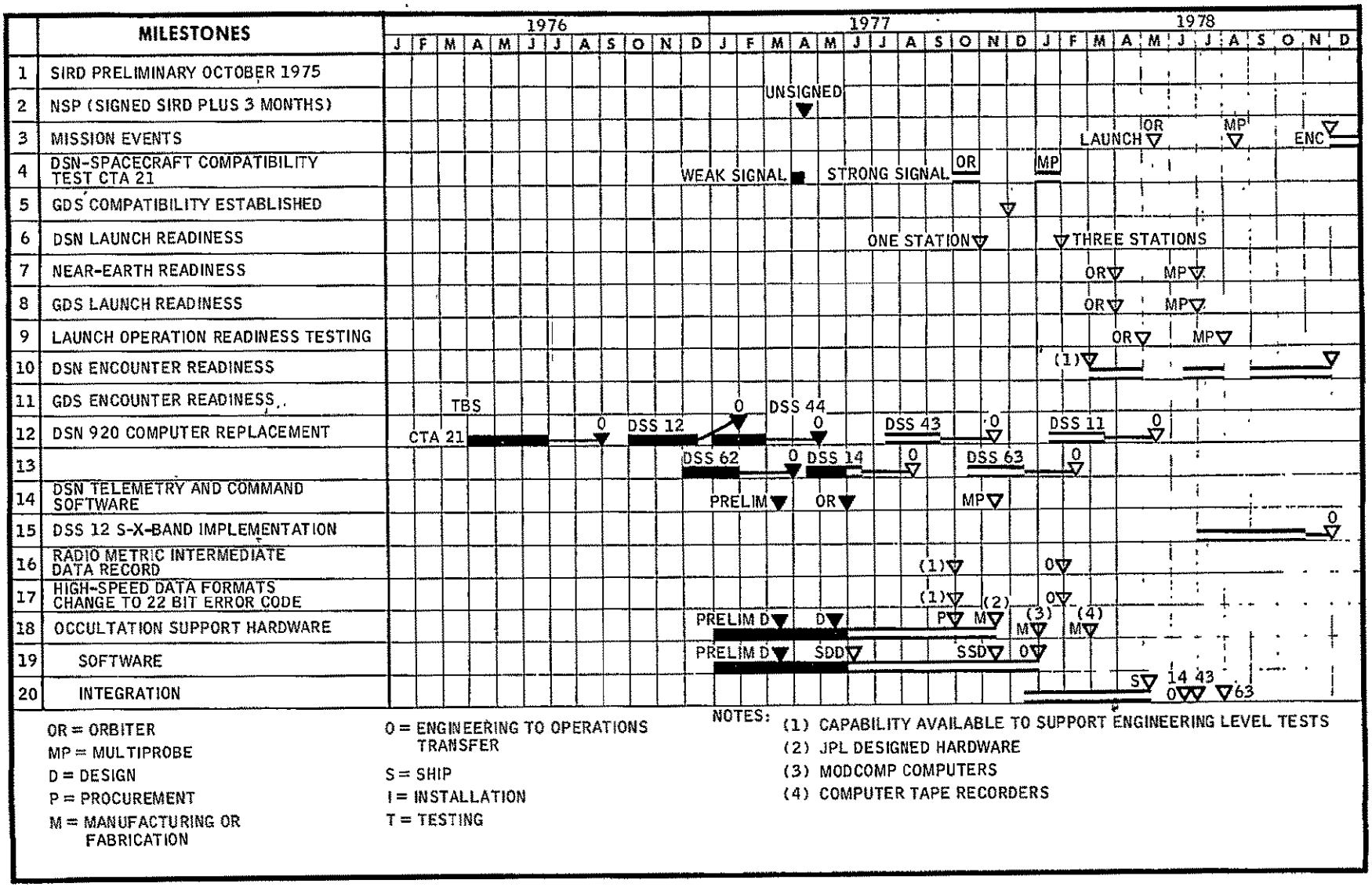

Fig. 1. DSN major milestone schedule: Pioneer Venus 1978 Orbiter and Multiprobe

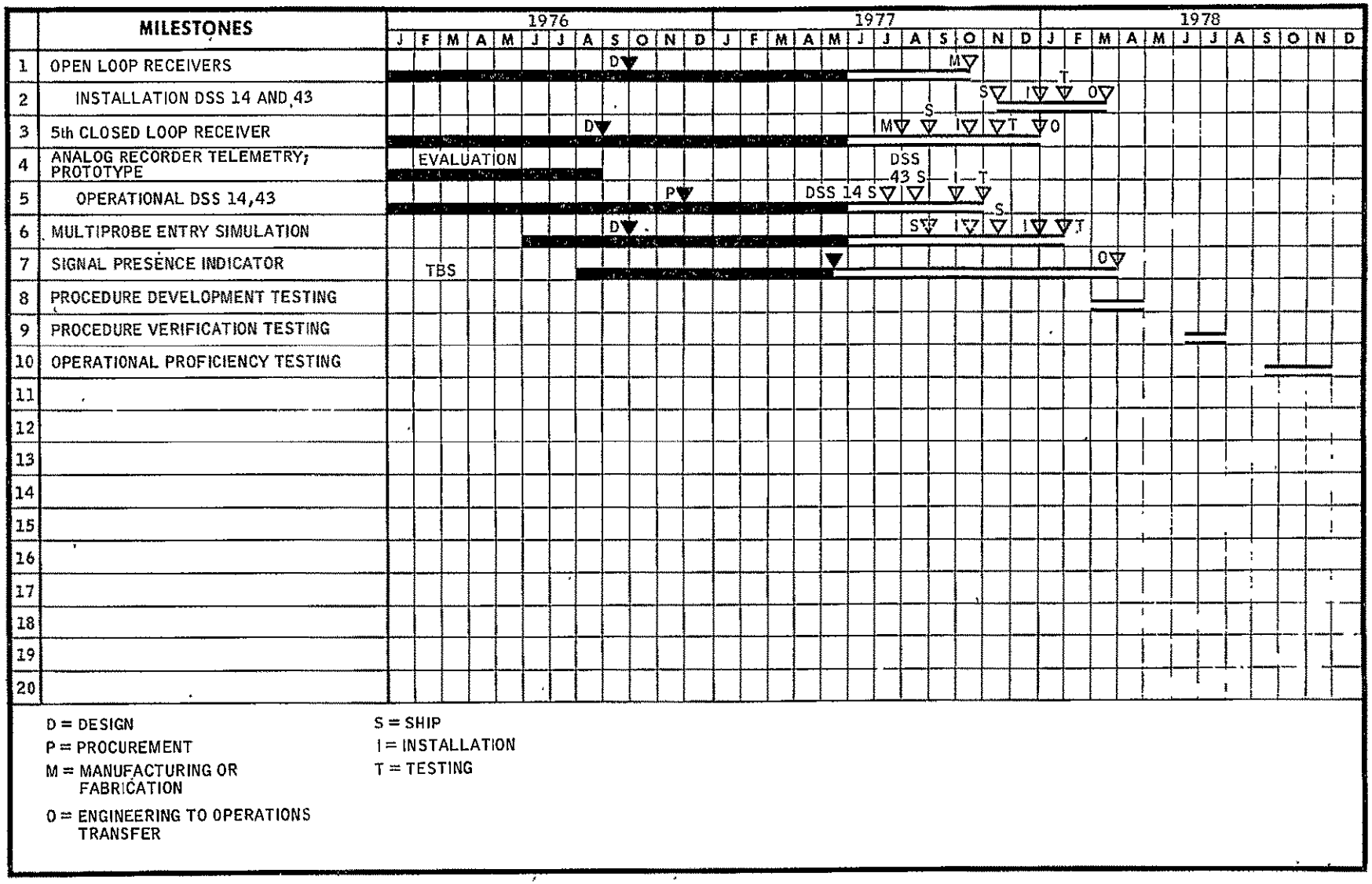

Fig. 2. DSN major milestone schedule: Pioneer Venus 1978 Multiprobe telemetry recovery

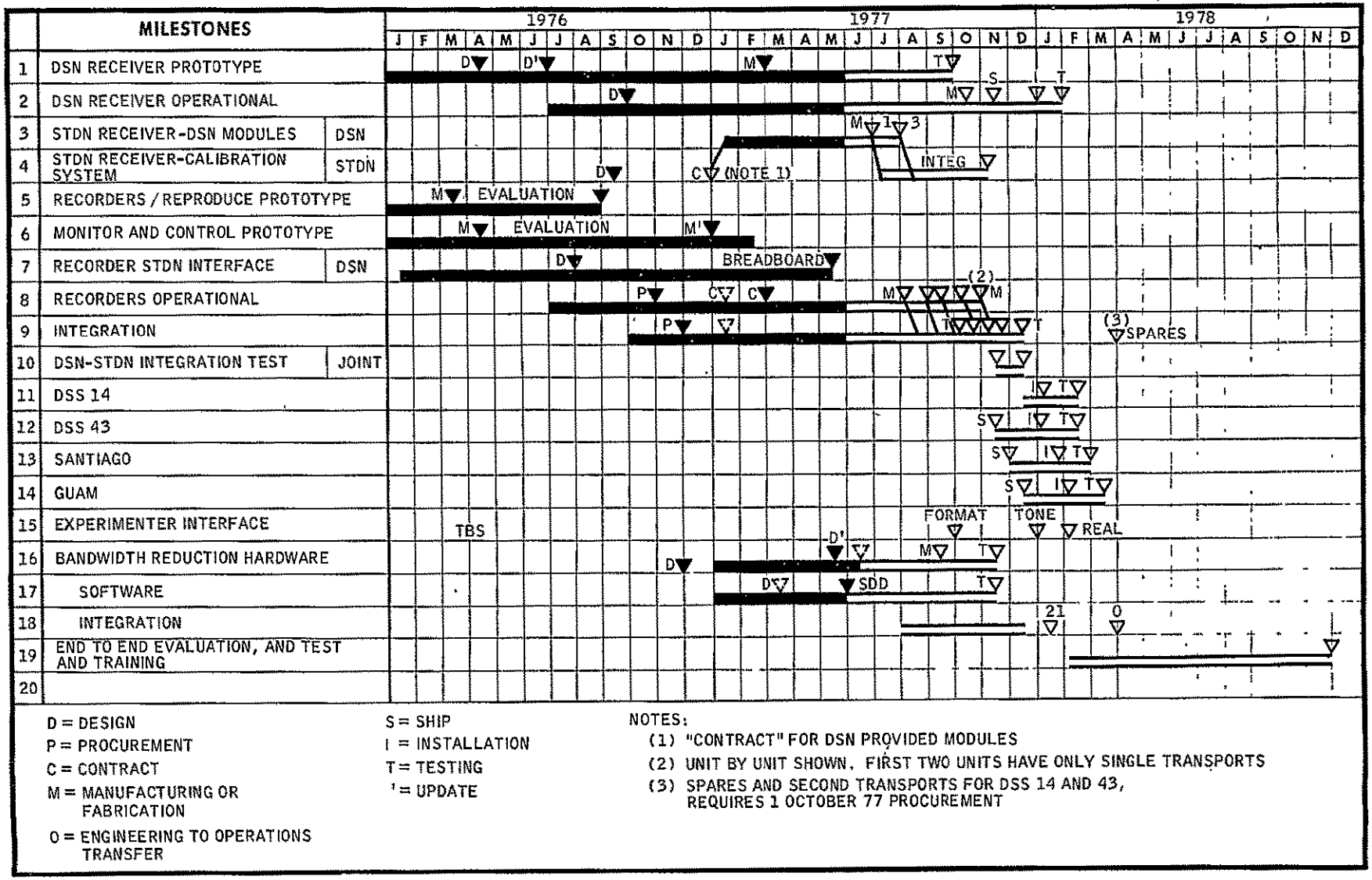

Fig. 3. DSN major milestone schedule: Pioneer Venus 1978 Multiprobe DLBI Wind Measurement Experiment

Summary Report and Status of the Deep Space Network-Voyager Flight Project Telecommunications Compatibility

A. I. Bryan and R. P. Kemp
TDA Engineering

B. D. Madsen
Telecommunications Systems Section

The DSN-Voyager telecommunications compatibility tests are an ongoing series of Engineering level tests to determine the flight-ground interface compatibility and performance characteristics between these two systems. This report provides a summary and status of tests conducted between CTA 21-Voyager Flight 1 spacecraft, CTA 21-Voyager Flight 2 spacecraft, and MIL 71-Voyager Flight 1 spacecraft.

I. Introduction

The purpose of this report is to provide an assessment and status of telecommunications compatibility between the Deep Space Network (DSN) and the Voyager (VGR-77) spacecraft. This assessment and status is derived from test results obtained between the Network, as represented in the Compatibility Test Area (CTA 21) and Spacecraft Monitoring Station (MIL 71) and by the Voyager Flight 1 (VGR 77-2) and Voyager Flight 2 (VGR 77-3) Spacecraft Telecommunications Systems.

II. Test Objectives

The objectives of these tests were to verify telecommunications design compatibility between the DSN and the Voyager flight spacecraft. The test criteria and parameters simulated direct communications between a Voyager spacecraft and a Deep Space Station (DSS). DSN-Voyager flight spacecraft design compatibility had been previously established as reported in Ref. 1.

A selected set of standard tests, as specified in the Deep Space Network-Flight Project Interface Compatibility Test Design Handbook, were performed for verifying Telecommunications Radio Frequency, Command, Telemetry, and Radio Metric compatibility.

III. Test Conditions

The tests that were performed between CTA 21 and the Voyager flight spacecraft were conducted with the spacecraft located in the Space Simulator Facility (SSF) at JPL. CTA 21-

VGR 77-2 testing was performed during the period 9-12 March 1977, and CTA 21-VGR 77-3 testing was performed during the period 28-30 April 1977. During each of these tests the SSF was simulating environmental flight conditions. The Radio Frequency Subsystems were configured as follows:

(1) Voyager 77-2

(a) S-Band

(i) Receiver 1, Channel 18 (2114.676697 MHz).

(ii) Receiver 2, Channel 18 (2114.676697 MHz).

(iii) Ultra Stable Oscillator (USO), Channel 14 (2295.000000 MHz).

(iv) Exciter Chain 1, equipped with traveling wave tube (TWT) amplifier.

(v) Exciter Chain 2, equipped with solid state amplifier.

(b) X-Band

(i) Exciters, Chain 1 and Chain 2, equipped with TWT amplifiers.

(2) Voyager 77-3

(a) S-Band

(i) Receiver 1, Channel 14 (2113.312500 MHz).

(ii) Receiver 2, Channel 14 (2113.312500 MHz).

(iii) Ultra Stable Oscillator (USO), Channel 18 (2296.481481 MHz).

(iv) Exciter Chain 1, equipped with a Watkins-Johnson flight-rated TWT amplifier.

(v) Exciter Chain 2, equipped with a Ford Aerospace flight-rated solid state amplifier.

(b) X-Band

(i) Exciter Chain 1, equipped with a Hughes Aircraft Co. nonflight-rated TWT amplifier.

(ii) Exciter Chain 2, equipped with a Watkins-Johnson flight-rated TWT amplifier.

The DSN, as represented by CTA 21, was configured to simulate a Voyager Flight Project-committed 64-meter antenna station. The ground hardware included both Block III and Block IV Receiver-Exciter Subsystems and the new Mark III Data Subsystems (MDS) for telemetry, command, and radio metric data.

The S-band and X-band RF links between CTA 21 and the SSF were open air links which had previously been calibrated for amplitude and phase stability. The DSN software provided at CTA 21 was the operational 26-meter antenna station software for the MDS.

The test that was performed between MIL 71 and the Voyager Flight 1 spacecraft was conducted with the spacecraft located in Building AO, Cape Canaveral Air Force Station, Florida. This test was performed on 25 May 1977 and consisted of S-band testing only because of the excessive RF losses at X-band. The Radio Frequency Subsystem for this test was configured as follows:

Voyager 77-2

S-Band

(i) Receiver 1, Channel 18 (2114.676697 MHz).

(ii) Receiver 2, Channel 18 (2114.676697 MHz).

(iii) Ultra Stable Oscillator (USO), Channel 14 (2295.000000 MHz).

(iv) Exciter Chain 1, equipped with a Watkins-Johnson flight-rated TWT amplifier.

(v) Exciter Chain 2, equipped with a Ford Aerospace flight-rated solid state amplifier.

The DSN, as represented by MIL 71, Kennedy Space Center, Florida, was configured to simulate a Voyager Flight Project-committed 64-meter antenna station. The ground hardware included both Block III and Block IV Receiver-Exciter Subsystems and the new Mark III Data Subsystems (MDS) for telemetry, command, and radio metric data.

The S-band RF links between MIL 71 and Building AO were open air links which had previously been calibrated for amplitude stability. The DSN software provided at MIL 71 was the operational 64-meter antenna station software for the MDS.

In support of the Voyager Flight Project Mission specifications, the following uplink modulation indices were utilized:

(1) Ranging, 45° (−3.0 dB carrier suppression).

(2) Command, 20° (−0.54 dB carrier suppression for mission nominal) and 56° (−5.0 dB carrier suppression for mission threshold).

IV. Test Results

Tables 1, 2, and 3 (telecommunications compatibility test summaries) provide a listing of test configurations, test criteria, parameters, and results. Refer to Figs. 1 and 2 for DSN and spacecraft RFS mode configurations. Significant test results and comments are discussed below.

A. Radio Frequency Acquisition and Tracking

All objectives of these tests were met with no problems noted. In the CTA 21-Voyager Flight 1 test series, a special test was performed to simulate the approximate 1.5-MHz doppler shift when in the noncoherent mode of operation. Initial test conditions were as follows:

(1) Uplink frequency 2114.676697 MHz (Channel 18).

(2) Downlink frequency 2294.998855 MHz (Channel 14).

(3) Biased doppler frequency approximately 481 kHz.

In order to alleviate this condition, a possible work-around solution for the 26-meter DSS was tested and is illustrated in Fig. 3. A spare X-3 Frequency Multiplier and Distribution Amplifier was mounted on the Block III Receiver and its input jack (J1) was connected to the station spare Hewlett-Packard Synthesizer. The HP Synthesizer was driven by a spare station 1-MHz frequency standard. The X-3 Frequency Multiplier and Distribution Amplifier 22-MHz output (J4) was connected to J-2 of the 57/221 Frequency Shifter (module 4A210) and the 66-MHz output (J8) was connected to J1 of the 66/70 Balanced Mixer (module 4A205). The HP Synthesizer was programmed for a frequency of 22.0136609 Hz (a ratio of 240/221 for the Ultra Stable Oscillator, 2294.998855 MHz) and the biased doppler read 999998 Hz. This test verified that the 26-meter DSS can support noncoherent doppler conditions with existing station hardware resources.

In addition, in the CTA 21-Voyager Flight 2 test series, a special test was performed to simulate the 7.2-kbps coded data, 22.5-kHz subcarrier possible interference problem to be encountered during initial Goldstone acquisition. Initial test conditions were as follows:

(1) Spacecraft Configuration

(a) Downlink frequency 2296.481481 MHz (Channel 18).

(b) 40-bps uncoded data, 22.5-kHz subcarrier (launch mode).

(c) Downlink frequency ramp rate of −100 Hz per second at S-band (actual doppler expected during initial Goldstone pass).

(2) DSN Configuration

(a) Block III Receiver (input terminated in dummy load).

(b) Block III Subcarrier Demodulator Assembly (configured for proper data rate and subcarrier frequency).

(c) Telemetry Processor Assembly (Channel 1 configured for 7.2-kbps coded data, Channel 2 configured for 40-bps uncoded data).

The objectives of this test were really two fold: (1) to determine how fast the various steps of complete acquisition could be completed, and (2) would the 7.2-kbps, 22.5-kHz beat frequency (as observed on the receiver dynamic phase error) jeopardize or impede the overall acquisition sequence? The test is described below in the time sequence in which it was performed.

Sequence	Description
T = 0	The Block III Receiver input was switched to the receiving antenna and a sweep search of the VCO was initiated.
T + 10 s	RF acquisition was completed.
T + 20 s	Subcarrier Demodulation acquisition was completed.
T + 2 min 24 s	Symbol Synchronizer Assembly acquisition completed.

Sequence	Description
T + 5 min	Spacecraft switched from 40-bps uncoded data to 7.2-kbps coded data. 22.5-kHz subcarrier remained unchanged.
T + 5 min 18 s	Subcarrier Demodulation acquisition completed on new data rate.
T + 6 min 05 s	Maximum Likelihood Decoder acquisition.
T + 6 min 35 s	Symbol Synchronizer Assembly acquisition completed on new data rate.

Photographs of the Block III Receiver dynamic phase error for both the 40-bps uncoded data and the 7.2-kbps coded data modes were recorded. The 7.2-kbps – 22.5-kHz beat frequency is clearly distinguishable, but apparently does not hamper overall system data processing if RF acquisition has been established.

It is concluded from this test, therefore, that if Goldstone can definitely establish RF acquisition within the 5 minutes from their initial view period to the data rate switch, there should be no problem in providing maximum data recovery to the Project.

B. Telemetry

The CTA 21-Voyager Flight 1 tests were supported using a version of the standard 26-meter DSS telemetry software that would operate at all data rates, including the high rate 115.2 kbps. All lock status and signal-to-noise ratio data were processed and displayed. However, this version of the software did not provide Original Data Records or Wide-Band Data capability.

The CTA 21-Voyager Flight 2 tests were supported using the 64-meter DSS telemetry software. The software performed satisfactorily for processing and displaying all lock status and signal-to-noise data. However, a special test to transmit 115.2-kbps data to the MCCC was not fully successful. The MCCC was able to frame synchronize long enough to recognize that the data contained all ones, but were not able to maintain continuous lock (periodic frames were being lost). This condition was verified by the software CDE who acknowledged a known problem with the wide-band data communications buffer. A fix for this problem was initiated and was subsequently successfully demonstrated for rates up to 67.2-kbps during a GDS test during the week of 16 May 1977 between CTA 21 and the MCCC. The telemetry rates of 89.6-kbps and 115.2-kbps remained an open item. In addition, an Original Data Recording was made during this test and successfully played back to the MCCC.

The MIL 71-Voyager Flight 1 tests were supported using the 64-meter DSS telemetry software. The software performed satisfactorily for processing and displaying all lock status and signal-to-noise data.

The telemetry rates of 80 bps and 1280 bps were tested for the first time during this series of tests and operation was satisfactory.

The theoretical 3.0-dB difference between MCD SNR and SSA SNR values was not obtained during these compatibility tests. The actual difference observed was approximately 2.2-2.5 dB. This condition is apparently unique to the MIL 71 equipment as it has not been encountered at CTA 21 or DSS 12 during Systems Performance Testing. This condition was first observed during Systems Acceptance Testing at MIL 71 and was further verified during special rate 7:1/2 and rate 7:1/3 telemetry performance testing. This condition does not impact compatibility.

C. Command

Command testing at both CTA 21 and MIL 71 with both Voyager flight spacecraft was performed at nominal uplink signal levels and at signal levels below expected project mission conditions. Two separate, non-timed commands (2N: X-band ranging channel ON, and 2NR: X-band ranging channel OFF) were successfully sent to the spacecraft and successfully executed.

D. Radio Metric

The CTA-Voyager Flight 1 tests were designed to acquire spacecraft internal group delay measurements under both hot and cold conditions. Because of spacecraft constraints while in the environmental chamber, however, only one such set of measurements was possible for a particular RFS mode. A total of three tests were completed with test RM-2-6 performed while hot only. All tests included both S- and X-band measurements.

All objectives of the CTA 21-Voyager Flight 2 tests were successfully completed with the exception of a zero delay measurement. This measurement is required in order to compute the overall link delay so that the spacecraft delay can be determined. However, before the zero delay measurement could be performed, the Space Simulator Facility configuration was de-implemented and the Zero Delay Transponder was shipped to Florida. Therefore, the ranging tests that were performed provide only the overall measurement through the link and spacecraft. These tests will be repeated during the

DSN-Voyager Flight 2 testing with MIL 71 for the final ranging delay measurement and calibration.

Because of excessive RF link losses between MIL-71 and Building AO, there were no ranging tests performed at either S- or X-band during the MIL 71-Voyager flight tests.

V. Present Status and Future Plans

The DSN-Voyager Flight Project Telecommunications Compatibility Test Program has successfully verified compatibility for RF Acquisition and Tracking, Telemetry, Command, and Radio Metric Data (Ranging). All known problems encountered to date have been dealt with, and the solution to each problem has been resolved by either an engineering change or operational work-around.

The next DSN-Voyager Telecommunications Compatibility Test is scheduled for 14 June 1977 between MIL 71 and the Voyager 77-3 spacecraft. This test will be limited to S-band testing only as the spacecraft will be located in Building AO.

Additional test time has been scheduled for both flight spacecraft when they are located in the Spacecraft Assembly and Encapsulation Facilities (SAEF) 1 and 2 at Kennedy Space Center. These tests will be performed at X-band and will include extensive ranging delay calibrations and measurements.

Reference

1. Bryan, A. I., et al., "Summary Report and Status of the Deep Space Network — Mariner Jupiter/Saturn 1977 Flight Project Telecommunications Compatibility," *The Deep Space Network Progress Report 42-38*, pp. 16-37, Jet Propulsion Laboratory, Pasadena, Calif., Apr. 15, 1977.

Table 1. DSN-Voyager Flight 1 spacecraft telecommunications compatibility test summary [a]

Date	Test title	Test No.	DSN mode	S/C RFS mode	Test conditions	Criteria	Performance	Time, min
3/10/77	DL threshold one way	RF-1-2	$000\frac{1}{6}00$	4510-11	S-band DL frequency: 2294.998880 MHz 12 Hz, 2 BLo	−159.0 ± 1.0 dBm	−158.0 dBm	16
					X-band DL frequency: 8414.995955 MHz 30 Hz, 2 BLo		−145.3 dBm	
3/9/77	DL threshold one way	RF-1-3	$000\frac{1}{6}00$	6734-16	S-band DL frequency: 2294.998860 MHz 12 Hz, 2 BLo	−159.0 ± 1.0 dBm	−158.0 dBm	54
					X-band DL frequency: 8414.995785 MHz 30 Hz, 2 BLo		−145.7 dBm	
3/10/77	DL threshold two way	RF-1-4	$002\frac{1}{6}00$	4510-11	S-band DL frequency: 2296.481560 MHz 12 Hz, 2 BLo	−159.0 ± 1.0 dBm	−158.0 dBm	27
					X-band DL frequency: 8420.432470 MHz 30 Hz, 2 BLo		−144.5 dBm	
3/10/77	DL threshold two way	RF-1-5	$122\frac{1}{6}00$	6730-16	S-band DL frequency: 2296.481600 MHz 12 Hz, 2 BLo	−159.0 ± 1.0 dBm	−158.5 dBm	60
					X-band DL frequency: 8420.432555 MHz 30 Hz, 2 BLo		−145.5 dBm	
3/10/77	UL receiver threshold	RF-2-1	$002\frac{1}{6}00$	4510-11	S-band UL frequency: 2114.676672 MHz	⩽ 152.0 dBm	−155.0 dBm	13
3/10/77	UL receiver threshold	RF-2-4	122000	6630-16	S-band UL frequency: 2114.676768 MHz	⩽ 152.0 dBm	−156.0 dBm	19
3/10/77	Transmitter phase jitter	RF-5-1	$000\frac{1}{2}00$	4500-11	S-band DL frequency: 2294.998880 MHz (one-way)	⩽ 3.0 deg rms	1.04 deg rms	66
			$000\frac{5}{6}00$		X-band DL frequency: 8414.936540 MHz (one-way)	< 11.0 deg rms	5.35 deg rms	
					S-band UL frequency: 2114.676672 MHz			
			$002\frac{1}{2}00$	4510-11	S-band DL frequency: 2296.481504 MHz (two-way)	⩽2.3 deg rms	2.14 rms	
			$002\frac{5}{6}00$		X-band DL frequency: 8420.373140 MHz (two-way)	⩽ 8.4 deg rms	6.56 deg rms	
3/10/77	Transmitter phase jitter	RF-5-3	$002\frac{1}{2}00$		S-band UL frequency: 2114.676672 MHz			18

[a]See Table 4 for definition of terms used.

Table 1 (contd)

Date	Test title	Test No.	DSN mode	S/C RFS mode	Test conditions	Criteria	Performance	Time, min
3/10/77	Transmitter phase jitter (contd)				S-band DL frequency: 2296.481504 MHz (two-way)	⩽ 2.3 deg rms	1.68 deg rms	
			$002\frac{5}{6}00$		X-band DL frequency: 8420.373140 MHz (two-way)	⩽ 8.4 deg rms	6.20 deg rms	
3/12/77	DL RF spectrum analysis	RF-6-1	102300	7513-12	S-band UL frequency: 2114.676672 MHz S-band DL frequency: 2296.481420 MHz	Observe presence of unpredicted spectral components through the S-band solid state amplifier (SSA)	None observed	15
3/12/77	Special test for dual-doppler condition	RF-7-1	001100	7737-16	S-band UL frequency: 2114.676672 MHz (Channel 18) S-band DL frequency: 2294.998855 MHz (Channel 14) UL signal level: −107.5 dBm DL signal level: −93.0 dBm	Install spare synthesizer and X-3 Frequency Multiplier Distribution Amplifier; adjust Synthesizer for 1 MHz biased doppler and record synthesizer frequency of 22.0136609 MHz	Biased doppler read: 999998 MHz	15
3/9/77	Telemetry processing	TM-3-1	$000\frac{3}{6}\frac{2}{1}\frac{1}{2}$	6730-16	S-band DL signal level: −120.0 dBm CTA 21 three-way (SE two-way)	0.0 BER Ability to process	MCD SNR: 9.6 dB X-band SSA SNR: 4.7 dB S-band SSA SNR: 26.3 dB	18
3/10/77	Telemetry	TM-3-2	$000\frac{3}{6}\frac{2}{1}\frac{1}{2}$	6734-16	S-band DL signal level: −120.0 dBm X-band DL signal level: −120.0 dBm CTA 21 three-way (SE two-way)	0.0 BER Ability to process	MCD SNR: 10.1 dB X-band SSA SNR: 5.5 dB S-band SSA SNR. 30.7 dB	
3/9/77	Telemetry processing	TM-3-6	$000\frac{3}{6}\frac{2}{1}\frac{1}{2}$	6730-16	S-band DL signal level: −120.0 dBm CTA 21 three-way (SE two-way)	0.0 BER Ability to process	MCD SNR: 10.175 dB X-band SSA SNR: 12.3 dB S-band SSA SNR: 25.5 dB	31

Table 1 (contd)

Date	Test title	Test No.	DSN mode	S/C RFS mode	Test conditions	Criteria	Performance	Time, min
3/10/77	Telemetry processing	TM-3-10	000 $\frac{3}{6}\frac{2}{1}\frac{1}{2}$	6734-16	S-band DL signal level: −120.0 dBm	0.0 BER	MCD SNR: 9.6 dB	23
					X-band DL signal level: −115.0 dBm	Ability to process	X-band SSA SNR: 5.0 dB	
					CTA 21 three-way (SE two-way)		S-band SSA SNR: 29.6 dB	
3/10/77	Command processing	CM-1-1	011000	4512-11	S-band UL frequency: 2114.676672 MHz	Proper subcarrier and bit sync acquisition. Verification of command execution		21
					UL carrier suppression: −5.0 dB			
					Subcarrier offset: 0.0 Hz @ −144 dBm, P_T		OK	
					+0.2 Hz @ −143 dB, P_T		OK	
					−0.2 Hz @ −143 dB, P_T		OK	
3/10/77	Command processing	CM-1-2	011000	4533-11	S-band UL frequency: 2114.676672 MHz	Proper subcarrier and bit sync acquisition. Verification of command execution		37
					UL carrier suppression: −5.0 dB			
					Subcarrier offset:			
					0.0 Hz @ −144 dBm, P_T		OK	
					+0.2 Hz @ −143 dBm, P_T		OK	
					−0.2 Hz @ −143 dBm, P_T		OK	
3/10/77	Range delay calibration verification test	RM-2-1	102 $\frac{3}{6}$ 00	4513-11	S-band UL frequency: 2114.676672 MHz	< 1000 ns		90
					S-band DL frequency: 2296.481420 MHz			
					S-band DL signal level: −100.0 dBm			
					X-band DL frequency 8420.431875 MHz			
					X-band DL signal level: −100.0 dBm			
					SPACECRAFT COLD			
					UL signal level: −110.0 dBm		'S' delay: 724.46 ns 'X' delay: 652.65 ns	
					−120.0 dBm		'S' delay: 733.04 ns 'X' delay: 657.40 ns	
					−130.0 dBm		'S' delay: 735.14 ns 'X' delay: 659.14 ns	

Table 1 (contd)

Date	Test title	Test No.	DSN mode	S/C RFS mode	Test conditions	Criteria	Performance	Time, min
3/10/77	Range delay calibration verification test (contd)				SPACECRAFT HOT			
					UL signal level: −112.0 dBm		'S' delay: 715.45 ns 'X' delay: 648.75 ns	
					−120.0 dBm		'S' delay. 739.92 ns 'X' delay: 651.05 ns	
					−130 dBm		'S' delay: 735.99 ns 'X' delay: 654.9 ns	
3/10/77	Range delay calibration verification test	RM-2-3	$102\frac{3}{6}00$	4533-11	S-band UL frequency: 2114.676672 MHz	< 1000 ns		43
					S-band DL frequency: 2296.481480 MHz			
					S-band DL signal level: −100.0 dBm			
					X-band DL frequency: 8420.432215 MHz			
					X-band DL signal level: −100.0 dBm			
					SPACECRAFT COLD			
					UL signal level: −110.5 dBm		'S' delay: 741.34 ns 'X' delay: 664.02 ns	
					−120.0 dBm		'S' delay: 747.51 ns 'X' delay: 668.4 ns	
					−130.0 dBm		'S' delay: 749.18 ns 'X' delay: 658.23 ns	
3/12/77	Range delay calibration verification test	RF-2-6	$102\frac{3}{6}00$	7733-16	S-band UL frequency: 2114.676768 MHz	< 1000 ns		
					S-band DL frequency: 2296.481600 MHz			
					S-band DL signal level: −100.0 dBm			
					X-band DL frequency: 8420.432555 MHz			
					X-band DL signal level: −100.0 dBm			

Table 1 (contd)

Date	Test title	Test No.	DSN mode	S/C RFS mode	Test conditions	Criteria	Performance	Time, min
3/12/77	Range delay calibration verification test (contd)				SPACECRAFT HOT			
					UL signal level: -111.0 dBm		'S' delay: 719.92 ns 'X' delay: 662.40 ns	
					-120.0 dBm		'S' delay: 720.81 ns 'X' delay: 665.35 ns	
					-130.0 dBm		'S' delay: 726.23 ns 'X' delay: 671.69 ns	

Table 2. DSN-Voyager Flight 2 spacecraft telecommunications compatibility test summary [a]

Date	Test title	Test No.	DSN mode	S/C RFS mode	Test conditions	Criteria	Performance	Time, min
4/29/77	DL threshold one-way	RF-1-2	000$\frac{1}{6}$00	6554-11	S-band DL frequency: 2296.481100 MHz 12 Hz, 2 BLo	−158.0 ± 1.0 dBm	−157.5 dBm	18
					X-band DL frequency. 8420.430770 MHz 30 Hz, 2 BLo		−148.0 dBm	
4/30/77	DL threshold one-way	RF-1-3	000$\frac{1}{6}$00	6737-17	S-band DL frequency: 2296.481100 MHz 12 Hz, 2 BLo	−158.0 ± 1.0 dBm	−159.0 dBm	16
					X-band DL frequency: 8420.430600 MHz 30 Hz, 2 BLo		−149.0 dBm	
4/29/77	DL threshold two-way	RF-1-4	002$\frac{1}{6}$00	4550-11	S-band DL frequency: 2295.000240 MHz 12 Hz, 2 BLo	−158.0 ± 1.0 dBm		35
					X-band DL frequency. 8415.000885 MHz 30 Hz, 2 BLo			
4/30/77	DL threshold two-way	RF-1-5	122$\frac{1}{6}$00	6733-17	S-band DL frequency: 2295.000040 MHz 12 Hz, 2 BLo	−158.0 ± 1.0 dBm	−159.0 dBm	23
					X-band DL frequency: 8415.000205 MHz 30 Hz, 2 BLo		−149.0 dBm	
4/29/77	UL receiver threshold	RF-2-1	002$\frac{1}{6}$00	4550-11	S-band UL frequency: 2113.312512 MHz	⩽152.0 dBm	−155.0 dBm	11
4/29/77	UL receiver threshold	RF-2-4	122000	4570-11	S-band UL frequency: 2113.312512 MHz	⩽152.0 dBm	−155 5 dBm	12
4/29/77	Transmitter phase jitter	RF-5-1	000$\frac{3}{4}$00	4840-11	S-band DL frequency: 2296.481080 MHz (one-way)	⩽3.0 deg rms	1.98 deg rms	109
			000$\frac{5}{6}$00		X-band DL frequency: 8420.430685 MHz (one-way)	⩽11.0 deg rms	6.55 deg rms	
					S-band UL frequency: 2113.312512 MHz			
			002$\frac{3}{4}$00	4550-11	S-band DL frequency: 2295.000100 MHz (two-way)	⩽2.3 deg rms	0.63 deg rms	
			002$\frac{5}{6}$00		X-band DL frequency: 8415.000205 MHz (two-way)	⩽8.4 deg rms	10.09 deg rms	
4/30/77	Transmitter phase jitter	RF-5-3	000$\frac{3}{4}$00	6727-17	S-band DL frequency: (one-way) 2296.481100 MHz	⩽3.0 deg rms	1.91 deg rms	109

[a]See Table 4 for definition of terms used.

Table 2 (contd)

Date	Test title	Test No.	DSN mode	S/C RFS mode	Test conditions	Criteria	Performance	Time, min
4/30/77	Transmitter phase jitter (contd)		$000\frac{5}{6}00$		X-band DL frequency: (one-way) 8420.430770 MHz	≤11.0 deg rms	6.55 deg rms	
			$002\frac{3}{4}00$	6737-17	S-band UL frequency: 2113.312512 MHz			
					S-band DL frequency (two-way) 2295.000004 MHz	≤2.3 deg rms	2.21 deg rms	
					X-band DL frequency: (two-way) 8415.000205 MHz	≤8.4 deg rms	8.28 deg rms	
4/30/77	Special rf acquisition test (simulated Goldstone initial acquisition)	RF-7-2	000112	6713-17	Spacecraft simulated −100 Hz/s S-band doppler for initial Goldstone pass and data switch sequence	Acquire RF, SDA, TPA for 40-bps uncoded and then switch to 7.2-kbps coded data	Acquired satisfactorily	30
4/30/77	Command processing	CM-1-	011000	6713-17	S-band UL frequency: 2114.676672 MHz	Proper subcarrier and bit sync acquisition		12
					UL carrier suppression; −5.0 dB			
					Subcarrier offset:			
					0.0 Hz @ −144 dBm, P_T		OK	
					+0.2 Hz @ −144 dBm, P_T		OK	
					−0.2 Hz @ −144 dBm, P_T		OK	
4/30/77	Command processing	CM-1-2	011000	6733-17	S-band UL frequency: 2114 676672 MHz	Proper subcarrier and bit sync acquisition		50
					UL carrier suppression: −5.0 dB	Verification of command execution		
					Subcarrier offset:			
					0.0 Hz @ −144 dBm, P_T		OK	
					+0.2 Hz @ −144 dBm, P_T		OK	
					−0.2 Hz @ −144 dBm, P_T		OK	
4/29/77	Telemetry processing	TM-3-1	$000\frac{3}{6}\frac{2}{1}\frac{1}{2}$	4570-11	S-band DL signal level: −122.8 dBm	0.0 BER	MCD SNR: 10.1 dB	83
					CTA 21 three-way (SE two-way)	Ability to process	X-band SSA SNR: 8.6 dB	

Table 2 (contd)

Date	Test title	Test No.	DSN mode	S/C RFS mode	Test conditions	Criteria	Performance	Time, min
4/29/77	Telemetry processing (contd)				X-band = 7.2 kbps coded S-band = 40 bps uncoded		S-band SSA SNR: 29.1 dB	
4/29/77	Telemetry processing	TM-3-2	000 3/6 2/1 1/2	4570-11	S-band DL signal level: −121.9 dBm X-band DL signal level: −122.9 dBm CTA 21 three-way (SE two-way) X-band = 29.9 kbps coded S-band = 40 bps uncoded	0 0 BER Ability to process	MCD SNR: 4.8 dB X-band SSA SNR: 1.8 dB S-band SSA SNR: 15.3 dB	24
4/29/77	Telemetry processing	TM-3-6	000 3/6 2/1 1/2	4553-11	S-band DL signal level: CTA 21 three-way (SE two-way) X-band = 44 8 kbps coded X-band = 40 bps uncoded	0.0 BER Ability to process	MCD SNR: 10.175 dB X-band SSA SNR: 8.4 dB	10
4/29/77	Telemetry processing	TM-3-10	000 3/6 2/1 1/2	6733-17	S-band DL signal level: −111.0 dBm X-band DL signal level. −111.0 dBm CTA 21 three-way (SE two-way) X-band = 115.2 kbps coded S-band = 40 bps uncoded	0.0 BER Ability to process	MCD SNR 9.9 dB X-band SSA SNR: 5.8 dB S-band SSA SNR: 19.2 dB	39
4/29/77	Range delay calibration verification test	RM-2-1	102 3/6 00		S-band UL frequency: 2113.312512 MHz S-band DL frequency: 2295.000080 MHz S-band DL signal level: −100.0 dBm X-band DL frequency: 8415.000290 MHz X-band DL signal level: −100.0 dBm SPACECRAFT HOT UL signal level: −110.0 dBm	<1000 ns	No zero delay obtained 'S' range 6055.04 ns 'X' range 6838.55 ns	90

Table 2 (contd)

Date	Test title	Test No.	DSN mode	S/C RFS mode	Test conditions	Criteria	Performance	Time, min
4/29/77	Range delay calibration verification test (contd)				–120.0 dBm		'S' range 6065.9 ns 'X' range 6844.7 ns	
					–130.0 dBm		'S' range bad data point	
					Receiver VCO temp: 36.35°C		'X' range bad data point	
4/29/77	Range delay calibration verification test	RM-2-3	$102\frac{3}{6}00$	4573-11	S-band UL frequency 2113.312512 MHz S-band DL frequency: 2295.000080 MHz S-band DL signal level: –100.0 dBm X-band DL frequency: 8415.000290 MHz X-band DL signal level: –100.0 dBm	<1000 ns	No zero delay obtained	46
					SPACECRAFT HOT			
					UL signal level: –110.0 dBm		'S' range 6052.3 ns 'X' range 6818.7 ns	
					–120.0 dBm		'S' range 6079.5 ns 'X' range 6823.0 ns	
					–130.0 dBm		'S' range 6050.6 ns	
					Receiver VCO temp. 35.64°C		'X' range 6831.9 ns	
4/30/77	Range delay calibration verification test	RF-2-6	$102\frac{3}{6}00$	6713-17	S-band UL frequency: 2113.312512 MHz S-band DL frequency: 2295.000060 MHz S-band DL signal level: –100.0 dBm X-band DL frequency: 8415.000205 MHz X-band DL signal level: –100 0 dBm	<1000 ns	No zero delay obtained	45

Table 2 (contd)

Date	Test title	Test No.	DSN mode	S/C RFS mode	Test conditions	Criteria	Performance	Time, min
4/30/77	Range delay calibration verification test (contd)				SPACECRAFT HOT			
					UL signal level: −110.0 dBm			'S' range 6060.1 ns
								'X' range 6847.1 ns
					−120.0 dBm			'S' range 6070.8 ns
								'X' range 6850.0 ns
					−130.0 dBm			'S' range 6068.4 ns
					Receiver VCO temp: 37.77°C			'X' range 6851.8 ns

Table 3. DSN (MIL 71)-Voyager Flight 1 spacecraft telecommunications test summary [a]

Date	Test Title	Test No.	DSN mode	S/C RFS mode	Test conditions	Criteria	Performance	Time, min
5/25/77	DL threshold one-way	RF-1-2	000300	4543-17	S-band DL frequency: 2294.998880 MHz 10 Hz, 2 BLo	−158.0 ± 1.0 dBm	−157.8 dBm	15
5/25/77	DL threshold one-way	RF-1-3	000300	6760-17	S-band DL frequency. 2294.998880 MHz 10 Hz, 2 BLo	−158.0 ± 1.0 dBm	−158.0 dBm	38
5/25/77	DL threshold two-way	RF-1-4	002300	4553-17	S-band DL frequency: 2296.481460 MHz 10 Hz, 2 BLo	−158.0 ± 1.0 dBm	−158.8 dBm	18
5/25/77	DL threshold two-way	RF-1-5	002300	6773-17	S-band DL frequency: 2296.481460 MHz 10 Hz, 2 BLo	−158.0 ± 1.0 dBm	−158.2 dBm	38
5/25/77	UL receiver threshold	RF-2-1	002300	4513-17	S-band UL frequency: 2114.676672 MHz	≤−152.0 dBm	−152.0 dBm	20
5/25/77	UL receiver threshold	RF-2-2	002300	4533-17	S-band UL frequency: 2114.676672 MHz	≤−152.0 dBm	−151.0 dBm	55
5/25/77	UL receiver threshold	RF-2-3	002300	4553-17	S-band UL frequency: 2114.676672 MHz	≤−152.0 dBm	−154.2 dBm	11
5/25/77	UL receiver threshold	RF-2-4	002300	6773-17	S-band UL frequency: 2114.676672 MHz	≤−152.0 dBm	−153.5 dBm	16
5/25/77	Command processing	CM-1-1	112300	4553-17	S-band UL frequency: 2114.676672 MHz UL carrier suppression: −5.0 dB	Proper subcarrier and bit sync acquisition		19
					Subcarrier offset: 0.0 Hz @ −144 dBm, P_T		OK	
					+0.2 H @ −144 dBm, P_T		OK	
					−0.2 Hz @ −144 dBm, P_T		OK	
5/25/77	Command processing	CM-1-2	112300	6773-17	S-band UL frequency: 2114.676672 MHz	Proper subcarrier and bit sync acquisition		38
					UL carrier suppression −5.0 dB	Verification of command execution		
					Subcarrier offset 0.0 Hz @ −144 dBm, P_T		OK	

[a]See Table 4 for definition of terms used.

Table 3 (contd)

Date	Test Title	Test No.	DSN mode	S/C RFS mode	Test conditions	Criteria	Performance	Time, min
5/25/77	Command processing (contd)				+0.2 Hz @ −144 dBm, P_T		OK	
					−0.2 Hz @ −144 dBm, P_T		OK	
5/25/77	Telemetry spectrum analysis and modulation index	TM-1-4	002311	4533-17	S-band UL frequency: 2114.676672 MHz S-band DL frequency: 2296.481460 MHz TLM bit rate: 7.2 kbps Subcarrier frequency: 360 kHz	No unexpected radiation components within 40 dB of carrier	None observed	8
5/25/77	Telemetry spectrum analysis and modulation index	TM-1-10	002311	4533-17	S-band UL frequency: 2114.676672 MHz S-band DL frequency: 2296.481460 MHz TLM bit rate. 1200 bps Subcarrier frequency: 22.5 kHz	No unexpected radiation components within 40 dB of carrier	None observed	10
5/25/77	Telemetry performance verification test	TM-2-10	002311	4533-17	S-band DL signal level: −141.0 dBm TLM bit rate. 1200 bps coded STb/No = 5.0 dB Subcarrier frequency: 22.5 kHz	Ability to process	MCD SNR: 4.144 dB SSA SNR: 1.64 dB	16
5/25/77	Telemetry performance verification test	TM-2-13	002311	4533-17	S-band DL signal level: −131.0 dBm TLM bit rate: 7.2 kbps coded STb/No = 8.0 dB Subcarrier frequency: 360 kHz	Ability to process	MCD SNR: 8.795 dB SSA SNR. 5.45 dB	40
5/25/77	Telemetry performance verification test	TM-2-14	002311	4533-17	S-band DL signal level −141.0 dBm TLM bit rate: 1280 bps coded STb/No = 5.0 dB Subcarrier frequency: 22.5 kHz	Ability to process	MCD SNR: 3.992 dB SSA SNR 1.81 dB	12
5/25/77	Telemetry performance verification test	TM-2-15	002311	4533-17	S-band DL signal level: −146.3 dBm TLM bit rate: 80 bps coded STb/No = 6.0 dB Subcarrier: 22.5 kHz	Ability to process	MCD SNR: 4.044 dB SSA SNR: 1.49 dB	40

Table 4. Definition of terms for Tables 1, 2, and 3

BER	bit error rate
BIT RATE	clock frequency of the telemetry bit information
bits/s	bits per second
BLo	two-sided receiver loop noise bandwidth at threshold
CPA	Command Processor Assembly
CMF	Communications Monitor and Formatting Assembly
CTA 21	The Deep Space Network Ground Station Compatibility Test Area at JPL
dB	decibel
dBm	decibel referenced to one milliwatt
DL	RF downlink signal
DSN mode	The Deep Space Network Ground Station operational configuration
FDS	Spacecraft Flight Data Subsystem
JPL	Jet Propulsion Laboratory
MCD	Maximum Likelihood Convolutional Decoder
MDA	Metric Data Assembly
MDS	Spacecraft Modulation/Demodulation Subsystem
MDS	The DSN-MARK III Data Subsystems Implementation Project
No	noise spectral density
P_C	Power in RF carrier
P_T	Power total
PRA	Planetary Ranging Assembly
PFR	Problem/Failure Report
RDA	Ranging Demodulator Assembly
RF	radio frequency
RFS	Spacecraft Radio Frequency Subsystem
RU	range unit
SAF	Spacecraft Assembly Facility (JPL Building 179)
S/C RFS Mode	The Spacecraft Radio Frequency Subsystem operational configuration
SDA	Subcarrier Demodulator Assembly
SER	symbol error rate
SNR	signal-to-noise ratio
SPS	symbols per second
SSA	Symbol Synchronizer Assembly
SSF	Space Simulator Facility (JPL Building 150)
STb/No	signal-to-noise spectral density ratio
SYMBOL RATE	clock frequency of the telemetry symbol information
TBD	to be determined
TBS	to be supplied
TDL	Telemetry Development Laboratory
TLM	telemetry
TPA	Telemetry Processor Assembly
TWT	Traveling Wave Tube Amplifier
UL	RF uplink signal
Uplink Doppler	ramp rate of uplink RF carrier frequency
Uplink Offset	uplink RF carrier frequency displacement relative to the spacecraft receiver rest frequency
USO	ultra stable oscillator
VCO	voltage controlled oscillator

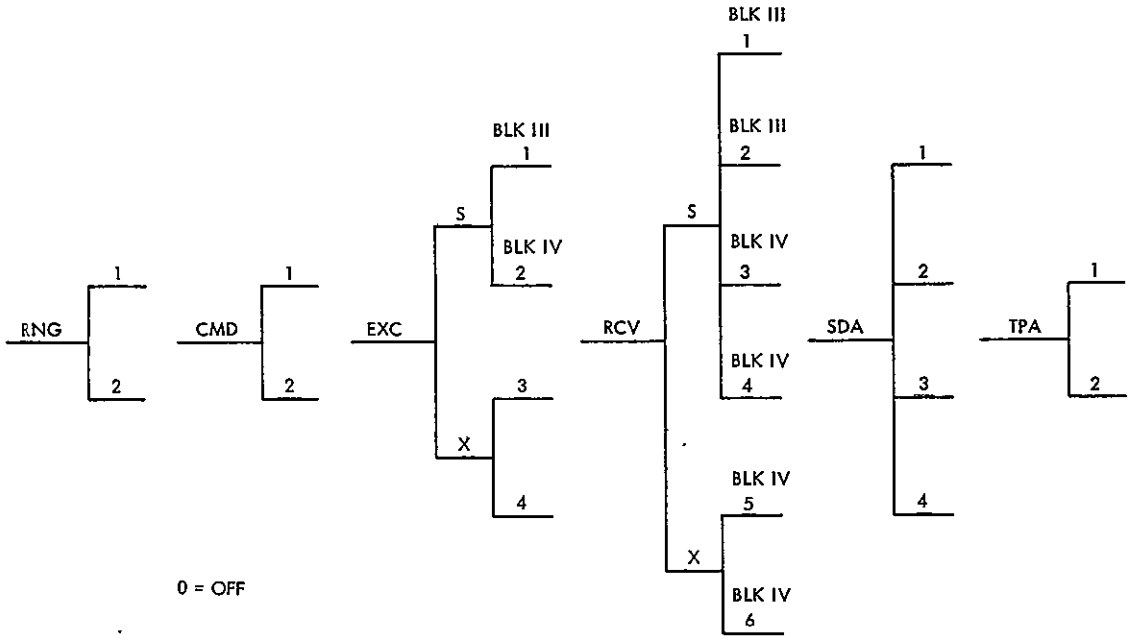

Fig. 1. DSN modes

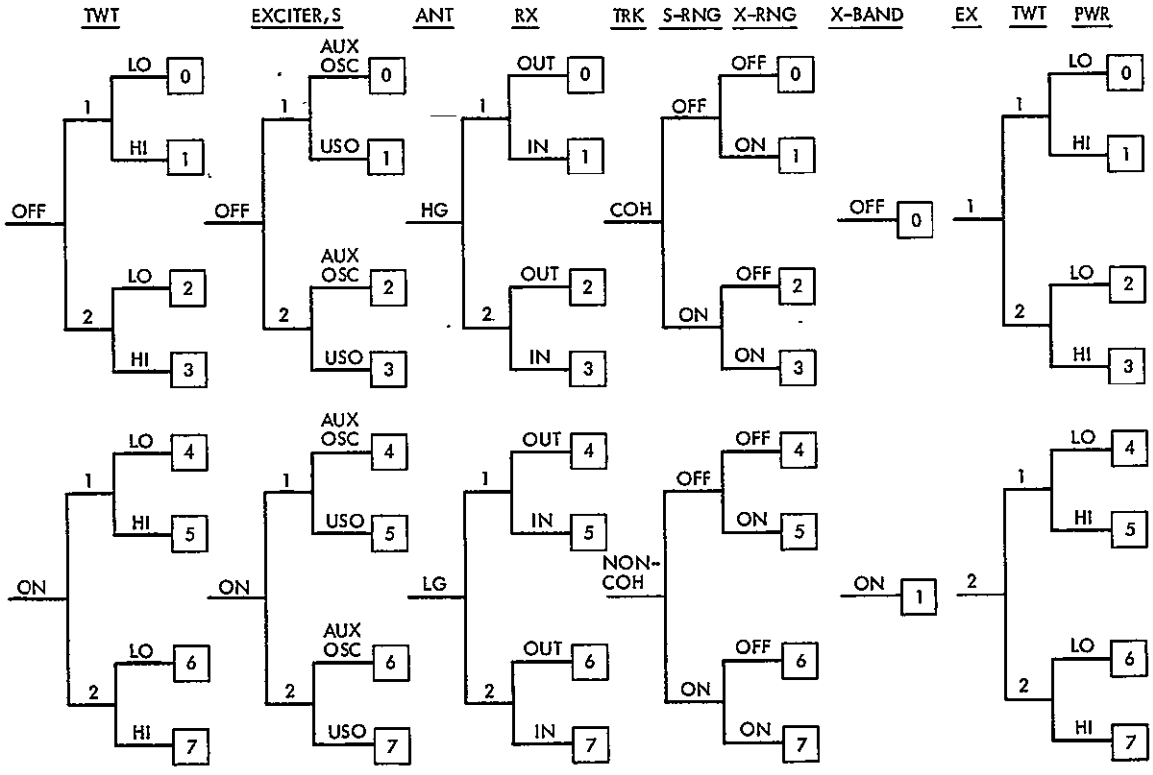

Fig. 2. Voyager operational RFS modes

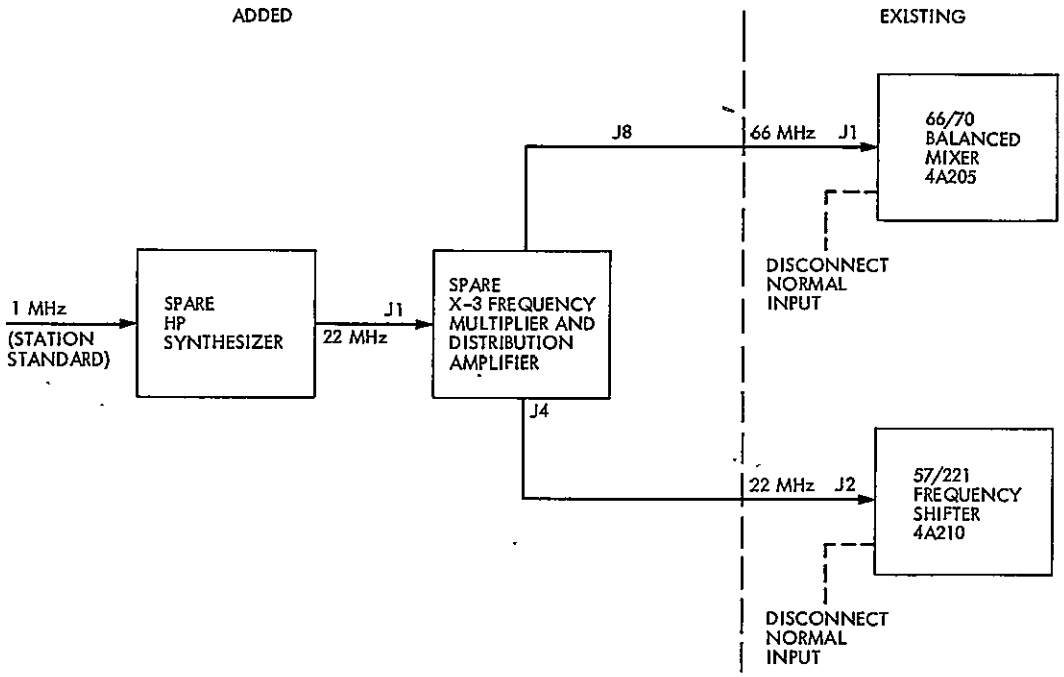

Fig. 3. Dual-channel 1.5-MHz doppler work-around block diagram

Viking Extended Mission Support

T. W. Howe
Deep Space Network Operations

D. J. Mudgway
TDA Mission Support

This report covers the period 1 March 1977 through 30 April 1977 and includes DSN Mark III Data System (MDS) testing, status of Viking-related tracking and command support as well as the status of the Viking DSN Discrepancy Reporting System. The DSN Operations support of Viking events and Radio Science activities are also discussed. Current progress on the major new reconfiguration of the Network is presented in the context of support for the Viking Extended Mission.

I. Viking Operations

A. Status

As of 30 April 1977, all four Viking spacecrafts continued to perform their assigned tasks. Lander 2 was sent a final set of commands on 14 April for its automatic survival mission. This automatic function will continue to operate for the next six months, providing information about the Martian weather, quakes, soil analysis, and photos. The data will be relayed to Earth via Viking Orbiter 2 (VO-2) every week and a half. The temperature at the Lander 2 location has reached the frost point of carbon dioxide but no frost has been seen in Lander 2's photos. Lander 1 remains actively controlled from the Earth with data being received by both direct and relay links.

Both Viking Orbiters continue photography and temperature and water vapor mapping of Mars, most of which is now cloudy and dusty. Every two weeks VO-1 comes within photo range of Phobos. A close encounter with Phobos will occur during the last part of May.

B. Maneuvers

Two Mars Orbit Trim (MOT) maneuvers were performed on each of the Viking Orbiters during this reporting period. VO-2 MOT-9 occurred on 2 March 1977, with a burn time of just under 10 seconds. DSS 14 was prime for this maneuver. However, much of the maneuver was performed in the blind. The station lost lock when the switch from high-gain antenna to low-gain antenna took place, and because of the proximity to periapsis and high doppler rates, the station could not reacquire until shortly before Earth occultation. Lock was achieved with enough time to establish that readings were nominal and that a "no-go" command was not required.

VO-1 MOT-13 took place on 11 March 1977, with a motor burn lasting 49 seconds. Both DSS 63 and DSS 14 supported the preburn positioning of the spacecraft for the maneuver.

DSS 14 sent the "go" command and completed the motor burn and spacecraft unwind activities. MOT-13 was nominal.

VO-1 MOT-14 occurred on 24 March 1977 with a motor burn duration of 9 seconds, resulting in a change of orbit period to 23.5 hours. The entire maneuver was conducted in the blind. DSS 42 supported the maneuver, and since the spacecraft was operating on the low-gain antenna, telemetry data was below the threshold of this station. Playback of the maneuver data took place following the return to the high-gain antenna and during the DSS 63 view period. All MOT parameters were nominal.

The final MOT of this reporting period took place on 18 April 1977 during the DSS 43 view period. VO-2 MOT-10 was accomplished on the spacecraft high-gain antenna at burn attitude. DSS 43 used receiver number 4 configured for X-band to measure the difference in downlink signal levels between VO-1 and VO-2. Link performance was normal throughout the maneuver. Later analysis by the Viking Flight Path Analysis Group determined that MOT-10 was a 5 sigma maneuver and resulted in an orbit period error of 32 seconds.

C. Radio Science

Viking Radio Science activities continued at a brisk pace during this reporting period. Six different types of activities were supported.

1. **Occultation.** VO-2 occultations continued during the entire reporting period. VO-1 occultations resumed on 22 March 1977 and continued during the remainder of the period. It was noted by the Radio Science Team that Earth occultation coverage was very sparse. The causes of this poor coverage were conflicts in DSS coverage, orbiter maneuvers, lander direct links, Voyager ranging passes, etc.

2. **Long/short baseline ranging for Voyager.** This experiment was conducted for the Voyager Project using the Viking Orbiter spacecrafts on seven occasions during March and April. The experiment called for near simultaneous ranging at S- and X-band frequencies using up to three separate DSN stations.

3. **Solar Wind Experiment.** This experiment took place on 7 April 1977 during a DSS 43/14 overlap. The experiment compared the S- and X-band doppler perturbations caused by solar winds on the downlink signals from VO-2. It was similar to the experiment conducted during May 1976 and used four doppler streams, two S- and two X-band, at a sample rate of one per second for the entire 4.5-hour overlap.

4. **Viking/Quasar VLBI Experiment.** The VLBI experiment was completed four times during March and April. The basic purpose of this experiment is to determine the position of Mars relative to the quasar reference frame.

5. **Lander and Orbiter near-simultaneous ranging.** This test is used primarily to calibrate for ranging group delay due to interplanetary and ionospheric plasma. The Orbiter S- and X-band ranging can be used to measure the total electron content in the beam between the spacecraft and the station, and these calibrations are extrapolated back to the Lander ranging measurement time to get a more accurate Lander measurement. This experiment was conducted five times during March.

6. **Voyager dedicated demonstration day.** This experiment used DSS's 14 and 43 on 13 and 14 April 1977 to determine the effect of the 64-meter antenna subreflector movement on range measurements. It also involved near-simultaneous ranging between DSS 11, 14, 42, and 43.

D. Orbiter Visual Imaging Science

The first 16 kbps from either Viking Orbiter since Mars Orbit Insertion of VO-1 took place on March 26 and 28. The telemetry SNR averaged between 1.8 and 1.0 dB, with the lowest SNR influenced by icing conditions on the DSS antenna. On 28 March, both Orbiters played back 16 kbps, with VO-1 SNR about 2 dB with the spacecraft ranging channel on and VO-2 SNR about 3 dB with the ranging channel off. The bit error tolerance on VO-1 was set to five bits in order to permit ground processing of the data.

II. Network Support

Table 1 continues the listing of DSN tracking support for Viking reported in the last article of this series. It can be seen that the total number of passes and hours tracked has decreased from the last report. This is due in part to the fact that DSS 14 was taken out of operation on 16 April for the MDS reconfiguration. DSS 12 has taken up some of this slack by supporting 24 Viking passes during April. During the first three months of this calendar year DSS 12 had supported only five passes.

Table 2 lists the total number of commands transmitted for Viking during 1977. Table 3 shows the Discrepancy Report (DR) status for 1977. The total number of new DR's has decreased during this reporting period while the total of closed DR's has increased significantly.

The DSN Post-Track Report was eliminated on 1 March 1977. This report summarized pertinent data and events which occurred during a DSS tracking period. The report was transmitted to JPL and the Viking Project at the conclusion of each tracking period and was used by cognizant personnel at JPL as

the official source for data used to generate quick-look reports, post-track performance, data analysis and data validation functions. The requirement was to transmit this report within three hours of the end of track. Since teletype reporting and data transmission has decreased in the past few years, many of the DSS's do not have qualified teletype operators on duty throughout the week. This made it difficult for them to comply with the three-hour reporting requirement.

A new system is presently in use in which the information formally reported in the Post-Track Report is now reported by voice by the DSS to the Network Operations Controller at the conclusion of each pass. This information is logged and then made available for Project use.

III. Mark III Data Subsystem Testing

As indicated in the last report, DSS 12 had completed its Viking MDS test schedule and had been placed under configuration control. DSS 62 had completed the OVT portion of the schedule and was about to begin the remainder of the program. DSS 44 had not completed the MDS implementation and had not yet begun the test program.

During this reporting period, both DSS 62 and DSS 44 completed the Viking tests and are now under configuration control. A brief description of the tests conducted during March and April and the results are as follows:

A. DSS 62

1. **Demonstration pass – 6 March 1977.** This pass was a complete success. No problems were encountered. Key items accomplished during the pass were processing of VO-1 engineering data, transmission of a test command, processing of monitor data, and radio metric data.

2. **Demonstration pass – 17 March 1977.** Although many minor operational problems occurred during this pass, all items of the sequence of events were successfully completed. DSS 62 was placed under configuration control following this pass.

3. **System Interface Test – 20 March 1977.** This test was successful with all test objectives completed. A problem in the interface between the simulation center and the simulation conversion assembly at DSS 62 caused a delay of approximately five hours in the telemetry portion of the test. Following the location of a faulty communications buffer and its replacement, sufficient time remained to complete the telemetry test. This was the final DSS 62 Viking MDS test.

B. DSS 44

1. **Operational Verification Test – 6 March 1977.** This was the first DSS 44 OVT and considered a success. Two anomalies occurred but did not affect the final outcome of the test. Engineering data was not received at JPL throughout the test, and monitor data would halt approximately every five minutes. This latter problem was created when both Telemetry Processor Assemblies were interfaced simultaneously with the Digital Instrumentation Subsystem Computer.

2. **Operational Verification Test – 10 March 1977.** This test was a complete success. All items of the SOE were completed. This was the final OVT for DSS 44.

3. **System Interface Test – 18 March 1977.** The test was classified as a success. All items of the sequence were completed. An interface problem between the high-speed data line and the input to the DSS simulation conversion assembly, which caused block errors, persisted throughout the test. In spite of this problem the acceptance criteria of five minutes of good data for each data rate and mode was met. No retest was required.

4. **Demonstration pass – 24 March 1977.** This first demonstration pass for DSS 44 was successful with all items completed. The same test criteria used previously at DSS's 12 and 62 were repeated for this test.

5. **Demonstration pass – 30 March 1977.** The second demonstration pass for DSS 44 was again successful. The MDA was declared red prior to this pass but did not compromise the test.

6. **Demonstration pass – 20 April 1977.** With one minor exception, this final demonstration pass was successful. A command bit verification failure occurred when the command system went from Idle 1 to Idle 2. Following reinitialization of the Command Processor Assembly, the problem did not reoccur. DSS 44 was placed under configuration control.

C. DSS 14

DSS 14 began it's MDS reconfiguration on 16 April 1977. The Viking test program is scheduled to begin in the middle of June and will be reported on in the next article of this series.

IV. Implementation

Following the completion of the Viking Prime Mission on 15 November 1976 and the period of solar conjunction which continued through mid-January 1977, the Deep Space Network embarked on a major reconfiguration effort. This was called the Mark III-DSN Data Subsystem (MDS) implementation task and involved all stations of the Network during CY'77. It was carefully phased with the principal Flight Project Support activity, and the launch of the new Voyager Mission, as shown in the schedule in Fig. 1.

As the Viking Extended Mission increased in tempo following the solar conjunction period, important relativity experiments were conducted with DSS 14, 42 and 63 (Ref. 1, 2) while the MDS implementation activity got under way with DSS 12, 44 and 62. As each of these stations was withdrawn in turn from Viking Extended Mission Support, the MDS reconfiguration was accomplished, and the station was returned to operational support following an appropriate period of testing and crew retraining.

Some delays were experienced on the first station (DSS 12), due to unforeseen technical problems, but the time was made up on the other 26-meter stations, which were completed on schedule. By early April, these stations had been placed under configuration control and were supporting flight operations, and DSS 14, the first 64-meter station, was taken down for its reconfiguration.

It was planned to take advantage of the DSS 14 downtime for the MDS reconfiguration to carry out a number of rather long, overdue modifications and upgrades in the following areas:

(1) Relocation of microwave tricone equipment, and modifications to the XRO feed cone.

(2) Rehabilitation and upgrade of the main electrical power system.

(3) Modification and improvements to the hydrostatic pump equipment.

(4) Improvements to the water cooling and treatment plant.

(5) Transmitter crowbar modifications and maser bypass.

Together with the MDS related tasks, this represented a substantial effort, and a special manager was assigned for the Project to coordinate and manage the resources necessary to accomplish this job on schedule. Some 87 individual modification kits were provided to the station and installed during the months of April and May.

The test schedule which followed the implementation phase is shown in Fig. 2. This allowed completion of the reconfiguration by 15 June, at which point the Viking Extended Mission Ground Data System Schedule became effective, as shown in Fig. 3.

Following a Test Readiness Review on 6 June, the tests shown in Fig. 3, were commenced, culminating in demonstration passes and the return of DSS 14 to operational status on 8 August.

V. Reconfiguration and Capabilities

The MDS modification consists of the installation of minicomputer and ancillary assemblies which replace and/or augment existing station equipments. Each minicomputer assembly consists of a Modcomp minicomputer and associated peripheral and interfacing equipment. The primary minicomputer assemblies to be installed at each station are as follows:

(1) Telemetry Processor Assembly – replaces and expands telemetry functions of existing Telemetry and Command Processor and Data Demodulator Assembly.

(2) Command Processor Assembly – replaces command functions of existing Telemetry and Command Processor.

(3) Communications Monitor and Formatter – functions as part of Ground Communications Facility to provide for high-speed data communications between the Mission Control and Computing Center and MDS minicomputer assemblies. Also provides centralized data reporting and data formatting.

(4) Metric Data Assembly – a new assembly which assumes and expands the tracking data acquisition and processing functions previously performed by the Tracking Data Handling Subsystem and the Digital Instrumentation Subsystem.

The ancillary assemblies provide functions and services necessitated by the installation of the minicomputer assemblies. The ancillary assemblies and their basic functions are as follows:

(1) DIS MK III Interface Assembly – functions to provide a communications interface between minicomputer assemblies, providing data switching and routing functions via Star Switch Controller units.

(2) Time Format Assembly – provides basic timing inputs (GMT and interrupts) to the minicomputer assemblies.

(3) Data Systems Terminal – functions to provide centralized operator control and display for the minicomputer assemblies within a DSS.

The essential elements of the new MDS configuration as it will be used to support the Viking Extended Mission is shown in Fig. 4, for 64-meter and 26-meter conjoint stations.

VI. Network Configurations for Viking Extended Mission

The capabilities provided to the Viking Extended Mission by this configuration were the same as that provided for the Prime Mission, with exceptions as follows:

A. 26-Meter Stations

1. **Telemetry Subsystem.** Simultaneously processes two subcarriers at 8-1/3 bps uncoded and up to 2000 bps block-coded.

Changes: Telemetry Processing Assembly now replaces Telemetry and Command Processor and handles one low rate uncoded and one medium-rate block-coded stream per Telemetry Processing Assembly. Internal bit sync previously provided internal up to the Telemetry and Command Processor; this is now provided externally by the Symbol Synchronizing Assembly, one for each stream, coded or uncoded. The Digital Original Data Record is now provided by the Communications Monitor and Formatter Assembly, with the temporary Original Data Record being written by the Telemetry Processing Assembly for the recovery of data to the Digital Original Data Record.

2. **Command Subsystem.** Single channel PSK, 8 symbols/sec, Manchester-coded for Orbiter, with provision for manual entry.

Changes: Command subsystem incorporates additional functions of symbol-by-symbol command confirmation and Viking bit inversion to conform to industry standard. Provision for use of prepunched Mylar tapes is deleted.

3. **Monitor and Control Subsystem.** Local display and transmission to NOCC of station configuration, status and performance data. Existing monitor formats will continue to be available to cover the unmodified stations, with interfaces to Network Operations Control Center and Viking Mission Control and Computing Center remaining unchanged.

Changes: Special Viking high-speed data blocks for Viking Mission Control and Computing Center will be provided, and all 26-meter Deep Space Stations will be provided with Station Monitor Consoles, prior to the MDS reconfiguration.

4. **Tracking Subsystem.** Single channel, S-band doppler at all 26-meter stations with S-band ranging using planetary ranging assembly at DSS 12. Ranging is shared at Stations 42, 43 and 61, 63.

Changes: Metric Data Assembly now replaces Tracking Data Handling Subsystem with a temporary Original Data Record storing radio metric data at the highest sample rate, 10 samples/sec for subsequent retrieval. All text predicts are now transmitted to the Digital Instrumentation Subsystem for printing on line printer assembly. All predicts are transmitted to the Metric Data Assembly for transfer via the star switch controller to the Digital Instrumentation Subsystem for punching the Antenna Pointing Subsystem drive tape.

5. **Test and Training Subsystem.** High-speed simulation data from the Network Operations Control Center or Viking Mission Control and Computing Center will be received at the station by the Communications Monitor and Formatter Assembly, and routed directly to the Simulation Conversion Assembly, without passing through the star switch controller. The addition of convolution coding hardware and a MJS software module does not change existing Viking capability.

6. **Voice and High Speed Data Subsystems.** Provides one 7200-bps high speed line, and one voice line per station.

B. 64-Meter Stations

1. **Telemetry Subsystem.** Simultaneously processes two low-rate (33-1/3 bps) uncoded and two high-rate (16 kbps) block-coded subcarriers.

Changes: Total number of simultaneous data streams is reduced from six to four as described above. Telemetry Processing Assembly now replaces Telemetry and Command Processor Assembly, and each Telemetry Processing Assembly will handle one low-rate and one high-rate data channel in association with a Block Decoder Assembly for decoding the coded channel. Internal bit sync previously provided by the Telemetry and Command Processor Assembly has been replaced by the Symbol Synchronizer Assembly, one for each data stream. The low- and medium-rate Digital Original Data Record resides in the Communications Monitor and Formatter Assembly with a temporary Original Data Record being written by the Telemetry Processing Assembly for recovery of data to the Digital Original Data Record.

The high-rate Digital Original Data Record is written and recalled by the Telemetry Processing Assembly as a separate function.

2. **Command Subsystem.** Dual-channel PSK (8 symbols/sec) Manchester-coded for Orbiters to either Block III or Block IV exciters with provision for automatic or manual entry. The punched Mylar tape command capability is deleted.

Changes: DSS Command Subsystem incorporates additional functions of symbol-by-symbol command confirmation and Viking bit inversion to conform to industry standards. Functions formerly accomplished by the Telemetry and Command Processor Assembly are now carried on by the Command Processor Assembly, with a temporary Original Data Record providing data retrieval for the Digital Original Data Record running in the Communications Monitor and Formatter Assembly.

3. **Tracking Subsystem.** Two S-band doppler channels or one S-band and one X-band channel are provided. Simultaneously, two S-band or one S-band and one X-band ranging channel using the planetary ranging assembly are available.

Changes: Metric data assembly now replaces Tracking Data Handling Subsystem, with a temporary Original Data Record storing radio metric data at the highest sample, 10 samples/sec for subsequent retrieval. All text predicts are now transmitted to the DSS Monitor and Control Subsystem line printer assembly.

All binary predicts are transmitted to the Metric Data Assembly for transfer via the star switch controller to the Digital Instrumentation Subsystem for punching the Antenna Pointing Subsystem drive tape. A Meteorological Monitor Assembly, contained in the Technical Facility Subsystem, will transmit ground weather and ionospheric data via high-speed data circuits to the Network Operations Control Center.

4. **Monitor and Control Subsystem.** Local display and transmission to Network Operations Control Center of Deep Space Station configuration status and performance data. Existing monitor formats will continue to be available to cover the unmodified stations, with interfaces to Network Operations Control Center and Viking Mission Control and Computing Center remaining unchanged.

Changes: Special Viking high-speed blocks for Viking Mission Control and Computing Center will be provided and all 64-meter stations will continue to use SMC IIA, Station Monitor Consoles.

5. **Ground Communications Facility Voice and High-Speed Data Subsystems.** Provides one 7200-bps high-speed data line, one voice line per station, and one 56 kbps wideband data line per 64-m station.

6. **Test and Training Subsystem.** High-speed simulation data from Network Operations Control Center or Viking Mission Control and Computing Center will be received at the stations and routed directly to the Simulation Conversion Assembly via a communications buffer without passing through the star switch controller. The addition of convolution coding hardware and a Voyager software module does not change existing Viking capability. Wideband simulation data is routed directly to the Simulation Conversion Assembly as in the Prime Mission configuration.

C. Conjoint Stations

The functional design for DSS 42 and 61 conjoint stations following the reconfiguration provides all the characteristics described above for DSS 11, 12, 44, and 62 with the following exceptions:

(1) A second Symbol Synchronizer Assembly permits simultaneous processing of one low-rate and one medium-rate Viking data stream to the Telemetry Processing Assembly, thereby retaining the simultaneous four-stream capability in the conjoint 64-meter wing.

(2) Timing and test and training services are shared with the conjoint 64-meter stations.

(3) Ranging is shared with the conjoint 64-meter stations.

(4) Star switch controller and Communications Monitor and Formatter, shared with the conjoint 64-meter stations, provide combined capability for two high-speed data channels to the Complex.

VII. Future Plans

The DSN plans to continue the MDS reconfiguration around the Network as shown in the schedules in Fig. 1 and 3, with DSS 42/43 and DSS 61/63, following in order after DSS 14. The Viking Extended Mission Operations have been integrated with the Ground Data System schedule of Fig. 3, in such a way as to minimize the impact to the Mission data return as a result of the reconfiguration described above. Subsequent reports will describe the implementation and test activity as this work proceeds.

Acknowledgment

The authors would like to thank F. H. (Jim) Taylor, whose VO-75 OPAG Telecom Daily Status Reports have proved extremely useful in compiling these reports.

References

1. Johnston, D. W., "Viking Mission Support," in *The Deep Space Network Progress Report 42-38*, pp. 38-42, Jet Propulsion Laboratory, Pasadena, Calif., Apr. 15, 1977.
2. Johnston, D. W., "Viking Mission Support," in *The Deep Space Network Progress Report 42-39*, pp. 4-8, Jet Propulsion Laboratory, Pasadena, Calif., June 15, 1977.

Table 1. VEM tracking support 1977

DSS	Jan		Feb		Mar		Apr	
	Tracks	Hours	Tracks	Hours	Tracks	Hours	Tracks	Hours
11	23	135	22	142	10	100.12	17	118:00
12	4	11	1	6	–	–	24	175:59
14	52	341	59	392	50	368 35.	20	176 21
42	21	247	25	226	58	453:24	17	138:36
43	68	721	62	627	–	–	63	603:21
44	-0-		-0-		7	7 02	1	3:56
61	35	261	29	227	12	72:07	40	317:45
62	-0-		2	7	4	22:25	9	55:10
63	38	327	28	202	66	525·53	15	78:01
Total	241	2043	228	1830	207	1549·38	206	1667:09

Table 2. VEM commands transmitted

DSS	Jan	Feb	Mar	Apr
11	1521	1394	1027	117
12	-0-	-0-	-0-	1314
14	769	1404	1206	274
42	2072	953	1778	8
43	919	2523	-0-	2094
44	-0-	-0-	2	1
61	605	1116	1328	1925
62	-0-	-0-	1	1991
63	795	472	2039	381
Total	6681	7862	7381	6180

Table 3. DSN VEM discrepancy reports

DSS	Jan		Feb		Mar		Apr	
	Open	Closed	Open	Closed	Open	Closed	Open	Closed
11	4		3	4	4	6	1	3
12	4						5	2
14	14	2	11	19	4	33	3	9
42		1	2	3		7		2
43	10	13	11	10		12	9	11
44						2		1
61	1	9	1	6		3		1
62				8	1	2	2	1
63	1	4	7	3	1	18		6
Others[a]	4	3	3	9	2	10	4	7
Total	38	32	38	62	12	93	24	43

[a]DSN, NDPA, NOCA

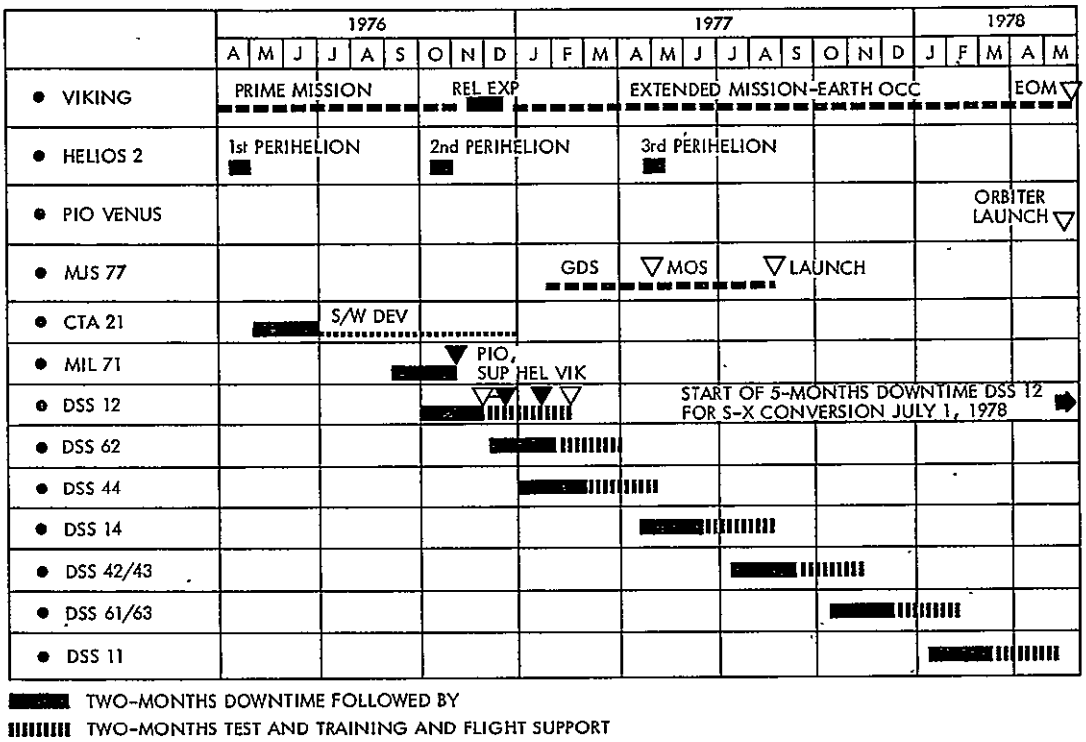

Fig. 1. Mark III-DSN Data Subsystems Implementation Schedule

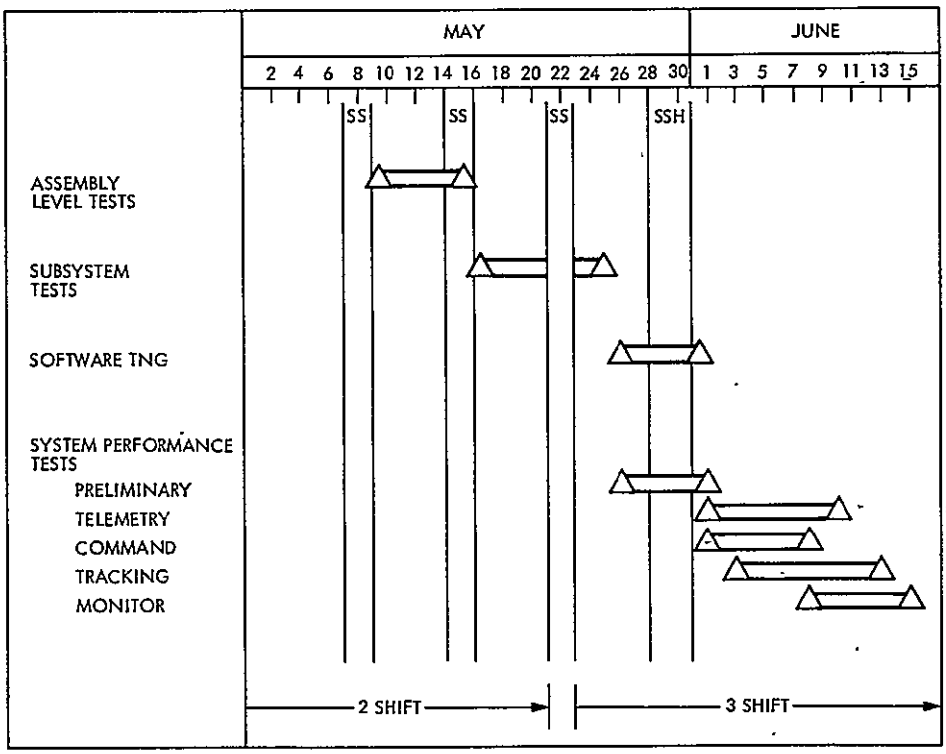

Fig. 2. DSS 14 Downtime Project, Test Schedule

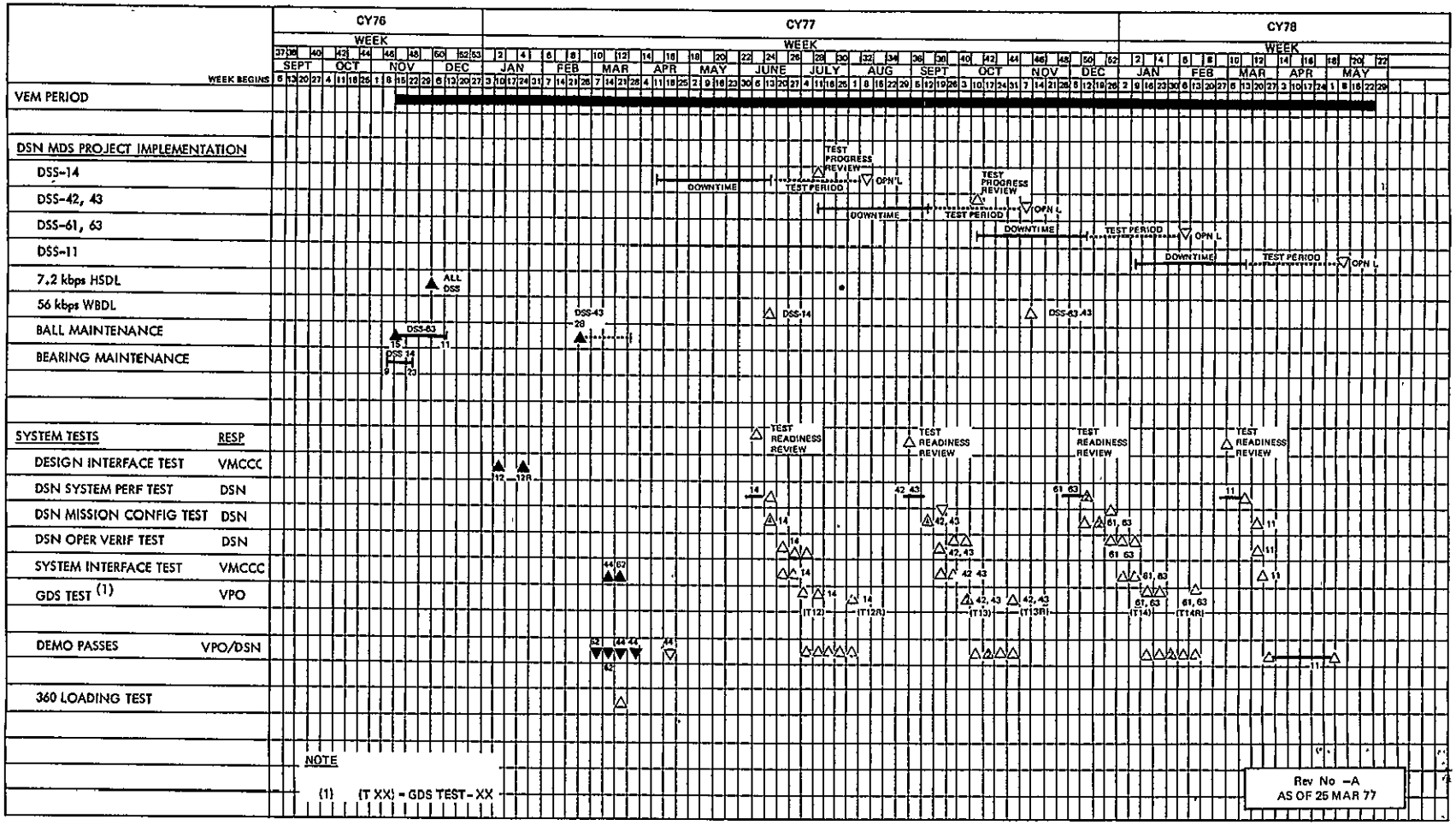

Fig. 3. Viking Extended Mission Ground Data System Schedule

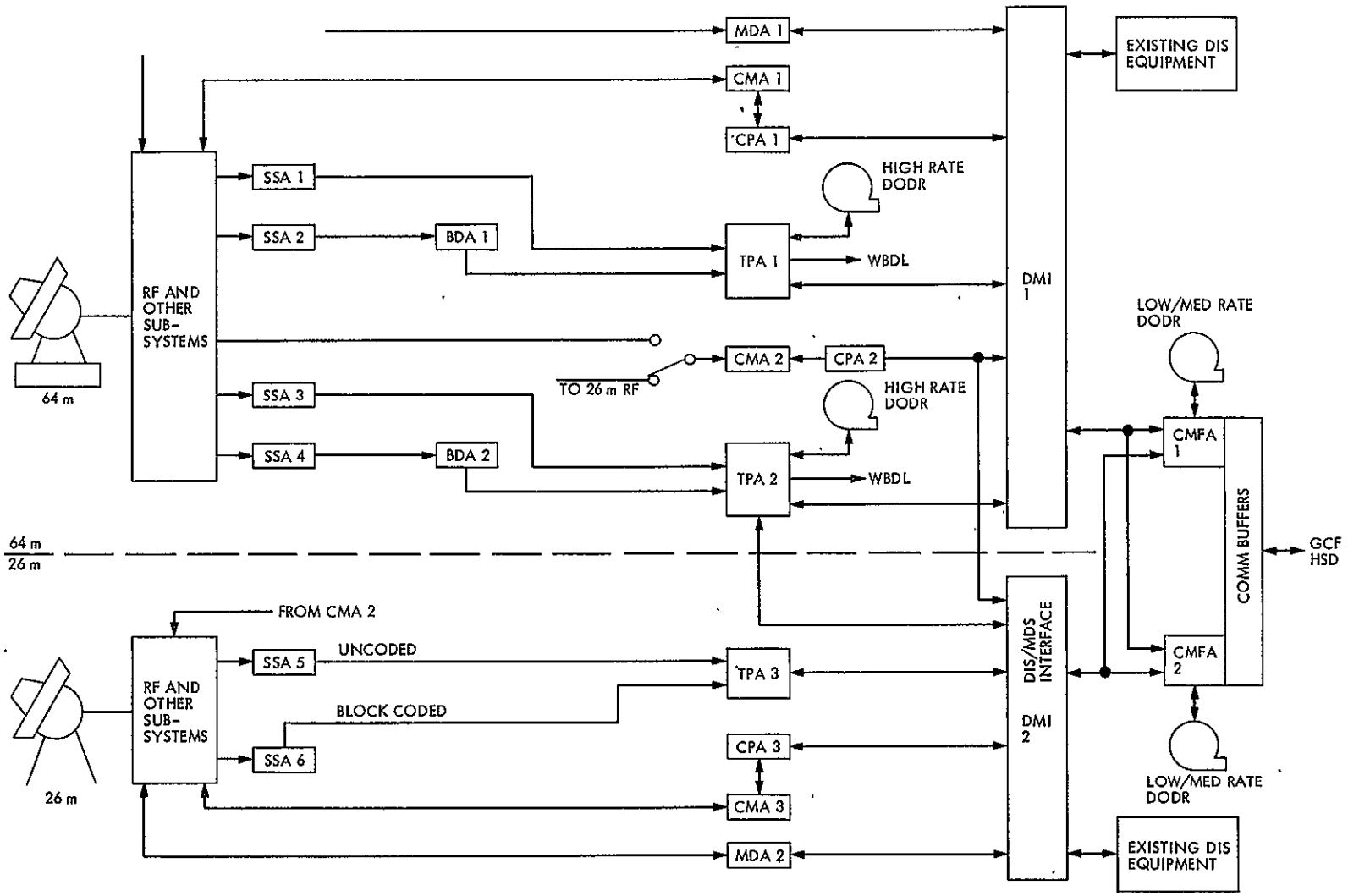

Fig. 4. Mark III-DSN Data Subsystems Implementation, New Configuration, Conjoint Stations

Helios Mission Support

P. S. Goodwin
TDA Mission Support

E. S. Burke and G. M. Rockwell
Deep Space Network Operations

This article reports on activities of the Network Operations organization in support of the Helios Project from 15 April through 15 June 1977.

I. Introduction

This article is the sixteenth in a continuing series of reports that discuss Deep Space Network support of Helios Mission Operations. Included in this article is information concerning Helios-2's superior conjunction period, Faraday rotation experimentation during solar conjunction, updated Mark III data system status, and other Mission-oriented activities.

II. Mission Operations and Status

The Helios-1 spacecraft has continued in a normal manner during this period with no significant events occurring. Because of the distance and position of Helios-1 at this time, STDN cross-support at Goldstone has been discontinued. The last STDN pass of this series was conducted on 10 May 1977, and no further coverage of this type will be attempted until October 1977, when conditions will again be favorable.

On 10 May 1977 the Helios-2 spacecraft entered the longest superior conjunction period of its entire Helios Mission. This period will last until 18 October 1977. Helios-2 passed inside the 3-degree Sun-Earth-probe (SEP) angle zone on 20 May 1977 and entered a blackout period on 2 June 1977. This blackout will last until 26 June 1977, when tracking coverage will resume. Because of the length of this solar conjunction period, considerable scientific interest has arisen for DSN tracking coverage during this time. More detail on the specific experiments being conducted while Helios-2 is in this phase of its mission will be discussed later in this article.

Prior to entering superior conjunction, Helios-2 passed through its third perihelion on 23 April 1977 (Ref. 1). The specific detail of this perihelion was that the spacecraft was 149.93 km from Earth, 43.48 km from the Sun, was traveling at a velocity of 68.6368 km/s, and had a communications round-trip-light-time (RTLT) of 16 minutes 40.36 seconds. This perihelion period was supported by DSS 63 in Spain with a bit rate of 2048 bits per second (bps) in Format 1, and data mode 0. In general, all subsystems and experiments functioned properly.

One anomaly occurred during this period, which affected Experiments 1, 2, 3, and 10 on board the Helios-2 spacecraft on 17 May 1977 over DSS 63. The regulator output voltage dropped from 28 volts to 24 volts, Experiment 10 sensor "A" current increased from 105.6 to 170 mA, and Experiment 1 sensor "A" current rose from 1.34 to 2.2 mA (soft limit) and

4.3 mA (hard limit). Subsequent data showed further breakdown of regulator output voltage. It has not been determined what happened, because data received during this time were extremely noisy. It is suspected that a regulator or double regulator switch occurred, which was experienced a few months ago with Helios-1. Over DSS 43 Experiments 1, 2, and 3 were reconfigured with no problems, but Experiment 10 was left off until further troubleshooting could be conducted.

Overall tracking time for both Helios spacecraft is shown in Table 1.

Periods of high scientific interest for Helios-1 and -2 are listed below:

(1) 20 May – 5 June: Helios-2 to be inside the 3-degree zone of superior conjunction. Facilities to measure the Faraday rotation and the signal bandwidth are requested as frequently as possible. Normal coverage requested for Helios-1.

(2) 6 June – 21 June: Helios-2 to be in solar occultation. No coverage for Helios-2 requested. Normal coverage requested for Helios-1.

(3) 22 June – 18 July. Helios-2 to be inside the 3-degree zone of superior conjunction. Facilities to measure the Faraday rotation and the signal bandwidth are requested as frequently as possible. Normal coverage requested for Helios-1.

(4) 18 July: Aphelion of Helios-1.

(5) 25 July: Aphelion of Helios-2.

(6) 30 September – 11 October: Helios-2 to be inside the 3-degree zone of superior conjunction. For requirements, see (1), above.

(7) 8 October – 15 October: Helios-1 to be inside the 3-degree zone of superior conjunction. Facilities to measure the Faraday rotation and the signal bandwidth are requested as frequently as possible. Normal coverage requested for Helios-2.

(8) 9 October – 2 November: Helios-1 to be in its perihelion phase (R 0.4 AU solar distance). This will be the most scientifically interesting of the current orbit phases of Helios-1. Adequate coverage is requested.

(9) 14 October – 7 November: Helios-2 to be in its perihelion phase (R 0.4 AU). Maximum scientific-interest orbit phase for Helios-2. Adequate coverage is requested, especially during that period when both spacecraft will be within 0 4 AU; i.e., from 14 October through 2 November.

(10) 8 – 11 October: Sun-radial lineup of Helios-1 and Helios-2. This lineup will have a high scientific value because it will happen in or close to the perihelion phase when the distance between the two spacecraft is less than 0.1 AU.

(11) 18 – 29 October: Long period of solar spiral lineup Helios-1 and Helios-2. Scientifically it is a very interesting period. As much coverage as possible for both spacecraft requested.

III. Special Activities

A. Mark III Data System (MDS) Support of Helios

The 26-meter subnetwork, made up of stations 12 at Goldstone, California, 44 in Australia, and 62 in Spain, continues to function in a nominal manner using the MDS in support of Helios. The MDS's performance has improved with the updating of its software, which has made the system much more reliable and more efficient. The latest updated software packages were for the Metric Data Assembly (MDA), the Command Processor Assembly (CPA), and the Monitor and Control Subsystem.

At this writing the MDS implementation at DSS 14 (Goldstone) is continuing. Test and training will begin at DSS 14 during June. Helios will be involved in a combined projects data flow test, to check out representative data rates and data types from all projects. Following this test, Helios will conduct demonstration tracks in the same manner that was used for the 26-meter MDS stations. A report on these test and training activities will be presented in the next article of this series.

B. Radio Science Activity

Scientific interest in the Helios-2 mission is very high at this time due to the current superior conjunction phase. One of the major experiments being conducted is the Faraday Rotation Experiment (Experiment 12). The experiment involves the 64-meter subnetwork and utilization of each station's automatic polarizer and Meteorological Monitor Assembly (MMA). At present only DSSs 43 (Australia) and 63 (Spain) are involved. Station 14 (Goldstone) will become involved after it is once again operational following MDS modification.

Significant rotation of the plane of polarization of the received signal is observed to occur whenever the Helios-to-Earth radio signal passes through the solar corona near superior conjunction. The large-scale variations in the polarization

data arise most probably from the changing orientation of the solar corona as it rotates through the signal path. If the polarities of the large-scale interplanetary magnetic field sector structure can be mapped into the solar corona (thus fixing the sign of the coronal magnetic field), the most probable distribution of the product $N \cdot \bar{B}$ (electron density X magnetic field) as a function of heliographic longitude may be determined. This effort is a continuation of the original Helios Experiment 12. The 1977 superior conjunction will probably be the last opportunity to observe this phenomenon with the spacecraft line-of-sight relatively motionless for an extended period of time.

The data types desired by the experimenters are signal polarization angle data, ellipticity data, and Faraday rotation data. These data are sampled by the MMA and recorded on digital tape (refer to Fig. 1). This tape is first played back to JPL in near-real-time, and then is shipped, along with polarimetry chart recordings, to the experimenter at JPL for analysis. At this writing, the first data packages have just arrived at JPL and no results are yet available. A future article in this series will report the results of this experiment.

Radio Science Experimenters are also conducting Solar Wind Experiments (SWE) during this superior conjunction period. These experiments involve remote sensing of the solar wind velocity near the Sun. Data are gathered by simultaneously tracking a Helios spacecraft at two widely separated DSN stations and recording doppler counts and (real-time-generated) pseudoresiduals, from which the solar wind velocity will be estimated. These measurements are scientifically important because they will allow extensive velocity measurements throughout the solar wind acceleration region and will be the first direct measurement of solar wind velocity very close to the Sun. Because of Helios-2's long solar occultation, observations in 1977 are unique and offer an important opportunity to thoroughly study this region of the solar atmosphere. The desired coverage of the experimenters is listed in Table 2. Results of this experiment will be reported in a future article in this series.

Reference

1. Goodwin, P. S., Burke, E. S., and Rockwell, G. M., "Helios Mission Support," in *The Deep Space Network Progress Report 42-39*, pp. 17-22, Jet Propulsion Laboratory, Pasadena, Calif., June 15, 1977.

Table 1. Helios tracking coverage

Month	Spacecraft	Station type	Number of tracks	Tracking time, h.min
April	Helios 1	26 Meter	51	313.26
		64 Meter	9	62:03
	Helios 2	26 Meter	50	377:39
		64 Meter	23	162:11
May	Helios 1	26 Meter	44	340:59
		64 Meter	0	0
	Helios 2	26 Meter	36	143 22
		64 Meter	37	215:47

Table 2. Requested coverage for solar wind experiment

Spacecraft	Period (1977)	Coverage[a]
Helios 2	April 23 - November 1	At least 3 passes per week. Passes not required when Helios is too close to the sun for tracking (approx. June 19 ± 10 days). Within 1° of sun 64-m antennas (43/63) are requested.
Helios 1	April 23 - September 1	At least 1 pass per week.
Helios 1	September 2 - November 1	At least 2 passes per week.

[a]Minimum of one hour of simultaneous coverage is desired for each pass.

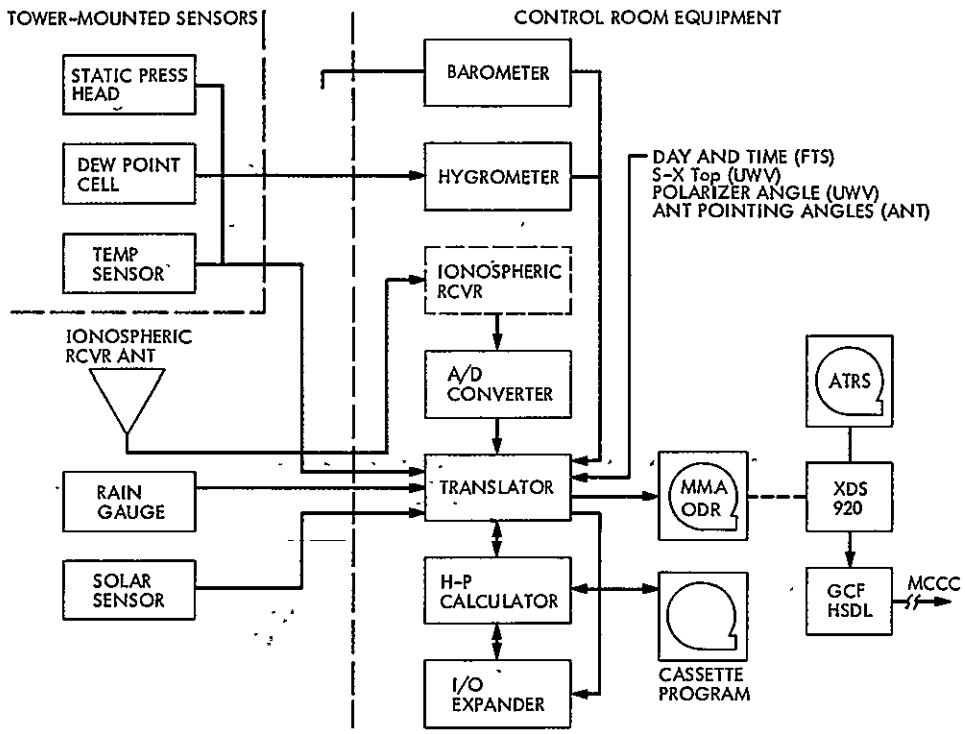

Fig. 1. Simplified MMA system block diagram

DSN Progress Report 42-40 May and June 1977

Deep Space Network to Viking Orbiter Telecommunication Link Effects During 1976 Superior Conjunction

F. H. J. Taylor
Telecommunications Systems Section

Viking superior conjunction occurred November 25, 1976 with an angular separation between the sun and Mars of one-quarter degree. For three years prior to this date, the Viking Project and the Deep Space Network had planned the spacecraft and ground station activities and configuration during the three-month superior conjunction period. This article describes, in a narrative and qualitative manner, the planning for and the observations made during Viking superior conjunction. These results are built upon observations made during previous Mariner missions and will, in turn, be useful for the next Viking conjunction and for future Mariner-class superior conjunction planning.

I. Background

The end of the Viking primary mission was determined in part by the onset of the superior conjunction. Superior conjunction is the period of time when the spacecraft is nearly behind the sun as seen from the deep space tracking stations on the earth. Previous tracking experience, on Mariner Mars 1969, Mariner Mars 1971, Mariner Venus-Mercury 1973, had demonstrated that significant communication link degradation can occur whenever the angular separation of the spacecraft and the sun, as seen from the tracking station, is small.

The minimum angular separation of the spacecraft and the sun occurred on November 25, 1976 when the Viking spacecraft, in orbit around Mars for the Orbiters and on the surface of Mars for the Landers, were 0.25 deg from the center of the sun. For several hours, the spacecraft actually were occulted behind the edge of the solar disc, and no uplink or downlink communications were possible. For about one month on either side of November 25, the angular separation (called sun-earth-probe angle) was less than 10 deg and significant perturbations occurred in the downlink telemetry.

This article discusses primarily four link quantities: uplink carrier signal strength; downlink carrier signal strength; signal-to-noise ratio for the Orbiter low-rate engineering telemetry channel; and signal-to-noise ratio (SNR) for the high-rate science data channel. In addition, some mention is made of the low bit error rate and the high bit error rate, on the basis of counted bit errors in known frame synchronization words.

II. Viking Superior Conjunction Predictions

The Project required link predictions for planning the mission activities. It was critically important to know the latest

time it was prudent to command the Orbiter prior to minimum sun-earth-probe angle. It was important to know the dates when the high-rate channel should be switched to lower data rates so as to maximize the total amount of scientific data returned without undue risk of losing the data entirely because of the degraded link conditions.

The successive Mariner Projects and Viking each generated superior conjunction link predictions on the observed experience of the previous projects. The original Viking predictions were made on the basis of observed degradation which occurred during Mariner Mars 1969 and Mariner Mars 1971 superior conjunctions. As these Projects had available during their superior conjunctions only low-gain antennas, the only data quantities for which degradation could be determined at the receiving stations were S-band downlink carrier strength and single-subcarrier 8-1/3-bit/second (bps) telemetry data signal-to-noise ratio.

The amount of degradation is known to be a function of (a) the activity of the sun and (b) the angle between the ground receiving antenna boresight and the sun. The Viking superior conjunction would occur during the minimum level of the 11-year solar activity cycle. However, observations during previous conjunctions made it clear that day-to-day solar variations also had significant effects on the S-band communications links.

The major degradation factors are defined as (a) the noise temperature increase occurring at the Deep Space Station and (b) spectral spreading or "scintillation." The noise temperature increase is caused by the ground antenna sidelobes or main beam pointing toward the solar disc. The S-band receiving system noise temperature was predicted to increase from a normal of 20 to 25 kelvins at a 64-meter station to several thousand kelvins. In addition, for sun-earth-probe angles of less than about 2 degrees, large variations during the period of a single station pass were predicted. These variations were due to the "quadripod effect," named for the four-legged support structure holding the antenna subreflector. This structure creates asymmetries in the antenna pattern, primarily sidelobes which cross the solar disc.

For most closed-loop operations, the dominating degradation factor is the spreading of the uplink and downlink signal spectra from a line to several tens of hertz for small sun-earth-probe angles. The Viking observations did not separate these two causes.

The Viking predictions appear in Figs. 1 and 2. Figure 1 shows the predicted sun-earth-probe angle as a function of calendar date late in 1976. The minimum angle was predicted to be approximately one-quarter of a degree, with Mars actually being obscured from earth by the solar disc for about half a day. Figure 2 shows the predicted degradation for the S-band downlink carrier strength and for the 8-1/3-bps single-subcarrier telemetry uncoded signal-to-noise ratio, each prediction a function of calendar-date. The predictions are given in three curves. Curve A defines the predicted "peak-to-peak" variation expected on either the downlink carrier level or the signal-to-noise ratio during a given day's pass. Curve B defines the average degradation in the S-band downlink carrier level (but excluding the peak-to-peak variation just mentioned). Curve C similarly defines the average degradation of the low-rate telemetry signal-to-noise ratio. The degradation curves are based on Mariner Mars 1971 observed degradations as a function of the sun-earth-probe angle, with these angles translated to Viking calendar dates by means of Fig. 1.

III. Mariner Venus-Mercuy 1973 Experience

The Mariner Venus-Mercury 1973 superior conjunction occurred at a time intermediary between the generation of the Viking predictions and the flight mission itself. This spacecraft included several new features of interest to Viking. It had an articulated high-gain antenna for the downlink, although the uplink was received via a low-gain antenna. It also had an experimental X-band transmitter, of the same type as would be used on Viking. And it also had dual-subcarrier downlink telemetry mode, with the high-rate channel coded, just as Viking although with different bit rates. The minimum sun-earth-probe angle of 1.66 deg occurred on June 5, 1974.

Figure 3 compares the previous superior conjunctions with that predicted for Viking, as the information was available in the autumn of 1974. Solar activity is defined, in this figure, in terms of two quantities: sunspot number and "Ottawa flux." These quantities are predicted, observed, and published. The "Ottawa flux" is measured at 2800 MHz at the Ottawa (Canada) solar observatory. The units are watts per square meter per hertz $\times 10^{-22}$. To indicate the variability of sunspot number and Ottawa flux, the mean and standard deviations for the day of minimum sun-earth-probe angle are given.

On the earlier Mariner Mars 1971 mission, downlink telemetry had been blacked out for 20 days. In contrast, on Mariner Venus-Mercury 1973, S-band single-subcarrier telemetry was received throughout the conjunction period, although the bit error rate increased as the sun-earth-probe angle decreased. The difference between these two missions is attributed to two factors: the larger minimum sun-earth-probe angle; and the use of the high-gain antenna for the Mariner Venus-Mercury 1973.

Mariner Venus-Mercury observation data appear in Fig. 4. On this mission the superior conjunction caused a relatively slight degradation in the observed S-band downlink signal level and a somewhat greater degradation in the 33-1/3-bps signal-to-noise ratio. Comparing these degradations with those predicted for Viking showed (a) considerably smaller S-band carrier degradation than predicted for Viking, and (b) very nearly the same low-rate signal-to-noise degradation as predicted for Viking.

The Viking Project had great interest in being able to predict the degradation of block-coded high-rate data because the Orbiters would be accumulating scientific data right up to the end of the primary mission, limited only by the predicted solar effects of superior conjunction. There was no good theoretical basis for rationalizing whether high-rate coded data should be degraded more or less compared with low-rate uncoded data. A limited amount of Mariner Venus-Mercury dual-subcarrier operation occurred, down to a sun-earth-probe angle of 3.2 deg. This, by coincidence, corresponded to a time in the Viking mission 10 days before minimum sun-earth-probe angle and equal to the defined end of the Viking primary mission, which was November 15, 1976. Analysis of the Mariner Venus-Mercury 7350-bps block-coded data showed a mean degradation of 1.7 dB from the predicted signal-to-noise ratio of 5.3 dB. The standard deviation, indicating the amount of scatter on the data, was 1.1 dB. User comments on data quality were that the quality was poor and very noisy, even though the observed signal-to-noise ratio of 3.6 dB compares favorably with the "threshold" value of 3.0 dB assumed for Viking planning.

Noting briefly the radiometric data, the S-band doppler was too noisy to be usable for orbit determination on Mariner Mars 1969 and Mariner Mars 1971. The Mariner Venus-Mercury 1973 two-way S-band doppler and S-band ranging was usable through conjunction, although the noise level did increase. As for the X-band downlink, which provided a radio-frequency carrier for doppler tracking and ranging modulation modulated on the carrier, these radiometric quantities were too noisy to be of use on Mariner Venus-Mercury 1973.

The Mariner Venus-Mercury observations and their implications to Viking were presented at a meeting of the Viking Telecommunications Working Group on September 24, 1974. These observations proved (for the first time) that downlink telemetry data can be maintained to a sun-earth-probe angle of 1.6 deg and that high-rate coded data can be maintained to a sun-earth-probe angle of 3.2 deg. The predicted outlook for the Viking primary mission was good.

IV. Viking Orbiter Telecommunications Observations During Superior Conjunction

For the Viking superior conjunction, the spacecraft and network were configured as follows:

(1) Orbiter ranging channel "ON."

(2) Orbiter X-band transmitter "ON."

(3) Downlink in "cruise" mode (single-subcarrier) at 8-1/3-bps.

(4) High-gain antenna pointing updated frequently enough to limit pointing error to less than 0.5 deg.

(5) Ground transmitter power level 50 kW for overseas stations and 100 kW for DSS 14 for the 64-m stations.

(6) Deep Space Station personnel to include in the post-track teletype report hourly readings of S-band and X-band system noise temperature.

Within one month of November 25, 1976, a set of "standard" predictions were used by the Telecommunications Unit to assess link degradation. These neglected the slightly changing earth-to-Mars distance and the effects of station elevation angle on system noise performance. The predictions included:

Uplink carrier level (command and ranging modulation (ON)	−130 dBm (26-m station, 20 kW)
	−117 dBm (64-m station, 50 kW)
S-band downlink carrier level (single subcarrier, ranging ON)	−151.5 dBm (26-m stations)
	−143.0 dBm (64-m stations)
X-band downlink carrier level	−153.0 dBm (64-m stations only)
Signal-to-noise ratio	+20 dB (26-m stations, 8-1/3 bps)
	+30 dB (64-m stations, 8-1/3 bps)

Following is a qualitative "snapshot" of link conditions existing just before the total loss of downlink data. Included are some typical digital television displays of the link quantities, generated in plot format by the Viking mission and test computer. This "snapshot" is for November 23, 1976, at the start of the DSS 14 pass, when the sun-earth-probe angle was about 0.7 deg.

(1) *Downlink S-band signal level.* The two-way S-band downlink was degraded as much as 5 to 10 dB during

some station passes. The one-way downlink was not degraded more than 5 dB.

(2) *Downlink X-band signal level.* Degradation exceeded 20 dB in the two-way mode, with values of −170 to −175 dB below 1 mW. The degradation was only about 2 dB in the one-way mode and fairly stable.

(3) *Low-rate signal-to-noise ratio.* This parameter was also affected by the two-way or one-way operation, when the sun-earth-probe angle was smaller than 2 deg. It also varied considerably over long periods during a single station pass, possibly due to the quadripod effect, causing an increase in system noise temperature. The indicated signal-to-noise ratio, in the station telemetry and command processor computer, was as low as 2 to 3 dB at 64-m stations, sometimes, and as high as 7 or 8 dB.

(4) *Bit error rate for the low-rate data.* Bit error rate was quite variable, going from a low of 6×10^{-3} to as high as 4×10^{-2}. This variability is consistent with the variability noted in the signal-to-noise ratio. The bit error rate was significantly higher at 1-deg sun-earth-probe angle than it had been at 2 deg.

(5) *Uplink carrier signal level.* The average uplink carrier level was degraded by 1 dB at the most. The scatter was 5 dB peak-to-peak at this time, although scatter of as much as 8 dB peak-to-peak had been noted at 2 deg sun-earth-probe angle. These values are for 64-m stations, at 50 or 100 kW.

Computer-generated plots of these data are shown in Fig. 5, where the link is not disturbed greatly by the sun. Figures 6 through 10 then can be compared with Fig. 5 to show the increasing effects of superior conjunction on uplink and downlink quantities.

Figure 6 begins to show the solar effects. This is a composite of several digital television plots which have been combined to show the simultaneous effects on (a) two downlink receivers at DSS 14, (b) the low-rate signal-to-noise ratio, (c) the high-rate signal-to-noise ratio, and (d) the uplink carrier strength, as telemetered via the low-rate channel. This figure also shows Viking Orbiter 1 data, as did Fig. 5, but on November 10, 1976 when the sun-earth-probe angle was slightly larger than 4 deg. The top two plots in Fig. 6 show the downlink carrier as received by the two Block IV receivers at DSS 14 (Receivers 3 and 4). On this pass, Receiver 4 had reasonably steady performance, although the scatter is larger than the downlink carrier shown in Fig. 5, almost two months earlier. The "glitching" (upward vertical lines from the average level) on Receiver 3 was *not* caused by solar effects, since the same S-band downlink is not disturbed on Receiver 4. It was necessary to use cross-checks of this type, when possible, to eliminate "artifacts" caused by factors other than the sun.

The third plot on Fig. 6 shows the low-rate 8-1/3-bps signal-to-noise ratio. At approximately 1 hour and 20 minutes after the start of this plot, the Orbiter switched from the single-subcarrier to the dual-subcarrier mode. Under normal conditions, the low-rate telemetry decreases from a "saturated" value of about 23 dB in the single-subcarrier mode down to about 12 dB in the dual-subcarrier mode. Strikingly, on this figure, there is virtually no difference in the estimated signal-to-noise ratio in the two different modes.

One of the significant observations during Viking superior conjunction was that the estimated low-rate signal-to-noise ratio began to degrade more than one month prior to the time of minimum sun-earth-probe angle, much more so than would be expected from the counted bit error rate. On the other hand, the estimated high-rate (block-coded) signal-to-noise ratio did not degrade significantly until quite small sun-earth-probe angles. At the same time, the counted bit error rate for the high-rate block-coded data was much worse than would be expected from the signal-to-noise ratio. This effect is displayed by comparing the bottom three plots of Fig. 6. The fourth-from-top plot shows the estimated high-rate signal-to-noise ratio. It averages 7 or 8 dB. Were this correct, the bit error rate would be almost zero. The bottom plot shows the telemetered uplink carrier level. The large number of vertical bars during the period of high-rate mode operation indicates that the bit error rate was very high. (Each vertical spike indicates a bit error in a significant bit of the telemetered data.) Upon switch to the single-subcarrier mode, the amount of spiking decreases to zero. Another interesting effect on the links can be observed by comparing the bottom plot of Fig. 6 with the top plot of Fig. 5. Both are uplink carrier levels. In Fig. 5, well before superior conjunction, the scatter is at most 3 dB peak-to-peak, whereas in Fig. 6, only 15 days before minimum sun-earth-probe angle, the scatter has increased to about 6 dB peak-to-peak, and there are longer-term variations evident also. During the high-rate mode operation, the counted bit error rate was about 1 in 100. The "predicted" bit error, neglecting solar effects is about 1 in 10,000. Thus, the actual bit error rate was more than two orders of magnitude higher than would be indicated by a Gaussian noise distribution.

Additional insight into the solar effects on telemetered Orbiter data during this same station pass can be gained through examination of Fig. 7. The telemetry channels shown are (a) the pitch cruise sunsensor position and (b) the yaw

cruise sunsensor position, in the Orbiter attitude control subsystem. The vertical axes are data numbers, and the curves indicate the "limit cylces" of these sensors. Approximately the first one hour of the plots occurred while the Orbiter was in the single-subcarrier telemetry mode. This mode results in more of the Orbiter's downlink power being concentrated in the telemetry subcarrier than occurs in the dual-subcarrier mode. The bit rate of the low-rate subcarrier is 8-1/3-bps. When the downlink changed from the single-subcarrier to the dual-subcarrier mode, the bit error rate went from approximately 1 in 1000 to 1 in 100. In addition, on the plot, when the dual-subcarrier mode existed, the computer processed the high-rate data, which is at a bit rate of 1 kbps. Thus, in the high-rate mode, there are many more data points displayed per unit time. The result is that the bit errors predominate in the displayed data. As had been observed on previous Mariner projects, "structured" telemetry data, such as these attitude control limit cycles, are relatively immune to even a high bit error rate. With some imagination, one can discern the continuing trends in the limit cycles even through the very high bit error rate.

November 10, 1976 was the last date in which the dual-subcarrier data mode was used. Link conditions continued to degrade even after the single-subcarrier mode, with data set to the lowest possible bit rate, 8-1/3-bps. Figure 8 shows the link data on November 15, 10 days prior to the time for the minimum sun-earth-probe angle. The sun-earth-probe angle was 3 deg. The telemetered uplink signal strength shows a scatter of 10 dB peak-to-peak, the maximum amount observed during the Viking superior conjunction. The scatter seemed to decrease somewhat, to about 7 dB peak-to-peak, just prior to the total loss of downlink data. The cause for this is not known; possibly solar activity was slightly greater at the earlier date. Comparing the middle and bottom plots of Fig. 8 with the comparable data in Fig. 5, the downlink S-band signal level and the low-rate channel signal-to-noise ratio do not show much more scatter than is normal well away from superior conjunction. This is thought to be due to the heavy "weighting" which exists in the Deep Space Network software which displays the signal level and the signal-to-noise ratio. In terms of the predicted signal levels without solar effects:

(1) The uplink signal *mean* residual is not more than 1 dB, but there is a large amount of scatter about this mean value.

(2) The S-band downlink carrier level also shows little average degradation, not more than 1 dB.

(3) The 8-1/3-bps signal-to-noise residual shows a very large degradation, with an observed value averaging 2 dB against a predicted value of 20 dB for the 26-m DSS 61 performance.

(4) The bit error rate was not counted, however, the top plot shows that there are few high-order bit errors (four vertical spikes only) during 4 hours of tracking, compared with a bit error rate of 1 in 25 expected for 2-dB signal-to-noise ratio.

The final plots shown were taken on November 22, 1976, 3 days before the minimum sun-earth-probe angle, when this angle was under 1 deg. Figure 9 displays the link information for VO-1 which was one-way with DSS 14 and DSS 43 during this time. The stations' Receivers 1 and 2 were locked to VO-1 S-band downlink. At the same time, Fig. 10 displays the VO-2 link data. VO-2 was two-way with DSS 14 during a portion of its pass, and later was two-way with DSS 43 during a portion of that pass. In each station, Receiver 3 was locked to the VO-2 S-band downlink, and Receiver 4 was locked to the VO-2 X-band downlink. The bottom plot in each portion of the figure is the 8-1/3-bps signal-to-noise ratio.

The difference between one-way and two-way operation is apparent in Fig. 10. DSS 14 X-band receiver was unable to lock to the X-band downlink at all during two-way operation, whereas it received X-band with not more than 2 dB of signal level degradation during one-way. DSS 43 was able to lock to X-band downlink in two-way, but the indicated signal level was degraded between 10 and 15 dB compared with one-way operation. As for the low-rate signal-to-noise ratio, it was quite variable during the DSS 14 pass and less variable during the DSS 43 pass. There are other variations in S-band and X-band downlink carrier level (particularly near 6 hours on the plot) that do not have a known cause, unless it be receiver bandwidth setting or other configuration effect. The indicated signal-to-noise ratio did not seem to be affected at that time. Conversely, at about 9 hours on the plot, the signal-to-noise decreased to near zero, but the S-band downlink carrier level did not change significantly. Again, a configuration effect is suspected, or possibly severe noise temperature increases, "quadripod effect."

The VO-1 quantities in Fig. 9 show less overall variation than the VO-2 quantities in Fig. 10. The latter have been discussed. For VO-1, the top plot shows that significantly more bit errors occurred (vertical lines) near 4 hours and near 9 hours on the plot. The cause of these is not known, nor that of the changes in signal-to-noise ratio (bottom plot) just before 5 hours and after 8 hours. Again, configuration changes to optimize radioscience data may be the cause, as the superior conjunction period of the Viking mission emphasized radioscience experiments.

Qualitatively, the links recovered in the reverse order and at about the same rate, as a function of sun-earth-probe angle, as they degraded going into superior conjunction. To first order,

the performance a given number of days later than November 25, 1976 was the same as that number of days before November 25.

By January 1, 1977, the only residual effects seen in the links were:

(1) The uplink carrier level still showed more scatter about its average value than is typical well away from the sun.

(2) The low-rate signal-to-noise ratio, particularly at 8-1/3 bps, still showed 1- to 2-dB degradation. This was of no operational concern, since the channel had more than adequate margin.

V. Assessment of Superior Conjunction Prediction Capability

The residuals for the S-band downlink signal level and the single-subcarrier, low-rate uncoded, signal-to-noise ratio are shown in Figs. 11 and 12. A "residual" is the algebraic difference between the link quantity predicted and the quantity observed during the tracking pass. All basic Viking Orbiter link predictions were made on the basis of no solar degradation. Thus, the observed degradation would show up directly as an increasingly negative residual.

The data in Figs. 11 and 12 are for Viking Orbiter 2; that for Viking Orbiter 1 is similar. The "nominal" and the "worst case" degradation values from Fig. 2 are indicated. As can be seen in Fig. 11, the actually observed S-band downlink signal level residuals were usually equal to or smaller than the nominal degradation predictions. The actually observed degradation of the low-rate signal-to-noise ratio (Fig. 12) is somewhat greater than the "nominal," but somewhat less than the "worst case."

VI. Summary and Conclusions

The minimum sun-earth-probe angle on the Viking mission occurred on November 25, 1976.

The first evidence of solar effects was that the single-subcarrier signal-to-noise ratio gradually came out of "saturation" at the 64-m stations. The next sign was an increase in the scatter observed on the uplink signal level, then on the downlink S-band signal level. Deep into conjunction, the bit error rate on the coded high-rate data in the dual-subcarrier mode increased greatly, compared to the indicated signal-to-noise ratio. Finally, the X-band carrier level showed great variations between times when there was an uplink to the Orbiter ("two-way") and the times when the Orbiter had no uplink ("one-way"). This effect had also been noted on the Mariner Venus-Mercury spacecraft during its superior conjunction, and was caused by uplink carrier degradation being multiplied by the ratio of the X-band and the S-band frequencies during two-way operation.

For two successive days nearest the minimum sun-earth-probe angle of 0.25 deg, no closed-loop receiver lock could be maintained even at 64-m tracking stations. This is not unexpected, considering that for several hours on November 25, the geometric raypath from Mars to earth passed through the "edge" of the solar disc. The radioscience experimenters obtained "some" open-loop receiver data during the time that closed-loop receiver lock was lost. Following this time, as the sun-earth-probe angle increased, the link degradations gradually decreased. Performance was symmetrical going in and coming out, and generally followed the predicted degradations stated three years before the fact.

As during previous superior conjunctions, there was close cooperation between the Deep Space Network operations personnel, the Project telecommunications analysts, and the radioscience investigators.

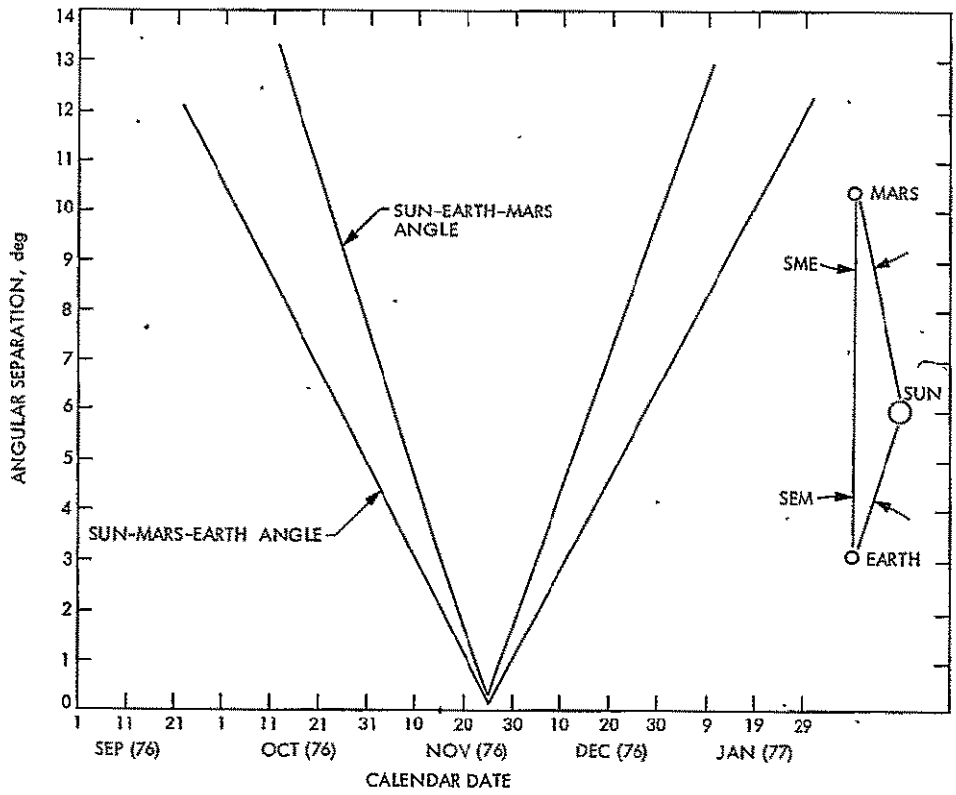

Fig. 1. Angular separation as a function of calendar date

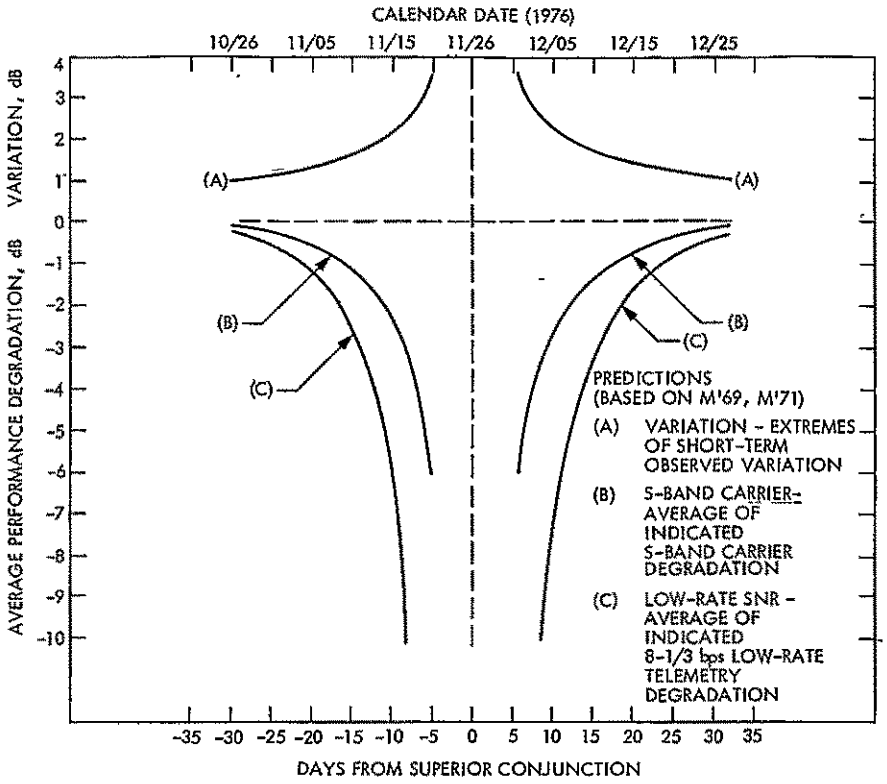

Fig. 2. Predicted degradation of Viking Orbiter links

	MARINER MARS 1969	MARINER MARS 1971	MARINER VENUS-MERCURY 1973	VIKING MARS 1975
DATE OF MINIMUM SEPARATION	4/30/70	9/7/72	6/5/74	11/25/76
MINIMUM SUN-EARTH-PROBE ANGLE	0.95°	1.05°	1.66°	0.23°
PREDICTED SOLAR ACTIVITY	MED-HIGH	MED	LOW	LOW
ACTUAL SOLAR ACTIVITY	MED-HIGH	MED-HIGH WITH FLARES	LOW-MED WITH FLARES	TBD*
AVERAGE SUNSPOT NUMBER				
MEAN	120.1	66.5	40.4	APPROX 40
STANDARD DEVIATION	30.1	24.3	31.9	
AVERAGE 2800-MHz SOLAR FLUX				
MEAN	167.8	121.6	90.7	APPROX 80
STANDARD DEVIATION	22.7	15.9	12.4	
COMMUNICATIONS CONFIGURATION AND MODE	LGA, 64-m S-BAND 8-1/3 bps	LGA, 64-m, S-BAND 8-1/3 bps	HGA, 64-m, S/X-BAND 33-1/3 bps RECEIVE LGA, S-BAND	HGA, 64-m, S/X-BAND 33-1/3 bps RECEIVE HGA, S-BAND
DOWNLINK BLACKOUT FOR TELEMETRY	?	20 days	NONE, BUT INCREASED BIT ERROR RATE	NONE EXPECTED IF CRUISE MODE
RADIO METRIC DATA	S-BAND RANGING	S-BAND RANGING	S-BAND RANGING NOISY S-BAND DOPPLER 1-WAY X-BAND DOPPLER	S/X-BAND RANGING S/X-BAND DOPPLER
COMMAND BLACKOUT PLANNED	?	20 days	20 days	TBD

*TBD = TO BE DETERMINED

Fig. 3. Comparison of superior conjunction characteristics

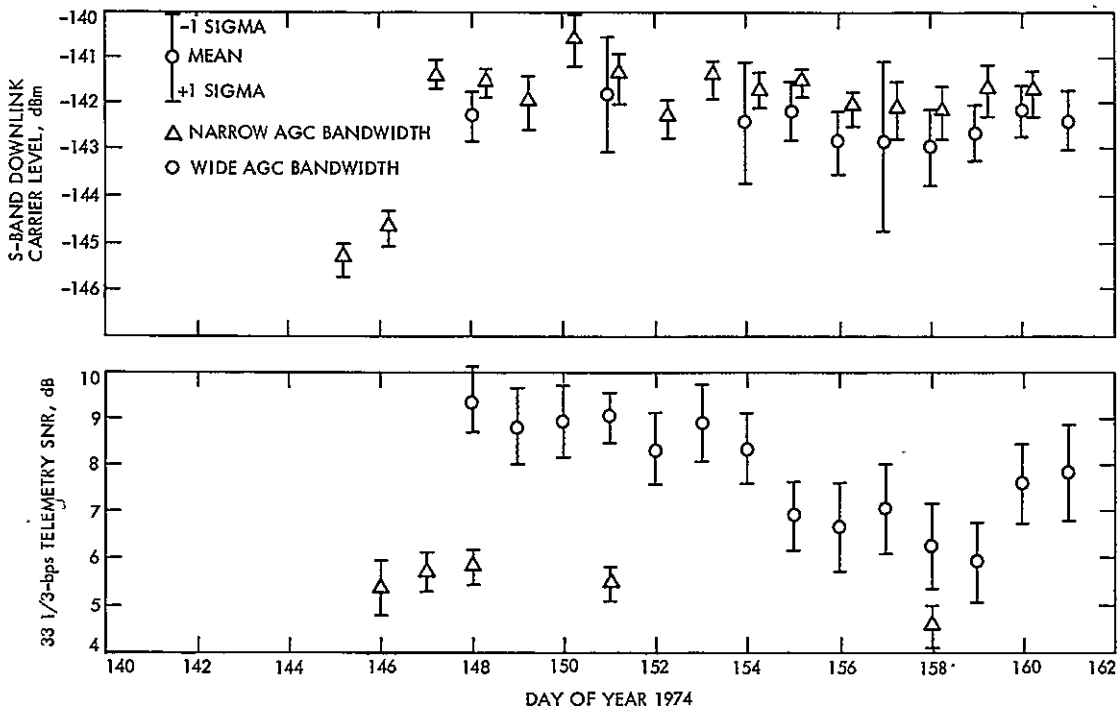

Fig. 4. Mean and standard deviation of Mariner Venus-Mercury 1973 link parameters from DSS 14

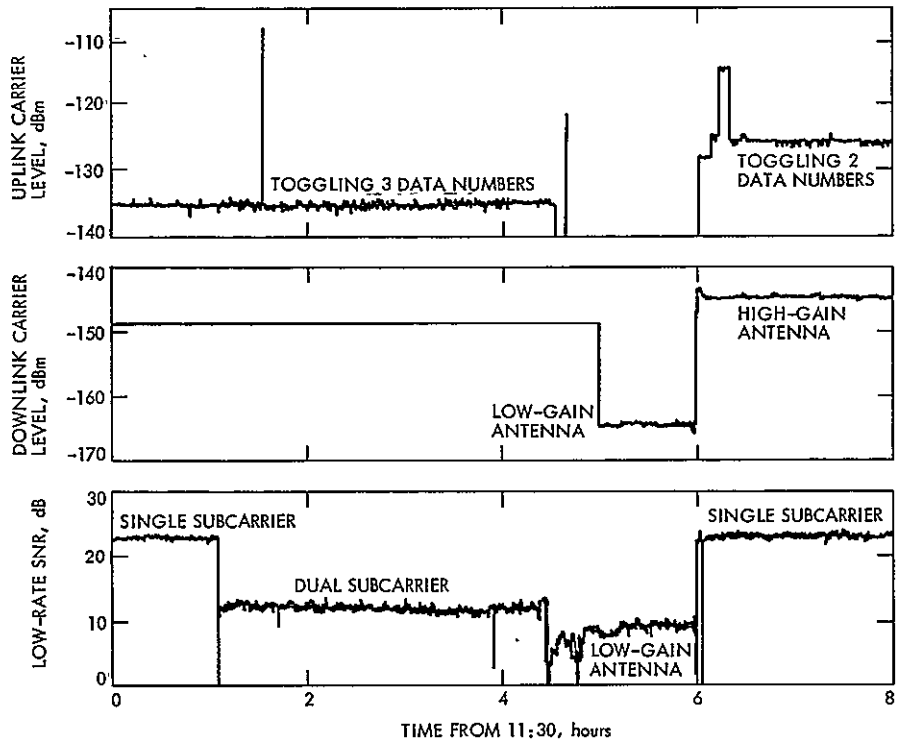

Fig. 5. Digital television hardcopy for typical link conditions without solar effects on communications on September 24, 1976

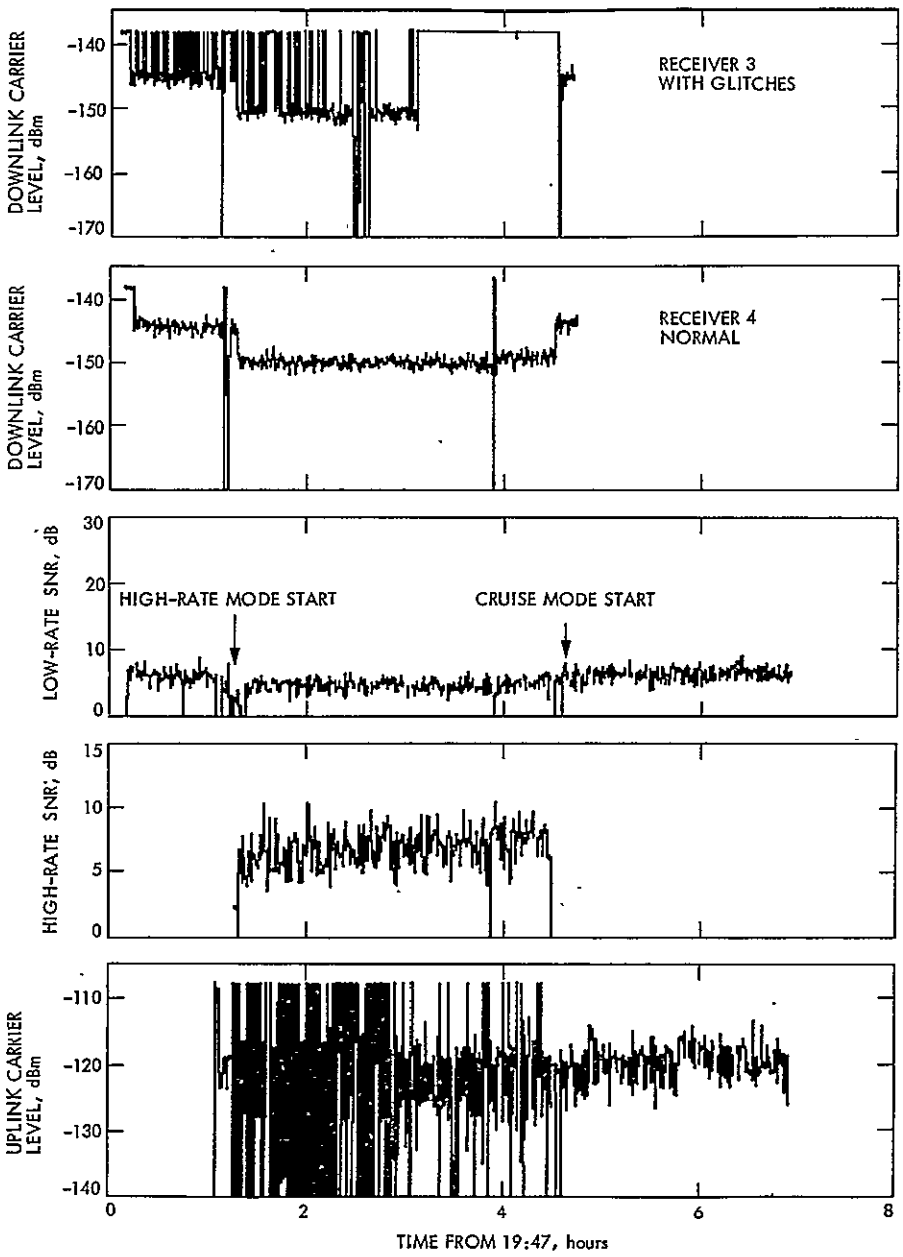

Fig. 6. VO-1 link quantities on November 10, 1976

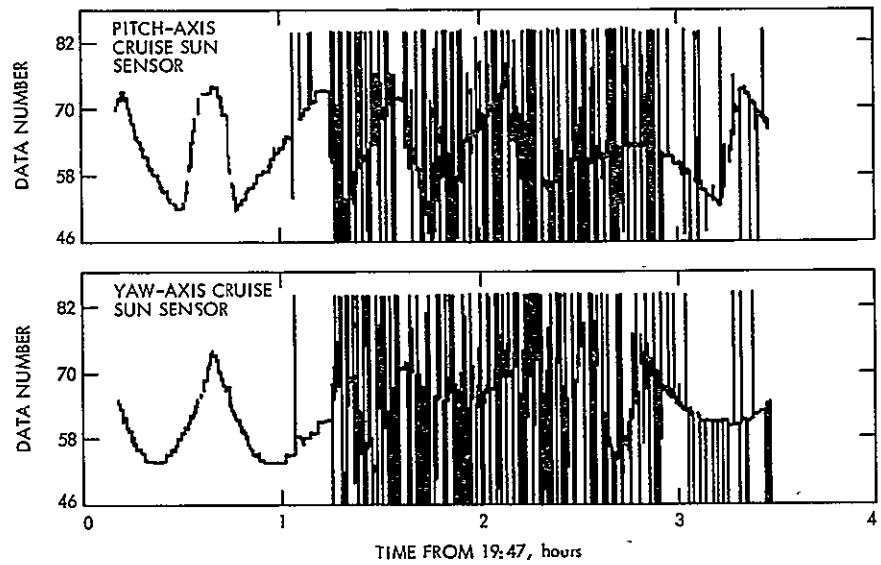

Fig. 7. Attitude control limit cycle telemetry data on November 10, 1976

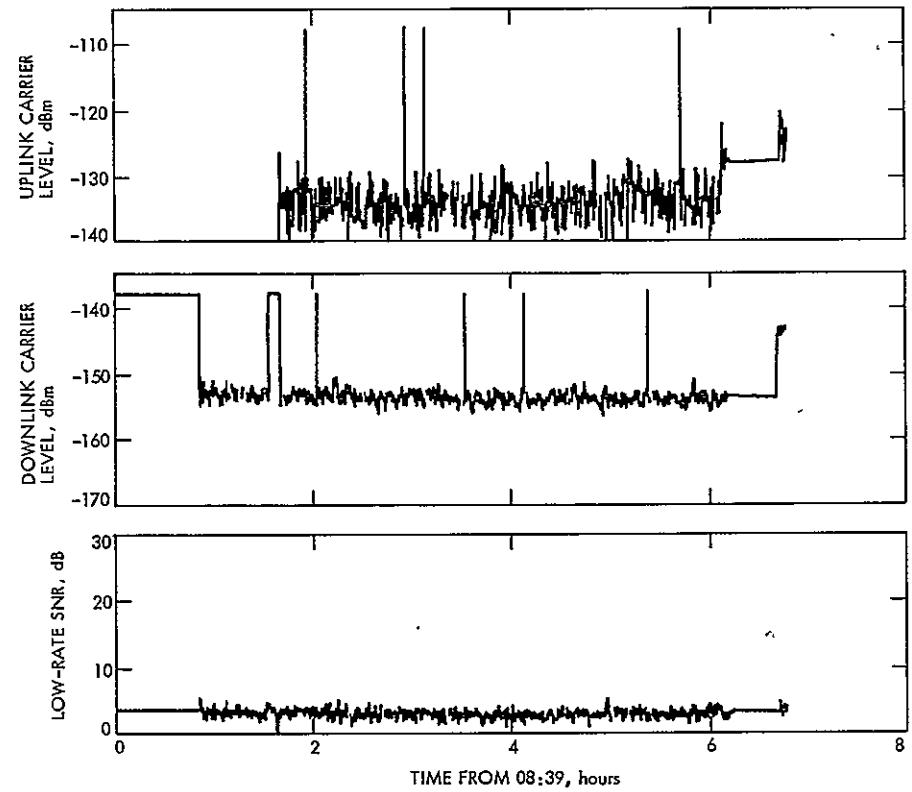

Fig. 8. VO-2 link quantities on November 15, 1976

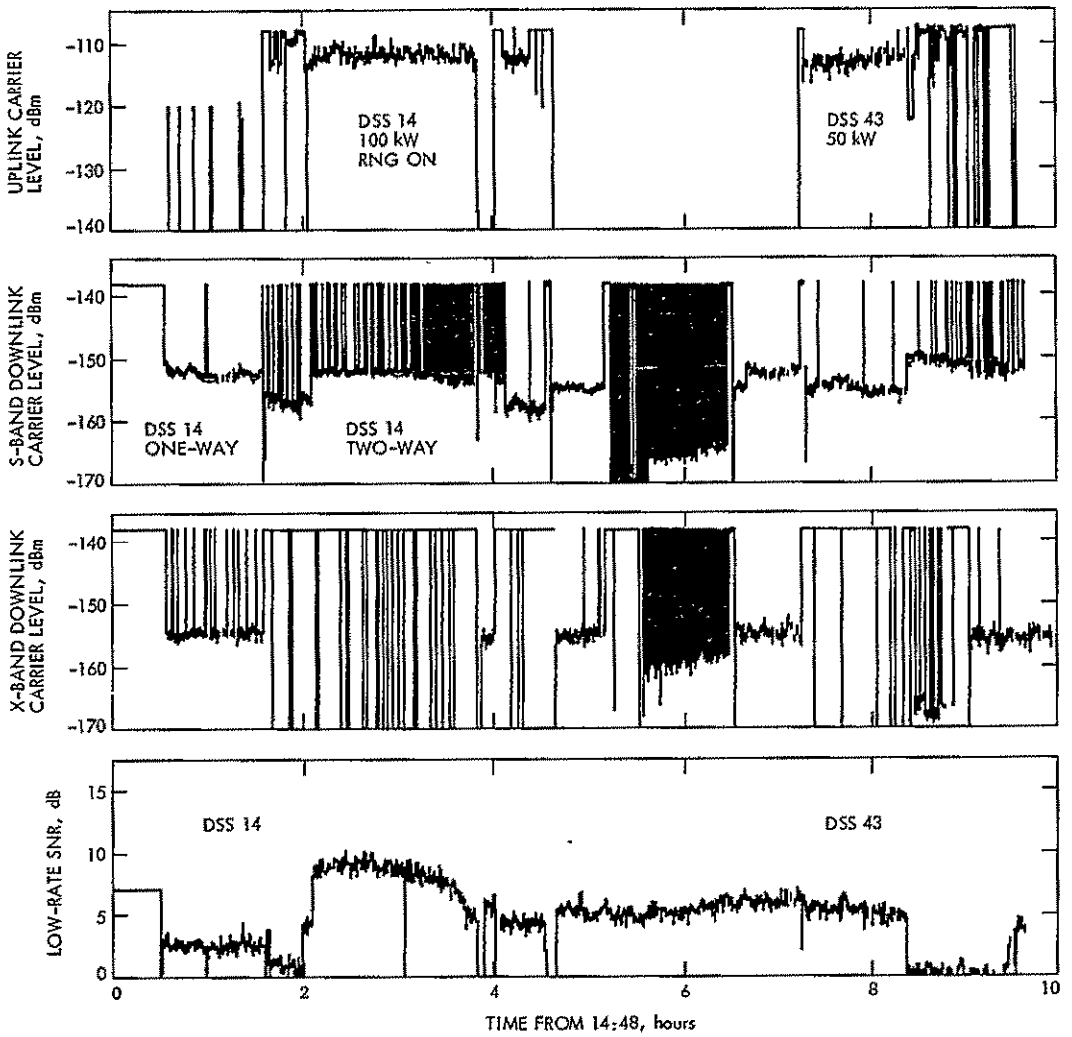

Fig. 9. VO-2 link quantities on November 22, 1976

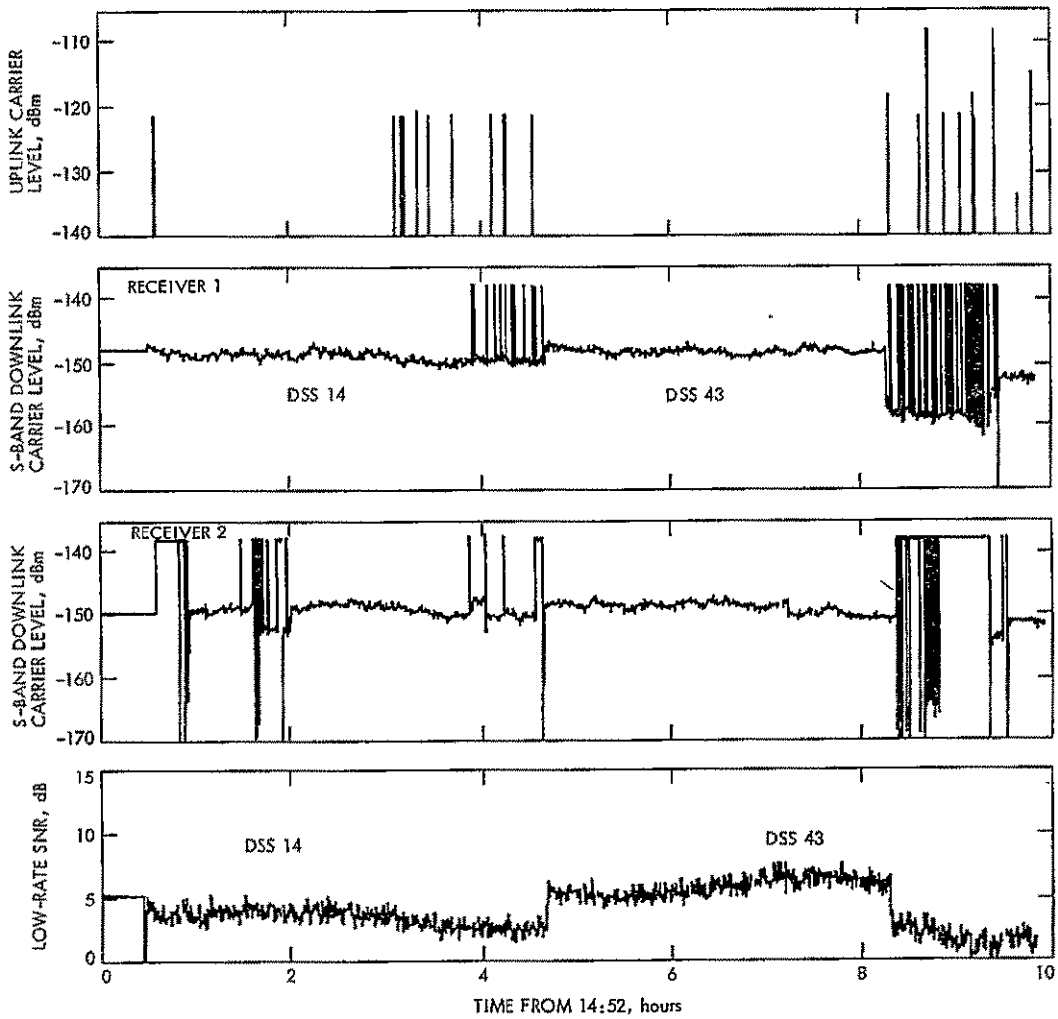

Fig. 10. VO-1 link quantities on November 22, 1976

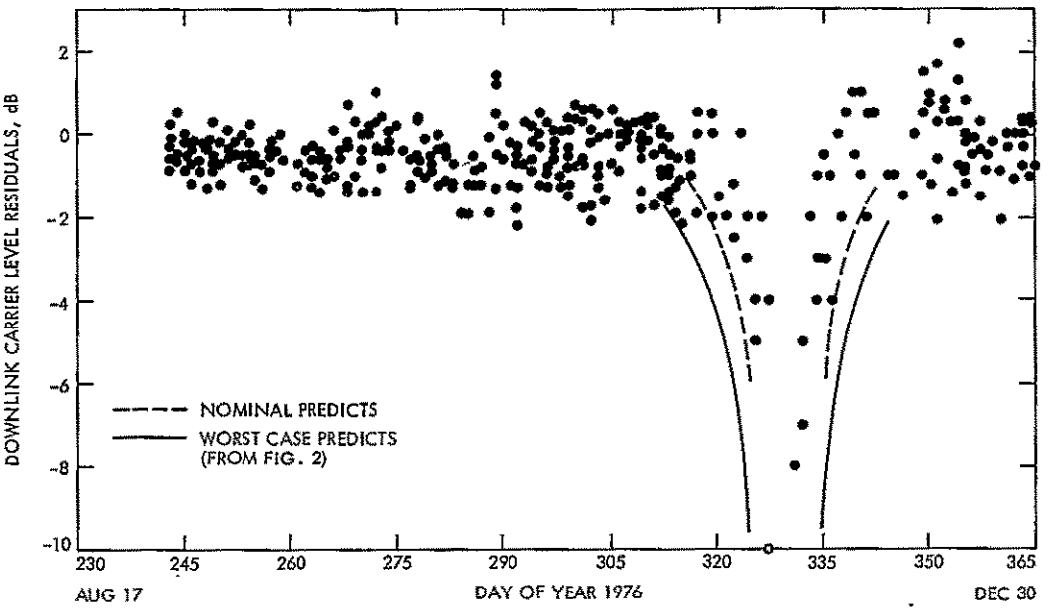

Fig. 11. VO-2 S-band downlink signal level residuals (64-m net)

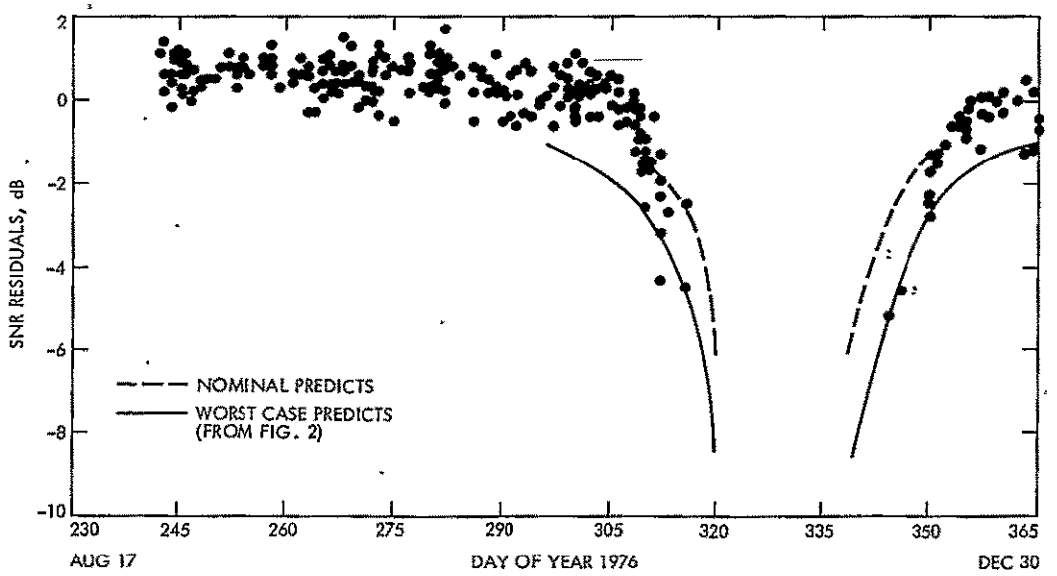

Fig. 12. VO-2 low-rate (33⅓ bps) SNR residuals

DSN Water Vapor Radiometer Development — A Summary of Recent Work, 1976-1977

S. D. Slobin and P. D. Batelaan
Radio Frequency and Microwave Subsystems Section

A water vapor radiometer (WVR) has been developed which measures the atmospheric noise temperature at two different frequencies. These noise temperatures are used in empirical-theoretical equations which yield tropospheric range delay, in centimeters, through the atmosphere along the beam of the WVR. This range correction is then applied, as needed, to measurements concerning spacecraft range and to VLBI baseline determinations. The results of the March 1976 Pt. Mugu tests are given and equipment modifications and JPL tests since that time are discussed.

I. Introduction

The water vapor radiometer (WVR) has undergone a number of developmental changes since its first field operation at El Monte Airport in May, 1975. The present instrument (Ref. 1) has a lower noise temperature, better waveguide matches, better stability and resolution, and more accurate absolute calibration than that which existed two years ago. The presently configured WVR, operating as a noise-adding radiometer (NAR), has noise temperatures of about 700 kelvins on the 22.235-GHz channel, and 750 kelvins on the 18.55-GHz channel. Two frequencies are used in order to separate the effects of liquid water (clouds) which contribute to atmospheric noise temperature but not to tropospheric delay. With a five-minute integration time on each of the six source positions (sky, cold termination, and ambient termination at two frequencies), the stability is better than 0.5 kelvins over an 8-hour period. This corresponds to a tropospheric delay stability of ±0.2 cm for the same period, assuming a homogeneous and constant atmosphere. Figure 2 of Ref. 1 shows the WVR in its configuration during the Pt. Mugu tests. Figure 1 herein shows the WVR as it is presently configured. The air-driven expansion refrigerator which gave cold termination temperatures of about -80°C at Pt. Mugu has been replaced with a pumped fluorocarbon refrigerator capable of maintaining cold load temperatures of about -130°C. For absolute self-contained radiometer calibrations it is desirable to have as cold a reference termination as possible (noncryogenic, for cost and maintenance reasons), since the atmospheric noise temperatures measured by the WVR are generally in the 20 to 100 K range (-253 to -173°C). Figure 2 shows the block diagram of the present system; it is essentially the same as shown in Ref. 1 for the Pt. Mugu instrument.

II. Pt. Mugu Tests, March 1976

The Pt. Mugu tests at the U.S. Navy Pacific Missile Test Center were carried out with the two channels of the WVR operating at 22.235 and 18.0 GHz. Another microwave instrument, known as SMILE (Scanning Microwave Inversion Layer Experiment), was also operating there at the same time. Its

operating frequencies were 22.235 and 31 GHz, because SMILE was originally a satellite instrument and 31 GHz is an atmospheric window, allowing visibility of the Earth's surface from orbit. Numerous "sky truth" instruments were used at Pt. Mugu to determine the real atmospheric properties such as the water vapor and refractive index altitude profiles.

During the period of the tests (about 10 days total) 23 rawinsondes[1] were launched, 34 meteorologically instrumented aircraft flights were made, and 12 microwave refractometer aircraft flights were made. These direct measurements of atmospheric parameters result in an inferred determination of tropospheric range delay. The radiometers probe the atmosphere along the line-of-flight of aircraft and rawinsonde; the microwave measurements are compared to the meteorological measurements and a relationship linking the two is developed.

The meteorological aircraft, provided by Meteorology Research, Inc. (MRI), flew only to an altitude of 3 km. Atmospheric measurements made by the on-board instruments were augmented with the upper-air measurements made with the rawinsondes. The rawinsondes normally send back information all the way up to an altitude of 30 km, but most of the water vapor (the critical parameter in the measurements as far as we are concerned) is below 3 km altitude and is measured by the aircraft instruments, which are much more accurate than the rawinsonde instrumentation.

The meteorological aircraft flew along atmospheric paths at elevation angles of 90, 30, 20, and 10 deg as seen by the WVR. This allowed measurements of tropospheric delay of as much as 6 times the zenith amount (at 10 deg elevation). The troposphere above 3 km altitude in the nonzenith flights was modeled by multiplying the rawinsonde-measured delay above 3 km by the factor 1/sine (elevation angle) to account for the increased atmospheric path length.

The microwave refractometer aircraft, provided by the Navy, flew to 3 km altitude and measured the index of refraction of the atmosphere directly. Conceptually, this instrument would have provided the best direct measure of tropospheric range delay, but unfortunately, problems in instrument calibration prevented the use of this most valuable data.

Figures 3 and 4 show tropospheric delay measurements on the four days when both radiometers, the meteorological aircraft, and the rawinsonde were all operating. Figure 3 shows the zenith measurements (with aircraft measurements augmented by the rawinsonde). Figure 4 shows delay measurements made along an atmospheric path at 10 deg elevation. The consistency among these measurements is remarkable, although it must be mentioned that the Pt. Mugu measurements were used to calibrate the WVR and then this calibration was folded back into the-raw-data, giving the very good agreement in the results shown. Whatever the case, a single set of regression coefficients linking tropospheric delay to microwave measurements was developed which yields consistently correlated values over a wide range of atmospheric conditions. On day 070, the sky was full of dark, threatening clouds, and a moderate amount of drizzle was experienced throughout the day. Two days later on day 072, Santa Ana winds arrived at 7 a.m. and the amount of water vapor in the atmosphere dropped by a factor of about 3, as seen in the drop of zenith tropospheric delay from 9 to 3 cm. For comparison, a normal day (68°F and 40% relative humidity) has a zenith tropospheric delay of about 7 cm. The 10-deg elevation plot shows the same delay variations and consistency of data. It can be seen by comparing the zenith and 10-deg graphs that evidence of horizontal inhomogeneity (nonstratification) of the atmosphere existed during the days shown. The zenith delay numbers of 9.0, 3.3, 8.5, and 7.2 cm should be multiplied by the factor 5.76 (1/sin(10 deg)) to model delay values to 10 degree elevation. These values turn out to be 51.8, 19.0, 49.0, and 41.5 cm, and the daily modeling errors become 3 cm, 5 cm, 5 cm, and 2-5 cm, respectively. This shows the value of direct line-of-sight microwave measurements rather than modeled zenith values.

The equation linking tropospheric delay and microwave measurements (as determined by the Pt. Mugu measurements) is presently

$$\Delta L = 2.640 + 0.273T_{22} + 0.000424T_{22}^2$$

$$+ 0.0858T_{18} + 0.00659T_{18}^2$$

where T_{22} and T_{18} are the "water noise temperatures" (due to vapor and liquid only) and are derived from the measured antenna noise temperatures by subtracting out the cosmic and oxygen noise temperatures at the particular elevation angle of interest. As an example of the use of the above equation, antenna temperatures of 30.5 and 20.9 K at 22 and 18.5 GHz, respectively, at an elevation angle of 30 deg, result in water noise temperatures of 21.6 K and 12.7 K, and a ΔL of 10.9 cm.

Following the Pt. Mugu tests, numerous equipment changes were made; and it is not believed that these affected the "Pt. Mugu coefficients" in the above expression. But, since Pt. Mugu is at sea level, these coefficients may be valid only at

[1] A rawinsonde is a radiosonde that is tracked in azimuth and elevation in order to gain information about wind direction and velocity.

that elevation. Further tests and studies will be made to determine the effects of altitude change.

III. JPL Tests

A large number of radiometer measurements were made from the roof of a building at JPL during the last part of 1976 and first part of 1977. These measurements monitored the results of equipment improvements and also helped to exercise the data reduction methods, which were vastly improved since the Pt. Mugu tests.

Figure 5 shows a typical radiometer determination of tropospheric delay during four days of March, 1977, using the Pt. Mugu coefficients. The radiometer pointed toward the west at an elevation angle of 30 deg and operated unattended during this period. The peak in tropospheric delay toward the end of day 62 indicates an influx of moisture-laden air into the Los Angeles area; and indeed, rain was reported at many locations west of Los Angeles, although none fell on the radiometer itself. The most stable atmospheric period is around day 65.0, where the tropospheric delay shows variations of at most ±0.2 cm over an 8-hour period. It is clear that the radiometer tracks small changes in atmospheric moisture content as seen in the variations at day 63.5. The absolute accuracy of the instrument is not known, as there were no rawinsondes or other meteorological instruments nearby with which to verify the delay values given.

IV. Future Work

Over the next year, a number of VLBI validation support tests will be made at Goldstone DSS 13. Interspersed between these tests will be calibration tests at Edwards AFB, wherein the WVR measurements may be compared to tropospheric delay measurements made by rawinsondes. Edwards AFB is an excellent location at which to calibrate the WVR because it is a desert location similar to Goldstone and has a similar altitude, although some altitude compensation is made in the WVR data reduction as far as oxygen noise contribution is concerned.

A new set of regression coefficients will be determined for the ΔL vs T_{22}, T_{18} equation (the "Edwards coefficients"). These will be compared with the Pt. Mugu coefficients to see if any differences are attributable to instrument change, altitude change, or some other pertinent variable. This determination will be necessary to ensure reliable portability of the WVR if measurements are to be made at a location other than Goldstone.

Reference

1. Batelaan, P. D., et al., "Development of a Water Vapor Radiometer to Correct for Tropospheric Range Delay in DSN Applications," *Deep Space Network Progress Report 42-33,* pp. 77-84, Jet Propulsion Laboratory, Pasadena, Calif., June 15, 1976.

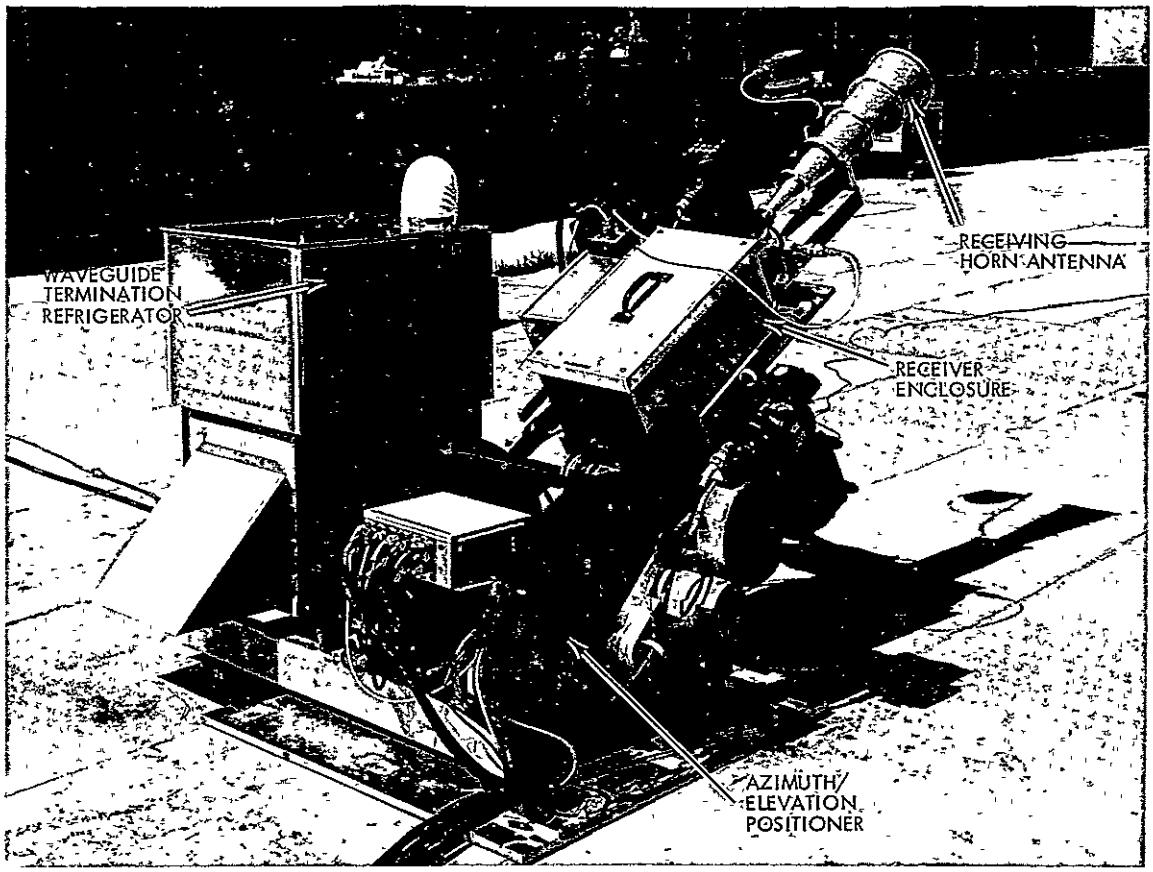

Fig. 1. Water vapor radiometer (present configuration, May 1977) mounted on the roof of Building 238 at JPL

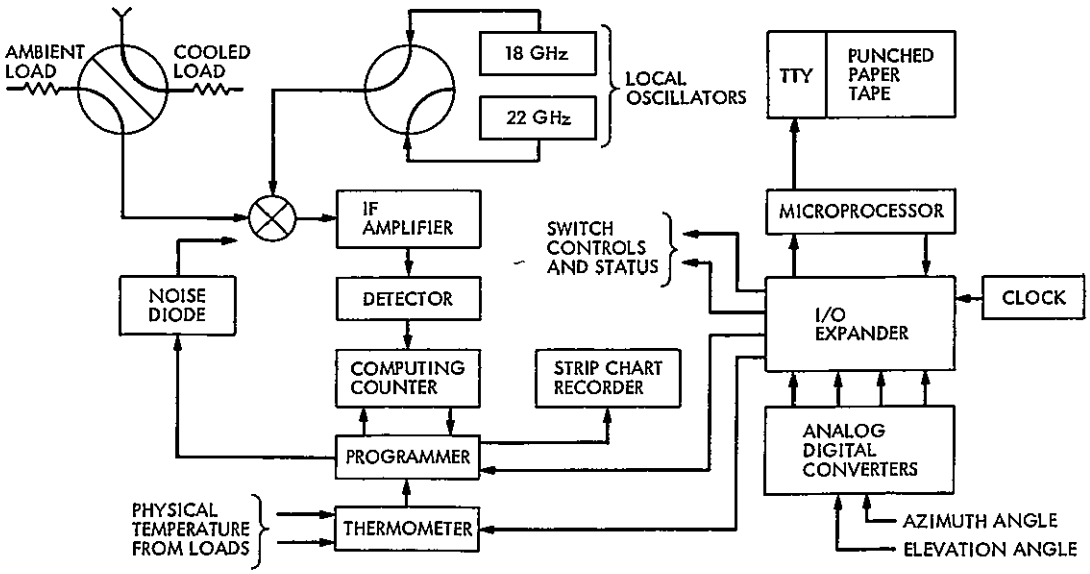

Fig. 2. Block diagram of water vapor radiometer

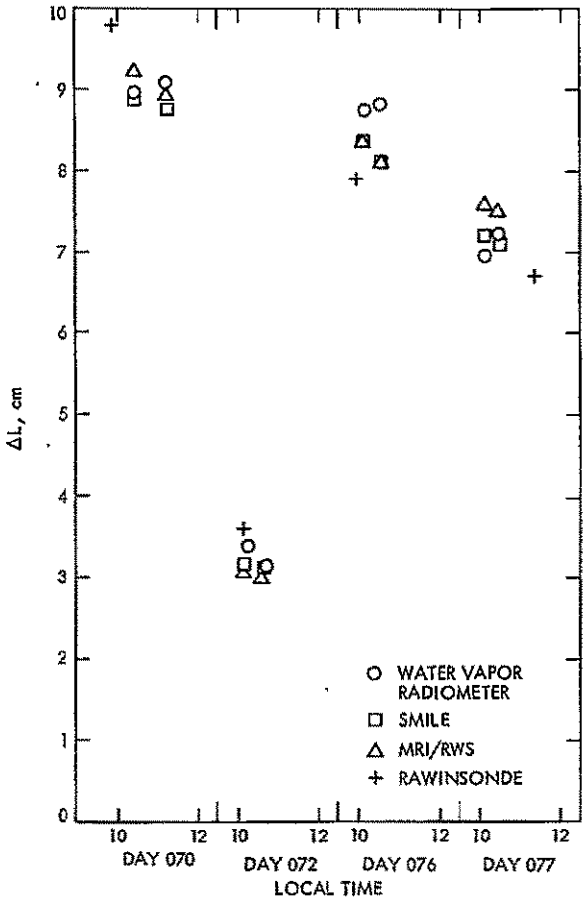

Fig. 3. Zenith tropospheric delay, Pt. Mugu, 1976

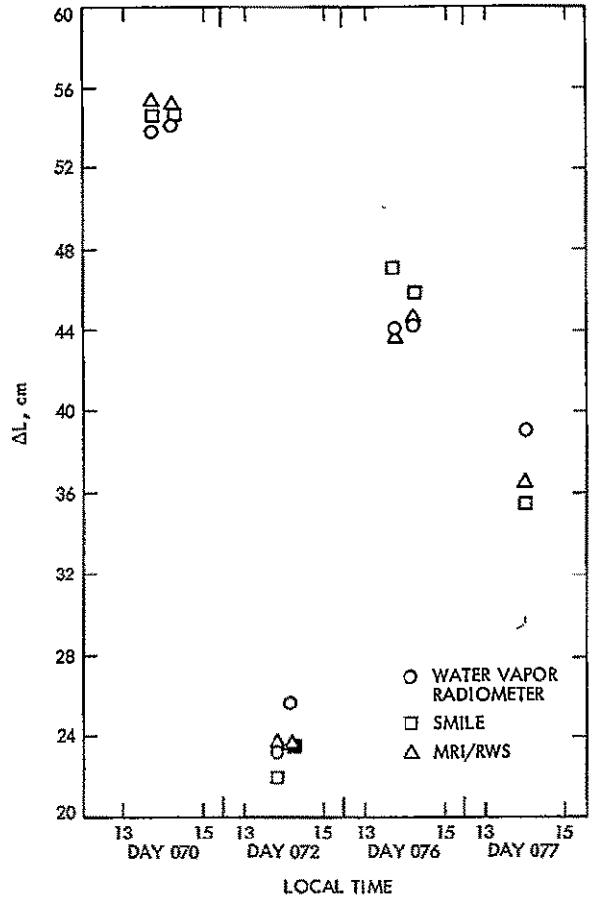

Fig. 4. 10-deg elevation tropospheric delay, Pt. Mugu, 1976

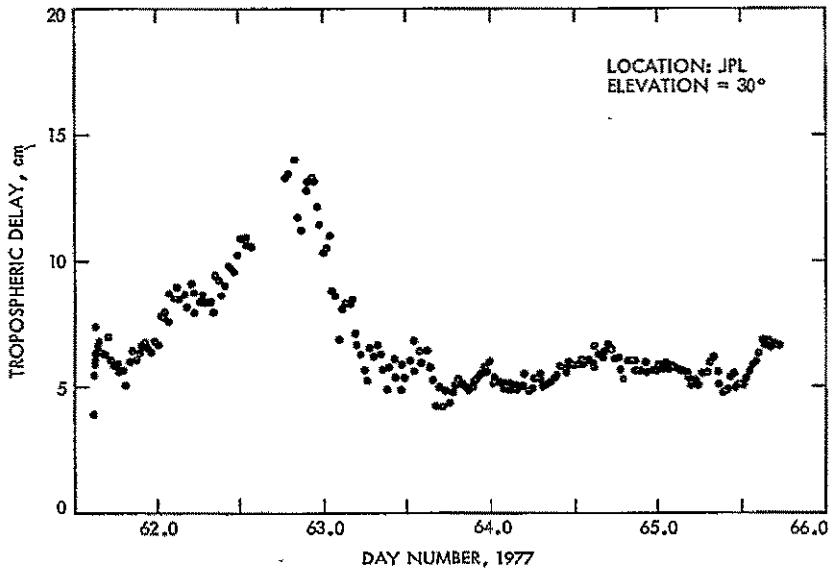

Fig. 5. Tropospheric delay results, JPL operational tests, March 1977

D9

Hydrogen Maser Frequency Standards for the Deep Space Network

P. R. Dachel and S. M. Petty
Radio Frequency and Microwave Subsystems Section

R. F. Meyer and R. L. Sydnor
Communications Systems Research Section

JPL has been operating two experimental hydrogen maser frequency standards at the Deep Space Network (DSN) stations at Goldstone, California, since 1970. Based on operating experience gained with these units and with a test bed maser system at JPL, a field-operable maser has been developed for use in the DSN. The first maser of this new design was installed at the DSN 64-meter station near Canberra, Australia, in December 1975. Second and third units are presently under construction for the remaining DSN 64-meter stations at Madrid, Spain, and Goldstone, California. While these DSN masers remain similar in basic configuration to the earlier experimental units, many design changes have been incorporated in both physics and electronics systems to effect improvements in the following areas: (1) short- and long-term frequency stability, (2) RF isolation of maser output lines, (3) lifetime of active physics components, (4) automatic fault detection and location, and (5) performance and reliability of the receiver-synthesizer system. Frequency stability measurements of the DSS 43 maser, using an updated experimental maser as a reference, resulted in a fractional frequency stability of 3.8×10^{-15} *long term* ($\tau = 90$ *seconds) and* 1.1×10^{-13} *short term* ($\tau = 1$ *second).*

I. Introduction

In 1965, the Jet Propulsion Laboratory initiated a development program for a field-operable hydrogen maser to meet the future requirements of the Deep Space Network. Two experimental hydrogen masers (Ref. 1) were subsequently built and installed at the DSN stations at Goldstone, California, during 1970. Based on operating experience gained with these units and with a test bed maser system at JPL, a prototype hydrogen maser was recently developed for use in the DSN. This article describes some of the unique features of this maser, and presents life expectancy, frequency stability, and other performance data obtained to date.

II. Hydrogen Maser

The DSN hydrogen maser (Fig. 1) consists of two assemblies; a physics unit and an electronics rack. The physics unit is mounted on a shock-absorbing base and consists of the maser

vacuum system, microwave front end, and four electronics modules that are associated with the hydrogen glow discharge. All other electronics, including the operating controls for the physics unit, are contained in the electronics rack.

A. Physics Unit

A simplified cross-sectional diagram of the physics unit is shown in Fig. 2 and characteristics are listed in Table 1.

1. **High Output Power.** Maser frequency stability in the time interval $0.1 \leqslant \tau \leqslant 10$ sec is primarily determined by maser signal/noise ratio and therefore maser output power. The DSN requirement is such that an output power level of at least -90 dBm is needed (see Fig. 3). This is achieved by increased hydrogen flow rate at the expense of ion pump element lifetime and hydrogen spectral line broadening. The DSN maser has a nominal power output of -88 dBm at an operating hydrogen pressure of 10^{-6} Torr. Ion pump lifetime is calculated to be 3 years at this pressure.

2. **Long-Term Stability Without Cavity Tuning.** For maximum reliability, it was decided that the long-term frequency stability specification (time interval $\tau \geqslant 30$ seconds) should be met without the aid of the automatic cavity tuner. This constraint, and the large hydrogen linewidth caused by high flux operation, placed stringent requirements on (1) the frequency stability of the RF cavity, and (2) the stability of the hydrogen flow rate.

These requirements were satisfied in the DSN maser (see Fig. 2) by (1) surrounding the RF cavity with a temperature-regulated oven placed inside the vacuum, (2) providing low thermal conduction standoffs between RF cavity, inner oven, vacuum housing, ion pump, and support frame interfaces, (3) use of low temperature coefficient Cer-Vit[1] in the RF cavity assembly, (4) surrounding vacuum housing, microwave front end, and ion pump with thermal insulation, and (5) maintaining a stable hydrogen flux level by closed loop control of the palladium valve with an oven-stabilized Pirani pressure gauge.

3. **Maintenance.** The separation of physics and electronics functions permits maximum access to the physics unit for maintenance, troubleshooting, etc. Components have been grouped into replaceable modules or assemblies wherever possible. Viton O-ring seals are used throughout and have proved satisfactory.

The time required for two qualified technicians to replace any physics unit component (excepting the ion pump body), and then again achieve vacuum, is one day or less. Perhaps the most complex and time consuming maintenance task would be replacement of an RF cavity component. This job requires one full day for disassembly and reassembly, and does not require hoists or other mechanical aids.

The repair of the physics unit requires specialized knowledge and skills which are not available in the DSN repair facility as yet, so development personnel normally will travel to the field station to make repairs of items inside the vacuum housing. All other repairs and maintenance will be handled in the normal manner.

The most lengthy portion of a maintenance task is the time necessary for the maser to reach thermal equilibrium after reassembly is completed and vacuum pumping is resumed. If the inner oven can remain on during maintenance (as in replacement of ion pump elements, hydrogen source assembly, palladium valve, Pirani gauge, or any electronics assemblies), long-term stability is obtained a few days after initial vacuum pumpdown. If, on the other hand, the vacuum housing must be opened, then the inner oven must be baked out at elevated temperature during pumpdown, and 4 to 5 weeks are required to obtain normal long-term stability (use of an autotuner can possibly reduce this time).

4. **Life Expectancy.** A number of physics components have displayed limited life expectancy in the past, and efforts to increase these figures have been a continuing goal. One purpose of the two experimental masers operating at Goldstone has been to evaluate the operating life of various components which are destined for use in the DSN maser. The results of these tests are described below.

At JPL, quartz storage bulbs are prepared by applying a single coat of FEP/TFE teflon mixture. After coating, they have not shown degradation as a function of time or number of exposures to air. The bulbs in the two experimental masers have each accumulated five years of operating time (and numerous exposures to air) with no noticeable degradation in maser performance.

The hydrogen glow discharge bulbs in the two experimental masers have been operating 5 years and 2 years respectively since last cleaning. These bulbs have been exposed to air during many periods of maser modification and maintenance. The palladium valves and copper plated RF cavities in the experimental masers have not shown degradation in 5 years of operation. Ion pump lifetime is calculated to be 3 years for the present output level of -88 dBm. It was found necessary to change vac-ion pump elements in one experimental maser after 3 years of field use. 2 1/2 years of field operation have accumulated on the other experimental maser's vac-ion pump elements.

[1]Trademark of Owens-Illinois Corp.

5. **Reliability.** The single field-operable DSN maser now in the field has experienced two failures. Immediately after installation, electrical vacuum feedthru seals, which rely on epoxy for the seal bonds, developed vacuum leaks. Temperature cycling of other units proved these seals to be unreliable. New nonmagnetic seals of tungsten-glass are now being used to solve this problem. Also, a matching capacitor in the glow discharge RF circuitry failed. This is the first failure to occur in more than 13 years of accumulated hours among 5 units. This failure is not believed to be design-related.

B. Electronics Rack

The power, control, receiving, synthesis, status, and alarm functions are provided by the electronics rack (Fig. 4), which contains 32 precalibrated plug-in assemblies that can be serviced by depot technicians.

1. **Physics Unit Control and Monitoring.** The upper half of the electronics rack (Fig. 5) contains ten plug-in control modules and the ion pump power supply. These units provide all monitoring and control functions for the physics unit. (Two other modules in this group, "Status Indicator" and "Autotuner," will be discussed separately.) Table 2 lists the various functions of these modules.

2. **Status and Alarm System.** Many control modules generate alarm signals if operating parameters exceed preset limits. The Status Indicator module displays these alarms in three forms: (1) a dynamic indication which is on only when the alarm condition exists, (2) a "latched" indication which remains on until a field technician notes the problem and resets, and (3) an audible alarm which is derived from the "latched" indication. The particular subsystem which is, or was, in an alarm condition is identified on the front panel.

3. **Automatic Cavity Tuner System.** The automatic cavity tuner (autotuner) uses an available station rubidium, cesium, or second hydrogen maser standard as a reference, and has a resolution of 0.001 sec per 100-sec period ($\Delta f/f = 1 \times 10^{-15}$ for 100-MHz inputs). It produces a varactor correction voltage proportional to the observed tuning error (integrated). The desired system loop gain is switch-selected, and the linear drift component of either the maser or reference standard does not affect the output. The autotuner has the ability to ignore unusually large or "noisy" counts, and can provide an alarm of this occurrence.

It was decided that neither the maser frequency, nor the reference frequency (usually a station rubidium or cesium standard multiplied to 100 MHz) should be offset by the required 0.01 Hz necessary for autotuner operation. Therefore, an offset frequency generator is being developed at JPL which synthesizes, for autotuner use, a signal precisely 0.01 Hz offset from the standard maser 100-MHz output. It is expected that this will be accomplished without significant degradation of the original frequency stability.

Additionally, the autotuner provides a valuable troubleshooting and monitoring capability to the station since it can be used off-line to measure frequency stability (at $\tau = 100$ seconds) between any two 5- or 100-MHz inputs.

4. **Phase-Lock Receiver.** The triple-conversion phase-lock receiver consists of 18 standard DSN modules in the lower half of the electronics rack and the modified Dana synthesizer at the top of the rack. The synthesis section provides 24 standard outputs ranging from 0.1 to 1400 MHz at 13 dBm and 70 to 100 dB isolation. The output frequencies are adjustable over a range of $\pm 2 \times 10^{-7}$ with a resolution of 7×10^{-18}. Other specifications are listed in Table 2.

5. **Reliability.** Major electronics failures during DSN maser production have occurred in three commercial components: the high-resolution synthesizer, the 1400-MHz multiplier, and the ultrastable low-voltage power supplies. These problem areas have been dealt with by (1) JPL redesign and testing assistance to the manufacturer, (2) JPL quality assurance and source inspection, and (3) a 2000-hour burn-in to aid in establishing a high confidence level.

C. Performance

Frequency stability measurements for the early experimental hydrogen masers, and for the first DSN maser (using an updated experimental maser as a reference), are shown in Fig. 3. Two measurements have been obtained thus far for the DSN maser: 1.1×10^{-13} for $\tau = 1$ sec, and 3.8×10^{-15} for $\tau = 90$ sec. Detailed characteristics for the physics and electronics units are shown in Tables 1 and 2.

D. Field Operation

The physics unit is prepared for shipment by attaching a cover to the shock-absorbing mounting base. A battery pack inside the cover supplies power to the ion pump to maintain vacuum during shipment. Since the ovens are off during shipment, normal long-term stability is not achieved until four weeks after turn-on. Upon installation at the station, power is obtained from a station-wide 120 VAC uninterruptable power supply system. The electronics rack is placed with other station electronic equipments where it is monitored by field technicians on a weekly basis. The physics unit is placed some

distance away in an isolated area where vibration and magnetic interference are under control.

Presently the DSN has committed hydrogen masers for use in the Jupiter/Saturn outer-planet missions, Very Long Baseline Interferometry (VLBI) experiments, and station time-sync calibrations. Each hydrogen maser installation will have an auxiliary backup standard consisting of a modified, high-performance Hewlett-Packard 5061A cesium standard. Each DSN hydrogen maser/cesium pair will interface with a microprocessor-based monitor and control system. This system will monitor many operating parameters of both standards, periodically measure stability between the two standards, and make an automatic phase-coherent switchover (with time loss $\leqslant 10$ nanoseconds) to the backup standard in the event the on-line standard degrades beyond pre-programmed limits.

Acknowledgement

The authors wish to make a special acknowledgement to Hubert Erpenbach, recently retired. Mr. Erpenbach was responsible for the successful solution of many physics problems, including the quartz bulb coating technique, RF cavity plating technique, and the long-life hydrogen source assembly.

Reference

1. Finnie, C., Sydnor, R., and Sward, A., "Hydrogen Maser Frequency Standard," in *Proc. 25th Annual Symposium on Frequency Control*, pp 348-351, April 1971.

Table 1. Physics unit characteristics (nominal unless otherwise stated)

Unloaded cavity Q	55,000 min.
Loaded cavity Q	35,000
Cavity	copper-plated Cer-vit cylinder with aluminum end plates and 250-gram quartz storage bulb
Dissociator power	125 MHz, 4 watts ave., 18 watts max.
Collimator	400-hole, 50-micron-diameter per hole
Beam shutter	1 mA taut-band meter movement
State selector	Hexapole permanent magnet, Alnico 8
Atomic line width	2 Hz
Cavity power output	–89 dBm min.
Ion pump capacity	200 liters/sec
Ion pump power input	4200 V @ 2.4 mA
Hydrogen pressure	1×10^{-6} torr
Vacuum background	1×10^{-7} torr
Hydrogen supply	2.25 liters @ 1250 psig initial pressure
DC magnetic field	500 microgauss
Magnetic shields	quantity 4 shielding factor (dc) 1000
Field windings	one main, two trim, 0 to ± 10 mA
Cavity tuning	Type
Coarse	mechanical 2.4×10^{-10}/turn 20 turns
Medium	mechanical 1.5×10^{-11}/turn 20 turns
Fine	varactor 2.0×10^{-12}/V 10 V max

Table 2. Electronics unit characteristics

1.420405751-GHz three-conversion phase-lock receiver		
Bandwidth	preselector	30 MHz
	20.4 MHz IF	4 KHz
	loop (2nd order)	100 Hz
Input signal level	maximum	−71 dBm
From physics unit	nominal	−90 dBm
	minimum	−110 dBm
Gain control	manual	39 dB
	automatic	20 dB
VCO frequency		100 MHz
Noise figure		4.0 dB
Stability (±5°C ambient)		6×10^{-16}
1.42-GHz phase noise		5×10^{-6} radians RMS/Hz (10 Hz offset)
AGC AM to PM conversion		0.16°/dB

Physics unit monitor and control	
Front panel controls	palladium valve temperature hydrogen discharge RF power level beam shutter attenuation magnetic field coil currents varactor voltage (manual mode)
Quantities continuously displayed	ion pump current, voltage hydrogen discharge forward and reflected power varactor voltage (dial calib.) magnetic field coil currents (dial calibration) maser output power
Quantities available for display on multifunction digital meter	pirani gauge output level oven currents palladium valve heater current beam shutter current field currents
Quantities available to remote monitor and control system via rear panel connector	All above plus: oven monitor thermistor outputs, power supply voltages, etc.
Other functions	Palladium valve "open-loop" (manual control) or "closed-loop" (controlled by Pirani gauge)
	Varactor diode "manual" (front panel digital control) or "automatic" (controlled by autotuner)
	Automatic turnoff of ion pump and/or palladium valve if certain potentially damaging failure modes occur

Table 2 (contd)

Status indicator and alarm	
Status and alarm system powered by self-contained uninterruptible power supply (UPS) system.	
UPS duration	12 hours
Transient suppression delay	4 msec, up to 10 sec for some parameters
Alarm outputs	Audio, visual, and remote
Main alarm output	green: operational yellow: operational but degraded red: nonoperational
Subsystems and functions monitored	receiver lock synthesizer lock IF level hydrogen glow discharge VSWR and temperature hydrogen source pressure oven temperatures ion pump power autotuner

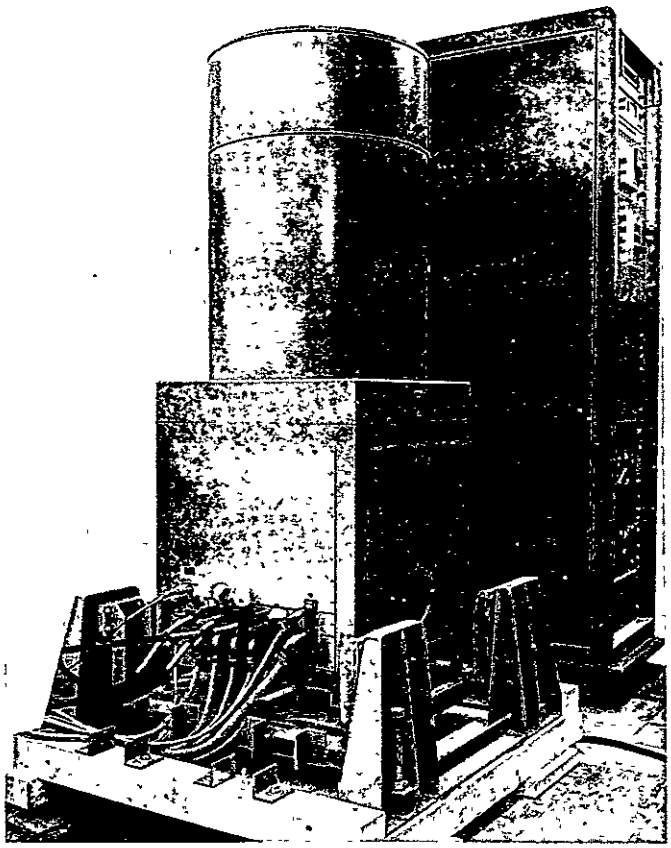

Fig. 1. DSN hydrogen maser

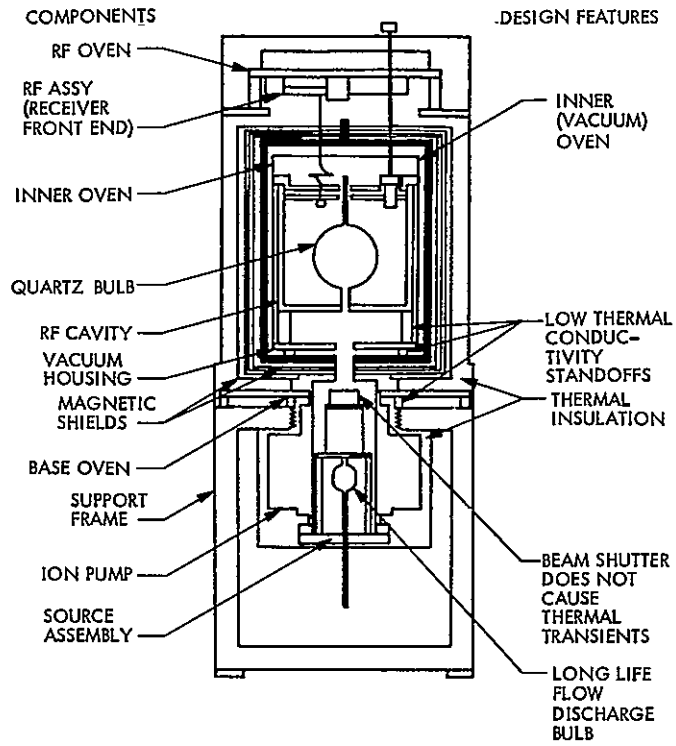

Fig. 2. Simplified cutaway view

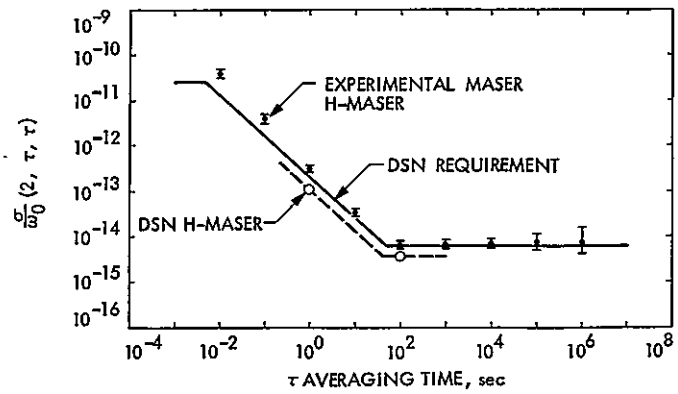

Fig. 3. JPL hydrogen maser frequency stability

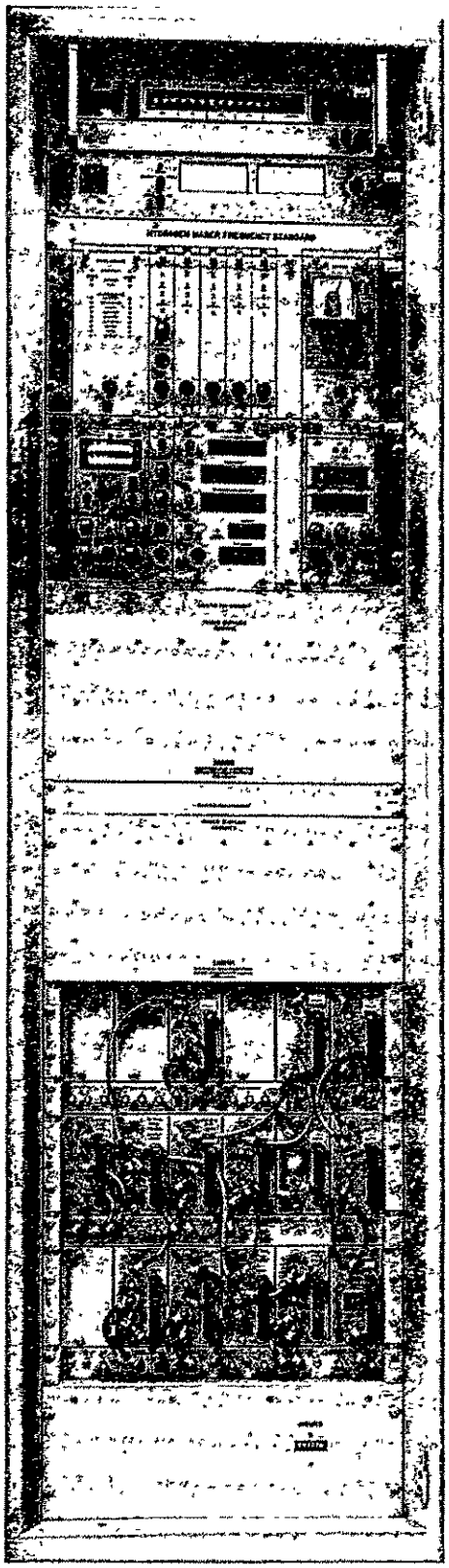

Fig. 4. Electronics rack

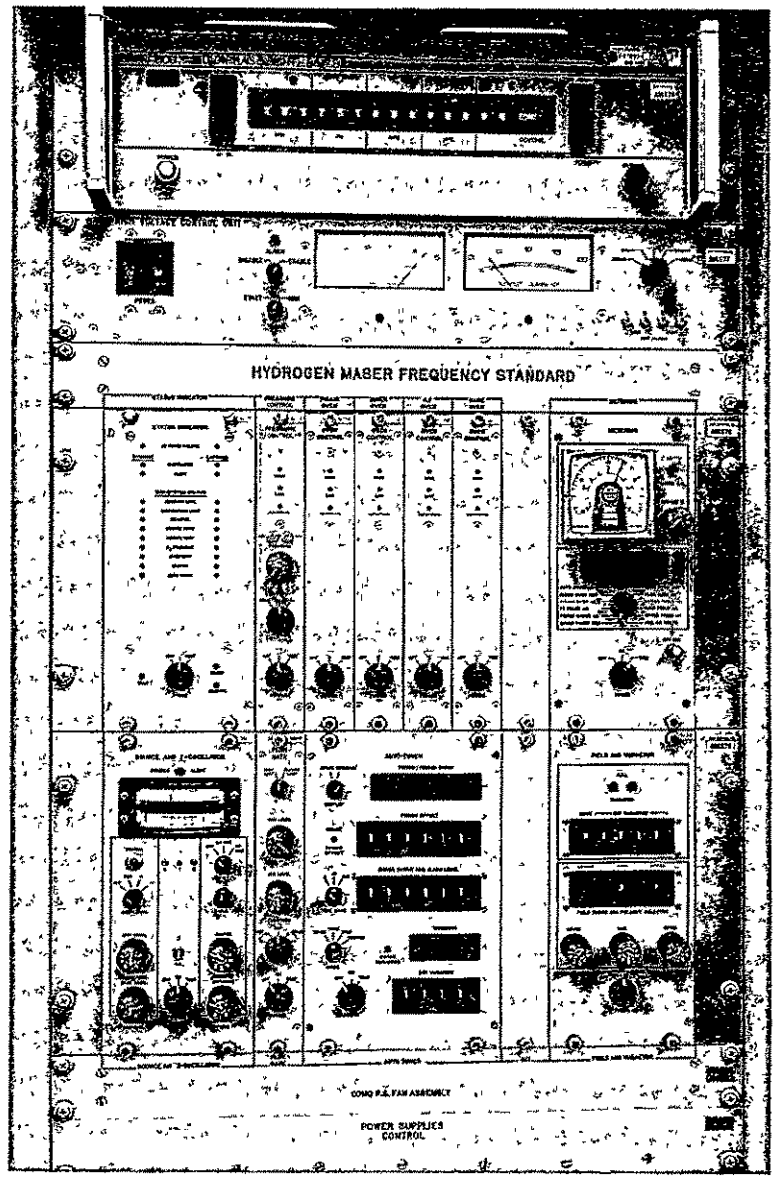

Fig. 5. Physics unit control panel, Electronics Rack

The Application of Differential VLBI to Planetary Approach Orbit Determination

J. K. Miller and K. H. Rourke
Navigation Systems Section

The development of multistation tracking techniques has resulted in improved orbit determination accuracies. Differential Very Long Baseline Interferometry (VLBI), which involves performing measurements of a spacecraft and nearby extra galactic radio source and differencing, potentially offers at least an order of magnitude improvement over data types currently implemented. In this article, the application of differential VLBI to planetary approach orbit determination is described.

I. Introduction

The accuracy of planetary approach orbit determination using radio metric data types is generally limited by station location and planet ephemeris errors. With conventional doppler and range data taken over a single station pass, station location errors translate into right ascension and declination errors in a geocentric frame. The accuracy of this data type is approximately 0.5 μrad and require relatively long data arcs to resolve spacecraft state errors.

The development of multistation tracking techniques has resulted in a considerable reduction in angle measurement error. Using the relative positions of Deep Space Stations (DSS) on Earth as a baseline, precise angle measurements are obtained by simply measuring the difference in time of arrival of a spacecraft radio signal at two or more stations. This technique is referred to as Very Long Baseline Interferometry (VLBI). A recent refinement involves eliminating common effects such as station location errors and transmission media delay by differencing the spacecraft radio signal with a nearby fixed radio source such as a quasar. This technique, referred to as differential VLBI (ΔVLBI), yields angle measurement precision of potentially 0.025 μrad.

There are two methods of implementing ΔVLBI. The first method involves the development of radio source catalogs and the determination of planet ephemerides in an inertial radio source fixed coordinate frame. A spacecraft orbit may thus be determined relative to a planet with the accuracy inherent in the ΔVLBI measurement. This method is often referred to as global ΔVLBI. The second method involves measuring angle rates and determining the planet position error from the observed acceleration of the spacecraft. This method, referred to as local ΔVLBI, results in less accurate spacecraft orbit determination ultimately attainable by global ΔVLBI, but is insensitive to planet ephemeris errors.

The development of radio source catalogs and determination of planet ephemerides to the required accuracy for global ΔVLBI will not be complete in the near future. However, local ΔVLBI, which uses only the inherent accuracy of the ΔVLBI data type is nearly available.

In this article, the application of local ΔVLBI to planetary approach orbit determination is described. A simplified model based on conic motion is developed for predicting the orbit determination error given the ΔVLBI measurement error. This

simplified model is applied to the large outer planets for an overall assessment of the effectiveness of ΔVLBI orbit determination. For Jupiter and Saturn the results are encouraging. As early as 61 days before Jupiter closest approach, the ΔVLBI measurement error is sufficiently accurate to detect the planet ephemeris error. As early as 10 days before encounter the orbit determination error may be reduced to within 200 km, permitting an approach trajectory correction maneuver if required. The results for Uranus and Neptune are less encouraging but may permit a late update of camera pointing for reconnaissance or antenna pointing for relay link. The critical parameter limiting the usefulness of ΔVLBI is the magnitude of approach velocity. Tour type missions with large values of V_∞ (greater than 10 km/sec) approach the planet with a mean motion too great to be detected until near encounter. Orbiter missions favor ΔVLBI orbit determination since approach velocity must be low for fuel economy.

As an example of the application of ΔVLBI, the proposed Jupiter Orbiter Probe (JOP) mission is selected. A comparison of ΔVLBI with current baseline radio metric data (e.g., doppler and range) revealed a dramatic improvement in approach orbit determination. Ten days before encounter, the orbit determination error is reduced from 600 to 310 km with a conservative data acquisition strategy. Doppler and range data does not achieve this level of accuracy until within 3 days of encounter with continuous spacecraft tracking coverage.

II. Analysis

The ΔVLBI measurement technique provides an accurate spacecraft state determination in a geocentric coordinate system relative to fixed radio sources. When coupled with doppler or loosely weighted range data, the 0.025-μrad angular measurement error translates into a 2-km position determination error at Mars opposition or approximately 20 km near Jupiter. Using ΔVLBI measurements, the position of a spacecraft relative to Earth may be determined with this precision. The spacecraft state error relative to a planet is therefore dominated by the planet ephemeris error during approach. In the vicinity of a planet, the motion of a spacecraft may be described by a hyperbola. As a spacecraft approaches a planet, gravity begins to accelerate the spacecraft. The planet position may be determined from the magnitude and direction of the acceleration vector. In the limit of direct impact ($e \to 1$) or far out on the hyperbola asymptote, the time-of-flight or $\hat{S}$ direction is related to the magnitude of acceleration and the B-plane parameters ($\mathbf{B} \cdot \hat{R}$ and $\mathbf{B} \cdot \hat{T}$) are related to the direction of acceleration. Because of the inverse square law of gravity, the time-of-flight or $\hat{S}$ direction is twice as sensitive to acceleration errors as the B-plane parameters. Therefore, the $\hat{S}$ direction position error may be determined with twice the precision as B-plane parameters during initial approach to the planet. The B magnitude and normal to B position error may be determined with equal precision.

A simplified model may be used to assess the potential accuracy of ΔVLBI orbit determination during planetary approach. Consider an out-of-plane (normal to B) position error of the planet during approach (δz_∞). Referring to Fig. 1, at some later time the normal to B acceleration will result in a displacement δz_T of the trajectory plane. From the geometry,

$$\delta z_T = \frac{x_T}{|\mathbf{B}|}\,\delta z_\infty, \tag{1}$$

and

$$x_T = |\mathbf{B}| - x_b. \tag{2}$$

From Ref. 1, the trajectory bending (x_b) is given by,

$$x_b = |\mathbf{B}|\left[1 - \frac{\exp(F)}{e}\right], \tag{3}$$

where F is the hyperbolic eccentric anomaly. Substituting Eqs. (2) and (3) into (1) yields

$$\delta z_T = \frac{\exp(F)}{e}\,\delta z_\infty \tag{4}$$

The differential bending of the trajectory (δz_T) is directly observable by ΔVLBI coupled with loosely weighted range data. Initial tracking establishes the direction and position of the approach asymptote with respect to the a priori position of the planet at encounter. The displacement of the planet from the a priori (δz_∞) is the out-of-plane orbit determination error. Referring again to Fig. 1, the differential bending per unit orbit determination error ($\delta z_T/\delta z_\infty$) is plotted as a function of mean anomaly for a parabola ($e = 1$). The mean anomaly is given by

$$M = \frac{V_\infty^3}{\mu}\,(t - t_{ca}) = e \sinh F - F, \tag{5}$$

where t is referenced to time of closest approach (t_{ca}).

Consider as an example the proposed JOP mission. For an approach velocity (V_∞) of 5.73 km/sec, the mean anomaly 10 days before encounter is −1.29 as determined from Eq. (5).

From the curve shown in Fig. 1, the differential bending is approximately 0.16 per unit orbit determination error. Thus, to achieve a 100-km orbit determination error 10 days before Jupiter encounter, a ΔVLBI position determination accuracy of 16 km (.16 X 100) would be required. This result is somewhat optimistic since it ignores the effect of nongravitational accelerations on determining the a priori coordinates of the approach asymptote in the B-plane.

For assessment of approach orbit determination error, a more convenient form of Eq. (4) is the reciprocal. Fig. 2 shows the ratio of orbit determination to ΔVLBI error as a function of mean anomaly with eccentricity as a parameter. The limiting slope of these curves is −2 and is achieved relatively close to encounter for eccentricity less than 10. A locus of minimum values as a function of mean anomaly is plotted with the eccentricity of the minimum identified. The orbit determination accuracy ratio is obtained by interpolation between the locus of minimums and the actual curves shown.

The orbit determination accuracy ratios shown in Fig. 2 assume a data arc starting at minus infinity. It will be necessary to start the data arc at some finite epoch where the gravity gradient is detectable. Consider a data arc beginning at t_1 and ending at t_2. The corresponding mean anomalies are M_1 and M_2. From Fig. 2, the orbit determination accuracy ratios for tracking from minus infinity are $\sigma_{OD_1}/\sigma_{VLBI}$ and $\sigma_{OD_2}/\sigma_{VLBI}$, respectively. The orbit determination accuracy ratio over the tracking interval from t_1 to t_2 is approximately,

$$\frac{\sigma_{OD_{12}}}{\sigma_{VLBI}} = \frac{1}{\frac{1}{\sigma_{OD_2}/\sigma_{VLBI}} - \frac{1}{\sigma_{OD_1}/\sigma_{VLBI}}} \tag{6}$$

III. Application to Outer Planets

During approach, ΔVLBI is a useful data type when the accuracy of position determination is roughly equal to the planet ephemeris error. At this point, the ΔVLBI orbit determination error decreases linearly with time, as shown in Fig. 2, until close to encounter, where the trajectory dynamics result in a dramatic reduction. Table 1 shows a comparison of ΔVLBI effectiveness for the large outer planets. The first column of Table 1 contains the planet ephemeris error. Current Earth-based optical measurement techniques yield angular accuracies that approach 0.5 μrad. The planet position error scales proportional to range from Earth. The second column contains the ΔVLBI position determination error which also scales proportional to range. The angle measurement accuracy is 0.025 μrad. We are interested in the time from encounter, where the ΔVLBI orbit determination error is equal to the planet position error. Referring to Fig. 2, this occurs at a mean anomaly of approximately −7.5, where the orbit determination accuracy ratio is 20 (Column 1 of Table 1 divided by Column 2) for orbit eccentricities in the range from 1 to 10. It remains to translate mean anomaly into time from encounter. The mean motion is given by

$$\frac{dM}{dt} = \frac{V_\infty^3}{\mu} \tag{7}$$

The hyperbolic approach velocity (V_∞) is dependent on interplanetary trajectory design. Low values of V_∞ favor ΔVLBI orbit determination since the resulting mean motion translates into a longer time for ground data processing and command response. An approximate lower bound for V_∞ may be obtained from the Hohmann transfer orbit. This orbit is the minimum energy transfer orbit from Earth to the target planet. The results of the analysis are shown in Table 1. The time from encounter shown in the last column is obtained by dividing the mean anomaly by the mean motion and may be considered indicative of the time available for ground data processing and command preparation. For Jupiter and Saturn, the time available is sufficient to permit an approach trajectory correction maneuver, if required, to alter the aiming point. The results for Uranus and Neptune are less attractive but may permit a late update of an orbit insertion maneuver or camera pointing sequence.

The above analysis is somewhat optimistic since it assumes a low V_∞ and resulting mean motion. The long flight times associated with the Hohmann transfer orbit make it undesirable from a mission design viewpoint. For tour-type missions, approach velocities of over 10 km/sec may be designed. Because of the cubic relationship of mean motion to V_∞, the effectiveness of ΔVLBI orbit determination would be considerably diminished. It should be noted however, that planet orbiter missions will have approach velocities in the range of Hohmann transfer orbits to minimize orbit insertion fuel expenditure.

IV. Jupiter Orbiter Probe Example

The proposed JOP mission was selected for detailed analysis. The trajectory parameters that pertain to approach orbit determination are:

Encounter date = 15 Nov. 1984

B = 0.1857 E7 km

θ = 20°

V_∞ = 5.73 km/sec

$\alpha_\infty = 196.9°$
$\delta_\infty = -5.81°$
} Approach asymptote in Earth mean equator of 1950 coordinates

The first phase of this analysis was devoted to comparison of ΔVLBI data sets with conventional radio metric data. Because of the newness of the ΔVLBI data type, a conservative data acquisition strategy was simulated. For simplicity, ΔVLBI data is modeled as a geocentric right ascension and declination angle measurement with an accuracy of 0.025 μrad. Since the location of radio sources in the Earth mean equator of 1950 coordinate system may not be known with precision, a bias is added to each angle measurement. It will be necessary to solve for these biases, and the assumed a priori uncertainty of 0.5 μrad is consistent with the error in planet ephemerides. The simulated data rate is one point per day. Deep Space Station 14 (Goldstone, California) and 42 (Australia) were selected for ΔVLBI measurements and a single doppler or range data point is taken from DSS 14 during each pass. The doppler measurement error is 1 mm/sec for a 60-sec count time and is compressed to one hour. Range data is loosely weighted at 20 km. For comparison, continuous doppler at a data rate of one point per hour was taken from the DSS station with the greatest elevation angle.

The results of this comparison are shown in Fig. 3. B-plane semi-major axis (SMAA) is plotted as a function of time from encounter. Estimated parameters are spacecraft state, Jupiter ephemeris and mass. Station location errors are considered. The ΔVLBI data arcs begin at encounter minus 50 days ($E - 50d$) and the estimated B-plane SMAA levels off around 600 km. The combined a priori planet position and ΔVLBI bias errors map into about 600 km SMAA in the B-plane. Around $E - 25d$ the gravity gradient is sufficient to affect the solutions, and SMAA error is reduced as the trajectory bending is detected through encounter. Also shown for comparison is a conventional doppler-only solution. The data arc starts at $E - 50d$ and levels off at 600 km SMAA due to planet ephemeris and station location errors. At about $E - 5d$ the trajectory dynamics resulting from Jupiter's gravity begin to affect the solution. Because of the high data rate (1 pt/hour), the doppler-only solution will overtake the ΔVLBI solution near encounter, providing a more accurate orbit estimate In this region, a more meaningful comparison would be obtained by increasing the doppler data rate coupled with ΔVLBI measurements from 1 pt/day to 1 pt/hour.

Other parameters that must be modeled and may need to be estimated include Jupiter's gravity harmonics and the masses of the larger inner satellites. The need to solve for these parameters may be ascertained by examining the sensitivity of the ΔVLBI measurement to the a priori parameter uncertainty. An acceleration uncertainty of 10^{-12} km/sec^2 approaches the threshold of ΔVLBI measurement accuracy when acting on the spacecraft for around 50 days. It becomes necessary to estimate or consider a gravitational parameter when the spacecraft trajectory passes sufficiently close to a body that the perturbative effect of the parameter uncertainty is sufficient to cause an acceleration uncertainty of 10^{-12} km/sec^2 or greater. We may define the distance from a body where the uncertainty in acceleration is sufficient to influence the spacecraft state solution as the radius of orbit determination corruption r_c. Table 2 contains a tabulation of r_c for the gravitational parameters of interest relative to Jupiter approach. Included are the mass and dominant zonal harmonics of Jupiter and the masses of Io, Europa, Ganymede, and Callisto.

The gravitational parameter uncertainties in Table 2 were obtained from analyses of doppler data taken from the Pioneer 10 and Pioneer 11 spacecraft (Ref. 2). With the exception of Jupiter's mass, the radii of orbit determination corruption for gravity parameters are relatively small. Jupiter's zonal harmonics do not influence spacecraft state solutions until within 1.25×10^6 km (less than 3 days before encounter). The satellites may present a problem as early as 14 days before encounter, depending on the position in their respective orbits.

The accuracy of ΔVLBI approach orbit determination is dependent on the data acquisition strategy. In general, the longer the data arc and the greater the number of data points, the smaller the orbit determination error. The final phase of this analysis is devoted to determining the effect of data quantity and density on orbit determination error. Figure 4 shows four data acquisition strategies that tend to bound the range of orbit determination errors that may be experienced during flight operations. The solid curves present results for a short data arc starting at $E - 50d$. At $E - 10d$, the one point per day data rate results in a B-plane SMAA of 310 km. With only three data points (taken at $E - 50d$, $E - 30d$, and $E - 10d$) the SMAA is 550 km. An additional data point at $E - 5d$ reduces the error in SMAA to 350 km. The relatively poor performance of these short data arcs may be attributed to the large a priori uncertainty in spacecraft approach velocity assumed for this analysis.

This is far too conservative. With conventional radio metric data taken over a long data arc of 100 days or more, the approach velocity should be determined to the same level of accuracy as the planet velocity (on the order of 10^{-5} km/sec). Referring again to Fig. 4, the dashed curves are representative of the results expected for a "long" data arc. The a priori on the approach velocity is set to virtually zero, permitting a precise determination of the B-plane coordinates of the approach asymptote. The one point per day data rate results in an SMAA of 190 km at $E - 10d$, and the three data point solution is 270 km.

The above results for the "long" data arc may be compared with the orbit determination error predicted by Eq. (6). For the JOP approach velocity of 5.73 km/sec, the mean anomaly is -6.45 at $E-50d$ and -1.29 at $E-10d$. From Fig. 2, the orbit determination accuracy ratios for $e=1.1$ are $\sigma_{OD_1}/\sigma_{VLBI}=19$ and $\sigma_{OD_2}/\sigma_{VLBI}=6.5$, respectively. An orbit determination accuracy ratio of $\sigma_{OD_{12}}/\sigma_{VLBI}=9.88$ is obtained from Eq. (6). For the specific case being analysed here, the ΔVLBI position measurement accuracy is 18 km and the expected orbit determination error is 178-km SMAA at $E-10d$. This result is consistent with the long arc results shown in Fig. 4.

References

1. Russell, R. K., "Gravity Focussing of Hyperbolic Trajectories," TM 391-424, Jet Propulsion Laboratory, Pasadena, Calif., March 30, 1973 (an internal document).
2. Null, G. W., "Gravity Field of Jupiter and Its Satellites from Pioneer 10 and Pioneer 11 Tracking Data," *Astron. J.*, Vol. 18, No. 12, Dec. 1976.

Table 1. Application of ΔVLBI to outer planet approach orbit determination

Planet	Planet position error[a]	ΔVLBI position error[b]	ΔVLBI = Planet Position Error: Mean anomaly M	Hohmann transfer V_∞	Mean motion dM/dt	Time from encounter
	km	km	rad	km/sec	rad/day	day
Jupiter	400	20	-7.5	5.6	0.123	-61
Saturn	740	37	-7.5	5.4	0.368	-20
Uranus	1480	74	-7.5	4.7	1 51	-5
Neptune	2324	117	-7.5	4.1	0.833	-9

[a]Assumes approximately 0.5 μrad error.

[b]Assumes 0.025 μrad measurement error.

Table 2. Radius of orbit determination corruption

Body	Parameter	σ_p	σ_a^a	r_c
Jupiter	GM_5	484 km^3/sec^2	10^{-12} km/sec^2	22 X 10^6 km
Jupiter	J_2	4 X 10^{-6}	10^{-12} km/sec^2	1.25 X 10^6 km
Jupiter	J_3	7 X 10^{-6}	10^{-12} km/sec^2	0 35 X 10^6 km
Jupiter	J_6	50 X 10^{-6}	10^{-12} km/sec^2	0.41 X 10^6 km
Io	GM_1	28 km^3/sec^2	10^{-12} km/sec^2	5 29 X 10^6 km
Europa	GM_2	32 km^3/sec^2	10^{-12} km/sec^2	5.66 X 10^6 km
Ganymede	GM_3	37 km^3/sec^2	10^{-12} km/sec^2	6.1 X 10^6 km
Callisto	GM_4	24 km^3/sec^2	10^{-12} km/sec^2	4.9 X 10^6 km

[a]Sensitivity threshold of ΔVLBI measurement to acceleration.

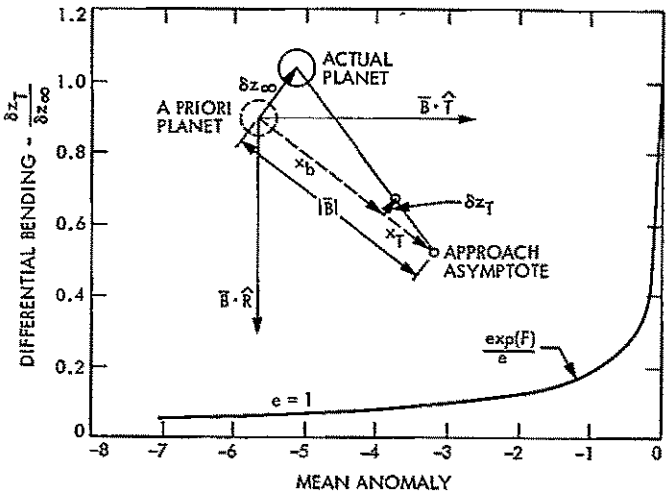

Fig. 1. Differential bending as a function of mean anomaly

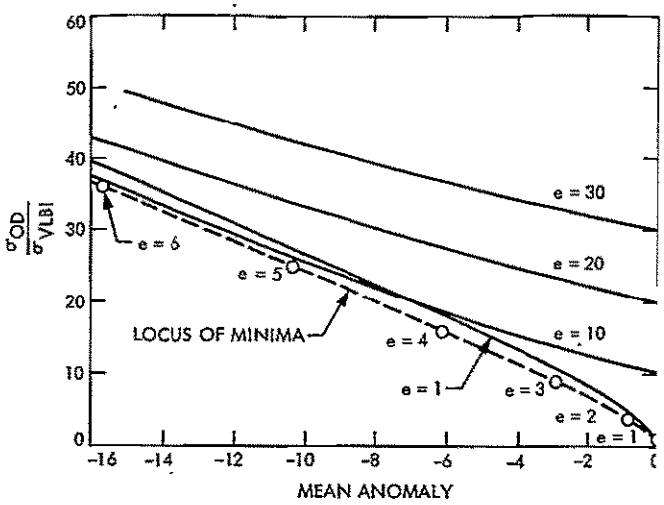

Fig. 2. Approach orbit determination ΔVLBI accuracy ratio as a function of mean anomaly

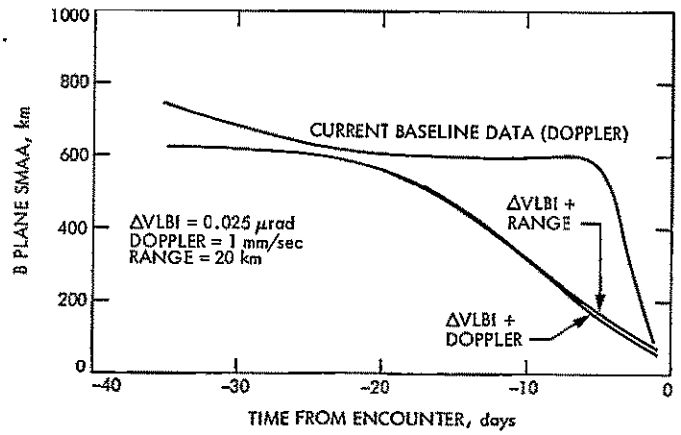

Fig. 3. Comparison of conventional and ΔVLBI data sets (JOP example)

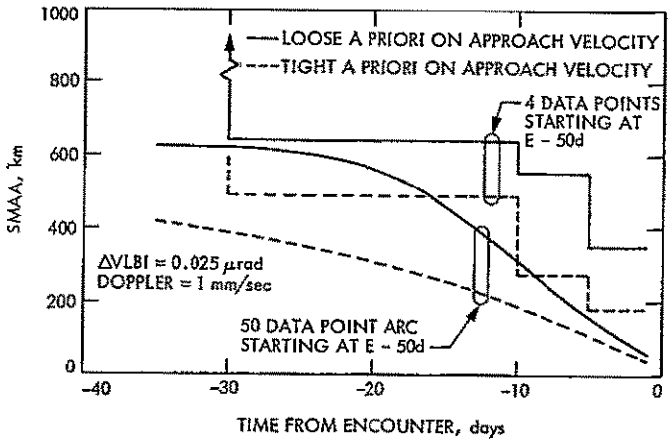

Fig. 4. ΔVLBI + doppler accuracy as a function of days from encounter and data rate (JOP example)

Maintenance and Operations Cost Model for DSN Subsystems

R. W. Burt
Radio Frequency and Microwave Subsystems Section

J. R. Lesh
Communications Systems Research Section

A procedure is described which partitions the recurring costs of the Deep Space Network (DSN) over the individual DSN subsystems. The procedure results in a table showing the maintenance, operations, sustaining engineering and supportive costs for each subsystem.

I. Introduction

In an earlier article (Ref. 1) a procedure was described for obtaining an M&O cost model for the DSN. The procedure consisted of first transforming the Work Authorization Document (WAD) into a computer file for ease of manipulation. Then each of the more than 600 WAD accounts was studied to determine if it was a recurring cost or an implementation-related nonrecurring cost. The nonrecurring accounts were deleted, and the remaining accounts were identified by their category of cost (i.e., maintenance, operations, sustaining engineering or support), location of expenditure as well as the particular subsystems to which each account pertained. Finally, by accumulating the recurring cost accounts over common identifiers, the reduced size cost breakdown model shown in Table 1 was obtained.

The purpose of this article is to describe the procedure by which Table 1 was transformed into a subsystem cost breakdown model. As in the previous article the goal of the entire cost modeling effort is to obtain results which are accurate to within 20%.

II. Extension to a Subsystem Model

The first step in establishing costs by subsystem was to find a reasonable way of establishing percentage breakdowns with an acceptable degree of accuracy. This was done as follows:

(1) Sustaining engineering: Used percentage breakdown of the total number of Engineering Change Orders (ECR's) written in 1976 by subsystem.

(2) Maintenance: Used the average of the percentage breakdown of the work orders at GDSCC stations and Equipment Event Reports (EER's) at CMF and DMC written for a six-month period in 1976 by subsystem.

(3) Operations: Assumed that the highest activity level for operational support occurs during the countdown and therefore used the percentage breakdown of total countdown manhours by subsystem.

These percentage breakdowns are given in Table 2. Further effort is needed to improve this table. The MDS implementation will have an impact on EER, ECR and work order

percentages. Operational support percentages are being further investigated with support from DSS 14 and DSS 12.

The next step was to use the percentage breakdowns in Table 2 to spread the category costs of the COSTMODEL file (Table 1) over the set of subsystems. The following relations were used in performing this task:

$$\text{MNT COST/SS} = \left(\frac{\text{EER\%} + \text{W.O.\%}}{2}\right) \cdot \text{MNT COST}$$

$$\text{SUP COST/SS} = \left(\frac{\text{MNT COST/SS} + \text{OPS COST/SS}}{\text{MNT COST} + \text{OPS COST}}\right) \cdot \text{SUPPORT COST}$$

$$\text{SUS COST/SS} = (\text{ECR\%}) \times \text{SUS COST FOR SUBSYSTEM}$$

for system = ALL

or

$$\text{SUS COST/SS} = \left(\frac{\text{ECR\%/SS}}{\text{ECR\% SUM FOR SUBSYSTEMS GIVEN IN SUBSYSTEM}}\right) \cdot \text{SUS COST}$$

$$\text{OPS COST/SS} = (\text{OPS\%/SS}) * \text{OPS COST}$$

for LOC = GDSCC; LOC = CTA;

LOC = NOCC

$$\text{OPS COST/SS} = \left(\frac{\text{GDSCC(MNT/SS + OPS/SS)}}{\text{GDSCC(MNT COST + OPS COST)}}\right) \cdot \text{OPS COST}$$

for LOC = SPAIN or LOC = AUST

where SS = subsystem. Table 3 illustrates the resulting subsystem distribution matrix

The next step of the procedure was to multiply the cost vectors of Table 1 by this subsystem distribution matrix. This has the effect of spreading each line item cost of Table 1 over each of its appropriate subsystems. Then the rows having common locations and categories can be combined to produce the simplified cost breakdown model of Table 4. Here we see that the number of line items has been reduced to 11 but that the column dimension has increased by the subsystem identifiers.

Finally, it is of interest to have a simplified cost breakdown model for each subsystem. To accomplish this we could simply sum each of the categories in each column of Table 4. However, the costs associated with the foreign complexes appear as a single line item in the JPL WAD. This means that the entries in Table 4 entitled AUST OPS and SPAIN OPS actually include the maintenance, operations and support costs of Australia and Spain, respectively. To separate these amounts from the total, the cost breakdowns of CTA 21 and Goldstone were examined. The examination revealed that the maintenance, operations and support costs are approximately equal. This implies that we can split the foreign line items such that one-third of the cost goes to each of these categories. After splitting these line items and summing over each of the categories we obtain the subsystem category cost model shown in Table 5.

It is important to note that there are two recurring costs associated with providing DSN service which are not included in these tables. These costs are (1) the costs associated *exclusively* with the GCF equipment at the DSN facilities and (2) the costs necessary for NASCOM relaying of signals. The exclusively GCF costs were separated from the main body of costs so that they could be handled separately; they will be added back into the cost model table at a later date. The total FY'77 amount for such accounts is $1.59 million, although the partitioning of this amount over the categories has not been accomplished. The NASCOM link costs were not included since they do not appear in the JPL WAD.

III. Conclusions

The subsystem category cost breakdown model in Table 5 is a significant step toward characterizing the manner in which DSN costs are incurred. Once the GCF, and possibly NASCOM, costs are included, the resulting model should serve as a valuable tool for comparing the economics of the present and proposed future DSN configurations.

Reference

1. Burt, R. W., and Kirkbride, H. L., "A Maintenance and Operations Cost Model for the DSN," in *The DSN Progress Report 42-38*, April 1977, pp. 109-114.

Table 1. Cost breakdown model

Item	Location	Category	Subsystems	FY'77 costs, $ X 10^3
1	AUST	OPS		4933
2	CTA	OPS	All	563
3	GDSCC	MNT	All	4349
4	GDSCC	MNT	TXR	283
5	GDSCC	OPS	All	1965
6	GDSCC	SUP	All	3792
7	JPL	MNT	All	284
8	JPL	OPS	All	673
9	JPL	SUP	All	1982
10	JPL	SUS	All	4622
11	JPL	SUS	ANT	622
12	JPL	SUS	ANT/FAC	303
13	JPL	SUS	DMC	71
14	JPL	SUS	DMC/FTS/PPR/DTT	295
15	JPL	SUS	DTK	80
16	JPL	SUS	DTK/APS	92
17	JPL	SUS	DTK/RCV/FTS	109
18	JPL	SUS	DTM	205
19	JPL	SUS	DTM/DCD	208
20	JPL	SUS	DTM/DCD/DTK/GHS/NCS	29
21	JPL	SUS	DTM/DCD/DTK/NCS/DMC/DTT/GHS/PPR/FTS	522
22	JPL	SUS	FAC	388
23	JPL	SUS	RCV	106
24	JPL	SUS	RCV/UWV/TXR	214
25	JPL	SUS	TXR	172
26	JPL	SUS	UWV	93
27	NOCC	OPS	All	2016
28	SPAIN	OPS		5076
			Grand total FY'77	34,047

Table 2. Percentage breakdowns by subsystem for various M&O activities

Subsystem	Percentage breakdown ECR	EER	WO (Work Orders)	OPS (Operations)
ANT	8.0	6.7	24.6	12.0
APS	1.4	1.4	2.2	1.0
DCD	5.9	6.1	6.0	11.0
DMC	6.1	9.6	8.1	4.0
DTK	4.7	0.9	2.6	12.0
DTM	11.8	12.3	10.7	28.0
DTT	0.7	0.2	0.6	7.0
FAC	22.3	7.7	0	0
FTS	4.6	2.5	4.3	0
GCF[a] = GHS,GWB, GTY,GVC	4.3	4.8	2.0	10.0
PPR,REC,AIS	1.7	7.1	2.6	3.0
RCV	16.9	26.5	7.8	4.0
TXR	6.9	2.6	5.6	6.0
UWV	2.9	4.6	15.2	1.0
SYS[b]	2.0	7.4	8.9	0

[a]Funded by accounts not exclusively devoted to GCF, i.e., SUBSYSTEM = ALL in Table 1.

[b]System level work not attributable to one subsystem.

Table 3. Cost factor matrix

NO.[a]	LOC[a]	CAT[a]	ANT	APS	DCD	DMC	DTK	DTM	DTT	FAC	FTS	GCF	PPR	RCV	TXR	SYS	UWV
1	AUST	OPS	.14	.02	.08	.06	.07	.20	.04	.02	.02	.06	.03	.11	.05	.04	.06
2	CTA	OPS	.12	.01	.11	.04	.12	.28	.07	.00	.00	.10	.04	.04	.06	.00	.01
3	GDSCC	MNT	.16	.02	.06	.09	.02	.12	.01	.04	.03	.03	.03	.17	.04	.08	.10
4	GDSCC	MNT	.00	.00	.00	.00	.00	.00	.00	.00	.00	.00	.00	.00	1.00	.00	.00
5	GDSCC	OPS	.12	.01	.11	.04	.12	.28	.07	.00	.00	.10	.04	.04	.06	.00	.01
6	GDSCC	SUP	.14	.02	.08	.06	.07	20	.04	.02	.02	.06	.03	.11	.05	.04	.06
7	JPL	MNT	.16	.02	.06	.09	.02	.12	.01	.04	.03	.03	.03	.17	.04	.08	.10
8	JPL	OPS	.12	.01	.11	.04	.12	.28	.07	.00	.00	.10	.04	.04	.06	.00	.01
9	JPL	SUP	.14	.02	.08	.06	.07	.20	.04	.02	.02	06	.03	.11	.05	.04	.06
10	JPL	SUS	.08	.01	.06	.06	.05	.12	.01	.22	.05	.04	.02	.17	.07	.01	.03
11	JPL	SUS	1.00	.00	.00	.00	.00	.00	.00	.00	.00	.00	.00	.00	.00	.00	.00
12	JPL	SUS	.26	.00	.00	00	00	.00	.00	.74	.00	.00	.00	.00	.00	.00	.00
13	JPL	SUS	.00	.00	.00	1.00	.00	.00	.00	.00	.00	.00	.00	.00	.00	.00	.00
14	JPL	SUS	.00	.00	.00	.47	.00	.00	.05	.00	.35	.00	.13	.00	.00	.00	.00
15	JPL	SUS	.00	.00	.00	00	1 00	.00	.00	.00	.00	.00	.00	00	.00	.00	.00
16	JPL	SUS	.00	.23	.00	.00	.77	.00	.00	.00	.00	.00	.00	.00	.00	.00	.00
17	JPL	SUS	.00	.00	.00	.00	.18	.00	.00	.00	.18	.00	.00	.64	.00	.00	.00
18	JPL	SUS	.00	.00	.00	.00	.00	1.00	.00	.00	.00	.00	.00	.00	.00	.00	.00
19	JPL	SUS	.00	.00	.33	.00	.00	.67	.00	.00	.00	.00	.00	.00	.00	.00	.00
20	JPL	SUS	.00	00	.22	.00	.17	.44	.00	.00	.00	.00	.16	.00	.00	.01	.00
21	JPL	SUS	.00	.00	.15	.15	.12	.29	.00	.02	.11	.11	.04	.00	.00	.01	.00
22	JPL	SUS	.00	.00	.00	.00	.00	.00	.00	1.00	.00	.00	.00	.00	.00	.00	.00
23	JPL	SUS	.00	.00	.00	.00	.00	.00	.00	.00	.00	.00	.00	1.00	.00	.00	.00
24	JPL	SUS	.00	.00	.00	.00	.00	.00	.00	.00	.00	.00	.00	.63	.26	.00	.11
25	JPL	SUS	.00	.00	.00	.00	.00	.00	.00	.00	.00	.00	.00	.00	1.00	.00	.00
26	JPL	SUS	.00	.00	.00	.00	.00	.00	.00	.00	.00	.00	.00	.00	.00	.00	1.00
27	NOCC	OPS	.12	.01	.11	.04	.12	.28	.07	.00	.00	.10	.04	.04	.06	.00	.01
28	SPAIN	OPS	.14	.02	.08	.06	.07	.20	.04	.02	.02	.06	.03	.11	.05	.04	.06

[a]These columns bear a one-to-one correspondence with the first three columns in Table 1.

Table 4. 1977 subsystem totals by location and category

LOC	CAT	ANT 77	APS 77	DCD 77	DMC 77	DTK 77	DTM 77	DTM 77	FAC 77	FTS 77	GCF 77	PPR 77	RCV 77	TXR77	UWV77	SYS77
AUST	OPS	69	79	405	306	335	987	183	99	99	296	168	518	257	281	197
CTA	OPS	70	8	62	23	66	158	39	0	0	59	23	24	34	6	0
GDSCC	MNT	678	78	261	383	74	522	43	165	145	145	139	748	461	435	348
GDSCC	OPS	246	28	216	79	232	550	136	0	0	204	78	82	124	28	0
GDSCC	SUP	531	76	303	228	265	758	152	72	64	228	114	417	190	228	152
JPL	MNT	45	6	17	26	6	34	3	11	9	9	9	48	11	28	23
JPL	OPS	84	9	74	27	79	188	46	0	0	70	27	28	42	9	0
JPL	SUP	277	40	159	119	139	396	79	40	34	119	59	218	99	119	79
JPL	SUS	1071	86	425	572	455	1056	47	1652	396	255	144	1092	547	251	51
NOCC	OPS	252	28	222	81	238	564	139	0	0	216	81	85	127	28	0
SPAIN	OPS	711	81	416	315	345	1015	188	102	102	305	173	543	264	289	203
Totals		4656	519	2560	2159	2234	6628	1055	2141	550	1903	1015	3813	2156	1702	1053

Table 5. Subsystem/category cost model for the DSN

Category	Subsystem														
	ANT	APS	DCD	DMC	DTK	DTM	DTT	FAC	FTS	GCF[a]	PPR	RCV	TXR	UWV	SYS
Maintenance	1191	138	552	616	307	1224	170	243	222	358	262	1153	646	653	505
Operations	1119	126	848	417	842	2127	484	67	67	749	323	576	501	261	133
Sustaining	1071	86	425	572	455	1056	47	1652	396	255	144	1092	547	251	51
Support	1275	169	735	554	630	1821	354	179	165	547	286	992	462	537	364
Total	4656	519	2560	2159	2234	6228	1055	2141	850	1903	1015	3813	2156	1702	1053

[a]Does not include costs in WAD accounts which are exclusively GCF related or the NASCOM costs associated with DSN service.

DSN Progress Report 42-40 May and June 1977

An Improved Digital Algorithm for Fast Amplitude Approximations of Quadrature Pairs

B. K. Levitt and G. A. Morris
Communications Systems Research Section

The authors have discovered a computationally fast algorithm for approximating the amplitude $A = \sqrt{I^2 + Q^2}$ of a quadrature pair (I,Q); specifically, the piecewise linear formula

$$\hat{A} = \begin{cases} X + \frac{1}{8}Y; & X \geqslant 3Y \\ \frac{7}{8}X + \frac{1}{2}Y; & X \leqslant 3Y \end{cases}$$

where $X \equiv max(|I|, |Q|)$, $Y \equiv min(|I|, |Q|)$. Assuming a uniformly distributed quadrature pair phase angle, the maximum approximation error is 0.028A, the mean error is 0.000066A, and the standard deviation about A is 0.00828A. This algorithm is far more accurate than modified versions of Robertson's approximation ($\hat{A} = X + bY$, b = 1/2 or 3/8 or 1/4) currently being used for most digital signal processing applications. An immediate application is the wideband digital spectrum analyzer under development for monitoring radio frequency interference (RFI) at DSN stations. The algorithm could also be used in digital radar processors.

Digital signal processors sometimes require the computation of the amplitude $A = \sqrt{I^2 + Q^2}$ of an inphase/quadrature component pair, I and Q (e.g., Fourier analyzers, radar receivers). The squaring and square root operations required to determine A exactly are computationally complex, and the intermediate terms, I^2 and Q^2, require double word storage. To simplify this calculation, Robertson (Ref. 1) in 1971 proposed the linear approximation $\hat{A} = X + 1/2\ Y$, where $X \equiv \max(|I|, |Q|)$, $Y \equiv \min(|I|, |Q|)$. The appeal of his scheme is that it can be trivially mechanized by digital shift, compare, and sum operations. Since then, many digital devices have been built incorporating either Robertson's formula or modified versions in which the digital coefficient 1/2 is changed to 3/8 or 1/4 to improve performance (Ref. 2). All of these first-generation algorithms are moderately accurate: assuming a uniformly distributed quadrature pair phase angle, they have

maximum errors of 7 to 12 percent, mean errors of 0.6 to 9 percent, and standard deviations about A of 4 to 9 percent (see Table 1).

More recently, several piecewise linear amplitude approximations have been discovered which are far more accurate than those previously mentioned, yet retain almost the same ease of simple digital implementation. In 1974, Braun and Blaser (Ref. 3) published several very accurate piecewise linear amplitude approximations in a British biweekly journal. They introduced a nondigital scale factor c, and approximated cA by the piecewise linear expression

$$c\hat{A} = \begin{cases} a_1 X + b_1 Y; & X \geqslant kY \\ a_2 X + b_2 Y; & X \leqslant kY \end{cases} \tag{1}$$

where the coefficients of X and Y were restricted to be digital fractions up to 8 bits in length, and k was arbitrarily set to 2. Converting X and Y to polar representation, the fractional amplitude approximation error has the form

$$\epsilon(\theta) \equiv \frac{c\hat{A} - cA}{cA} = \frac{1}{c}(a_i \cos\theta + b_i \sin\theta) - 1 \tag{2}$$

where $\theta \equiv \tan^{-1}(Y/X)\ \epsilon(0, \pi/4)$. The digital coefficients and the scale factor c in Eq. (1) were selected to minimize $\max|\epsilon(\theta)|$. Their results are shown in Table 1 along with mean and rms errors calculated under the earlier assumption that θ is a uniformly distributed random variable.

In 1976, Filip (Ref. 4) published 13 linear approximations for computing A: of these, only two were piecewise linear with digital coefficients. As shown in Table 1, they are not quite as accurate as the best of the Braun/Blaser approximations.

During the past year, while seeking to simplify the data processing hardware of the wideband digital spectrum analyzer being developed for monitoring RFI at DSN stations (Ref. 5), the authors discovered yet another useful approximation. Unaware at the time of the path that had been carved before us by Braun and Blaser and Filip, we independently adopted the piecewise linear approach of Eq. (1) to the problem, restricting $c = 1$ but not preselecting k, and considering digital coefficients up to 3 bits in length. As shown in Table 1, our resulting amplitude approximation is comparable in accuracy to the three best Braun/Blaser formulas. The superiority of these second-generation digital algorithms over their predecessors is illustrated by the plots of $\epsilon(\theta)$ in Fig. 1.

Let us elaborate briefly on the RFI application of this algorithm. As described in Ref. 5, the power in the ith spectral line, based on the jth observation of the input signal, has the form

$$P_{ij} = I_{ij}^2 + Q_{ij}^2 \tag{3}$$

Since the spectrum analyzer is of the multilook category, it makes L independent determinations of each spectral line power. The optimum test for detecting whether the ith spectral line consists of an external signal imbedded in internal noise, or noise alone, is to compare

$$P_i \equiv \frac{1}{L} \sum_{j=1}^{L} P_{ij} \tag{4}$$

with a threshold η, selected to achieve desired false alarm and miss probabilities. However, if the I_{ij}'s and Q_{ij}'s are K-bit words, the P_{ij}'s must be stored as 2K-bit words.

Suppose we elect to use a suboptimal detection scheme in which we average the L amplitudes

$$A_{ij} \equiv \sqrt{I_{ij}^2 + Q_{ij}^2}; \quad j = 1, \ldots, L \tag{5}$$

instead of the P_{ij}'s, and compare the random variable

$$A_i \equiv \frac{1}{L} \sum_{j=1}^{L} A_{ij}$$

with a new threshold η'. For sufficiently large L, this suboptimal approach costs us a performance loss of 0.19 dB (Ref. 6). If we use our new algorithm to approximate the A_{ij}'s prior to the averaging operation, the accuracy of the approximation is such that the additional performance loss is negligible. By using the amplitude approximation technique, we avoid the double-word processing required for optimal detection. The resulting hardware simplification represents a significant reduction in processing time and component costs.

References

1. Robertson, G. H., "A Fast Amplitude Approximation for Quadrature Pairs," *Bell Sys. Tech. J.*, Vol. 50, Oct. 1971, pp. 2849-2852.

2. Williams, J. R., and Ricker, G. G., "The Variable Law Detector," *IEEE Trans. Acoust., Speech, Signal Processing*, Vol. ASSP-23, Aug. 1975, p. 360.

3. Braun, F. G., and Blaser, H., "Digital Hardware for Approximating to the Amplitude of Quadrature Pairs (Square Root)." *Electron. Lett.*, Vol. 10, No. 13, June 27, 1974, pp. 255-256.

4. Filip, A. E., "A Baker's Dozen Magnitude Approximations and Their Detection Statistics," *IEEE Trans. Aerospace and Electronic Systems*, Vol. AES-12, Jan. 1976, pp. 86-89.

5. Levitt, B. K., "Analysis of a Discrete Spectrum Analyzer for the Detection of Radio Frequency Interference," in *The Deep Space Network Progress Report 42-38*, Jet Propulsion Laboratory, Pasadena, Calif., Apr. 15, 1977, pp. 83-98.

6. McEliece, R. J., and Rodemich, E. R., "An Asymptotic Analysis of a General Class of Signal Detection Algorithms," in *The Deep Space Network Progress Report 42-39*, Jet Propulsion Laboratory, Pasadena, Calif., June 15, 1977, pp. 30-35.

Table 1. Performance comparison of digital algorithms for fast amplitude approximation of quadrature pairs (for notation, refer to Eqs. 1 and 2)

Originators	a_1	a_2	b_1	b_2	k	c	max $\lvert\epsilon\rvert$	$\overline{\epsilon}$	$\sqrt{\overline{\epsilon^2}}$
Robertson	1		$\frac{1}{2}$		–	1	0.1180	0.0868	0.0921
	1		$\frac{3}{8}$		–	1	0.0680	0.0402	0.0476
	1		$\frac{1}{4}$		–	1	0.1161	-0.0065	0.0416
Braun/Blaser	$\frac{1}{2}$		$\frac{1}{4}$		–	0.52951	0.0557	0.0262	0.0392
	$\frac{3}{4}$	$\frac{1}{2}$	0	$\frac{1}{2}$	2	0.71041	0.0557	0.0019	0.0338
	$\frac{5}{8}$	$\frac{1}{2}$	$\frac{1}{8}$	$\frac{3}{8}$	2	0.62615	0.0179	0.0023	0.0108
	$\frac{5}{8}$	$\frac{65}{128}$	$\frac{9}{64}$	$\frac{3}{8}$	2	0.63127	0.0148	0.0016	0.0086
	$\frac{19}{32}$	$\frac{1}{2}$	$\frac{9}{64}$	$\frac{11}{32}$	2	0.60196	0.0136	0.0041	0.0080
Filip	1	$\frac{7}{8}$	0	$\frac{1}{2}$	4	1	0.0298	0.0062	0.0123
	1	$\frac{3}{4}$	$\frac{1}{4}$	$\frac{3}{4}$	2	1	0.0606	-0.0301	0.0341
Levitt/Morris	1	$\frac{7}{8}$	$\frac{1}{8}$	$\frac{1}{2}$	3	1	0.0277	0.0001	0.0082

D13

Life-Cycle Costing: Practical Considerations

I. Eisenberger and G. Lorden
Communications Systems Research Section

The history and methodology of life-cycle costing are presented and analyzed, contrasting the potential benefits of the technique with the difficulties of its application. Examples and a short survey of the literature are given

I. Introduction

The concept of life-cycle cost (LCC) of a system came into vogue in the sixties when the Department of Defense (DOD) began to recognize the fallacy of making procurement choices solely on the basis of prices bid. Studies of weapons systems and other procurements revealed that acquisition costs were typically smaller than costs of ownership such as the cost of labor and materials required to operate and maintain the system.

In recent years increasing attention has been paid to the need to consider all the costs of developing, installing, and using a system over its entire lifetime. As a consequence, LCC methodology has been developed and used as an aid to planning and decision-making in a broad range of governmental and industrial applications (see the bibliography in Section VI).

This report explains the LCC method, discusses its benefits and usefulness, and outlines some of the practicalities and problems involved in its application. Several examples from the LCC literature are given as illustrations and a bibliography is included to aid further study.

II. Life-Cycle Cost Methodology

The LCC of a system is conventionally defined as the present value, at the beginning of operation of the system, of all costs of the system. Symbolically,

$$LCC = \sum_{k=-(m-1)}^{n} \frac{C_k}{(1+i)^k}$$

where m is the number of years in the development/acquisition phase, n the operational lifetime, i the interest (discount) rate, and C_k the cost incurred in the kth year. To apply the formula, one must carry out the following key tasks:

(1) Estimate the useful life of the system.

(2) Estimate the yearly costs over the life-cycle.

(3) Choose a discount rate.

Task 1 often turns out to be more significant and difficult than it would appear to be. A discussion is given in Section V.

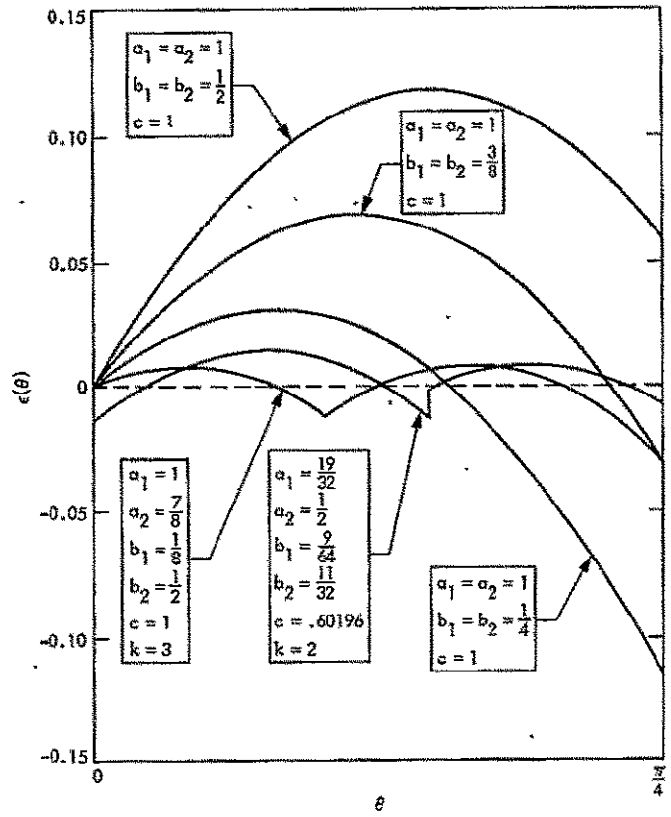

Fig. 1. Comparison of amplitude approximation errors of first- and second-generation digital algorithms (see Eq. 1 for definition of parameters)

Task 2 is the most challenging part of the LCC analyses. The major categories of costs to be estimated are:

(1) Research and development, testing and evaluation.

(2) Production and/or acquisition.

(3) Operation and maintenance.

(4) Salvage.

Within these broad areas it is necessary to identify specific cost items to be estimated. For example, the maintenance costs for the Air Force's Electronically Agile Radar (EAR) system were broken down as follows:

(1) Initial and pipeline spares.

(2) Replacement spares.

(3) On-equipment maintenance.

(4) Off-equipment maintenance.

(5) Inventory and supply management.

(6) Support equipment.

(7) Training and training equipment.

(8) Management and technical data.

These eight items were found to be comprised of 115 data elements.

Once the appropriate cost items are identified, how should their costs be estimated? Some items, like acquisition prices, are usually easy. Others, like operations and maintenance (O&M), suggest the need for a large and accurate data base, organized so as to be useful for the required analysis. Ideally, such a data base would indicate things like expenditures of labor and materials needed for similar systems (or subsystems).

Since a data base approaching the ideal is seldom available, how can the required estimates be obtained using only partial, inaccurate data obtained from experience with previous systems?

Several approaches are popular, as can be seen from investigation of the literature surveyed in Section VI. One consists of using *cost-to-cost estimating relationships* based on the idea (or observation) that certain costs can be tied to other related costs in a fixed ratio. This is particularly appealing when good data are available for a few key cost items. It may even be feasible to relate certain costs to the *prices* of system components or spares.

Another approach is called *non-cost to cost estimating*, which attempts to relate the costs to be estimated to appropriate non-cost variables of system components, such as performance or operating characteristics, reliability, size, or complexity. In its ultimate form, this approach seeks to derive a mathematical model (e.g., a regression model) that fits cost items to appropriate variables based on experience with previous systems.

Less ambitious though potentially useful schemes include the use of *specific analogies* with past systems or components to estimate costs of a new system and, if all else fails, consulting expert opinion (to get an expert guess).

Once the task of estimating yearly costs over system lifetime is accomplished, it may seem as though task 3, choosing a discount rate, would be quite simple. This is perhaps true, because the rate is merely a reflection of the "time value of money" and can be chosen in line with prevailing rates for government borrowing. However, such rates do fluctuate, and the difference in effect between an 8% rate and a 10% rate, say, can be crucial in comparing two alternatives where one involves much higher initial costs and lower recurring costs. An approach to the selection of discount rates (and the related problem of anticipating inflation rates) is presented in Section V.

III. Examples of Life-Cycle Costing

Reference 3 gives an interesting example, the results of a life-cycle cost analysis for an early warning radar. The cost components are given as percentages of the total LCC and are shown in Table 1. This example is typical of many in the literature that show the predominant contributors to LCC to be operation and maintenance costs, which here account for 72% of the total. Within both the operation and maintenance categories, labor costs are predominant in this example. Total labor costs (including training) represent 47% of the LCC.

Obviously, it is not easy to obtain good cost estimates for a list of categories such as these. Estimating repair labor, for example, requires consideration of multiple factors like failure rates, average time to repair, and hourly wages. Clearly, even the best possible estimates will be subject to error and uncertainty. However, as the example indicates, a much more costly error would be committed by neglecting entirely the costs that are hard to estimate.

Another example of life-cycle costing is given in Ref. 4, which analyzes the data problems incurred in estimating the life-cycle costs for a modern operational weapon system. The results of a life-cycle cost estimate made for the A-7D aircraft are shown in Table 2. The cost estimates were made on the basis of historical acquisition and operating data and are given in 1973 dollars. The acquisition phase covered the period 1967-1973 and the operational lifetime was assumed to be 15 years.

In this example, the unit ownership cost, $6.8 million, is about 57% of the total LCC and about 31% greater than the unit acquisition cost, $5.2 million. The authors make the point that the O&M, depot and to a large degree investment costs of ownership are highly sensitive to design, reliability, performance, and maintainability decisions made early in the acquisition stage. In short, as much as 79% of the costs of ownership are influenced by these early decisions. Thus, life-cycle costing can be a means of determining the long-term consequences of any changes in these attributes.

Reference 29 was designed to provide a framework for review of new weapon system life cycle operation and support (O&S) cost estimates and describes methodologies and techniques that the military departments can use to develop and record these estimates. To illustrate the cost estimation techniques given in the guide, an actual annual squadron cost calculation is made for a USAF A-10 Active Force Squadron (24 aircraft). Table 3 gives the detailed results of the calculation. Annual squadron cost estimates are also given, without details, for a National Guard Squadron ($8.2 M), a Reserve Force Squadron ($5.7 M) and a Combat Crew Training Squadron ($7.3 M). For each of these categories there are 18 aircraft per squadron. Using the schedule for delivering aircraft to the force structure, and assuming a 15-year life-cycle period (1976-1990), the force life-cycle O&S cost was estimated to be $329 M. To reflect the uncertainty in the estimation of each cost variable involved in the cost analysis, a high estimate of $3445 M and a low estimate of $3067 M are also listed.

IV. Benefits of Life-Cycle Costing

The chief benefit of life-cycle costing as a tool in economic decision-making is that, by forcing consideration of *all* costs, it frequently yields unexpected results and thereby leads to wiser decisions. As the examples of the previous section suggest, costs of operations and maintenance will often outweigh acquisition costs as a factor of selection among competing systems. In such cases, there is an obvious benefit in making as accurate an assessment of the costs as possible.

An additional benefit of LCC analysis is that the information compiled in using the technique can aid other management decisions – for example, by focusing attention on cost areas that are ripe for reduction. Thus LCC might lead to recognition of the need for new designs, new methods of operation, or new maintenance policies.

In a broader perspective, life-cycle cost can be regarded as one of the parameters describing a potential system to be traded off against system performance capabilities, availability, or the like. Only a systematic quantitative evaluation of all costs can serve as the basis for statements like "An extra x dollars spent on the system will buy y in additional performance."

V. Practical Considerations and Problems

Determining the useful life of a system is generally difficult. If wearout is the determinant of life-length, then the estimation problem is formidable in the case of a new, untried system. Moreover, if obsolescence plays the key role, then the analysis is even harder because a realistic determination of life-length depends much more upon the future availability of and need for improved (or modified) technology than upon the longevity of equipment. Whether a given system will actually be used for the next 5, 10, or 15 years is going to depend not only upon the present analysis of the cost-effectiveness of that system but also upon the future analysis of potential replacements as they become available 5, 10, or 15 years from now. Changes in system requirements or operations policies can, of course, further complicate matters.

Since the LCC method in effect amortizes the acquisition costs over system lifetime, the length of life is an important factor, particularly in the case of high-priced systems. As a means of avoiding the problem of estimating useful life, it is common practice to take arbitrarily chosen standard values for life-lengths.

However, even when arbitrary life-lengths are specified, it is often necessary to consider unequal lifetimes for competing systems. The comparison is facilitated by using the notion of *annualized cost* of a system, which is defined as the constant yearly cost of a hypothetical system having the same LCC. This hypothetical cost stream is uniquely determined by specifying its structure: zero initial cost and constant yearly costs during the operational period (thus amortizing the initial costs of the real system). Comparison of the annualized cost of competing systems having different life-lengths is equivalent to comparing the infinite cost streams generated by renewing each system at the end of every life-cycle.

Some of the difficulties of estimating yearly costs of a system have already been discussed in Section II. Data base inadequacies in the determination of O&M costs are a recurring theme of the case studies in the life-cycle cost literature. Even if this inadequacy can be partially overcome by the sort

of estimation approaches described in Section II, there is a further issue to consider – namely, the effect of changes in O&M policies or methods which will be made over the lifetime of the system. To rule out such considerations would be not only unrealistic but self-defeating, because the devising of improved methods of operation and maintenance is a vitally important means of controlling costs.

A statistical approach to the estimation of the effect of future improvements in efficiency has been gaining popularity as an adjunct to life-cycle costing (Ref. 19). This technique uses a *learning curve*, $L(t)$, which starts at 1 at the beginning of operation of the system and decreases over time to describe the factor by which costs in year t should be multiplied to reflect "learned" improvements in efficiency. The choice of such a curve will, of course, depend on the character of the system and its cost components and can be justified by experience with previous systems or the experience of other users of similar systems.

The preacquisition period of system development is one whose associated costs may be hard to assess. Nevertheless, if a life-cycle cost analysis is performed at a very early stage, it is important to consider such costs, inasmuch as they could be saved by aborting the development process. It is equally important to recognize that, just as the *complete* life-cycle cost must include R&D, the relevant quantity for deciding (at an advanced stage of development) whether to proceed to put the system into operation is the *future* life-cycle cost – namely, that part of the total cost which has not yet been incurred (plus whatever might be recovered by deciding not to adopt the system). Funds irrevocably spent should play no role in such a decision, although the complete life-cycle cost may still need to be assessed for reporting and other purposes.

The choice of a discount rate was mentioned in Section II as one of the basic tasks in evaluating a life-cycle cost. In addition to the uncertainties of determining the right value of this rate over the lifetime of the system, one faces the related complication that inflation will increase the yearly costs, e.g., for labor and materials. The standard approach in the literature is to choose a seemingly reasonable value, j, for the inflation rate and another value, i, for the discount rate. Thus, yearly costs are first estimated in *current* dollars (as of the beginning of system operation), then inflated by appropriate powers of $1 + j$, and finally discounted by dividing by powers of $1 + i$, as in the formula for LCC in Section II. The result is that if C_k^* is the kth year cost in current dollars (at the beginning of operation), then

$$LCC = \sum_{k=-(m-1)}^{n} C_k^* \frac{(1+j)^k}{(1+i)^k} = \sum_{k=-(m-1)}^{n} C_k^* V^k$$

where $V = (1 + j)/(1 + i)$. In effect, only the ratio of $1 + j$ to $1 + i$ matters in determining the LCC. What's more, for i and j in the usual range of 0 to 15%, the ratio is approximately a function of the difference $i - j$, the excess of the discount rate over the inflation rate. This difference $i - j$ has historically been greater than zero for most reasonably long periods and has typically been about 2 to 3%. This suggests choosing a value such as $V = 0.975$ for the purpose of the LCC formula. The important thing to observe is that the relative stability of $i - j$ historically (compared to the variability of i and j) gives this conceptualization of the LCC a good deal more assurance as a basis for economic evaluation.

VI. Major Areas of Interest in the Literature of LCC

As we mentioned in Section I, it was in the early 1960's that the interest in life-cycle costing was stimulated by the realization on the part of the DOD that if ownership costs had been considered on many procurements, design selection would have been different. As a result, the DOD made some trial procurements where ownership costs were considered in the award decision. To illustrate the versatility of the new technique, even at that time, we list some of the items selected for the trial, as given in Ref. 3.

(1) Nonmagnetic diesel engines for shipboard use.

(2) Replacement of siding on family housing.

(3) Solid-state 15-MHz oscilloscopes.

(4) Tachometer generators.

(5) Aircraft tires.

(6) Traveling wave tubes.

(7) Computers.

From these cases, initial "life-cycle costing" procurement policy evolved at DOD. Since that time a substantial portion of the literature on life-cycle costing is concerned with its application to specific systems and the problems involved when applied to that system. Refs. 1-8 are illustrations of the many case studies found in the literature.

Because the DOD is a strong advocate of life-cycle costing, many of the documents issued by the department as directives and guides to be used for various aspects of the procurement process include consideration of life-cycle costing. Some of these documents are listed in Refs. 9-12.

A distinctive feature of system cost-effective analysis is the use of the cost categories of research and development, initial

investment and annual operating costs. These categories are the major or most often mentioned cost categories found in the LCC literature. Thus, many reports are concerned with system and item cost analysis and with system cost-effective criteria. Refs. 13-18 present some of the writings which fall into this category.

Cost models are used in system, equipment and component selection processes to ensure a proper balance between cost and effectiveness. Although a number of standard models have been formulated, such as accounting models, simulation models, reliability models and economic analysis models, in practice it is almost always necessary to either adapt a standard model or construct a new model which will adequately describe a specific situation. A significant part of the literature is concerned with the construction and use of cost models as they relate to given systems. Refs. 19-24 illustrate this interest.

For many systems, such as sophisticated weapon systems, the concepts of reliability and maintainability play important roles with respect to life-cycle costing. Increasing the reliability of a system and improving system maintainability will reduce the cost and increase the efficiency of the system during its lifetime. Conversely, the financial cost of unreliability can be quite excessive. As a result, part of the literature of LCC discusses this aspect of life-cycle costing. Refs. 25-28 are examples of the interest shown in this phase of LCC.

VII. Conclusion

The value of the LCC concept and the validity of the techniques associated with it are strongly supported by its widespread use in non-defense as well as defense industries. The proven ability of industry to overcome complex problems that arise during the process of life-cycle costing should provide assurance to those contemplating its use, as to the concept's usefulness and versatility.

The principle underlying life-cycle costing is a simple one: determine not only the acquisition costs but also the costs involved in operating and maintaining the system during its lifetime before deciding whether or not to acquire the system.

This being so, one might ask why this valuable decision-making tool was not employed to any great extent until fairly recently. The answer probably lies in the fact that in many cases it is only when a detailed cost analysis is performed that one becomes aware of the magnitude of the nonacquisition costs relative to first costs, as well as the extent of the variability of these costs among the possible alternative systems. Thus, the importance of determining all costs is very often not evident until one performs the analysis, while at the same time there is no apparent reason to perform the analysis until the importance of the results is realized. It was not until this vicious circle was finally broken that the idea of life-cycle costing came into its own.

References

1. "Economic Analysis of Proposed Department of Defense Investments," Department of Defense Instruction No. 7041.3, Enclosure 2, p. 2, Department of Defense, Washington, D.C., Feb. 26, 1969.

2. Sloane, J. W., O'Toole, R. P., Gorden, C., "Baseline Economic Analysis for Erda Photoelectric Conceptual Design and Systems Analysis Studies," Engineering Memo 393-273, Jet Propulsion Laboratory, Pasadena, Calif., Sept. 8, 1975 (an internal document).

3. Earles, D. R., "LCC-Commercial Application, Ten Years of Life Cycle Costing," Proceedings of the 1975 Annual Reliability and Maintainability Symposium.

4. Frorello, M., "Estimating Life-Cycle Costs; A Close Study of the A-7D," Rand Corporation, Santa Monica, Calif., Feb. 1975.

5. "*Case Studies: Life Cycle Costing in Equipment Procurement*," Task 69-3, Contract No. SD-271, Logistics Management Institute, Washington, D.C., July 1969.

6. Kilpatrick, P. S., and Jones, A. L., "Life Cycle Cost Comparisons of Avionic System Design Alternatives," Proceedings of the National Aerospace Electronic Conference, 1974.

7. *Aircraft Field Experience Component Analysis* (Volumes I and II), Document D6-53584, The Boeing Company, Seattle, Washington, Sept. 1968.

8. Boden, W. H., "Designing for LCC," The Magnavox Company, Electronics and Aerospace Systems Convention, 1974.

9. *Acquisition of Major Defense Systems*, DOD 5000.1, Department of Defense, Washington, D.C., July 13, 1971.

10. *DOD Life Cycle Costing Procurement Guide (Interim)*. LCC-1, Department of Defense, Washington, D.C., July 1970.

11. *Economic Analysis and Program Evaluation for Resource Management*, DODI 7041.3, Department of Defense, Washington, D.C., October 18, 1972.

12. *Engineering Management*, Mil-Std-499A, Department of Defense, Washington, D.C., June 17, 1974.

13. Fiorello, M. R., *Getting 'Real' Data for Life-Cycle Costing*, Rand Corporation, Santa Monica, Calif., Jan. 1975.

14. *Guidebook for Systems Analysis/Cost-Effectiveness*, Prepared for U.S. Army Electronics Command, Fort Monmouth, New Jersey, ARINC Research Corporation, Mar. 1969 (AD 688154).

15. Blanchard, B. S., Jr., Lowery, E. L., *Maintainability*, McGraw-Hill, Inc., New York, 1969.

16. Fisher, G. H., *Cost Considerations in Systems Analysis*, R-490-ASD, The Rand Corporation, Santa Monica, Calif., Dec. 1970.

17. Goldman, A. S., *A Note: Problems in Life Cycle Support Cost Estimation*, General Electric Co., Santa Barbara, Calif.

18. Goldman, T. A. (ed.), *Cost-Effectiveness Analysis*, Frederick A. Praeger, New York, 1971.

19. Otto, T. W., Jr., *Life Cycle Cost Model, Research and Development*, Technical Report, ECOM-4338, Monmouth, New Jersey, July 1975.

20. *A Generalized Life Cycle Cost Model for Electronic Equipment*, Booz Allen Applied Research, Inc., Study performed for the U.S. Army Electronics Command, Systems/Cost Analysis Office, Fort Monmouth, New Jersey, March 10, 1970.

21. Hamilton, J. D., *Life Cycle Cost Modeling*, Technical Report No. 68-8, Army Material Command, Alexandria, Virginia, Dec. 1968.

22. O'Flaherty, J., *Weapon System Cost Model Objectives*, Client Report RAC-CA-26, Research Analysis Corporation, McLean, Virginia, Apr. 1971.

23. Paulson, R. M., Waina, R. B., Zacks, L. H., *Using Logistics Models in System Design and Early Support Planning*, R-550-PR, The Rand Corporation, Santa Monica, Calif., Feb. 1971.

24. Strope, D. H., *U. S. Army Missile Command's System-Oriented Cost Model* (Vol. 1), Report RF-TR-67-2, Research Analysis Corporation, McLean, Virginia, Nov. 1967.

25. Alexander, A. J., *R&D in Soviet Aviation*, R-589-PR, The Rand Corporation, Santa Monica, Calif., Nov. 1970.

26. *Use of Warranties for Defense Avionic Procurement*, Final Technical Report RADC-TR-73-249, ARINC Research Corporation, Annapolis, Maryland, June 1973.

27. Calabro, S. R., *Reliability Principles and Practices*, McGraw-Hill Co., Inc., New York, 1962.

28. Czajkowski, A. F., "A Conceptual Design Model for Reliability and Maintainability Analysis," Based on a doctoral dissertation, Oct. 1972.

29. Department of Defense. *Operating and Support Cost Development Guide for Aircraft Systems*, Cost Analysis Improvement Group, May 1974.

Table 1. Life-cycle cost breakdown for an early warning radar

	Percent of LCC
Acquisition costs	
Design, 12%	3.36
Fabrication, 72%	20.16
Installation and Checkout, 14%	3.92
Documentation, 2%	0.56
Total for acquisition	28%
Operation costs	
Personnel, 67%	8.04
Power, 32%	3.84
Fuel, 1%	0.12
Total for operation	12%
Logistic support costs (maintenance)	
Initial spares, 5.4%	3.24
Aircraft ground equipment, 2%	1.20
Initial training, 0.6%	0.36
Replacement spares, 18.5%	11.10
Repair material, 9.5%	5.70
Repair labor, 64%	38.40
Total for logistic support	60%

Table 2. Life-cycle costs for an A7-D aircraft

	M$/unit	Percent of LCC
Acquisition costs		
Airframe, 38%	1.97	16.5
Engine, 13%	0.68	5.6
Electronics, 13%	0.68	5.6
Spares, 20%	1.04	8.7
Other, 16%	0.83	6.9
Total for acquisition	5.20	43.3%
Ownership costs		
O&M, 48%	3.26	27.2
Investment, 15%	1.02	8.5
Depot, 16%	1.09	9.0
Base Support, 10%	0.68	5.7
Fuel, 4%	0.27	2.3
Training, 7%	0.48	4.0
Total for ownership	6.80	56.7%

Table 3. Annual operating and support costs for an A-10 aircraft squadron

	M$	Percent of total
Squadron operations		
Staff and aircraft manpower	1.100	8.90
Base manpower support	3.650	29.52
Aviation fuel	1.043	8.43
Base maintenance material	0.738	5.97
	6.531	52.82
Base operating support		
Base services manpower	0.802	6.49
Miscellaneous personnel support	0.353	2.85
	1.155	9.34
Logistics support		
Depot maintenance	1.263	10.22
Supply depot manpower and material	0.585	4.73
	1.848	14.95
Personnel support		
Training manpower	1.020	8.25
Medical manpower and material	0.215	1.74
Miscellaneous personnel support	0.312	2.52
	1.547	12.51
Recurring investment		
Replenishment spares	0.767	6.20
Aircraft ground equipment	0.136	1.10
Training munitions and missiles	0.381	3.08
	1.284	10.38
	12.365	

D14

Concatenated Shift Registers Generating Maximally Spaced Phase Shifts of PN-Sequences

W. J. Hurd
Communications Systems Research Section

L. R. Welch
University of Southern California

A large class of linearly concatenated shift registers is shown to generate approximately maximally spaced phase shifts of pn-sequences, for use in pseudorandom number generation. A constructive method is presented for finding members of this class, for almost all degrees for which primitive trinomials exist. The sequences which result are not normally characterized by trinomial recursions, which is desirable since trinomial sequences can have some undesirable randomness-properties.

I. Introduction

Binary maximal length linear recurring sequences, also known as pn-sequences, m-sequences, or maximal length linear shift register sequences, are known to have good randomness properties and hence are often used in pseudorandom number generation (Refs. 1, 2). Since all different phase shifts of the same sequence are essentially uncorrelated, weighted sums of several different phase shifts are also essentially uncorrelated for distances up to the minimum distance between the component phase shifts. Thus efficient methods for simultaneous generation of several maximally spaced phase shifts of the same pn-sequence are useful in generating pseudorandom numbers.

Various methods have been presented for generating several phase shifts of the same pn-sequence (Refs. 3-7). The major drawback in these techniques is that for high-degree recursions it is computationally infeasible to evaluate the distances between the phase-shifts. When the distances are computable or controllable, they are fairly small — at least small enough so that one could operate the generator long enough to see correlations between the phase shifts. Hurd (Ref. 8) has presented a method for generating approximately maximally spaced phase shifts of the product of two pn-sequences, and the autocorrelation properties of such sequences are good (Ref. 9), but the method is more efficient to implement in hardware than in software, and it has the minor disadvantage that the sequence is not quite maximal length.

We present here a large class of efficient algorithms for generating approximately maximally spaced phase shifts of pn-sequences; that is, the phase shifts approximately equipartition the period of the sequence. Second, we present a constructive method for finding an appropriate configuration for almost every degree for which there exists a primitive trinomial. The recursions which result are *not* generally trinomial recursions, which is desirable since some trinomial recursions have less desirable randomness properties than others (Refs. 10-12).

II. Description and Motivation

Figure 1 shows a general linear concatenation of shift registers. The algebraic description is as follows: There are N binary shift registers with lengths $L_0, L_1, \ldots, L_{N-1}$. The content of the ith stage of the kth register at time t is $A_i^k(t)$ and satisfies

$$A_{i+1}^k(t+1) = A_i^k(t) \text{ for } 1 \leqslant i < L_k \tag{1}$$

Each register has a linear output function

$$F^k(t) = \sum_{i=1}^{L_k} a_i^k A_i^k(t) \bmod (2) \tag{2}$$

which also serves as the input to the next register:

$$A_1^{k+1}(t+1) = F^k(t) \quad \text{(superscripts modulo } N\text{)} \tag{3}$$

The sequences $F^k(t)$ satisfy a linear recursion of degree $L = \Sigma L_k$.

The output of the generator is the N-tuple $[F^0(t), \ldots, F^{N-1}(t)]$. Alternate outputs are the pseudorandom numbers

$$X(t) = \sum_{k=0}^{N-1} F^k(t) 2^k \tag{4}$$

and

$$Y(t) = \sum_{k=0}^{N-1} F^k(t) \tag{5}$$

where the sums are integer sums (not mod (2)). When the sequence is maximal length, i.e., has period $2^L - 1$, the numbers $X(t)$ and $Y(t)$ are uniformly distributed and binomially distributed, respectively, neglecting the fact that the all zero's N-tuple cannot occur.

The $X(t)$ also have good multidimensional distribution properties. Letting $L_{min} = min\ \{L_0, L_1, \ldots, L_{N-1}\}$ we have:

Theorem I. When the sequence length is $2^L - 1$, $X(t)$ is uniformly distributed and L_{min} consecutive terms are mutually independent (neglecting the effect of the absence of the all-zero bit pattern in the collective register).

Proof: Since a repeat of the collective state of the registers causes a periodic repetition of the output sequence, and since the cycle length is $2^L - 1$, all bit patterns, except all zeros, must occur exactly once in each period. Since the output bits are fed into the next register, the bits in the representation of $[X(t-1), X(t-2), \ldots, X(t-L_{min})]$ are all present in the registers at time t. It follows that $[X(t-1), \ldots, X(t-L_{min})]$ is uniformly distributed in the L_{min}-cube (neglecting the effect of the absence of the all-zero bit pattern).

For the convenience of analysis, an alternate description can be given by defining sequences $A_i^k = [A_i^k(t): t \in Z]$ and $F^k = [F^k(t): t \in Z]$ and defining a delay operator D on sequence B to be $(DB)(t) = B(t-1)$. With this notation and the implicit assumption that component arithmetic is modulo 2, we have

$$A_1^{k+1} = DF^k \tag{6}$$

and

$$A_i^k = D^{i-1} A_1^k \tag{7}$$

From the definition of F^k,

$$F^k = \sum_{i=1}^{L_k} D^{i-1} a_i^k A_1^k = \left(\sum_{i=1}^{L_k} D^i a_i^k \right) F^{k-1} \tag{8}$$

(Again superscripts of F are taken modulo N.) Letting

$$f_k(D) = \sum_{i=1}^{L_k} D^i a_i^k,$$

we have

$$F^k = f_k(D) F^{k-1} \tag{9}$$

or

$$F^k = \left[\prod_{j=1}^{k} f_j(D) \right] F^0 \quad \text{for} \quad 0 \leqslant k \leqslant N-1 \tag{10}$$

In addition

$$F^0 = F^{N \bmod N} = \left[\prod_{j=1}^{N} f_j(D) \right] F^0 \tag{11}$$

where $f_N(D) = f_0(D)$. This last equation implies

$$\left[1 + \prod_{j=1}^{N} f_j(D)\right] F^0 = 0 \qquad (12)$$

Furthermore, $F^0, F^1, \ldots, F^{N-1}$ also satisfy this last equation. When this equation is expressed as a relation among the terms of F^0, it is seen to be a linear recursion with constant coefficients and the characteristic polynomial is

$$P(x) = 1 + \prod_{j=1}^{N} f_j(x) \qquad (13)$$

Of particular interest in this paper is the case where

$$f_k(x) = x^{a_k}[f(x)]^{b_k} \qquad (14)$$

We show that these recursions yield approximately maximally spaced phase shifts whenever the characteristic polynomial is primitive. Recursions of this class are easily implemented in N shift registers, interconnected with output functions which are all powers of one function, $f(x)$, plus some pure delays. If all of the powers b_k are unity, then all of the registers are identical except for some pure delays. In the simplest case, the functions are binomial. Such an example is shown in Fig. 2.

III. Analysis

For the configuration shown in Fig. 2, where all of the registers are the same except for the pure delays of a_k, the delay $d(k, k+1)$ from F^k to F^{k+1} is the same for all k, except for the a_k; i.e., it is a_k plus the delay associated with $f(x)$. However, it is not clear what the delay associated with $f(x)$ is, or what the delay is between nonadjacent registers, i.e., from F^k to F^{k+j} where $j \neq 1$. This complication arises because the sum of the delays between adjacent registers need not equal the period, but may be any integer multiple of the period. We show here that all of the delays are approximately $1/b$ times the period, or greater, where $b = \Sigma b_k$.

The polynomial

$$P(x) = 1 + \prod_{k=1}^{N} f_k(x)$$

introduced in the previous section has degree $L = \Sigma L_k$ provided $a^k_{L_k} = 1$ for all k. For good pseudorandom generators it is desirable that $P(x)$ be irreducible and primitive, and we now make that assumption.

Since all F^k satisfy the same recursion and the recursion is primitive, all of the F^k must be time delays of a common sequence F^0. It follows that $X(t)$ and $X(t-\tau)$ cannot be uncorrelated for all $\tau < 2^L - 1$. Whenever τ is the delay between F^k and F^j for some k and j, a component of $X(t)$ will be identical to a component of $X(t-\tau)$. The question arises as to how small the delay between two register outputs can be. The following lemma will allow us to answer that question for certain generators:

Lemma: Let $P(x)$ be an irreducible, primitive polynomial of degree n over $GF(2)$ and let $x^a[f(x)]^b = 1 \bmod [2, P(x)]$, where a and b are relatively prime, positive integers and $a \cdot b < 2^n - 1$. If $[f(x)]^k = x^{c_k} \bmod [2, P(x)]$ with $1 \leq k < b$ and $0 \leq c_k < 2^n - 1$, then there is an integer r_k with $1 \leq r_k < b$ such that

$$\left|c_k - \frac{r_k}{b}(2^n - 1)\right| < a.$$

Proof: Since P is primitive, there exists an $M \in [0, 2^n - 2]$ such that $f(x) = x^M \bmod [2, P(x)]$. Now $1 = x^a[f(x)]^b = x^{a+bM} \bmod [2, P(x)]$ or $a + bM = q(2^n - 1)$ for some integer q. It follows from the assumptions, that $1 \leq q$ and b, q are relative prime.

Next, for each k with $1 \leq k < b$ define q_k, r_k by

$$kq = q_k b + r_k \quad 0 \leq r_k < b$$

The range of k and the relative primeness of q and b implies $r_k \neq 0$. Now

$$kM = \frac{kq(2^n - 1) - a \cdot k}{b} = \frac{r_k(2^n - 1) - ak}{b} + q_k(2^n - 1)$$

Observing that $x^{c_k} = [f(x)]^k = x^{kM} \bmod [2, P(x)]$ we see that

$$c_k = \frac{r_k(2^n - 1) - ak}{b} \bmod (2^n - 1).$$

Since $1 \leqslant r_k < b$ and $ab < 2^n$

$$c_k = \frac{r_k}{b}(2^n - 1) - \frac{ak}{b}$$

and

$$\left|c_k - \frac{r_k}{b}(2^n - 1)\right| < a$$

This lemma can be used to bound the distances between output sequences from concatenated shift registers when the polynomials $f_j(x)$ are all powers of a common polynomial $f(x)$.

Theorem II. Let

$$P(x) = 1 + \prod_{j=1}^{M} x^{a_j}[f(x)]^{b_j},$$

$(a_j \geqslant 0, b_j > 0)$, be irreducible and primitive. Let

$$b = \sum_{j=1}^{N} b_j$$

and

$$a = \sum_{j=1}^{N} a_j.$$

Then the distance between F^k and F^j $(i \neq j)$ is at least $(2^n - 1)/b - a$.

Proof: The polynomial can be written $P(x) = 1 + x^a[f(x)]^b$. If a and b were not relatively prime, P would not be irreducible. The degree n is $a + b \cdot \deg f \geqslant a + b$, so clearly $a \cdot b < 2^a \cdot 2^b \leqslant 2^n$. Thus the lemma applies and $[f(x)]^k = x^{c_k}$ where

$$\left|c_k - \frac{r_k}{b}(2^n - 1)\right| < a.$$

Now

$$F^j = \prod_{m=i+1}^{j} D^{a_m}[f(D)]^{b_m} F^i \quad \text{if} \quad j > i$$

and

$$F^j = \left[\prod_{m=i+1}^{N-1} D^{a_m}[f(D)]^{b_m}\right] \left[\prod_{m=0}^{j} D^{a_m}[f(D)]^{b_m} F^i\right] \text{ if } j < i$$

In either case

$$F^j = D^l [f(D)]^k F^i$$

for some (l,k) with $0 \leqslant l \leqslant a$ and $0 \leqslant k < b$. It follows that

$$F^j = D^{l+c_k} F^i = D^{d(i,j)} F^i$$

From the lemma, it follows that

$$d(i,j) \geqslant \frac{2^n - 1}{b} - a$$

Now $d(i,j)$ is the distance *from* i to j. The above argument also applies to $d(j,i)$ so that

$$\min [d(i,j), d(j,i)] \geqslant \frac{2^n - 1}{b} - a$$

IV. A Class of Examples

Let $P(x) = x^n + x^b + 1$ be an irreducible primitive polynomial. In the field $GF(2^n)$, P has a root α. That is $\alpha^n + \alpha^b + 1 = 0$. Let $\beta = \alpha^{-b}$ so that $\alpha^n = (\beta^{-1} + 1)$ or $1 = \alpha^{-n}\beta^{-1}(1 + \beta)$. Raising both sides to the power b and substituting β for α^{-b} gives $1 = \beta^{n-b}(1 + \beta)^b$. Thus β is a root of $x^a(1 + x)^b + 1$ where $a = n - b$. Since α is primitive, b and n are relatively prime and it follows that a and b are relatively prime. Furthermore, if b is relatively prime to $2^n - 1$ then β is also primitive. Therefore, any concatenated shift register with outputs functions $D^{a_k}(1 + D)^{b_k}$, $0 \leqslant k \leqslant N - 1$, where

$$\sum_{k=0}^{N-1} a_k = a, \qquad \sum_{k=0}^{N-1} b_k = b,$$

with b relatively prime to $2^n - 1$, satisfies the conditions of theorems I and II. We therefore have the theorem:

Theorem III. Let $P(x) = 1 + x^b + x^n$ be an irreducible, primitive polynomial with $GCD(b, 2^n - 1) = 1$. Any concatenated shift register with output functions

$$f_k = x^{a^k} (1 + x)^{b^k},$$

and output sequences $F_k(t), 0 \leqslant k \leqslant N - 1$, such that

$$\sum_{k=0}^{n-1} a_k = a$$

and

$$\sum_{k=0}^{N-1} b_k = b,$$

has the following properties, neglecting the effect of the all-zero state:

(1) $X(t) = \sum_{k=0}^{N-1} 2^k F^k(t)$ is uniformly distributed.

(2) $X(t - 1), \ldots, X(t - L)$ are mutually independent for $L \leqslant \min_k (a_k + b_k)$.

(3) $X(t)$ and $X(t + \tau)$ are uncorrelated for $1 \leqslant \tau < \dfrac{2^n - 1}{b} - a$.

We observe that the characteristic polynomial of the recursion P is of the form $P(x) = (1 + x)^b x^a + 1$. This is *not* a trinomial unless b is a power of 2.

Almost all primitive trinomials satisfy theorem III, that is, all but those few where b and $2^n - 1$ are not relatively prime. An extensive list of primitive trinomials up to degree 1000 is given by Zierler and Brillhart (Refs. 13, 14).

When b is not a prime, the class of examples, and theorem III, extend to the cases where c divides b, and c is relatively prime to $2^n - 1$. Letting $\beta = \alpha^{-c}$, then β is a root of the primitive polynomial $(1 + x^{b/c})^c \; x^{n-b} + 1$, which can be implemented in a concatenation of c or fewer registers.

V. Computer Implementation

Members of the class of Section IV are easily implemented by computer programs. In these implementations the bits in position k of L_k consecutive computer words are used to represent the kth register. The number of registers equals the number of bits in a computer word.

For example, consider the system derived from the primitive polynomial $x^{159} + x^{34} + 1$ (Ref. 13) and implemented on a 32-bit machine. Since $GCD(34, 2^{159} - 1) = 1$, the above transformation can be applied and gives the primitive polynomial

$$P(x) = 1 + x^{125} (1 + x)^{34}$$

Now define

$$f_0(x) = x^3 \cdot (1 + x) = x^3 + x^4$$

$$f_1(x) = f_2(x) = x^3 \; (1 + x)^2 = x^3 + x^5$$

$$f_3(x) = \ldots = f_{31}(x) = x^4 \; (1 + x) = x^4 + x^5 .$$

Then

$$1 + \prod_{i=0}^{31} f_i(x) = 1 + x^{125}(1 + x)^{34} = P(x).$$

Let $M3$ be the computer word with 1's in positions 0, 1 and 2, and 0's elsewhere; let $M4$ be the computer word with 1's in positions 0 and 3 through 31 and 0's elsewhere; and let $M5$ be the computer word with 1's in positions 1 through 31 and 0's elsewhere. Then the following Boolean expression generates consecutive outputs

$$Z = [M3.AND.X(t - 3)] \; .XOR. \; [M4.AND.X(t - 4)] \; .XOR. \; [M5.AND.X(t - 5)]$$

and the new $x(t)$ is a left or right cycle of Z, one place.

References

1. Golomb, S. W., *Shift Register Sequences,* San Francisco, Holden Day, 1967.
2. Tausworthe, R. C., "Random Numbers Generated by Linear Recurrence Modulo Two," *Math. Comp.*, Vol. 19, pp. 201-209, Apr. 1965.
3. Lewis, T. G. and Payne, W. H., "Generalized Feedback Shift Register Pseudorandom Number Algorithm," *J. Assoc. Computing Machinery,* Vol. 20, No. 3, July 1973, pp. 456-468.
4. Davies, A. C., "Delayed Versions of Maximal Length Linear Binary Sequences," *Electronics Letters*, Vol. 1, No. 1, 1965, p. 61.
5. Davies, A. C., "Further Notes on Delayed Version of Linear Binary Sequences," *Electronics Letters*, Vol. 1, No. 7, Sept. 1965, pp. 190-191.
6. Latawiec, K. J., "A New Method of Generation of Shifted Linear Pseudorandom Sequences," *Proc. IEE*, Vol. 121, No. 8, Aug. 1974, pp. 905-906.
7. Hurd, W. J., "Efficient Generation of Statistically Good Pseudonoise by Linearly Interconnected Shift Registers," *IEEE Trans. Comp.*, Vol. C-23, No. 2, Feb. 1974, pp. 146-152.
8. Hurd, W. J., "A Wideband Gaussian Noise Generator Utilizing Simultaneously Generated pn-sequences," *Proc. 5th Hawaii Internat'l Conf. System Sci.*, pp. 168-170, Jan 1972.
9. Maritsas, D. G., "The Autocorrelation Function of the Two Feedback Shift Register Pseudorandom Source," *IEEE Trans. Comp.*, Oct. 1973, pp. 962-964.
10. Lindholm, J. H., "An Analysis of the Pseudo-Randomness Properties of Subsequences on Long n-sequences," *IEEE Trans. Inform. Th.*, Vol. IT-14, pp. 569-576, July 1968.
11. Toothill, J. P. R., Robinson, W. D., and Adams, A.G., "The Runs Up-and-Down Performance of Tausworthe Pseudo-Random Number Generators, *J. ACM*, Vol. 18, No. 3, July 1971, pp. 381-399.
12. Toothill, J. P. R., Robinson, W. D., and Eagle, D. J., "An Asymptotically Random Tauseworthe Sequence," *J. ACM,* Vol. 20, No. 3, July 1973, pp. 469-481.
13. Zierler, N., and Brillhart, J., "On Primitive Trinomials (Mod 2)," Information and Control, Vol. 13, No. 6, Dec. 1968, pp. 541-554.
14. Zierler, N., and Brillhart, J., "On Primitive Trinomials (Mod 2), II," *Inform. Contr.*, Vol. 14, No. 6, June 1969, pp. 566-569.

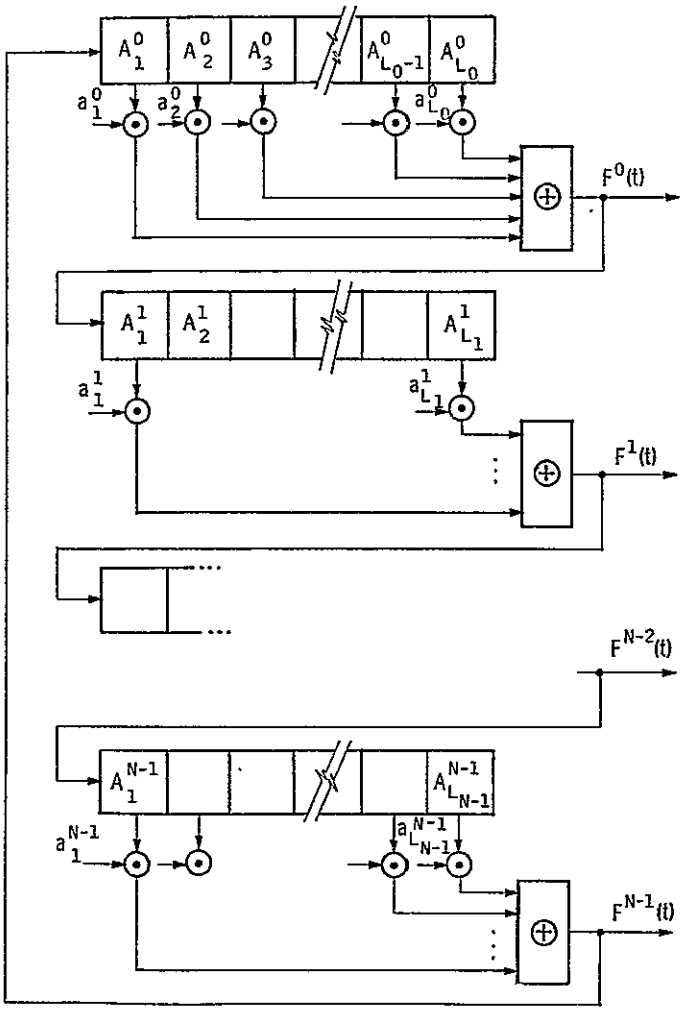

Fig. 1. A linear concatenation of N shift registers

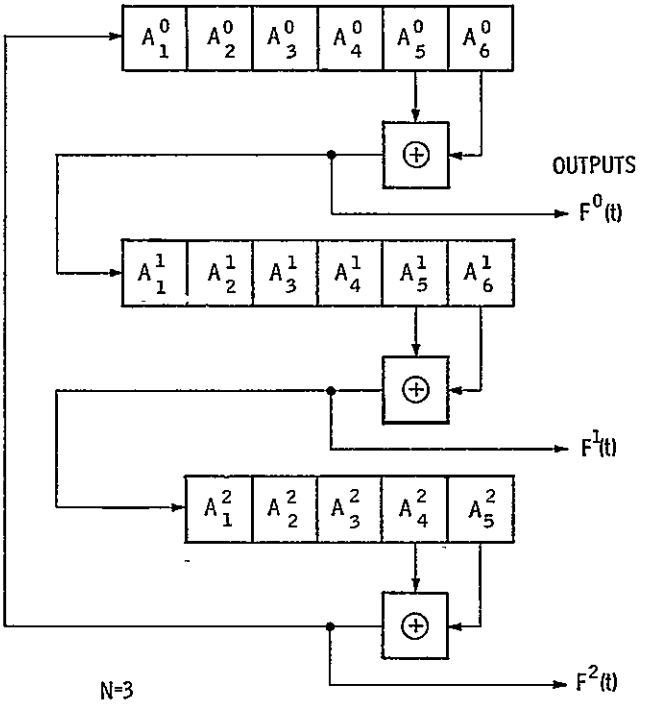

N=3

$L_0 = L_1 = 6$; $L_2 = 5$

$f_k(x) = x^{L_k - 1}(1+x)$

$P(x) = 1 + x^{14}(1 + x)^3$

Fig. 2. An example concatenation with $b_k = 1$

DSN Progress Report 42-40 May and June 1977

On the Fundamental Structure of Galois Switching Functions

B. Benjauthrit
TDA Engineering

I. S. Reed
University of Southern California

It is shown that the fundamental structure of Galois switching functions follows naturally from that of Boolean switching functions. An expanded formula for deriving multinomial Galois switching functions is provided with illustrations of its application.

I. Introduction

Due to its simple and systematic properties, the Boolean field and its algebra have been applied successfully to binary-valued logic. Since the Galois or finite field is the natural extension of the Boolean field, more and more researchers have become interested in utilizing finite fields in the design of multivalued logics. It will be evident later that multivalued logic, using Galois field theory or algebra, is now as realizable as Boolean switching logic. This may be considered to be a consequence of the recent efforts of Menger (Ref. 1), Benjauthrit and Reed (Ref. 2), and Pradhan (Ref. 3). The second paper provided a systematic method of deriving any multinomial Galois switching functions via what is referred to as "Galois differences." The third paper furnished still another expansion for obtaining such switching functions.

Though both methods provide a systematic technique for deriving a unique Galois switching function from a given truth table description of the function, each requires tedious computation. Specifically, the first method often contains many redundant terms in its formulation, whereas the second method requires a great number of multiplications and additions. By some algebraic manipulations, an expanded formula is obtained which combines the best features of both methods. This formula enables one to compute the coefficients of the desired function more directly and probably with less effort.

II. Summary of Existing Results

Since most of the basic properties of Galois fields have been given in the literature, they will not be described here. Instead, use will be made of these properties as necessary and the reader will be directed to the appropriate references. Two basic theorems are now stated.

Let $q = p^n$ be the order or the number of field elements of Galois field $GF(q)$ whose field power is n and characteristic is a prime p. Denote the set of all nonzero field elements by $GF^*(q)$. Also, let the symbol Σ_F signify the sum of all elements over F. Then, according to Ref. 2, one has the following theorem.

Theorem 1. For every function F: $GF(p^n)^m \to GF(p^n)$, there exists a unique function f: $\{0,1,\cdots,p^n-1\} \to GF(p^n)$ such that

$$F(x_1,\cdots,x_m) = \sum f(k_1,\cdots,k_m)\, x_1^{k_1}\cdots x_m^{k_m}$$

where the function f is given by

$$f(\underline{0}) = F(\underline{0})$$

$$f(k_1,0,\cdots,0) = \underset{x_1^{k_1}}{\Delta} F(\underline{0}) = \sum_{GF'(p^n)} [F(\underline{0}) - F(\gamma_1,0,\cdots,0)]\,\gamma_1^{-k_1}$$

$$f(k_1,k_2,\cdots,0) = \underset{x_1^{k_1}x_2^{k_2}}{\Delta^{(2)}} F(\underline{0})$$

$$= \sum_{GF'(p^n)} \sum [F(\underline{0}) - F(0,\gamma_2,0,\cdots,0) - F(\gamma_1,0,0,\cdots,0) + F(\gamma_1,\gamma_2,0,\cdots,0)]\,\gamma_1^{-k_1}\gamma_2^{-k_2}$$

$$f(k_1,\cdots,k_m) = \underset{x_1^{k_1}\cdots x_m^{k_m}}{\Delta^{(m)}} F(\underline{0})$$

$$= \sum^{m}\cdots\sum_{GF'(p^n)} [F(\underline{0}) - F(0,\cdots,0,\gamma_m) - \cdots - F(\gamma_1,0,\cdots,0)$$

$$+ F(0,\cdots,0,\gamma_{m-1},\gamma_m) + \cdots + F(\gamma_1,\gamma_2,0,\cdots,0)$$

$$- \cdots (-1)^m F(\gamma_1,\cdots,\gamma_m)]\,\gamma_1^{-k_1}\cdots\gamma_m^{-k_m}$$

and

$$\underset{x_{i_1}\cdots x_{i_p}}{\Delta^{(p)}} F(\underline{0}) = \underset{x_{i_p}}{\Delta}\left[\underset{x_{i_1}\cdots x_{i_{p-1}}}{\Delta^{(p-1)}} F(\underline{0})\right], \text{ for } p = 1,2,\cdots,m$$

The function $F(x_1, \cdots, x_m)$ has the following "power series" expansion:

$$F(x_1, \cdots, x_m) = F(\underline{0}) + \left[\Delta_{x_1} F(\underline{0})\right] x_1 + \cdots + \left[\Delta_{x_m} F(\underline{0})\right] x_m$$
$$+ \left[\Delta_{x_1^2} F(\underline{0})\right] x_1^2 + \cdots + \left[\Delta_{x_m^2} F(\underline{0})\right] x_m^2 + \cdots + \left[\Delta_{x_m^q} F(\underline{0})\right] x_m^q$$
$$+ \left[\Delta^{(2)}_{x_1 x_2} F(\underline{0})\right] x_1 x_2 + \cdots + \left[\Delta^{(2)}_{x_{m-1}^q x_m^q} F(\underline{0})\right] x_{m-1}^q x_m^q$$
$$+ \left[\Delta^{(m)}_{x_1 \cdots x_m} F(\underline{0})\right] x_1 \cdots x_m + \cdots + \left[\Delta^{(m)}_{x_1^q \cdots x_m^q} F(\underline{0})\right] x_1^q \cdots x_m^q$$

where $F(0) \equiv F(0, \cdots, 0)$.

Now, from Ref. 3, the next theorem follows.

Theorem 2. Any function $F(x_1, \cdots, x_m)$ can be expressed as

$$F(x_1, \cdots, x_m) = \sum_{GF(q)}^{m} \cdots \sum g(\gamma_1, \cdots, \gamma_m) F(\gamma_1, \cdots, \gamma_m) \tag{1}$$

where

$$g(\gamma_1, \cdots, \gamma_m) = \prod_{i=1}^{m} [1 - (x_i - \gamma_i)^{q-1}], \quad \gamma \in GF(q) \tag{2}$$

Also from Ref. 3, we obtain the following lemmas:

Lemma 1. The sum of ith power of nonzero elements over the field $GF(q)$ is null for $0 < i < q - 1$ and unity for $i = q - 1$. Mathematically,

$$\sum_{GF^*(q)} \alpha^i = \begin{cases} 0, & \text{for } 0 < i < q - 1 \quad (3a) \\ -1, & \text{for } i = q - 1 \quad (3b) \end{cases}$$

Note that Lemma 1 is not restricted to $q > 2$ here because, for $q = 2$, (3a) does not hold for $i \neq 0$ and thus only (3b) implies.

Lemma 2.

$$1-(x-\gamma)^{q-1}=\begin{cases}1-x^{q-1}, & \gamma=0\\ 1-\sum_{i=0}^{q-1}(-1)^{q-1-i}\binom{q-1}{q-1-i}\gamma^{q-1-i}x^{i}, & \gamma\in GF'(q)\end{cases}$$

III. The Expanded Formula

For later use, a generalized version of Lemma 1 is first stated and proven.

Lemma 3. For any positive integer m,

$$\sum_{GF'(q)}^{m}\cdots\sum\gamma_1^{i_1}\cdots\gamma_m^{i_m}=\begin{cases}(-1)^m, & \text{for } i_1=q-1,\cdots,i_m=q-1\\ 0, & \text{otherwise}\end{cases}$$

Proof. The lemma follows directly from the factorizability property of the summation and by repeated applications of Lemma 1. For example, when $m=2$, one has

$$\sum_{GF'(q)}\sum\gamma_1^{i_1}\gamma_2^{i_2}=\left[\sum_{GF'(q)}\gamma_1^{i_1}\right]\left[\sum_{GF'(q)}\gamma_2^{i_2}\right]$$

$$=\begin{cases}-\sum_{GF'(q)}\gamma_2^{i_2}\ (\text{for } i_1=q-1)=\begin{cases}1, & i_2=q-1\\ 0, & \text{otherwise}\end{cases}\\ 0, \quad \text{otherwise}\end{cases}$$

Q.E.D.

The following two lemmas and their consequence are also useful.

Lemma 4. Let p be prime and $1\leqslant i\leqslant p^n-1$ for any integer $n\geqslant 1$. Then,

$$\binom{p^n}{i}\equiv 0 \bmod p \tag{4}$$

Proof. We shall prove the lemma by induction on n. For $n=1$,

$$\binom{p}{i}=\frac{p(p-1)\cdots(p-i+1)}{i!}=\frac{pk}{i!},\ \text{an integer}$$

This implies that $i!|pk$. But $i < p$ and, thus, the gcd$(i!, p) = 1$. Hence, $i!|k$ so that $\binom{p}{i} = p \cdot$ integer and relation (4) holds.

Hypothesize that relation (4) is true for n. We must now show that it is also true for $n + 1$. In so doing, express the polynomial $(1 + x)^{p^{n+1}}$ in two ways:

$$(1+x)^{p^{n+1}} = \sum_{i=0}^{p^{n+1}} \binom{p^{n+1}}{i} x^i \tag{5}$$

and

$$(1+x)^{p^{n+1}} = ((1+x)^{p^n})^p = \left(\sum_{j=0}^{p^n} \binom{p^n}{j} x^j \right)^p$$

$$= \sum_{j_1=0}^{p^n} \cdots \sum_{j_p=0}^{p^n} \binom{p^n}{j_1} \cdots \binom{p^n}{j_p} x^{j_1+\cdots+j_p}$$

$$= \sum_{i=0}^{p^{n+1}} x^i \sum_{j_1+\cdots+j_p=i} \binom{p^n}{j_1} \cdots \binom{p^n}{j_p} \tag{6}$$

It follows that

$$\binom{p^{n+1}}{i} = \sum_{\substack{j_1+\cdots+j_p=i \\ 0 \leqslant j_\nu \leqslant p^n}} \binom{p^n}{j_1} \cdots \binom{p^n}{j_p}, 0 \leqslant i \leqslant p^{n+1} \tag{7}$$

Let $1 \leqslant i \leqslant p^{n+1} - 1$. If $0 \leqslant j_\nu \leqslant p^n$ and

$$\sum_{\nu=1}^{p} j_\nu = i$$

then, some j_μ satisfies the condition $1 \leqslant j_\mu \leqslant p^n - 1$. By the induction hypothesis,

$$\binom{p^n}{j_\mu} \equiv 0 \bmod p$$

Then, each term in the sum of (7) is 0 mod p so that

$$\binom{p^{n+1}}{i} \equiv 0 \bmod p$$

On the other hand, suppose that all the j_v are either 0 or p^n. Then, the product in (7) is 1. This can happen only if $i = ap^n$, where $1 \leqslant a \leqslant p-1$; in this case, the number of such terms on the right side of (7) is $\binom{p}{a}$, a multiple of p, and thus (4) also follows.

Q.E.D.

Lemma 5. Let p be prime, and $0 \leqslant i \leqslant p^n - 1$ for any integer $n \geqslant 0$. Then,

$$\binom{p^n - 1}{i} \equiv (-1)^i \bmod p \tag{8}$$

Proof. It is trivial for the case $n = 0$. Let $n \geqslant 1$ and use induction on i. Relation (8) is obviously true for $i = 0$. By the Pascal triangle relationship, if $0 \leqslant i \leqslant p^n - 1$, then

$$\binom{p^n - 1}{i} + \binom{p^n - 1}{i+1} = \binom{p^n}{i+1}$$

By Lemma 4, the right side is 0 mod p, and the induction hypothesis is (8). Hence, relation (8) is true for the case i replaced by $i + 1$.

Q.E.D.

By multiplying both sides of relation (8) in Lemma 5 by the quantity $(-1)^{p^n-1-i}$ and noting the identity $+\equiv -$ *for* $p = 2$, one obtains the following corollary.

Corollary 1. Let p be prime and $0 \leqslant i \leqslant p^n - 1$ for any integer $n \geqslant 0$. Then

$$(-1)^{p^n-1-i}\binom{p^n - 1}{i} \equiv 1 \bmod p$$

Since $\gamma^{q-1} = 1, \gamma \in GF'(q)$, and with Corollary 1, Lemma 2 yields:

Lemma 6.

$$\prod_{i=1}^{m} [1 - (x_i - \gamma_i)^{q-1}] = \begin{cases} \prod_{i=1}^{m} [1 - x_i^{q-1}], & \gamma = 0 \qquad (9a) \\ \prod_{i=1}^{m} \left[-\sum_{j=1}^{q-1} \gamma_i^{-j} x_i^j \right], & \gamma \in GF'(q) \qquad (9b) \end{cases}$$

With the above theorems and lemmas, one can now state and prove the following expanded formula.

Theorem 3. For every function $F: GF(q)^m \to GF(q)$, there exists a unique function f: $[1, \cdots, q-1] \to GF(q)$ such that

$$F(x_1, \cdots, x_m) = \begin{cases} \sum_{GF(q)}^{m} \cdots \sum g(\gamma_1, \cdots, \gamma_m) F(\gamma_1, \cdots, \gamma_m) \\ \sum_{k_1=0}^{q-1} \cdots \sum_{k_m=0}^{q-1} f(k_1, \cdots, k_m) x_1^{k_1} \cdots x_m^{k_m} \end{cases}$$

where

i) $$g(\gamma_1, \cdots, \gamma_m) = \prod_{i=1}^{m} [1 - (x_i - \gamma_i)^{q-1}]$$

$$= \begin{cases} 1 + \sum_{i=1}^{m} (-1)^i \sum_{j_1 < j_2 < \cdots < j_i} x_{j_1}^{q-1} x_{j_2}^{q-1} \cdots x_{j_i}^{q-1}, \quad \gamma = 0, 1 \leqslant j_l \leqslant m \\ \prod_{i=1}^{m} -\sum_{j=1}^{q-1} \gamma_i^{-j} x_i^j, \quad \gamma \in GF'(q) \end{cases} \tag{10a}$$

and

$$g(\gamma_1, \cdots, \gamma_k, 0, \cdots, 0) = \left[\prod_{i=1}^{k} -\sum_{j=1}^{q-1} \gamma_i^{-j} x_i^j \right] \left[1 + \sum_{i=1}^{m-k} (-1)^i \sum_{j_1 < j_2 < \cdots < j_i} x_{j_1}^{q-1} x_{j_2}^{q-1} \cdots x_{j_i}^{q-1} \right] \tag{10b}$$

for any k, $1 \leqslant k \leqslant m$, $\gamma \in GF'(q)$, and $k < j_l \leqslant m$

ii) $$f(0, \cdots, 0) = F(0, \cdots, 0)$$

$$f(k_1, 0, \cdots, 0) = -\sum_{GF'(q)} F(\gamma_1, 0, \cdots, 0) \gamma_1^{-k_1}$$

$$\vdots$$

$$f(q-1, 0, \cdots, 0) = -\sum_{GF(q)} F(\gamma_1, 0, \cdots, 0)$$

$$f(k_1, k_2, 0, \cdots, 0) = \sum_{GF'(q)} \sum F(\gamma_1, \gamma_2, 0, \cdots, 0) \gamma_1^{-k_1} \gamma_2^{-k_2}$$

$$f(q-1, q-1, 0, \cdots, 0) = \sum_{GF(q)} \sum F(\gamma_1, \gamma_2, 0, \cdots, 0)$$

$$f(k_1, \cdots, k_i, 0, \cdots, 0) = (-1)^i \sum_{GF'(q)}^{i} \cdots \sum F(\gamma_1, \cdots, \gamma_i, 0, \cdots, 0) \gamma_1^{-k_1} \cdots \gamma_i^{-k_i}$$

$$f(q-1, \cdots, q-1, 0, \cdots, 0) = (-1)^i \sum_{GF(q)}^{i} \cdots \sum F(\gamma_1, \cdots, \gamma_i, 0, \cdots, 0)$$

$$f(k_1, \cdots, k_m) = (-1)^m \sum_{GF'(q)}^{m} \cdots \sum F(\gamma_1, \cdots, \gamma_m) \gamma_1^{-k_1} \cdots \gamma_m^{-k_m}$$

$$f(q-1, k_2, \cdots, k_m) = (-1)^m \left[\sum_{GF'(q)}^{m-1} \cdots \sum F(0, \gamma_2, \cdots, \gamma_m) \gamma_2^{-k_2} \cdots \gamma_m^{-k_m} \right.$$

$$\left. + \sum_{GF'(q)}^{m} \cdots \sum F(\gamma_1, \cdots, \gamma_m) \gamma_2^{-k_2} \cdots \gamma_m^{-k_m} \right]$$

$$f(q-1, q-1, k_3, \cdots, k_m) = (-1)^m \left[\sum_{GF'(q)}^{m-2} \cdots \sum F(0, 0, \gamma_3, \cdots, \gamma_m) \gamma_3^{-k_3} \cdots \gamma_m^{-k_m} \right.$$

$$+ \sum_{GF'(q)}^{m-1} \cdots \sum F(0, \gamma_2, \cdots, \gamma_m) \gamma_3^{-k_3} \cdots \gamma_m^{-k_m}$$

$$+ \sum_{GF'(q)}^{m-1} \cdots \sum F(\gamma_1, 0, \gamma_3, \cdots, \gamma_m) \gamma_3^{-k_3} \cdots \gamma_m^{-k_m}$$

$$+ \sum_{GF'(q)}^{m} \cdots \sum F(\gamma_1, \cdots, \gamma_m) \gamma_3^{-k_3} \cdots \gamma_m^{-k_m} \Bigg]$$

$$f(q-1, \cdots, q-1, k_{i+1}, \cdots, k_m) = (-1)^m \Bigg[\sum_{GF'(q)}^{m-i} \cdots \sum F(0, \cdots, 0, \gamma_{i+1}, \cdots, \gamma_m) \gamma_{i+1}^{-k_{i+1}} \cdots \gamma_m^{-k_m}$$

$$+ \sum_{GF'(q)}^{m-i-1} \cdots \sum F(0, \cdots, 0, \gamma_i, \cdots, \gamma_m) \gamma_{i+1}^{-k_{i+1}} \cdots \gamma_m^{-k_m} + \cdots$$

$$+ \sum_{GF'(q)}^{m-i-1} \cdots \sum F(\gamma_1, 0, \cdots, 0, \gamma_{i+1}, \cdots, \gamma_m) \gamma_{i+1}^{-k_{i+1}} \cdots \gamma_m^{-k_m} + \cdots$$

$$+ \sum_{GF'(q)}^{m-i-2} \cdots \sum F(0, \cdots, 0, \gamma_{i-1}, \cdots, \gamma_m) \gamma_{i+1}^{-k_{i+1}} \cdots \gamma_m^{-k_m} + \cdots$$

$$+ \sum_{GF'(q)}^{m-i-2} \cdots \sum F(\gamma_1, \gamma_2, 0, \cdots, 0, \gamma_{i+1}, \cdots, \gamma_m) \gamma_{i+1}^{-k_{i+1}} \cdots \gamma_m^{-k_m} + \cdots$$

$$+ \sum_{GF'(q)}^{m} \cdots \sum F(\gamma_1, \cdots, \gamma_m) \gamma_{i+1}^{-k_{i+1}} \cdots \gamma_m^{-k_m} \Bigg]$$

$$f(q-1, \cdots, q-1) = (-1)^m \sum_{GF(q)}^{m} \cdots \sum F(\gamma_1, \cdots, \gamma_m) \tag{10c}$$

In words, for those coefficients containing no $q-1$ as their arguments, we simply expand the function around the point(s) being considered. For any coefficients containing $q-1$ as its arguments, the function's "initial value(s)" must be included in the expansion. Finally, the last coefficient $f(q-1, \cdots, q-1)$ includes all points, i.e., all function output values, in its expansion.

Proof.

i) The result follows directly from Theorem 2 and Lemma 6.

ii) Coefficients (10c) can be derived from either Theorem 1 or Theorem 2. However, since these two theorems have been independently proven to be correct (Refs. 2 and 3), the uniqueness of Lagrange's expansion of m-variable functions (Ref. 4)

guarantees that they both lead to the same unique function. For simplicity, Theorem 1 will be employed here, together with Lemma 1 or Lemma 3.

For $m = 1$,

$$f(k_1) = \sum_{GF'(q)} [F(0) - F(\gamma_1)]\, \gamma_1^{-k_1}$$

$$= F(0) \sum_{GF'(q)} \gamma_1^{-k_1} - \sum_{GF'(q)} F(\gamma_1)\, \gamma_1^{-k_1}$$

$$= \begin{cases} -\sum_{GF'(q)} F(\gamma_1)\, \gamma_1^{-k_1}, & 0 < k_1 < q-1 \\ -\sum_{GF(q)} F(\gamma_1), & k_1 = q-1 \end{cases}$$

For $m = 2$,

$$f(k_1, k_2) = \sum_{GF'(q)} \sum_{GF'(q)} [F(0,0) - F(0,\gamma_2) - F(\gamma_1, 0) + F(\gamma_1, \gamma_2)]\, \gamma_1^{-k_1} \gamma_2^{-k_2}$$

$$= F(0,0) \left[\sum_{GF'(q)} \gamma_1^{-k_1} \right] \left[\sum_{GF'(q)} \gamma_2^{-k_2} \right]$$

$$- \left[\sum_{GF'(q)} \gamma_1^{-k_1} \right] \left[\sum_{GF'(q)} F(0,\gamma_2)\, \gamma_2^{-k_2} \right]$$

$$- \left[\sum_{GF'(q)} \gamma_2^{-k_2} \right] \left[\sum_{GF'(q)} F(\gamma_1, 0)\, \gamma_1^{-k_1} \right]$$

$$+ \sum_{GF'(q)} \sum_{GF'(q)} F(\gamma_1, \gamma_2)\, \gamma_1^{-k_1} \gamma_2^{-k_2}$$

Therefore,

$$f(k_1,k_2)=\begin{cases}\sum\limits_{GF'(q)}\sum F(\gamma_1,\gamma_2)\gamma_1^{-k_1}\gamma_2^{-k_2}, & 0<k_1,k_2<q-1\\ \sum\limits_{GF'(q)}F(0,\gamma_2)\gamma_2^{-k_2}+\sum\limits_{GF'(q)}\sum F(\gamma_1,\gamma_2)\gamma_2^{-k_2}, & k_1=q-1,\ 0<k_2<q-1\\ \sum\limits_{GF'(q)}F(\gamma_1,0)\gamma_1^{-k_1}+\sum\limits_{GF'(q)}\sum F(\gamma_1,\gamma_2)\gamma_1^{-k_1}, & 0<k_1<q-1,\ k_2=q-1\\ \sum\limits_{GF(q)}\sum F(\gamma_1,\gamma_2), & k_1=k_2=q-1\end{cases}$$

Now, assuming it is true for the m case, we shall show that the $m+1$ case follows:

$$f(k_1,\cdots,k_m,k_{m+1})=(-1)^{m+1}\sum_{GF'(q)}^{m+1}\cdots\sum F(\gamma_1,\cdots,\gamma_m,\gamma_{m+1})\gamma_1^{-k_1}\cdots\gamma_m^{-k_m}\gamma_{m+1}^{-k_{m+1}}$$

$$f(q-1,k_2,\cdots,k_m,k_{m+1})=(-1)^{m+1}\left[\sum_{GF'(q)}^{m+1-1}\cdots\sum F(0,\gamma_2,\cdots,\gamma_m,\gamma_{m+1})\gamma_2^{-k_2}\cdots\gamma_m^{-k_m}\gamma_{m+1}^{-k_{m+1}}+\sum_{GF'(q)}^{m+1}\cdots\sum F(\gamma_1,\cdots,\gamma_m,\gamma_{m+1})\gamma_2^{-k_2}\cdots\gamma_m^{-k_m}\gamma_{m+1}^{-k_{m+1}}\right]$$

$$\vdots$$

$$f(q-1,q-1,k_3,\cdots,k_m,k_{m+1})=(-1)^{m+1}\left[\sum_{GF'(q)}^{m+1-2}\cdots\sum F(0,0,\gamma_3,\cdots,\gamma_m,\gamma_{m+1})\gamma_3^{-k_3}\cdots\gamma_m^{-k_m}\gamma_{m+1}^{-k_{m+1}}+\cdots+\sum_{GF'(q)}^{m+1}\cdots\sum F(\gamma_1,\cdots,\gamma_m,\gamma_{m+1})\gamma_3^{-k_3}\cdots\gamma_m^{-k_m}\gamma_{m+1}^{-k_{m+1}}\right]$$

$$\vdots$$

$$f(q-1,\cdots,q-1)=(-1)^{m+1}\sum_{GF'(q)}^{m+1}\cdots\sum F(\gamma_1,\cdots,\gamma_m,\gamma_{m+1})$$

which are exactly the coefficients (10c) when $m+1$ is redefined as m. This completes the proof.

It is not difficult to show that a similar proof of Theorem 3 can also be obtained from Theorem 2, especially for case $m=1$. For case $m=2$, from Theorem 2 and Lemma 6, one has

$$F(x_1, x_2) = \sum_{GF(q)}\sum g(\gamma_1, \gamma_2) F(\gamma_1, \gamma_2)$$

$$= [1 - x_1^{q-1} - x_2^{q-1} + x_1^{q-1} x_2^{q-1}] \; F(0,0)$$

$$+ [1 - x_1^{q-1}] \sum_{GF'(q)} \left[- \sum_{k_2=1}^{q-1} \gamma_2^{-k_2} x_2^{k_2} \right] F(0, \gamma_2)$$

$$+ [1 - x_2^{q-1}] \sum_{GF'(q)} \left[- \sum_{k_1=1}^{q-1} \gamma_1^{-k_1} x_1^{k_1} \right] F(\gamma_1, 0)$$

$$+ \sum_{GF'(q)}\sum \left[- \sum_{k_1=1}^{q-1} \gamma_1^{-k_1} x_1^{k_1} \right] \left[- \sum_{k_2=1}^{q-1} \gamma_2^{-k_2} x_2^{k_2} \right] F(\gamma_1, \gamma_2)$$

Again, using basic properties of the summation and with some simple manipulation, one obtains

$$F(x_1, x_2) = F(0,0) + \sum_{k_1=1}^{q-2} \left[- \sum_{GF'(q)} F(\gamma_1, 0) \gamma_1^{-k_1} \right] x_1^{k_1} - \left[\sum_{GF(q)} F(\gamma_1, 0) \right] x_1^{q-1}$$

$$+ \sum_{k_2=1}^{q-2} \left[- \sum_{GF'(q)} F(0, \gamma_2) \gamma_2^{-k_2} \right] x_2^{k_2} - \left[\sum_{GF(q)} F(0, \gamma_2) \right] x_2^{q-1}$$

$$+ \sum_{k_1=1}^{q-2} \sum_{k_2=1}^{q-2} \left[\sum_{GF'(q)}\sum F(\gamma_1, \gamma_2) \gamma_1^{-k_1} \gamma_2^{-k_2} \right] x_1^{k_1} x_2^{k_2}$$

$$+ \cdots + \left[F(0,0) + \sum_{GF'(q)} F(0, \gamma_2) + \sum_{GF'(q)} F(\gamma_1, 0) + \sum_{GF'(q)}\sum F(\gamma_1, \gamma_2) \right] x_1^{q-1} x_2^{q-1}$$

which contains exactly the coefficients given in (10c). To complete the proof, an induction on m may be accomplished similar to the previous case.

Q.E.D.

IV. Examples

We now provide two examples to illustrate the effectiveness of Theorem 3. For convenience and to the point, let us consider Example 1 described in Ref. 3. By partitioning as follows,

$$(y^1, y^2) = y$$

$$(x^1, x^2) = x_1$$

$$(x^3, x^4) = x_2$$

$$(x^5, x^6) = x_3$$

and representing (0, 0) by 0, (0, 1) by 1, (1, 0) by α, and (1, 1) by β, the given six-input two-output variable function is represented as shown in Table 1; the all-zero rows are omitted here.

Using Theorem 2 and observing that rows 1, 2, 7 and rows 3, 4, 5, 6 have the values of x_2, x_3, y and x_1, x_2, respectively, in common, we obtain

$$y = \beta\,[1-(x_2-\beta)^3]\,[1-x_3^3]\,\{[1-x_1^3]+[1-(x_1-1)^3]+[1-(x_1-\beta)^3]\}$$

$$+\,[1-(x_1-\alpha)^3]\,[1-(x_2-\beta)^3]\,\{\alpha\,[1-x_3^3]+[1-(x_3-1)^3]+[1-(x_3-\alpha)^3]+[1-(x_3-\beta)^3]\}$$

Making use of Lemma 2 and noting the identity $+\equiv -$, y can be simplified as

$$y = x_2+\alpha x_2^2+\beta x_2^3+x_1x_2+\alpha x_1x_2^2+\beta x_1x_2^3+\beta x_1^2x_2+x_1^2x_2^2$$

$$+\,\alpha x_1^2x_2^3+\alpha x_1^3x_2+\beta x_1^3x_2^2+x_1^3x_2^3+x_2x_3^3+\alpha x_2^2x_3^3+\beta x_2^3x_3^3$$

Now by applying Theorem 3 and Table 2, we can verify the above result termwise as follows:

$$f(0,1,0) = \sum_{GF'(4)} F(0,\gamma_2,0)\,\gamma_2^{-1} = 0+0+\beta\cdot\alpha = 1$$

$$f(0,2,0) = \sum_{GF'(4)} F(0,\gamma_2,0)\,\gamma_2^{-2} = 0+0+\beta\cdot\beta = \alpha$$

$$\vdots$$

$$f(1,1,0) = \sum_{GF'(4)} F(\gamma_1,\gamma_2,0)\,\gamma_1^{-1}\,\gamma_2^{-1} = 0+0+\alpha\cdot\beta+0+\alpha\cdot\beta\cdot\alpha+0+\beta\cdot\alpha\cdot\alpha = 1$$

$$f(3,3,0) = \sum_{GF(4)} F(\gamma_1, \gamma_2, 0) = 0+0+0+\beta+0+0+0+\beta+0+0+0+\alpha+0+0+0+\beta = 1$$

$$\vdots$$

$$f(0,3,3) = \sum_{GF(4)} F(0, \gamma_2, \gamma_3) = 0+\cdots+0+\beta+0+0+0 = \beta$$

$$\vdots$$

$$f(3,3,2) = \sum_{GF'(4)} F(0,0,\gamma_3)\gamma_3^{-2} + \sum\sum_{GF'(4)} F(0,\gamma_2,\gamma_3)\gamma_3^{-2} + \sum\sum_{GF'(4)} F(\gamma_1,0,\gamma_3)\gamma_3^{-2}$$

$$+ \sum\sum\sum_{GF'(4)} F(\gamma_1,\gamma_2,\gamma_3)\gamma_3^{-2}$$

$$= [0+0+0] + [(0+\cdots+0+1+0+0+0)+(0+\cdots+0+1+0+0+0)\alpha+(0+\cdots+0+1+0+0+0)\beta] = 0$$

As another example, consider the four-input two-output specification given in Table 2 of Ref. 2. Using the same representation for $GF(3^2)$,

$$0 = 00,\ 1 = \alpha^0 = 10,\ \alpha = 01,\ \alpha^2 = 12,\ \alpha^3 = 22,\ \alpha^4 = 20,\ \alpha^5 = 02,\ \alpha^6 = 21,\ \alpha^7 = 11$$

and the same partition

$$x_1 = \{u_1, u_2\},\ x_2 = \{u_3, u_4\},\ \text{and } F = \{v_1, v_2\};$$

the truth table is obtained as given in Table 3.

Employing Theorem 3 here and Table 1 in Ref. 2, Eq. (16) of Ref. 2 may be verified term by term as follows:

$$f(1,0) = -\sum_{GF'(9)} F(\gamma_1, 0)\gamma_1^{-1} = -\alpha - \cdots - \alpha = -\alpha - \alpha = -\alpha^5 = \alpha$$

$$f(0,3) = -\sum_{GF'(9)} F(0, \gamma_2)\gamma_2^{-3} = -1 - \cdots - 1 = -1 - 1 = -\alpha^4 = 1$$

$$f(1,1) = \sum\sum_{GF'(9)} F(\gamma_1, \gamma_2)\gamma_1^{-1}\gamma_2^{-1} = 1$$

$$f(5,7) = \sum\sum_{GF'(9)} F(\gamma_1, \gamma_2)\gamma_1^{-5}\gamma_2^{-7} = 1$$

The sum of the output functions F results in

$$f(8,8) = \sum_{GF(9)}\sum F(\gamma_1, \gamma_2) = 1$$

The remaining 75 terms can be similarly verified to be all zeros. Hence,

$$f(x_1, x_2) = \alpha x_1 + x_2^3 + x_1 x_2 + x_1^5 x_2^7 + x_1^8 x_2^8$$

It is evident that employing either Theorem 1 or Theorem 2 to compute $F(x_1, x_2)$ of the above example would be tedious. This is especially true for Theorem 2.

Observe that Theorem 3 always requires a fixed number of computations; i.e., q^m computations for m variables over $GF(q)$. For truth tables whose rows contain a great number of zeros, the technique of Theorem 2 is no worse than that of Theorem 3; in fact, it is even better at times. However, for large m and large number of nonzero elements in the truth table, the advantage of Theorem 3 can truly be appreciated. The advantages and disadvantages of Theorem 3 over Theorems 1 and 2 are a subject of further investigation. But, for now, it is obvious that the technique provided in Theorem 3 is suitable both for hand and computer calculations.

V. Conclusion

Any Galois switching function can be expressed as the sum of minterms with a set of uniquely defined coefficients, or it can be expressed as the sum of its output-valued functions with also another set of uniquely defined coefficients. From these two approaches, we have derived an expanded version of the two methods. With this expanded formula, the function can be obtained more simply and directly from its given table of description. The novelty of the technique is illustrated by example.

Acknowledgments

The authors would like to thank Mr. B. D. L. Mulhall and Dr. J. S. L. Wong for their early support and encouragement in the research that led to this paper. Thanks are also due to Dr. C. A. Greenhall for his assistance on mathematical proofs.

References

1. Menger, K. S., Jr., "A Transform for Logic Networks," *IEEE Trans. Computers*, Vol. C-18, pp. 241-251, Mar. 1969.
2. Benjauthrit, B., and Reed, I. S., "Galois Switching Functions and Their Applications," in *The Deep Space Network Progress Report 42-27*, pp. 68-80, Jet Propulsion Laboratory, Pasadena, Calif., June 15, 1975.
3. Pradhan, D. K., *Structure and Minimization of Finite Field Functions*, Dept. of Computer Science, University of Saskatchewan, Regina, Saskatchewan, Feb. 1975.
4. Van der Waerden, B. L., *Algebra*, Vol. I, Federick Unger Publishing, 1966.

Table 1. Truth table of six-input two-output variable function

Row	x_1	x_2	x_3	y
	.	.	.	.
	.	.	.	.
	.	.	.	.
1	0	β	0	β
	.	.	.	.
	.	.	.	.
	.	.	.	.
2	1	β	0	β
	.	.	.	.
	.	.	.	.
	.	.	.	.
3	α	β	0	α
4	α	β	1	1
5	α	β	α	1
6	α	β	β	1
	.	.	.	.
	.	.	.	.
	.	.	.	.
7	β	β	0	β
	.	.	.	.
	.	.	.	.
	.	.	.	.

Table 2. Galois field operations

Addition over $GF(4)$					Multiplication over $GF(4)$				
+	0	1	α	β	.	0	1	α	β
0	0	1	α	β	0	0	0	0	0
1	1	0	β	α	1	0	1	α	β
α	α	β	0	1	α	0	α	β	1
β	β	α	1	0	β	0	β	1	α

Table 3. An input-output truth table

x_1	x_2	F	x_1	x_2	F	x_1	x_2	F	x_1	x_2	F
0	0	0	α^5	α^5	α^7	α^7	α^7	0	α^4	α^4	α^3
0	α	α^3	α^5	1	α^7	α^7	α^2	1	α^4	α^6	α^6
0	α^5	α^7	α^5	α^7	α^5	α^7	α^4	1	α^4	α^3	α^3
0	1	1	α^5	α^2	α^7	α^7	α^6	0	α^6	0	α^7
0	α^7	α^5	α^5	α^4	α^6	α^7	α^3	1	α^6	α	α^4
0	α^2	α^6	α^5	α^6	α^6	α^2	0	α^3	α^6	α^5	α^3
0	α^4	α^4	α^5	α^2	0	α^2	α	α^7	α^6	1	1
0	α^6	α^2	1	0	α	α^2	α^5	α^4	α^6	α^7	0
0	α^3	α	1	α	α^2	α^2	1	0	α^6	α^2	α^2
α	0	α^2	1	α^5	1	α^2	α^7	α^6	α^6	α^4	α^5
α	α	1	1	1	α^7	α^2	α^2	α^4	α^6	α^6	0
α	α^5	α	1	α^7	α^3	α^2	α^4	α	α^6	α^3	α^2
α	1	α^5	1	α^2	α^5	α^2	α^6	α^7	α^3	0	α^4
α	α^7	α^3	1	α^4	α^7	α^2	α^3	1	α^3	α	0
α	α^2	α^6	1	α^6	α^4	α^4	0	α^5	α^3	α^5	0
α	α^4	α^2	1	α^3	0	α^4	α	α^3	α^3	1	1
α	α^6	α^4	α^7	0	1	α^4	α^5	α^5	α^3	α^7	α^6
α	α^3	α^3	α^7	α	α	α^4	1	α^5	α^3	α^2	α^3
α^5	0	α^6	α^7	α^5	α^2	α^4	α^7	α^5	α^3	α^4	α^4
α^5	α	α^6	α^7	1	0	α^4	α^2	0	α^3	α^6	α^7
									α^3	α^3	α^2

Phase Fluctuation Spectra: New Radio Science Information To Become Available in the DSN Tracking System Mark III-77

A. L. Berman
TDA Engineering Office

The DSN Tracking System Mark III-77 currently being implemented at the Deep Space Stations will automatically provide doppler noise (rms phase jitter) computed concurrently over three evenly spaced decades of data sample interval and associated time-scale:

Data sample interval, sec	*Time-scale, sec*
0.1	*1.8*
1.0	*18.0*
10.0	*180.0*
100.0	*1800.0*

It is here suggested that these data translate directly into "average" phase fluctuation spectra, and hence represent a new and convenient source of radio science information. Temporal phase fluctuation spectra derived from Viking and Helios doppler noise data yield a power law relationship with frequency as follows:

$$P_{\phi}(f) \sim f^{-2.42}$$

for the following approximate range of frequencies:

$$3.3 \times 10^{-2}\ \text{Hz} > f > 5.6 \times 10^{-4}\ \text{Hz}$$

I. Introduction

In early 1978, the DSN Tracking System Mark III-77 will initiate the continuous and automatic computation of doppler noise concurrently at four sample rate intervals evenly spanning three orders of magnitude:

0.1 sec
1.0
10.0
100.0

The process used to compute the noise will be the same for all of the sample rate intervals and is characterized by

(1) The number of contiguous doppler (frequency) samples used in each computation is fixed (at 18).

(2) The noise is computed for a least squares linear curve fit to the (18) data samples.

The above process is similar to the process by which doppler noise is currently computed in the Network Operations Control Center (NOCC), the only exception being that the current algorithm uses 15 samples, versus 18 samples in the new algorithm. It is significant that the number of samples used for each of the different sample interval noise calculations is fixed, as this results in the time-scale of the noise observations being proportional to the data sample interval. As there is considerable interest in doppler phase fluctuation spectra, particularly during solar conjunctions, it is here suggested that "average" temporal doppler phase fluctuation spectra may be routinely available in the DSN Tracking System Mark III-77 and require little additional processing. Extraction of the basic (noise) data by the user would be from the Archival Tracking Data File (ATDF) of the Tracking Data Management System.

II. Average Doppler Phase Fluctuation Spectra Computed from Viking and Helios Doppler Noise

In Ref. 1, R. Woo used dual S- and X-band closed loop doppler data from the Mariner-Venus-Mercury (MVM) spacecraft at a Sun-Earth-Probe (SEP) angle of ~11.5 deg to obtain typical differenced S-X phase fluctuation spectra. It is here desired to investigate whether doppler noise relationships derived by this author and J. A. Wackley (Refs. 2, 3, and 4) yield comparable spectra information.

In Ref. 2, doppler noise was found to be functionally dependent upon sample interval (15 samples, least squares linear curve fit) as:

$$\text{Noise} \propto \left(\frac{60}{\tau}\right)^{0.285}; \text{ Helios}$$

$$\text{Noise} \propto \left(\frac{60}{\tau}\right)^{0.294}; \text{ Viking}$$

where τ = data sample interval in seconds.

In the following analysis, a combined Helios and Viking noise variation with data sample interval will be utilized, as follows:

$$\text{Noise} \propto \left(\frac{60}{\tau}\right)^{0.29}$$

From Refs. 3 and 4 one has the following noise average values for $\tau = 60$ seconds and at an SEP of 11.5 deg:

$$\text{Noise} = 0.023 \text{ Hz; Helios}$$

$$\text{Noise} = 0.024 \text{ Hz; Viking}$$

Likewise combining the above, one constructs a composite Helios and Viking noise relationship with data sample interval at an SEP of 11.5 deg of

$$\text{Noise}(\tau) = 0.0235 \left(\frac{60}{\tau}\right)^{0.29} \text{ Hz}$$

Obtaining the relationship between doppler noise and "rms phase fluctuation" presents some difficulty; previously (Ref. 5), it was assumed that:

$$\text{rms phase } (\tau) = \tau \text{ noise } (\tau)$$

To check this assumption, a phase fluctuation of the form:

$$\text{phase } (t) = \sin 2\pi (t/T + K)$$

T = phase fluctuation period, Hz^{-1}

K = arbitrary phase, cycles

was passed through a simulated model of the DSN Noise algorithm (but without the linear curve fit). The results are seen in Fig. 1, and indicate

$$\frac{1}{4} \leqslant \frac{\tau \text{ noise } (\tau)}{\text{rms phase } (\tau)} \leqslant \frac{9}{4}$$

for the range

$$\tau/2 \leqslant T \leqslant 30\tau$$

It will be assumed here that:

$$\frac{\tau \text{ noise } (\tau)}{\text{rms phase } (\tau)} \cong \frac{3}{5}$$

or

$$\text{rms phase } (\tau) \cong \frac{5}{3}\ \tau \text{ noise } (\tau)$$

for fluctuations in the region:

$$\tau/2 \leqslant T \leqslant 30\tau$$

Introducing a factor of $\sqrt{2}$ to obtain a one-way spectrum from two-way doppler noise,

$$\text{rms phase } (\tau) \cong \frac{1}{\sqrt{2}}\frac{5}{3}\tau\left[0.0235\left(\frac{60}{\tau}\right)^{0.29}\right] \text{ Hz sec}$$

$$= \frac{100}{\sqrt{2}}\left[0.0235\left(\frac{60}{\tau}\right)^{0.29}\left(\frac{\tau}{60}\right)\right] \text{ cycles}$$

$$= \frac{2.35}{\sqrt{2}}\left(\frac{\tau}{60}\right)^{0.71} \text{ cycles}$$

$$= \sqrt{2}\pi 2.35\left(\frac{\tau}{60}\right)^{0.71} \text{ rad}$$

and hence

$$\text{mean square phase} = 2\pi^2 5.52\left(\frac{\tau}{60}\right)^{1.42} \text{ rad}^2$$

$$= 109\left(\frac{\tau}{60}\right)^{1.42} \text{ rad}^2$$

Now define the following:

f = phase fluctuation frequency, Hz

T = phase fluctuation period, Hz^{-1}

$T = f^{-1}$

The least squares linear curve fit to the 15 data samples (substantially) "fits out" fluctuations with periods greater than T where:

$$T \cong 2 \times 15\tau = 30\tau$$

The mean square phase fluctuations in rad^2 can then be considered:

$$\int_{(30\tau)^{-1}}^{(\tau/2)^{-1}} P_\phi(\nu)\,d\nu \approx \int_f^\infty P_\phi(\nu)\,d\nu$$

where

$$f = (30\tau)^{-1}$$

$P_\phi(f) \equiv$ temporal phase fluctuation spectra derived from doppler noise, $\text{rad}^2\,\text{Hz}^{-1}$

so that

$$\int_f^\infty P_\phi(\nu)\,d\nu \approx 109\left(\frac{30\tau}{1800}\right)^{1.42} \text{ rad}^2$$

$$= 109(1800)^{-1.42} f^{-1.42} \text{ rad}^2$$

$$= 2.6 \times 10^{-3} f^{-1.42} \text{ rad}^2$$

Differentiating both sides with respect to f:

$$\frac{d}{df}\int_f^\infty P_\phi(\nu)\,d\nu = -P_\phi(f) \text{ rad}^2\text{Hz}^{-1}$$

$$\frac{d}{df}2.6 \times 10^{-3} f^{-1.42} = -(1.42)2.6 \times 10^{-3} f^{-2.42} \text{ rad}^2\text{Hz}^{-1}$$

$$= -3.7 \times 10^{-3} f^{-2.42} \text{ rad}^2\text{Hz}^{-1}$$

or

$$P_\phi(f) = 3.7 \times 10^{-3} f^{-2.42} \text{ rad}^2\text{Hz}^{-1}$$

For data sample intervals between 1 sec and 60 sec (from Ref. 2), the corresponding applicable frequency range is:

$$3.3 \times 10^{-2}\text{Hz} > f > 5.6 \times 10^{-4}\text{Hz}$$

Values of this average phase fluctuation spectrum for various frequencies are presented below:

f, Hz	$P_\phi(f)$, rad^2 Hz^{-1}
10^1	1.4×10^{-5}
10^0	3.7×10^{-3}
10^{-1}	9.8×10^{-1}
10^{-2}	2.6×10^{2}
10^{-3}	6.7×10^{4}
10^{-4}	1.8×10^{7}
10^{-5}	4.7×10^{9}

Figures 2 and 3 are taken from Ref. 1 and are differenced S-X phase fluctuation spectra for the MVM spacecraft at an SEP of approximately 11.5 deg; overplotted on Figs. 2 and 3 is the doppler noise derived phase fluctuation spectrum at a similar SEP:

$$P_\phi(f) = 3.7 \times 10^{-3} f^{-2.42} \text{ rad}^2 \text{ Hz}^{-1}$$

The agreement between the two is seen to be quite reasonable; Woo (Ref. 1) indicates finding the relationship between the S-X differenced phase spectra ($W_{\phi d}(f)$) and f to be:

$$W_{\phi d}(f) \sim f^{-2.5} \text{ to } f^{-2.6}$$

which is compared to the doppler noise derived phase fluctuation spectra

$$P_\phi(f) \sim f^{-2.42}$$

Table 1 presents a comparison of the frequency dependence of other determined or measured temporal solar plasma spectra (as computed from the equivalent power law three-dimensional spatial power spectra).

III. Doppler Noise Derived Average Phase Fluctuation Spectra as a Function of SEP

The Viking data utilized in Ref. 2 spanned a range of SEP angle as follows:

$$6.4^\circ \gtrsim \text{SEP} \gtrsim 0.9^\circ$$

Figure 4 shows the exponent solutions from Table 2, Ref. 2, translated into average spectra as in Section II and plotted as a function of SEP. No significant correlation of spectral frequency dependence with SEP is seen. In Ref. 6, H. Chang hypothesizes that at low SEPs (hence strong scintillation) the temporal solar plasma spectra change from power law to exponential; the data in Fig. 4 do not appear to support this contention. It is here considered that doppler noise data may be quite useful in further study of phase fluctuation spectra (frequency dependence) as a function of SEP.

Combining the results of Section II with the ISEDC doppler noise model from Ref. 2, one can construct an average phase fluctuation spectrum as a function of the relevant geometry:

$$P_\phi(f,\alpha,\beta) = \left[\frac{ISEDC \text{ Hz}}{0.0235 \text{ Hz}}\right]^2 3.7 \times 10^{-3} f^{-2.42} \text{ rad}^2 \text{ Hz}^{-1}$$

$$= 6.7 f^{-2.42} \left(A_0 \left[\frac{\beta}{(\sin\alpha)^{1.3}}\right] F(\alpha,\beta) + A_1 \left[\frac{1}{(\sin\alpha)^5}\right] \right)^2 \text{ rad}^2 \text{ Hz}^{-1}$$

where

$A_0 = 1.182 \times 10^{-3}$

$A_1 = 4.75 \times 10^{-10}$

α = Sun-Earth-Probe angle, rad

β = Earth-Sun-Probe angle, rad

$$F(\alpha,\beta) = 1 - 0.05 \left[\frac{(\beta - \pi/2 + \alpha)^3 - (\alpha - \pi/2)^3}{\beta}\right]$$

$$-0.00275 \left[\frac{(\beta - \pi/2 + \alpha)^5 - (\alpha - \pi/2)^5}{\beta}\right]$$

IV. Summary

It is here suggested that average phase fluctuation spectra can be easily obtained from doppler noise computed concurrently over different time scales. Using such data from the Viking and Helios solar conjunctions, an average phase fluctuation spectrum at 11.5 deg SEP is calculated to be

$$P_{\phi}(f) = 3.7 \times 10^{-3} f^{-2.42} \text{ rad}^2 \text{ Hz}^{-1}$$

and can be extrapolated to the full range of SEP via the ISEDC doppler noise model. Concurrent doppler noise computations at four evenly decade separated data sample intervals

$$0.1 \text{ sec} \leqslant \tau \leqslant 100.0 \text{ sec}$$

combined with a least squares linear curve fit are expected to provide average phase fluctuation spectra data for the frequency range:

$$2.8 \times 10^{-1} \text{ Hz} > f > 2.8 \times 10^{-4} \text{ Hz}$$

It is expected that these data may be quite useful in studying the frequency dependence of phase fluctuation spectra as a function of SEP, particularly at low SEPs ($\lesssim 5°$) for which there currently exist few published results.

Concurrent computation of doppler noise estimations is being implemented as a standard and automatic capability of the DSN Tracking System Mark III-77 and will become routinely and conveniently available to users in early 1978.

Acknowledgment

I am indebted to L. Y. Lim, who graciously simulated the DSN doppler noise model and plotted the output via the very efficient MBASIC* language.

*A trademark of the California Institute of Technology.

References

1. Woo, R., Yang, F., Yip, K. W., and Kendall, W. B., "Measurements of Large Scale Density Fluctuations in the Solar Wind Using Dual Frequency Phase Scintillations", *Ap. J.*, 210, Jan. 1977.

2. Berman, A. L., "A Comprehensive Two-Way Doppler Noise Model for Near-Real-Time Validation of Doppler Data," in *The Deep Space Network Progress Report 42-37*, Jet Propulsion Laboratory, Pasadena, Calif., Feb. 15, 1977.

3. Berman, A. L., Wackley, J. A., and Rockwell, S. T., "The 1976 Helios and Pioneer Solar Conjunctions – Continuing Corroboration of the Link Between Doppler Noise and Integrated Signal Path Electron Density," in *The Deep Space Network Progress Report 42-36*, Jet Propulsion Laboratory, Pasadena, Calif., Dec. 15, 1976.

4. Berman, A. L., and Wackley, J. A., "Viking S-Band Doppler RMS Phase Fluctuations Used to Calibrate the Mean 1976 Equatorial Corona," in *The Deep Space Network Progress Report 42-38*, Jet Propulsion Laboratory, Pasadena, Calif., Apr. 15, 1977.

5. Berman, A. L., "Proportionality Between Doppler Noise and Integrated Signal Path Electron Density Validated by Differenced S/X Range," in *The Deep Space Network Progress Report 42-38*, Jet Propulsion Laboratory, Pasadena, Calif., Apr. 15, 1977.

6. Chang, H., "Analysis of Dual-Frequency Observations of Interplanetary Scintillations Taken by The Pioneer 9 Spacecraft," Doctoral dissertation, Department of Electrical Engineering, Stanford University, May 1976.

Table 1. Typical values of the logarithmic slope of temporal solar plasma spectra with frequency [a]

Source	Reference	Log $P_\phi(\nu)$/Log ν	Frequency range (ν), Hz	Distance (closest approach or in situ), AU	Measurement
Berman		-2.42	$3.3 \times 10^{-2} > \nu > 5.6 \times 10^{-4}$	0.016-0.111	S-band doppler noise
Woo et al.	1	-2.5/-2.6	$5 \times 10^{-1} > \nu > 1 \times 10^{-4}$	0.2	Differenced S- and X-band phase
Chang	6	-2.5	$1 \times 10^{1} > \nu > 1 \times 10^{0}$	0.1-1	Dual-frequency interplanetary scintillation (IPS)
Unti et al.	6	-2.55	$1.3 \times 10^{1} > \nu > 5 \times 10^{-3}$	~1	In situ proton density
Intriligator and Wolfe	6	-2.3	$1 \times 10^{-3} > \nu > 1.\times 10^{-4}$	~1	In situ proton density
Coleman	6	-2.2	$1 \times 10^{-2} > \nu > 1 \times 10^{-5}$	0.9-1	In situ magnetic field and plasma velocity spectra

[a] Assumes the temporal (columnar) spectrum is proportional to $\nu^{-(x-1)}$ if the three-dimensional spatial power spectrum is power law with exponent $-x$.

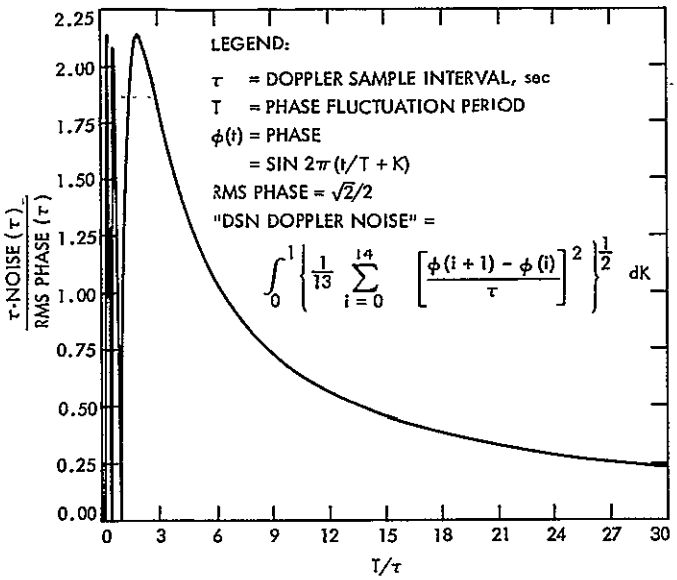

Fig. 1. Ratio of DSN doppler noise to rms phase fluctuation as a function of phase fluctuation frequency

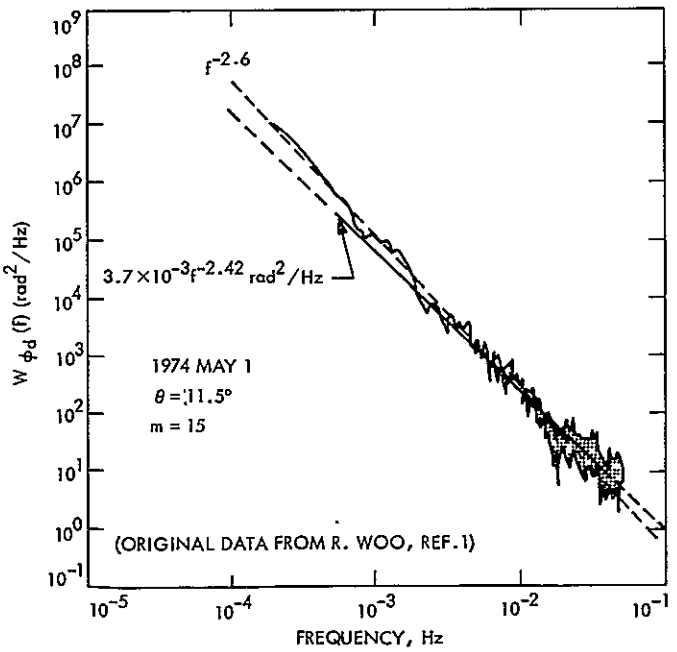

Fig. 2. Comparison of MVM differenced phase spectra to Viking-Helios doppler noise phase fluctuation spectra

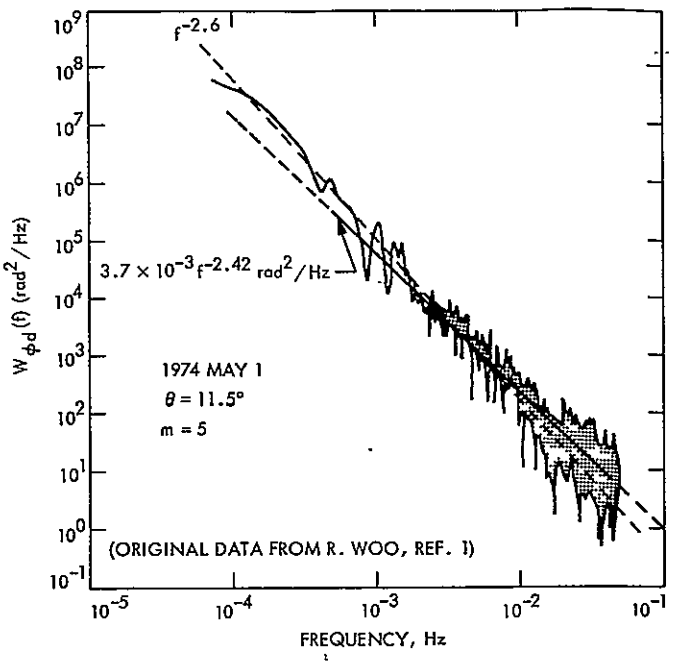

Fig. 3. Comparison of MVM differenced phase spectra to Viking-Helios doppler noise phase fluctuation spectra

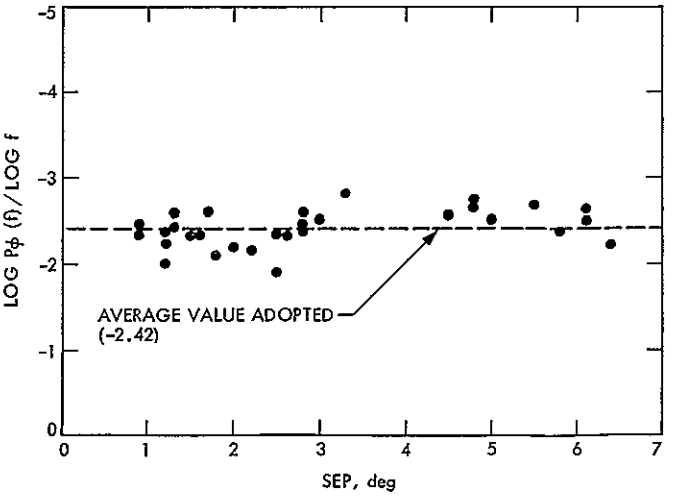

Fig. 4. Logarithmic slope of phase fluctuation spectra vs frequency as determined from Viking doppler noise

DSN Radio Science System Mark III-78 Real-Time Display Capability

A. L. Berman
TDA Engineering Office

This article describes the current plan to provide radio science real-time display capability in response to multimission radio science requirements. The implementation occurs in two phases, as follows:

Phase I: Provides display of doppler frequency and high-resolution graphical display of all closed-loop radio metric parameters.

Phase II: Provides spectrum displays of open-loop receiver output.

I. Introduction

The Radio Science System was recently instituted as a Deep Space Network (DSN) data system. A review of Radio Science System functional requirements was held on February 4, 1977 (see Ref. 1 for a detailed description of the review). At the review, the question of real-time radio science data display capability was broached and designated as requiring subsequent resolution. This article describes the plan generated to provide radio science real-time data display capability during the Voyager era.

Radio science data is conveniently categorized as either originating from the closed (phase-locked)-loop receiver assembly ("closed-loop data") or the open-loop receiver assembly ("open-loop data"). Data acquired by the closed-loop receiver assembly consists of the following major types of radio metric data:

(1) Single-frequency doppler.

(2) Dual-frequency doppler

(3) Single-frequency range.

(4) Dual-frequency range.

(5) Differenced range minus integrated doppler (DRVID).

These data are utilized by both Navigation and Radio Science; although Navigation is the prime user, the data is nonetheless extremely important for its radio science content. Open-loop data, primarily acquired during signal transit through the solar and planetary atmospheres, is dedicated to and solely used by Radio Science. Real-time (tracking system) displays of closed-loop data are scheduled for implementation in early 1978, in

concert with implementation of the DSN Tracking System Mark III-77. These displays will consist of tabular digital television (DTV) displays of all closed-loop radio metric data types available from the DSS Tracking Subsystem metric data assembly (MDA), with the notable exception of doppler frequency.[1]

Multimission Radio Science real-time display requirements were compared to planned Tracking System display capability; Radio Science requirements not satisfied by the planned Tracking System capability were as follows:

(1) Closed-loop radio metric data

Doppler frequency.

High-resolution graphical displays of all parameters.

(2) Open-loop radio science data

Spectrum displays of the open-loop receiver bandwidth.

To provide these capabilities, a phased implementation program was planned as follows:

Phase I: Provide doppler frequency and high-resolution graphical display of all closed-loop radio metric parameters.

Phase II: Provide spectrum displays of the open-loop receivers.

These phases are described in detail in Sections II and III, which follow.

II. Phase I — Real-Time Display of Closed-Loop Radio Metric Data

In Phase I, the following additional capability (to that already provided by the tracking system) will be made available to NOCC and Project Radio Science:

(1) Computation of doppler frequency. This will be performed in the tracking real-time monitor (RTM) of the NOCC Tracking Subsystem.

(2) High-resolution graphical display of radio metric closed-loop parameters. Graphical resolution will be approximately 240 X 640, full screen.

(3) Display channels. Three full (quad) channels will be made available for Radio Science displays. Current NOCC users of these channels will be supplied with single-channel, dual-format display devices.

Phase I implementation is scheduled to commence in October 1977 and is planned for delivery to operations in August 1978, in accordance with Voyager Radio Science requirements. Fig. 1 illustrates the Phase I functional data flow.

III. Phase II — Real-Time Display of Closed-Loop Radio Metric Data and Open-Loop Spectrum Data

Phase II of the Radio Science real-time display implementation provides the capability to display in NOCC and for Project Radio Science spectrum displays of open-loop receiver output, for the primary purpose of ascertaining signal presence in the open-loop receiver bandwidth during critical operations. Key to the Phase II implementation is the addition of a second Video Assembly Processor (VAP) and associated RAMTEK television distribution device, which will:

(1) Contain the necessary software to process and display the spectrum displays.

(2) Serve as a backup for the NOCC Display Subsystem.

Digitized spectrum displays from the Spectral Signal Indicator Assembly[2] of the Receiver-Exciter Subsystem will be provided to the Occultation Data Assembly (ODA) of the DSS Radio Science Subsystem, where the data will be formatted for immediate high-speed data (HSD) transmission to the NOCC. When received by the NOCC Display Subsystem, the data is prepared for display by software residing in the (second) VAP. It is expected that the capability will exist to update the spectrum displays as often as every 5-30 seconds. Phase II implementation is currently scheduled to commence in October 1978 and is planned for delivery on June 1, 1979. The goal is to have the capability available to support the Voyager second Jupiter occultation. Phase II functional data flow is seen in Fig. 2.

[1] DSN Network Operations Control Center (NOCC) validation and project navigation utilize doppler pseudoresiduals (actual-predicted doppler frequency) in place of doppler frequency.

[2] Originally implemented for use during the Pioneer Venus wind experiment.

Acknowledgments

I would like to thank H. W. Baugh, H. W. Cooper, E. Garcia, R. W. Tappan, and J. M. Williams for their participation in the feasibility studies which have resulted in the here described plan to provide radio science display capability.

Reference

1. Mulhall, B. D. L., "DSN Radio Science System Description and Requirements," in *The Deep Space Network Program Report 42-39*, pp. 119-129, Jet Propulsion Laboratory, Pasadena, Calif., June 15, 1977.

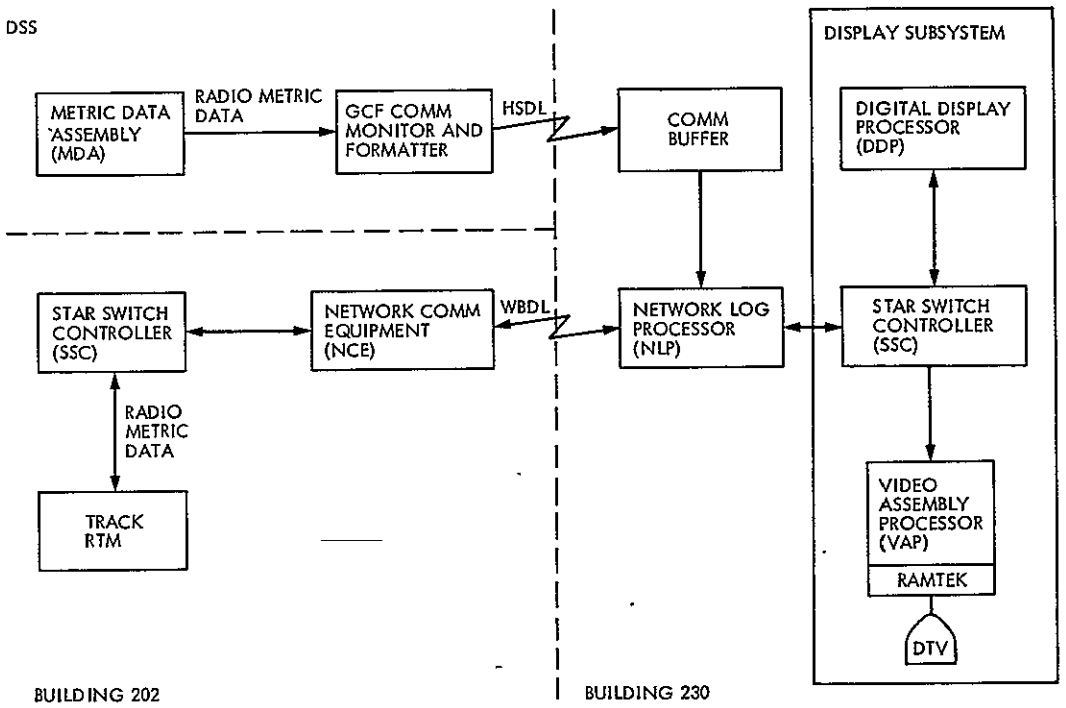

Fig. 1. DSN Radio Science System planned implementation Phase I: NOCC real-time display of closed-loop radio metric data

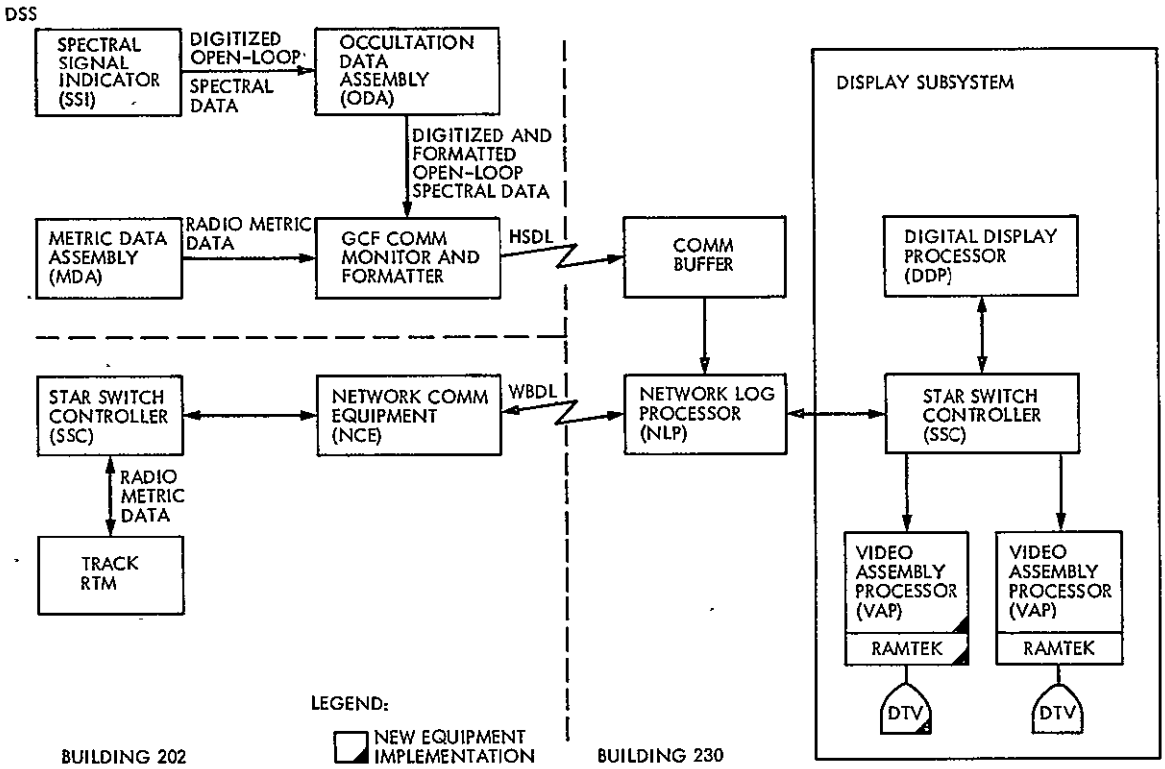

Fig. 2. DSN Radio Science System planned implementation Phase II: NOCC real-time display of closed-loop radio metric and open-loop spectrum data

D18

Dual-Frequency Feed System for 26-Meter Antenna Conversion

R. W. Hartop
Radio Frequency and Microwave Subsystems Section

New cassegrain feed cone assemblies are being designed as part of the upgrade of three 26-meter diameter antennas to 34-meter diameter with improved performance. The new dual-frequency feed cone (SXD) will provide both S- and X-band feed systems and traveling wave masers, with a reflex reflector system to permit simultaneous operation analogous to the 64-meter antennas.

I. Introduction

In order to extend the capabilities of a subnet of 26-meter antennas, it is planned to upgrade three stations to 34-meter diameter and generally improve their structural and microwave performance. The portion of this task that involves adding X-band receiving capability and improving the S-band feed performance in support of Voyager and later missions is described in this article.

II. SXD Cone Assembly

A new cassegrain feed cone assembly, designated the SXD cone (for dual S- and X-band), is being designed to replace the 15-year old S-band cassegrain monopulse (SCM) feed cone. The microwave design of the SXD cone is essentially complete and fabrication of components for the first cone (for DSS 12) is nearing completion. Assembly of the components into the cone shell is scheduled to commence not later than November 1977. Remaining design tasks involve support bracketry, cables, connector interfaces, and other details.

Figure 1 shows the basic layout of the major components within the SXD cone. The feeds are tilted toward each other to accommodate the reflex geometry. Above the large S-band horn will be mounted an ellipsoidal reflector that focusses the energy toward a dichroic plate above the X-band feed. The dichroic plate reflects S-band energy but is nearly transparent to X-band energy. Thus, the antenna will be capable of operating simultaneously at the two frequency bands in the same manner as the 64-meter antennas.

The S-band feed will contain two quarter-wave plate polarizers and three rotary joints so that complete polarization selectability will be available in the future as requirements arise. Present plans are to implement only a manually selected right- or left-hand circular polarization capability for the initial installation. Since no orthogonal-mode transducer is provided (space limitations prohibit its use without a new horn design), it will not be possible to receive two polarizations simultaneously as the 64-meter antennas are equipped to do. A diplexer and the necessary filtering and isolation is provided to permit simultaneous transmission of S-band uplink signals of 20 kW (up to 100 kW in the future).

The X-band feed is the same design as the XRO Mod II feed (Ref. 1), except that the mounting flange is adapted to the geometry of the SXD cone. This feed is capable of remote selection of either right- or left-hand circular polarization. There are no present plans for an X-band uplink on the 26- or 34-meter antennas.

Table 1 presents the design requirements for the SXD cone assembly. It is anticipated that all requirements will be met. Testing of the completed cone assembly is scheduled for the second quarter of 1978. Two more SXD cones for Australia (DSS 44) and Spain (DSS 62) will be fabricated and assembled to complete the subnet in 1979.

Reference

1. Hartop, R. W., "Selectable Polarization at X-Band," in *The Deep Space Network Progress Report 42-39*, pp. 177-180, Jet Propulsion Laboratory, Pasadena, Calif., June 15, 1977.

Table 1. SXD cone assembly design requirements

Parameter	S-band		X-band
	Transmit	Receive	Receive
Frequency, MHz	2110 ±10	2285 ±15	8420 ±20
Gain, dBi	55.3 ±0.7	$56.1^{+0.3}_{-0.9}$	$66.9^{+0.3}_{-0.9}$
System Noise Temperature, K	–	27.5 ±2.5[a]	25.0 ±3.0

[a]With diplexer, 21.5 ±2 5K in receive-only mode.

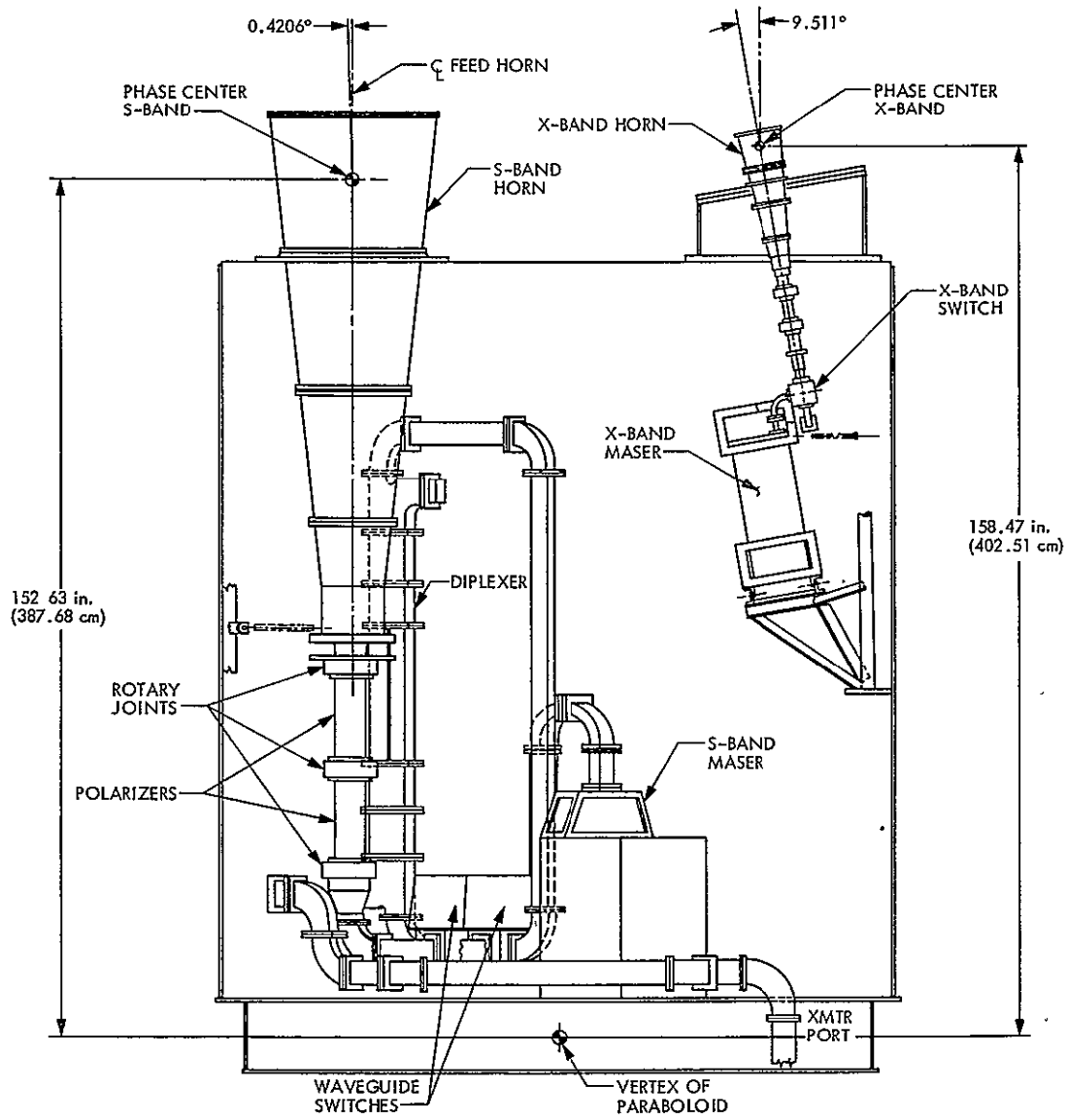

Fig. 1. SXD cone assembly layout

Intermodulation Components in the Transmitter RF Output Due to High Voltage Power Supply Ripple

E. J. Finnegan
Radio Frequency and Microwave Subsystems Section

A study was conducted to determine if it would be economically feasible to eliminate the 400-Hz motor-generator sets used to provide power to the high-voltage power supplies of the 20-kW transmitters and replace them with a 60-Hz high-voltage power supply. The efficiency of a power supply that runs from the 60-Hz line directly would pay for itself in about seven years and could be designed so that the transmitter would meet all the incidental phase and amplitude modulation specifications.

I. Introduction

A study was conducted to determine if it would be economically feasible to eliminate the 400-Hz motor-generator (MG) sets used to provide power to the high-voltage power supplies of the 20-kW transmitters and replace them with a 60-Hz high-voltage power supply. After the data were analyzed and it was determined that the payoff point would be seven years, the question came up as to what the intermodulation components would be due to the ripple voltage of the new 60-Hz power supply. This article covers the question of modulation in the radiated output of the transmitter that may be introduced if the 400-Hz motor-generator was replaced with a single 60-Hz power supply excited from the main power line.

II. Conclusion

It was determined by cost analysis that it takes seven years to break even when the single 60-Hz power supplies replace the present 400-Hz MG set and high-voltage power supply. It may be noted in the data below that the low-frequency components have the larger ripple voltages. This is caused by the rotating machinery which would be automatically eliminated by the new 60-Hz power supplies.

III. Power Supply Design

The amplitude of ripple on the high-voltage power supply is what determines the amount of amplitude and phase modulation on the transmitters RF output; the ripple frequencies also determine the demand placed on the high-voltage power supply filter system. This ripple voltage is impressed directly on the klystron which in turn causes the beam voltage to rise and fall at the ripple amplitude, resulting in amplitude modulation. Also, the higher and lower voltage causes the electron beam to change in velocity, thus causing phase modulation (PM). The power supply can be designed using a three-phase full-wave bridge; this produces a 360-Hz ripple frequency. However, a better arrangement would be to wind the transformer so that it looks like a six-phase circuit; this would double the ripple frequency (720 Hz). The new power supply filter would be designed to have a cutoff frequency of approximately 20 Hz that is low enough to attenuate any 60-Hz frequencies and reduce any strong modulations to negligible amounts.

IV. DSN Survey

The DSN was surveyed to determine what the ripple voltages were throughout the DSN in order to check the modulation components in the transmitted RF. The specification for AM and PM modulation for the 20-kW transmitter calls for incidental phase modulation to be less than 1 degree rms and incidental amplitude modulation to be 60 dB below the main carrier. The ripple frequency and amplitude as reported from the DSN stations are listed below.

DSS	Ripple frequency, Hz	Peak-to-peak ripple amplitude
44	20	18
44	2400	4
62	20	20
62	2400	Negligible
63 & 61	2400	Negligible
42	20	16
42	2400	Negligible
43	20	5
43	2400	Negligible

V. Calculations

The calculations for determining incidental amplitude and phase modulation are shown below.

A. Amplitude Modulation Calculations

The total AM power in the sideband is expressed by the formula

$$P_0 = 20 \log_{10} \frac{0.8V_0}{V_r}$$

where

V_0 = beam voltage

V_r = beam ripple voltage in rms

Out specification calls for 60 dB or more below the carrier; this would calculate out to $16V_r$ or less.

B. Phase Modulation Calculation

The formula for calculating phase modulation (that is, the phase change with respect to the average phase) is

$$\frac{\Delta\theta}{\theta} = \frac{1}{2}\frac{\Delta V_0}{V_0}$$

or

$$\frac{\Delta\theta}{\theta} = \frac{\Delta V_0}{2V_0}$$

where

θ = electrical length of tube

At 18 kV (which is approximately 20 kW), the phase length is 45.81 radians for the 20-kW tube or 2620.0 degrees. This would calculate out to be 0.07291 deg/volt. The specification is a maximum of 1.0 degree rms phase modulation. In terms of power supply ripple voltage, this would be 13.8 volts rms (39 V p-p) or less in order to meet the specification.

VI. Summary

As can be seen, the present specification is adequate to cover the new power supply, and there should be no problem in meeting the specification and reducing the energy consumption.

It may also be noted that the incidental modulations caused by power supply ripple can be predicted mathematically if the ripple components are known.

P20

Measurement of Klystron Phase Modulation Due to AC-Powered Filaments

E. J. Finnegan
Radio Frequency and Microwave Subsystems Section

This article shows the experiment that was conducted in order to determine the intermodulation components in the RF spectrum of the S-band radar transmitter generated by having the klystron filaments heated by 400-Hz AC power.

I. Introduction

The klystron manufacturer recommended changing the filament power of the klystron on the high-powered transmitter from DC to AC to increase the filament/cathode life. Before proceeding it had to be decided if the AC filament excitation would be reflected in the RF output as incidental phase modulation (IPM), and, if so, would it degrade the RF spectrum.

II. Conclusion

When the klystron is being operated with 400-Hz (AC) on the filament, the IPM is buried in the 400-Hz equipment interference noise. The modulation sidebands were separated and identified and found to be −67 dB below the main carrier. This is well below the transmitter specifications, and operating the filaments on AC would not degrade the spectrum to where it would be detrimental to the radiated RF.

III. Measurement Technique

The technique used for measuring the phase modulation sideband was to use a double balanced mixer as a phase comparator to cancel out the IPM from the exciter. A sample of the drive (using a directional coupler) to the klystron was connected to the LO port of the mixer and a sample of the klystron output was connected to the RF port. A double balanced mixer (DBM) was used in order to increase the isolation between the LO and RF inputs. An inherent characteristic of a DBM is that the IF point is DC-coupled to the diodes. This means that the frequency response is from DC to some very high frequency, which lends itself to be used as a phase detector needed to detect the (400-Hz) filament frequency.

This phase-modulated frequency spectrum was then measured and displayed on a frequency analyzer that is capable of determining both the frequency and amplitude of the modula-

tion. It was very difficult to detect the phase modulation of the filaments because it was buried in the noise caused by the 400-Hz rotating machinery. The solution for this was to excite the filaments with a variable frequency source; this separated and identified the phase modulation generated by the filament power.

The second problem was that the frequency source used to drive the klystron did not have the frequency stability needed. It was found in earlier experiments that the generator used was too unstable to be detected by the spectrum analyzer. That is, after the frequencies were beat together, the difference frequency was moving too fast for the analyzer to capture and present on the scope. A frequency synthesizer, which has a high degree of stability, was used in order to stabilize the difference frequency. When these two problems were resolved, the experiment progressed smoothly.

IV. Equipment Setup

The equipment was arranged as shown in Figs. 1 and 2 with the frequency source being stabilized by a synthesizer. The RF mixer was connected as shown in Fig. 2 and the phase shifter was adjusted for zero volts DC. This configuration canceled all IPM frequencies except those generated from within the klystron itself. The variable frequency source was connected to the klystron filaments and set to approximately 380 Hz and 430 Hz in order to verify that the modulation observed with the spectrum analyzer was indeed generated by the filament. Shifting the frequency proved the modulation in the RF output was caused by the AC on the filaments. The filament IPM was 3.5 dB lower than the system 400-Hz noise. Figures 3 and 4 show the filament frequency at 426 Hz and 386 Hz, respectively. These recordings are graphs plotted from the spectrum analyzer.

V. Calculations and Results

Figures 1 and 2 show the equipment set up as the experiment was performed at DSS 13. Figures 3, 4, and 5 show the frequency spectrum as indicated by the spectrum analyzer. The bandwidth on Figs. 3 and 4 is 0 to 500 Hz and 0 to 1000 Hz in Fig. 5. As indicated above, Figs. 3 and 4 show the phase modulation from the filaments; Fig. 3 is with the filament power at 426 Hz and Fig. 4 at 386 Hz. Figure 5 expands the scale to 1000 Hz; as can be seen, the second harmonic (855 Hz) due to the filament excitation is present. It may be noted that when the filaments are excited by 400 Hz (as is normal in operation) the phase modulation would be buried in the system noise and therefore not obvious.

The equipment was adjusted in the following manner. The phase shifter was adjusted through 180 degrees and the DC shift was ±0.3 volts DC; it was then adjusted for zero volts. The spectrum analyzer was adjusted so that the indication presented on the scope recorded modulation below 0.1 volt. For instance, Fig. 3 shows the phase modulation due to the filaments to be −57.7 dB. This would be 57.7 dB below 0.1 volt. Therefore, if the maximum excursion on the S-curve is 0.3 volt, the phase modulation due to the filaments would be

$$dB_t = 20 \log \frac{0.3}{0.1} + (57.7) = 67.24 \text{ dB}$$

below the carrier. The second harmonic generated by the filament power would be 75.1 dB.

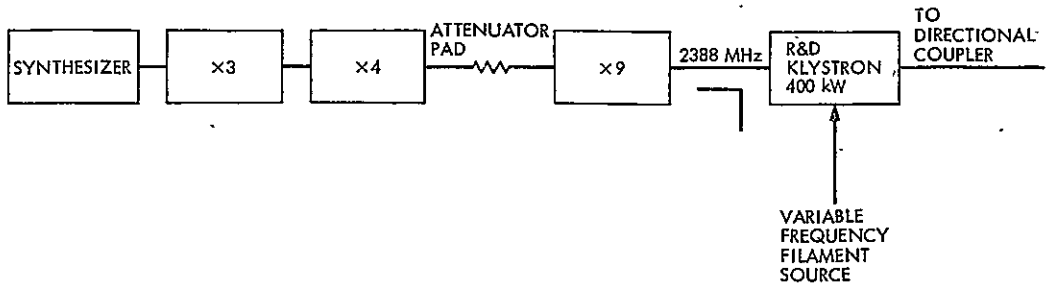

Fig. 1. RF drive chain

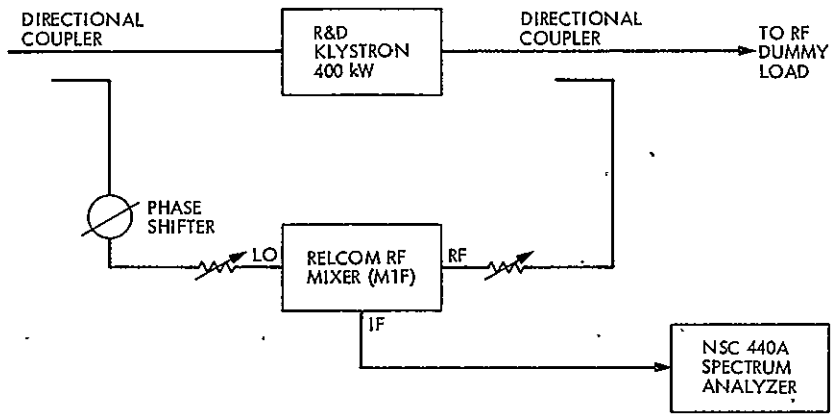

Fig. 2. Intermodulation setup

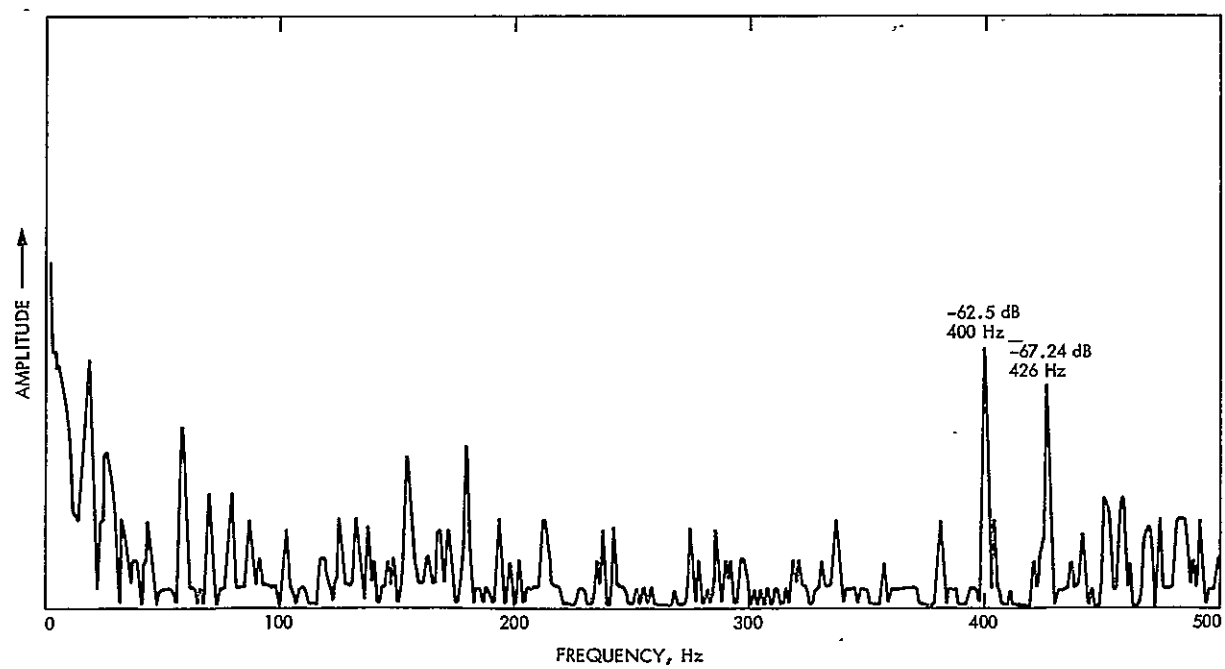

Fig. 3. Modulation due to AC filaments at 426 Hz

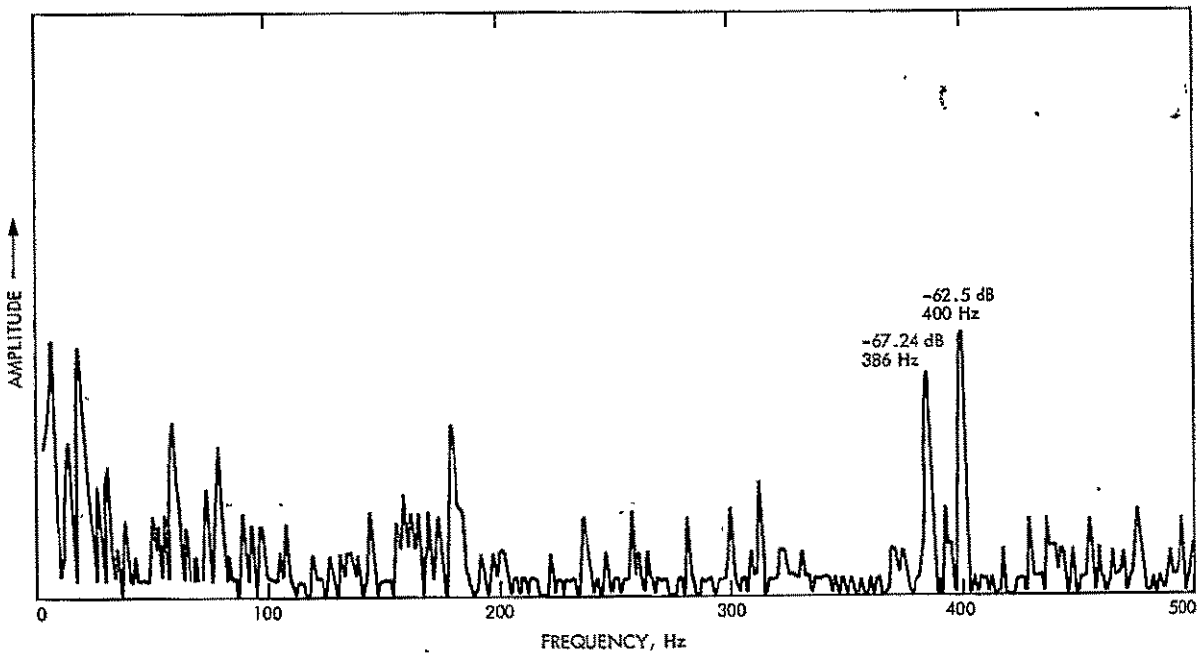

Fig. 4. Modulation due to AC filaments at 380 Hz

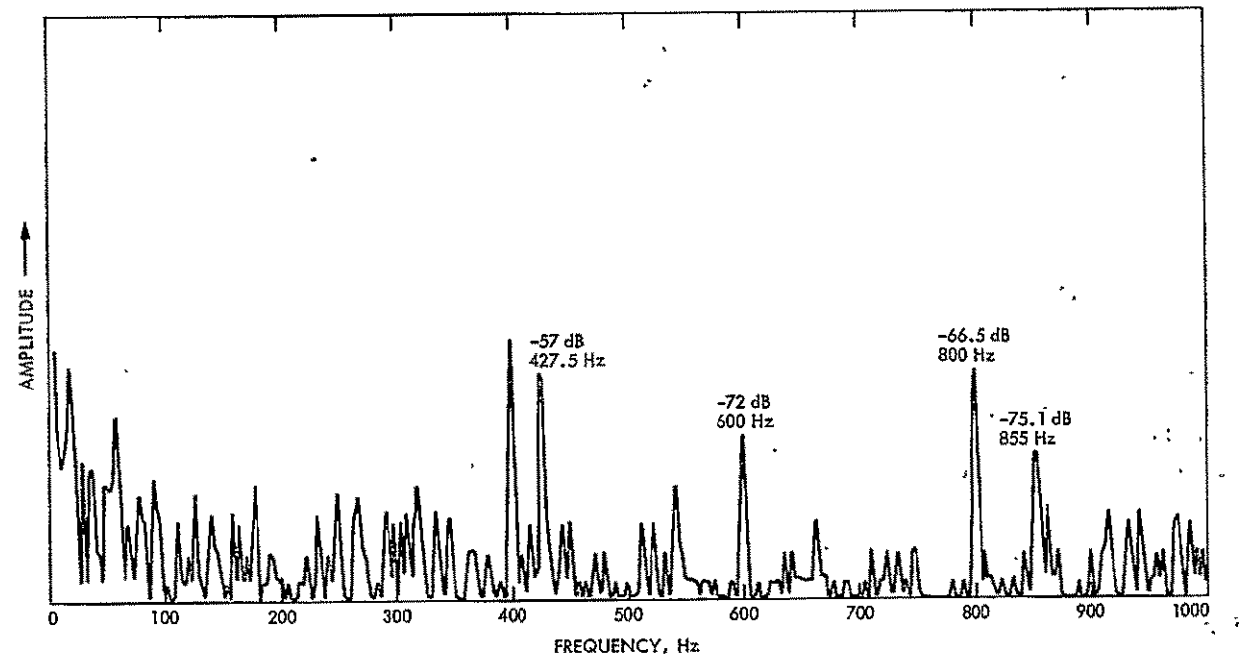

Fig. 5. Second harmonic modulation due to AC filaments (855 Hz)

D621

Comparative Thermodynamic Performance of Some Rankine/Brayton Cycle Configurations for a Low-Temperature Energy Application

F. L. Lansing
DSN Engineering Section

Various configurations combining solar-Rankine and fuel-Brayton cycles were analyzed in order to find the arrangement which has the highest thermal efficiency and the smallest fuel share. A numerical example is given to evaluate both the thermodynamic performance and the economic feasibility of each configuration. The solar-assisted regenerative Rankine cycle was found to be leading the candidates from both points of energy utilization and fuel conservation.

I. Introduction

In an effort to increase the thermal efficiency of power cycles driven by solar energy, the concept of a regenerative solar-assisted Rankine cycle was recently introduced. The main feature of this concept is that the heat addition in the cycle is made along a constant pressure close to atmospheric, by two heat reservoirs. Water is used as the working medium. The first heat reservoir is essentially a solar collector/boiler which supplies sufficient energy to convert liquid water to dry saturated steam, i.e., supplies a little more than the latent heat of vaporization. The evaporation temperatures are consistent with the capability of low concentration ratio collectors and range from 90°C to 160°C. The second heat reservoir is a high-temperature source of energy such as that obtained from fossil fuel combustion. This will superheat the steam, before expansion in the turbine, to a very high temperature comparable to that used in conventional power plants. The fraction of total heat input in the cycle provided by the second heat reservoir ranges from 20 to 25% as reported in Refs. 1 and 2. Since the working pressures of the cycle, the evaporation and condensation pressures, are close to each other in this case, the condition of steam leaving the turbine is still at a high superheat temperature and can be further exploited by adding regenerators to the cycle. Regenerators are favored when a thermal potential difference exists between turbine exhaust and feed water temperatures since they improve the cycle efficiency without affecting the net work output.

The regenerative solar-assisted Rankine cycle has a much higher thermal efficiency (about double) than its comparable

simple 100% Solar Rankine. It will be compared in performance with other dual cycles for the selection of the optimum cycle configuration.

II. Fuel Utilization Versus Fuel Conservation

Several inquiries were raised during the early stages of study about whether or not the solar-assisted cycle is superior from the viewpoints of fossil fuel conservation, "best" fuel utilization or economic feasibility. The inquiry about fuel conservation was made since the thermodynamic cycle requires that a fraction of its total energy input (20-25%) be from fossil fuel. If the cost of fuel keeps on rising with current inflation rates, the selection of a fuel-powered system, based on efficiency superiority alone, might be outweighed by less efficient systems that have lesser or no dependence on fossil fuel.

On the other hand, if the concept of partial assistance by fossil fuel in a cycle was accepted, then the next inquiry would be to look into how "well" the fuel was utilized. Figure 1 shows two different schemes in which both solar energy and fossil fuel are used via power cycles. Both schemes take in the same quantities of solar or fuel energy. The first scheme is composed of two physically separate cycles: a 100% fuel-powered, high-temperature Brayton cycle and a 100% solar-powered low-temperature Rankine cycle. The second scheme is the regenerative solar-assisted Rankine cycle. The choice of the Brayton (Joule) cycle for coupling with the Rankine one was based on the fact that the Brayton cycle is composed of two isobars (constant pressure processes) and two isentropics (constant entropy processes) which makes it convenient in matching the border lines of the two cycles. The analysis is seeking the answer to which of these two schemes is more efficient, i.e., conserving energy by producing the same output work from less input heat.

It should be borne in mind that purchasing electric power directly from a utility company is equivalent in principle to utilizing the fossil fuel via a Brayton cycle, and, if combined with a solar-thermal plant, will be treated as a combined scheme in which both solar and fossil fuel participated by unequal shares in the production of the net work as in Fig. 1a.

III. Main Assumptions

In the next comparative analysis between different configurations of the Brayton/Rankine cycles, the main assumptions and idealizations are made as follows:

(1) The working fluid is water.

(2) Operation will be on clear days only, when the sun is available and able to provide the required quantities of heat to run the system efficiently. No allowance for partial shading due to clouds or any unexpected side effects which hinders a full load operation of a 100% solar-powered Rankine cycle.

(3) All processes are reversible. The sources of irreversibilities in compression and expansion processes are assumed to change the thermal efficiency in each configuration with almost an even hand. This means that the descending order of thermal efficiency of the different configurations under study will be assumed to be unchanged when irreversibilities due to friction or turbulence do occur.

(4) All heat exchangers, whether they are recuperatois or regenerators, are adiabatic and ideal, i.e., have a 100% effectiveness.

(5) Both Brayton and Rankine cycles are operating at the same pressure limits in all configurations. The low pressure limit is usually determined by the cooling medium temperature. For example, a sink temperature ranging from 20°C (86°F) to 50°C (122°F) will correspond to a pressure range from 0.23 to 1.24 N/cm^2, respectively. On the other hand, the high pressure limit is determined by the ability of the solar collector to evaporate water into steam. An evaporation temperature ranging from 90°C to 160°C will correspond to a saturation water pressure ranging from 7 to 60.78 N/cm^2, respectively.

(6) Both cycles are chosen to have one common border line (or one common process) in the property diagram. This border line is the isentropic (reversible adiabatic) expansion in the Rankine cycle turbine, and it also represents the isentropic compression in the Brayton cycle compressor. The two mechanical components, the turbine and the compressor, have to be physically separate to identify the sequence of events in each cycle. However, because of their equal but opposite action along the border line, their combined effect, from a thermodynamics viewpoint, has zero energy exchange with the surroundings, i.e., a null effect and could be later dropped for simplicity.

IV. Cycle Configurations

Four configurations, using various combinations of the Rankine cycle and the Brayton cycle, were adopted for this study:

(1) A simple Rankine cycle and a simple Brayton cycle (two separate cycles).

(2) A simple Rankine cycle and a regenerative Brayton cycle (two separate cycles).

(3) A regenerative Rankine cycle and a regenerative Brayton cycle (two separate cycles).

(4) A combined regenerative Rankine and Brayton cycle (one cycle). This is called the "solar-assisted Rankine cycle."

Each of these configurations is explained in detail below.

A. Configuration 1

This configuration consists of two separate cycles: a simple Rankine cycle and a simple Brayton cycle. The flow diagram is shown in Fig. 2, and the cycles are presented on the temperature-entropy (t-S) diagram for water in Fig. 3. The simple Rankine cycle is started by extracting the condensate from the condenser well (state 1), and pumping it to the boiler (state 2). The heat added to the Rankine cycle is by means of a set of solar collectors for all three stages: sensible heating from state 2 to 3, evaporation from state 3 to 4, and a small amount of superheat from state 4 to 5. The small superheat portion is needed only to provide adequate comparison with other configurations on an equal basis and to avoid the presence of any wet steam in the matched Brayton cycle. State 5 is chosen such that, if followed by an isentropic expansion in the turbine, it will end up with state 6 as a dry and saturated condition. In the Brayton cycle, the heat is added entirely by combustion of any kind of fossil fuel. The cycle is working between the same solar-boiler pressure P_B and the Rankine cycle condenser pressure P_c. Superheated (or at least dry saturated) steam is the condition of the working fluid throughout the cycle. The obedience of superheated steam to ideal gas relations at low pressures and high temperatures makes the Brayton cycle in this case very close to an ideal-gas Brayton cycle. Dry and saturated steam (state a) is compressed isentropically in a compressor to state b. The fuel heat addition is followed to superheat to state c at constant pressure. An expansion in the turbine from state c to d and a heat rejection from state d to a will complete the cycle. It is important to note that the position restrictions made on state a and on the process a→b are artificial and do not necessarily represent all possible cycle positionings with respect to each other as indicated in assumption (6).

The total heat input to configuration 1 is determined by the area 1-1-2-3-4-5-c-d-k-1 in Fig. 3 which is the sum of the heat added by the sun (area i-1-2-3-4-5-j-i) and the heat added by the fuel (area j-b-c-d-k-j). The heat rejected is the sum of two parts: the part rejected from the Rankine cycle condenser (area i-1-6-j-i) and that rejected from the Brayton cycle cooler (area j-a-d-k-j). The net work done is the loop area shaded 1-2-3-4-5-c-d-a-1.

Figure 4 shows another way of doing configuration 1 with less mechanical components. The Rankine-turbine/Brayton-compressor connection is deleted, thus leaving the configuration identical to a simple, extra superheated Rankine cycle with two heat exchangers for heat addition and two heat exchangers for heat rejection. The configuration presented in Fig. 4 is totally equivalent, from a thermodynamics viewpoint, to that presented in Fig. 2.

B. Configuration 2

This configuration consists of two separate cycles: a simple Rankine cycle, as in configuration 1, and a regenerative Brayton cycle to improve the simple Brayton cycle of configuration 1. The flow diagram is sketched in Fig. 5 and the cycles are presented on t-S diagram for water in Fig. 6. The regenerator is working under a temperature potential difference $(t_d - t_b)$. In Fig. 6 the areas under the lines $\overline{be}$ and $\overline{df}$ are equal and according to assumption (4), the temperatures t_e and t_f are equal to t_d and t_b, respectively.

With the common process between the two cycles; the process from state 5 to 6 or from state a to b, the net work output in configuration 2 is *unchanged* compared to configuration 1 and is equal to the loop area 1-2-3-4-5-c-d-a-1. On the other hand, the total heat added in configuration 2 is reduced by the hatched area under line $\overline{be}$ as compared to configuration 1 due to the regeneration action. The result is a higher thermal efficiency for configuration 2 compared to configuration 1, provided that the temperature potential difference $(t_d - t_b)$ is positive.

C. Configuration 3

This configuration is one step forward in improving the efficiency of configuration 2 and is illustrated in Figs. 7 and 8. First, the regenerator in the Brayton cycle of configuration 2, given the name regenerator 1 in Fig. 8, is kept intact. Second, the superheated steam leaving the Brayton turbine at state f is still at a high-temperature potential that offers some energy savings if coupled with the Rankine cycle. The following two extra generators are used in the Rankine cycle:

(1) A vapor-vapor regenerator, given the name regenerator 2 in Fig. 8, in which the superheat energy needed from state 4 to 5 is provided by cooling from state f to g in Fig. 7. According to assumption (4), the areas in Fig. 7 under lines $\overline{fg}$ and $\overline{45}$ are equal and the

temperatures t_f and t_4 are equal to t_5 and t_g, respectively.

(2) A vapor-liquid regenerator, given the name regenerator 3 in Fig. 8, in which the sensible heat needed from state 2 to 3 is provided by cooling from state g to a. According to assumption (4), the areas in Fig. 7 under lines $\overline{ga}$ and $\overline{23}$ are equal and the temperatures t_g and t_1 ($\simeq t_2$) are equal to t_3 and t_a, respectively.

In this configuration, the net work output is still the same as in configurations 1 and 2, and is equal to the closed loop area 1-2-3-4-5-c-d-a-1. The heat addition in configuration 3, on the other hand, is different from both configurations 1 and 2. For the Rankine cycle, the heat is added only from state 3 to 4, i.e., the latent heat of vaporization part, and for the Brayton cycle, the heat is added only from state e to c. The sum of heat added to both cycles in this configuration is less than the heat added in configuration 2. The difference in heat addition is represented in Fig. 7 by the area under line $\overline{fa}$. The conclusion that can be made accordingly is that the thermal efficiency of configuration 3 is higher than that for configuration 2 which in turn is higher than the efficiency of configuration 1. The superiority of configuration 3 over configuration 1 is established by the fact that the heat rejection process from state d to a in the cooler is replaced entirely by three regenerators: (1) a part from d to f for regeneration from b to e in regenerator 1, (2) a part from f to g for regeneration from 4 to 5 in regenerator 2, and (3) a part from g to a for regeneration from 2 to 3 in regenerator 3.

D. Configuration 4

This configuration is identical from a thermodynamics viewpoint to configuration 3 but has less components to operate with. The configuration is sometimes called a "solar-assisted regenerative Rankine cycle" since it is not 100% powered by the sun. The Rankine-turbine/Brayton-compressor connection of configuration 3 is omitted and regenerators 1 and 2 are replaced by one regenerator doing their function exactly. The flow diagram for configuration 4 is presented in Fig. 9, and the thermodynamic cycle on the t-S diagram is identical to that illustrated in Fig. 7 except that the common process a→b or 5→6 is omitted. This configuration possesses the same high thermal efficiency of configuration 3 and is, therefore, superior to configurations 1 and 2.

V. Numerical Comparison of the Four Configurations

To calculate the efficiency and energy savings in the different configurations and the order of efficiency improvement in each case, a numerical comparison is set based on the following conditions:

(1) Maximum Brayton cycle temperature (t_c) 600°C.

(2) Condenser temperature 50°C.

(3) Condenser pressure 1.24 N/cm^2.

(4) Solar boiler evaporation temperature 100°C.

(5) Evaporation pressure 10.13 N/cm^2.

(6) Compression and expansion processes are isentropic.

(7) Heat exchangers are 100% effective.

(8) Neglect the pump work from state 1 to 2.

The numerical results of the various configurations are listed in Table 1. Also, a plot of the efficiency of each configuration against the percentage of the fuel share in each is illustrated in Fig. 10. The following remarks can be made from Table 1 and Fig. 10:

(1) The simple 100% solar-powered Rankine cycle gave a thermal efficiency of 14.43% as compared to 37.87% for the simple 100% fuel-powered Brayton cycle. This is mainly due to the large difference in heat source temperature of the solar-Rankine cycle (taken at 100°C in the example) compared with the fuel-Brayton cycle (taken at 600°C in the example). The lowest sink temperature in both cycles was the same at 50°C. On the other hand, the specific steam consumption (the amount of steam in kg needed to produce 1-kWh output at the turbine shaft) is 8.96 kg/kWh for the simple Rankine cycle versus 13.44 kg/kWh for the simple Brayton cycle. Small specific steam consumption means small size plant for the same power output and low maintenance cost.

(2) Configuration 1, which is a straightforward combination of the two simple Rankine/simple Brayton cycles, yielded a thermal efficiency of 19.19% with a partial assistance of the fuel in the heat input of 20.26%. The specific steam consumption dropped to 5.37 kg/kWh$_e$, which favors the combination of the Rankine/Brayton cycles for plant compactness.

(3) Configuration 2, which is a combination of the simple Rankine and the regenerative Brayton, showed a slight improvement of the thermal efficiency (19.40% versus 19.19% for configuration 1). The percentage improve-

ment in efficiency can be greater if the temperature difference for regeneration [$(t_d - t_b)$ in Fig. 6] was made larger at different working conditions. Note that the specific steam consumption was the same in configurations 1 through 3.

(4) The efficiency superiority of configuration 3 over the other configurations can be analyzed in conjunction with Fig. 1 as follows:

If two separate cycles, as shown in Fig. 1, were constructed such that they take in the same quantities of solar and fuel heat as those of configuration 3, the solar heat (77.1 units) is added to a 100% solar-powered Rankine cycle whose efficiency is 14.43% (case 1 in Table 1), and the fuel heat (22.9 units) is added to a 100% fuel-powered Brayton whose efficiency is 37.86% (case 2 in Table 1), the resulting net work output would be $\{(0.1443 \times 77.1) + (0.3786 \times 22.9)\}$, i.e., 19.80 units only. The latter is less than 22.90 units for configuration 3 with the same energy shares. The result is that configuration 3 (or identically configuration 4) will rank second to the 100% fuel-powered Brayton in energy conservation only. However, from the point of "fossil fuel" conservation, the answer is not definite at this stage.

VI. The "Economic Feasibility Ratio"

In order to establish the economic feasibility of each of the above configurations, a rough estimate is needed of the cost of heat energy input and the mechanical energy output. If X\$ is the cost of one energy unit (kWh_t) from a solar collection system, Y\$ is the cost of the same unit from fuel combustion, and Z\$ is the cost of electricity unit (as purchased from a utility company), the cost of input and output energy can be listed as in Table 2. An "Economic Feasibility Ratio" (EFR) can then be introduced as an indication of the size of payback period of the money invested in such energy utilization plants. The EFR is here defined as the cost of input heat energy to the cost of output mechanical energy. Higher EFR values means higher installation and operation cost than the cost savings (for a consumer) or the profit (for a utility company) of the mechanical energy output. The ratio (EFR) will reach unity if the costs were integrated over the payback period of the invested money. However, a nonintegrated value (or instantaneous value) of the EFR leads to a small payback period and a direction towards economic feasibility.

A rough estimate of the cost/kWh_t of solar heat could be found from the loan payment to cover the solar equipment divided by the heat collected during the payment period, which will be taken as the life period of the equipment. For example, to yield a 100°C boiling temperature, at good collector efficiency, a low concentration ratio collector that costs approximately \$150/m^2 (1977 price) is needed. The collector is capable of collecting a daily average of about 4 kWh_t/m^2 for a full year in a city like Los Angeles. If approximately three times the collector cost is needed for the whole installation (to include pipework, storage tanks, land cost, etc.) with a life period of 15 years, and an interest on the borrowed money of 8%, then the cost/kWh_t will be:

$$X = \frac{1.752 \times 150 \times 3}{4 \times 365 \times 15} = 3.6¢/kWh_t$$

which will be rounded off to $4¢/kWh_t$. The cost of gaseous fossil fuels alone, such as natural gas, propane etc., can be taken as $1.2¢/kWh_t$ and adding the cost of the equipment that goes with it, the cost Y may be taken as $2¢/kWh_t$. The cost of purchased electricity is taken roughly as $5¢/kWh_e$. In Table 2, the EFR is calculated for each configuration with these estimated costs. The 100% fuel-powered Brayton cycle has the least payback period, followed by the solar-assisted regenerative Rankine (case 5, Table 2), and the last in the list of economic feasibility is the simple 100% Rankine (case 1, Table 2). On the other hand, from the fuel conservation point of view, the 100% solar-powered with 0% fuel share is leading the list. The three Rankine/Brayton configurations follow with close boundaries of fuel share (19.4→22.9%), and tailing the list is the 100% fuel-powered Brayton cycle. The final selection of the "best" configuration combining both fuel conservation and energy utilization points, depends of course on the rate of escalation of X, Y, and Z.

VII. Summary

Various configurations combining solar-Rankine and fuel-Brayton cycles were studied in order to find the arrangement which has the highest thermal efficiency and the smallest fuel share. The solar-assisted regenerative Rankine cycle was leading the candidate configurations in this respect.

A simple criterion was defined for comparing the economic feasibility of each configuration, and a simple numerical example was given. Again, the solar-assisted regenerative cycle was found leading the other configurations in having a short payback period.

References

1. Lansing, F. L., "Computer Modelling of a Regenerative Solar-Assisted Rankine Power Cycle," *The Deep Space Network Progress Report 42-37,* pp. 152-168, Jet Propulsion Laboratory, Pasadena, Calif., Feb. 15, 1977.

2. Curran, H. M., and Miller, M., "Evaluation of Solar-Assisted Rankine Cycle Concept for the Cooling of Buildings," *Intersociety Energy Conversion Engineering Conference Record,* pp. 1391-1398, 1975.

Table 1. Numerical comparison of various Rankine/Brayton configurations

Case	Configuration description	Turbine work, Wh/kg	Compression work, Wh/kg	Net work output, Wh/kg	Heat Added, Wh/kg	Thermal efficiency, %	Specific steam consumption, kg/kWh	Fuel share in total heat input, %	Regeneration present
1	Simple Rankine 100% solar-powered (1-2-3-4-5-6-1 in Fig. 3)	111.6	0.02	111.6	773.2 (Solar)	14.43	8.96	0	No
2	Simple Brayton 100% fuel-powered (a-b-c-d-a in Fig. 3)	186.0	111.6	74.4	196.5 (Fuel)	37.86	13.44	100	No
3	Configuration 1 Combined simple Rankine/simple Brayton (Figs. 2, 3, & 4)	297.7	111.6	186.1	969.7 (773.2 Solar + 196.5 Fuel)	19.19	5.37	20.26	No
4	Configuration 2 Combined simple Rankine/regenerative Brayton (Figs. 5 & 6)	297.7	111.6	186.1	959.3 (773.2 Solar + 186.1 Fuel)	19.40	5.37	19.40	Yes
5	Configuration 3 Combined regenerative Rankine/ regenerative Brayton (Figs. 7, 8, & 9)	297.7	111.6	186.1	812.7 (626.6 Solar + 186.1 Fuel)	22.90	5.37	22.90	Yes

Table 2. Economic feasibility of various Rankine/Brayton Configurations

Case	Cost of energy added (1)	Cost of energy produced (2)	EFR* $\frac{(1)}{(2)}$
1	$100\,X$	$14.43\,Z$	5.54
2	$100\,Y$	$37.86\,Z$	1.06
3	$79.74\,X + 20.26\,Y$	$19.19\,Z$	3.75
4	$80.60\,X + 19.4\,Y$	$19.40\,Z$	3.72
5	$77.1\,X + 22.9\,Y$	$22.90\,Z$	3.09

*Calculated for $X = 4¢$, $Y = 2¢$ and $Z = 5¢$ per kWh.

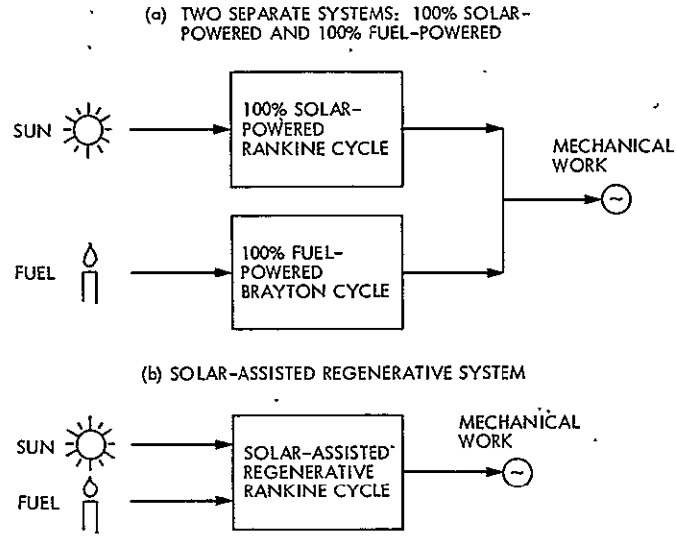

Fig. 1. Comparison between two systems

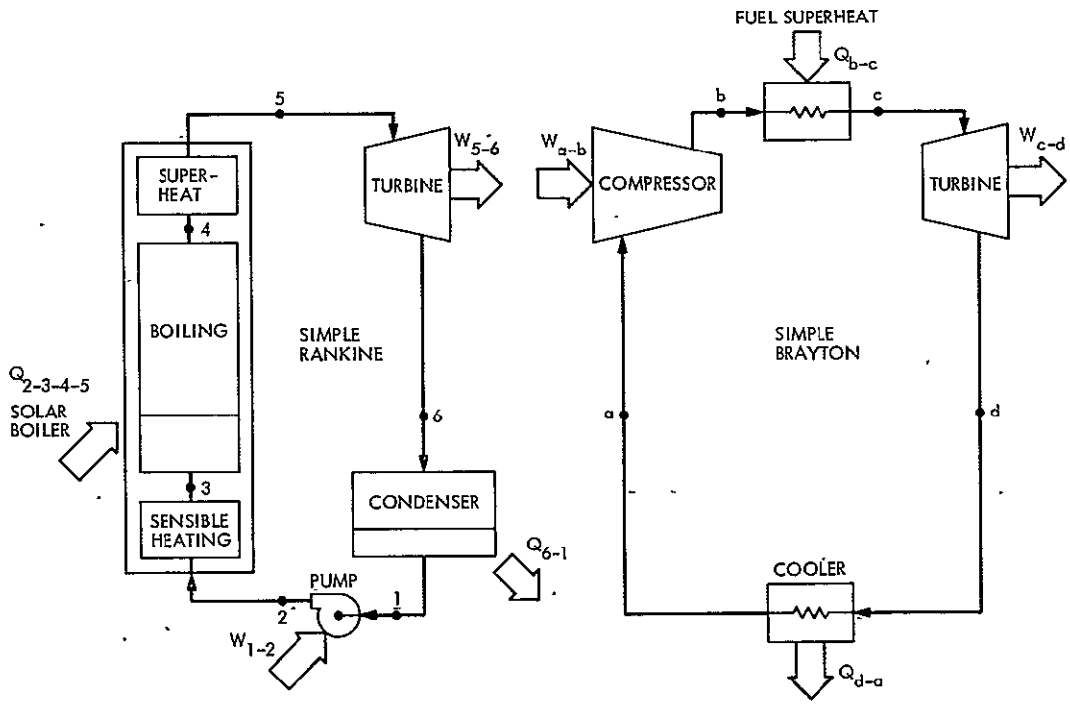

Fig. 2. Flow diagram of configuration 1: two physically separate cycles with common states 5 = b and 6 = a

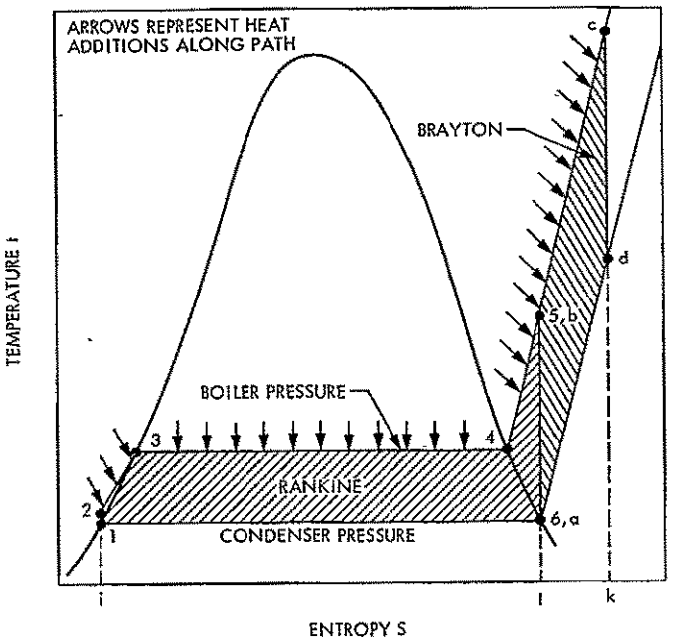

Fig. 3. Configuration 1 plotted on temperature-entropy diagram for water

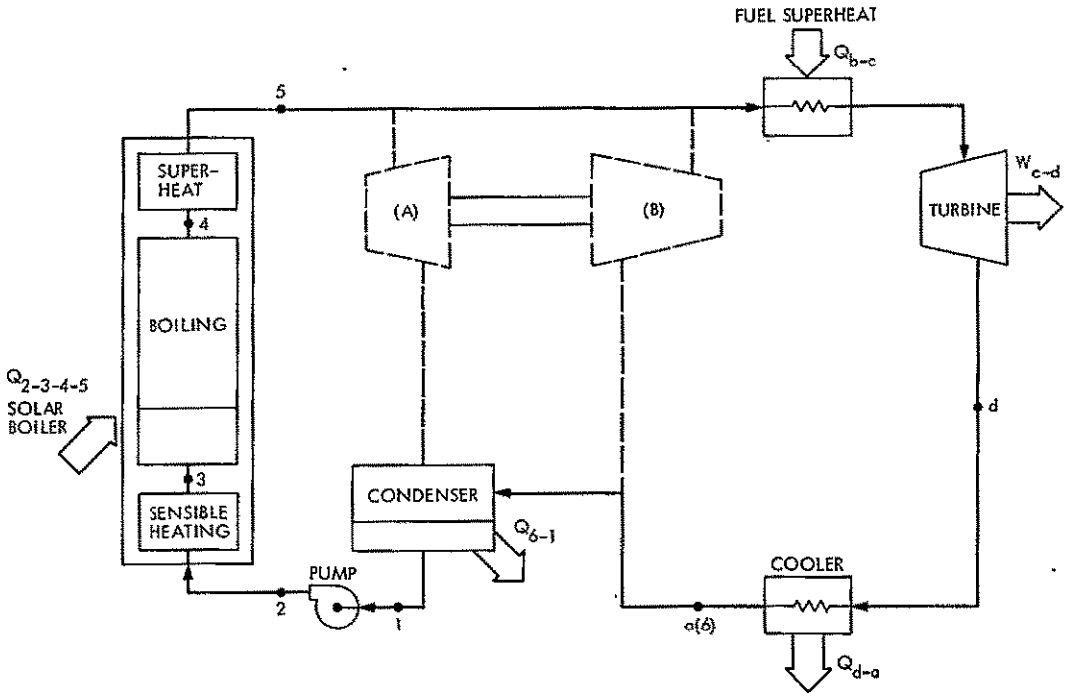

Fig. 4. Alternate flow diagram of configuration 1: deletion of Rankine turbine (A) and Brayton compressor (B) has no effect on the thermodynamics of the combined cycles

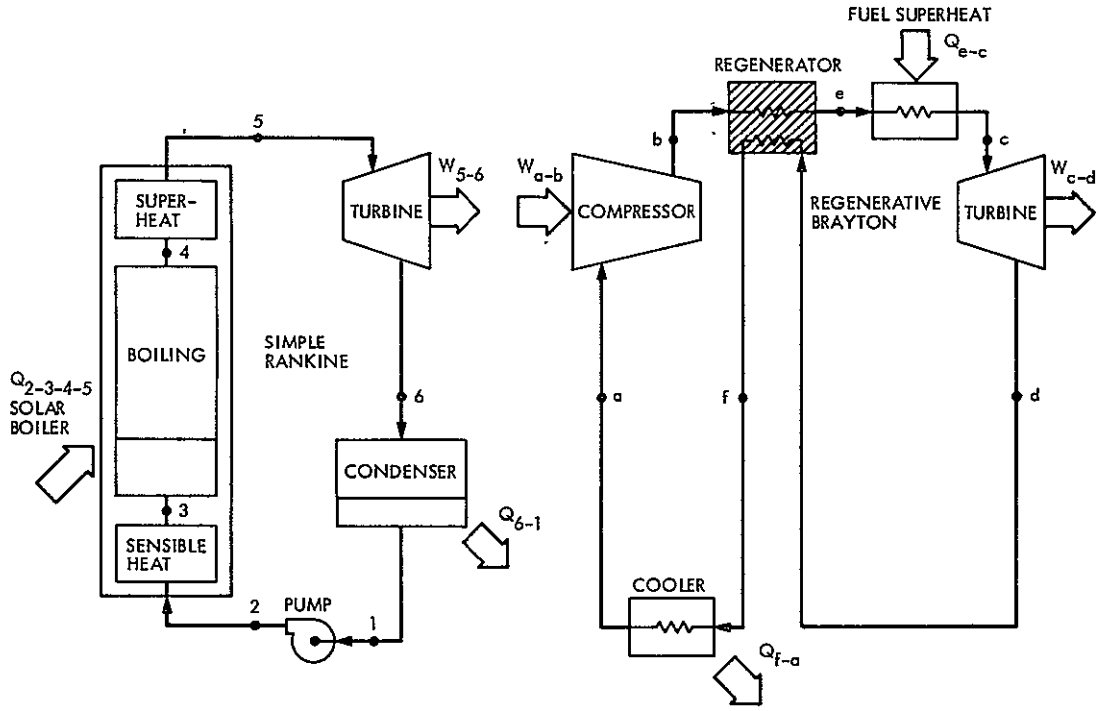

Fig. 5. Flow diagram of configuration 2

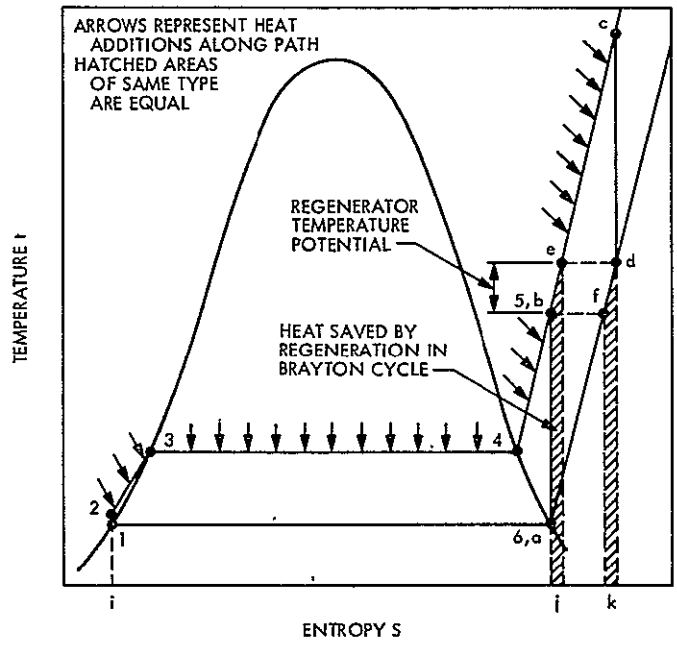

Fig. 6. Configuration 2 plotted on temperature-entropy diagram for water

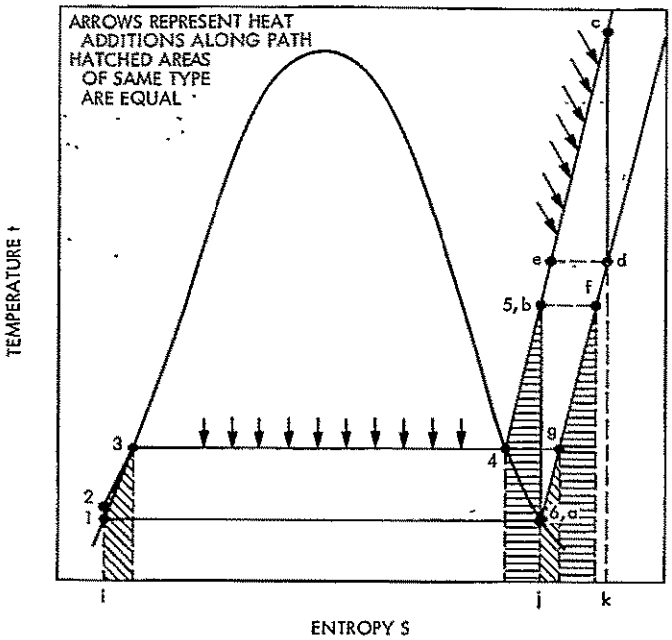

Fig. 7. Configuration 3 plotted on temperature-entropy diagram for water

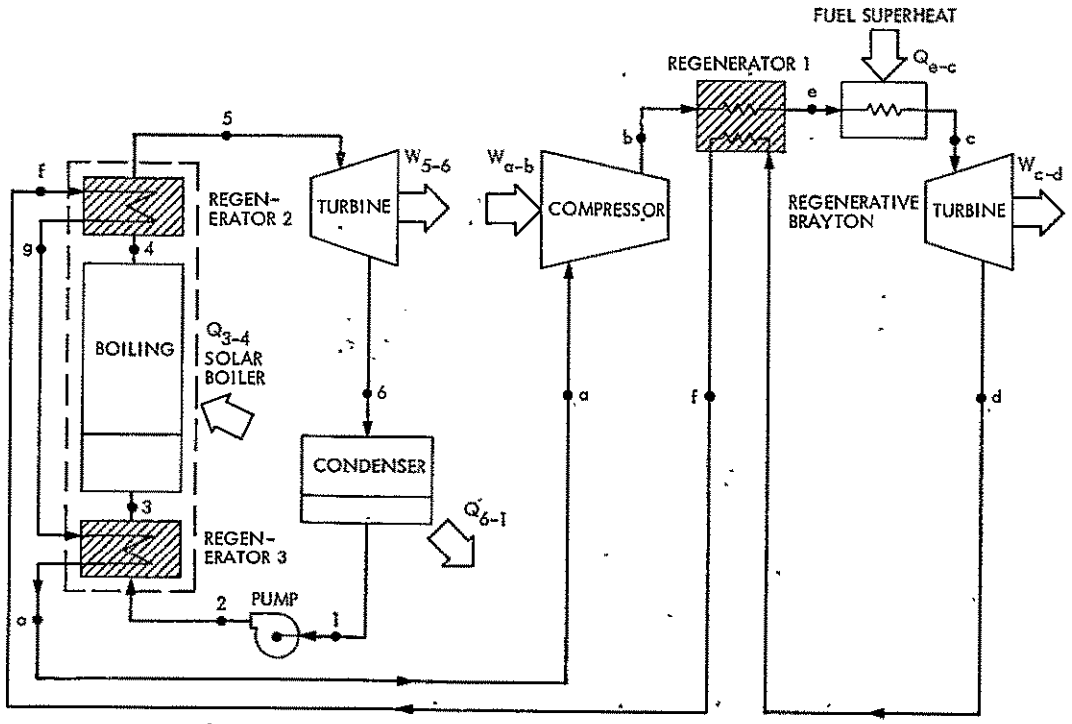

Fig. 8. Flow diagram of configuration 3

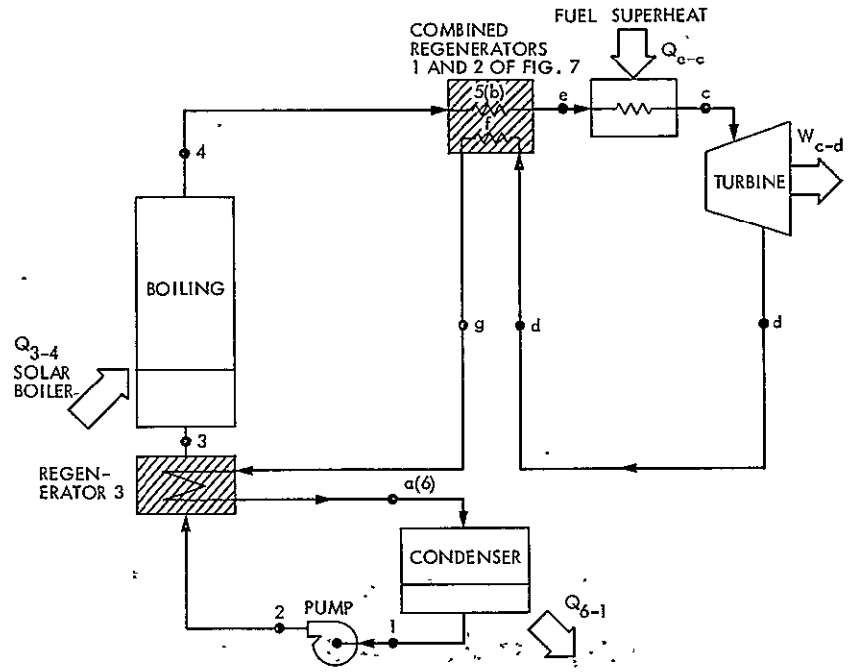

Fig. 9. Flow diagram of configuration 4: Rankine turbine/Brayton compressor deleted and regenerators 1 and 2 combined into one regenerator

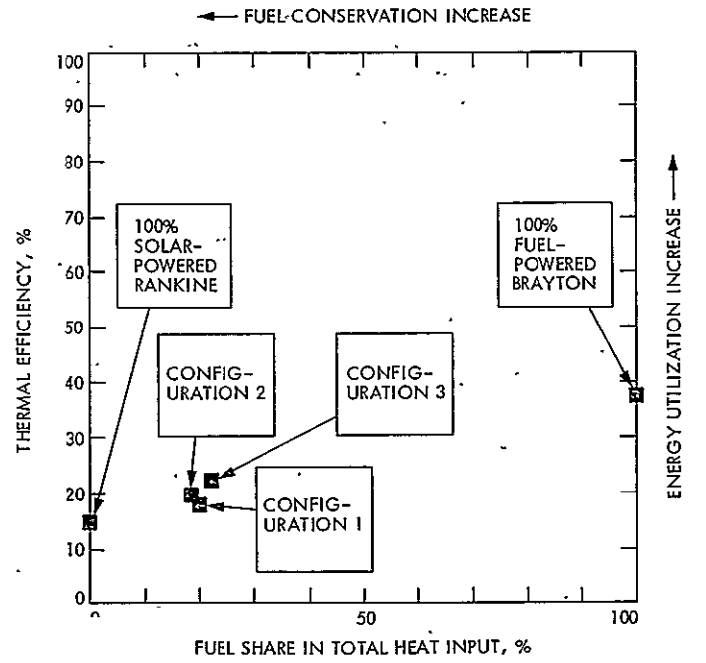

Fig. 10. Plot of thermal efficiency versus fuel share for various configurations in Table 1.

64-Meter Antenna Pedestal Tilt at DSS 43, Tidbinbilla, Australia

G. Gale and A. A. Riewe
DSN Engineering Section

It was discovered in 1973, that the 64-meter antenna pedestal at DSS 43 had settled causing a level reference plane to be tilted. This article discusses the tilt of the pedestal, its amplitude, rate of change, method of measurement, and the degree of confidence in the measurements. The effect of the tilt and a prognosis for the future effect on tilt are discussed along with recommendations.

I. Background

A foundation investigation was performed in May 1967 at the proposed 64-meter antenna site DSS 43 at Tidbinbilla, Australia. In addition, a geophysical study, consisting of several seismic refraction survey lines, was also conducted to supplement the information obtained from three borings made as part of the foundation investigation. The borings were 18 m (60 ft) from the center of the antenna site on radials of 120 degrees and extended to depths of 24, 27, and 28 m (78, 90, and 91 ft).

The soil and bedrock profiles revealed by the borings consisted of a thin surface layer of topsoil underlain by alluvium consisting of mixtures of clay, sand, and gravel which, in turn, was underlain by granite bedrock at depths between 15 and 18 feet and which extended to the depths of the borings. The alluvium was firm-to-stiff, porous in the upper 5 feet, becoming stiff-to-hard and dense with depth. The bedrock was observed to be very decomposed (weathered) in the upper 3 m (10 ft), becoming less weathered (more crystalline in appearance) with depth and finally merging into relatively fresh granite bedrock at depths in excess of 21 m (70 ft). Ground water, as observed in the borings, was on the order of 4 m (12 ft) below existing grades. The uniformity of the subsurface profile was substantiated by the seismic refraction study.

Footings for the pedestal and base of the instrument tower were both designed to obtain bearing on the very weathered, but dense granite. The pedestal obtained bearing at a depth of 6 m (20 ft) and the instrument tower at 8.75 m (28.5 ft). During construction, a visual appraisal of the full site excavation substantiated the uniformity of the founding material as revealed by the borings and laboratory test results. It is believed that the observed pedestal tilt is not caused by variation in the compressibility of the supporting bedrock materials.

II. Foundation Analysis

When the pedestal tilt was first discovered, as a result of the January 1973 level survey of the DSS 43 azimuth bull gear, informal inquiries were made through the Network Support Facility (Australia) to determine if any regional tilts were being observed at local Australian Government facilities. The Snowy Mountain Authority, which is in charge of the large hydroelectric development centered some 96 km (60 miles) south of DSS 42/43, stated that elevations over their project area had been monitored for several years but that the effort had been discontinued when no changes were detected.

Closer to DSS 43 (approximately 24 km, 15 miles) is the Mount Strombo Astronomical Observatory, which is operated by the Australian National University at Canberra. No tilt was observed at the observatory during the period that the DSS 43 tilt occurred.

Bench marks placed on the 26-meter antenna footings at DSS 42 were resurveyed after the 64-meter DSS 43 antenna tilt was noted, but no change in relative elevations was found to have occurred during the period of concern.

An investigation of the hydrostatic bearing loads was accomplished in mid-1974 to determine if the observed pedestal tilt might have been caused by an imbalance in the hydrostatic bearing loads. The pressures in the bearing recesses were determined and it was reported that the bearing pads were carrying the following loads:

Pad 1	7.918×10^5 newtons	(178 kips)
Pad 2	7.873×10^5 newtons	(177 kips)
Pad 3	9.208×10^5 newtons	(207 kips)

The above indicated imbalance in pad loads causes an imbalance in bearing pressure under the pedestal ring footing.

A settlement analysis using the results of consolidation tests run on samples obtained as part of the 1967 foundation investigation and the above nonuniform bearing pad loads indicates that differential settlement across the antenna pedestal on the order of 3.175 mm (1/8 in.) could result from the imbalance.

Pad 3, the most heavily loaded, is the pad located on the "back" or rear side of the antenna (Fig. 1). As the antenna generally looks northerly during tracking operations, Pad 3 is bearing over the southerly half of the pedestal, which is the portion experiencing settlements relative to the north side.

III. Reference Surface

The top surface of the azimuth drive bull gear is used as a reference surface by the hydrostatic bearing instrumentation in process of determining the flatness of the hydrostatic bearing runner surface. Any deviation from a gravity level plane by the top surface of the bull gear, unless compensated for, will reflect as errors in the runner flatness determination. Therefore, frequent measurements are made of this surface to assure that the proper corrections are made in the hydrostatic bearing determinations.

A survey was made of the level of the top surface of the bull gear at the time it was installed in 1967. A record was kept of the deviation from a true gravity plane at 10-deg intervals around the 360 deg of the bull gear. This record serves as the starting reference.

The reference plane is a gravity-level plane through the mean elevation of the original bull-gear data taken when the bull gear was installed. Since then, the heights of the 10-deg intervals have changed and plots of the data resemble sine curves indicating a tilt in the plane of the top surface of the bull gear (Fig. 2).

The concept of the sine curve can be best explained by the following example. If a circle is inscribed on a plane and the plane is tilted with respect to a gravity-level plane through the axis of rotation, a plot of the ordinate values vs angular position around the circle will be a sine curve. The amplitude of the curve is proportional to the tilt of the plane, and the phase angle will indicate the direction of the tilt. The ordinate values h may be expressed by the equation $h = A \sin(\beta + \varphi)$, where A is the amplitude and φ is the phase angle. The amplitude A and phase angle φ can be determined for a "best-fit plane" (sine wave) by applying a Fourier series approximation to the raw data h and angle in the following manner:

Let the curve through the data points be described as

$$P_1 \sin\beta + P_2 \sin 2\beta + \cdots + Q_1 \cos\beta + Q_2 \cos 2\beta + \cdots;$$

If only the fundamental is considered, neglecting the harmonic components, the function can be reduced to $P \sin\beta + Q \cos\beta$, where

$$P = \frac{2}{n} \sum_{1}^{n} h_n \times \sin\beta_n \text{ and } Q = \frac{2}{n} \sum_{1}^{n} \cos\beta_n$$

where n is 36, the number of equally spaced 10-deg points, and h_n is the height at angle β_n. The amplitude then is $A = \sqrt{P^2 + Q^2}$ and the phase angle $\varphi = \tan^{-1} Q/P$.

By applying this type of analysis to the data from the second survey made in January 1973, the "best fit plane" indicated that the top surface of the bull gear had tilted approximately 26 seconds from the "best fit plane" through the 1971 data taken just after the installation of the gear. Subsequent measurements made between 1973 and 1976 indicate that the angle of tilt is increasing at a rate of approximately 3.6 seconds per year. In 1976, the total tilt was 34 seconds (Fig. 3).

IV. Error Analysis

Eleven surveys have been made since January 1971. Each survey usually contains three traverses around the bull gear. Each traverse is a series of measurements of the incremental differences in heights between successive 10-deg intervals. The sum of the 36 increments in any set of measurements must be equal to 0.000 ± 0.25 mm (±0.010 in.) (closing error). If the closing error is greater than 0.25 mm (0.010 in.) that set of data is invalid. If the closing error is less than 0.25 mm (0.010 in.), the closing error is equally distributed through the 36 incremental measurements. The average of the three sets is used as the value for the height of the bull gear relative to a gravity plane.

The probable error of individual observations was determined from the data taken for 11 surveys made since 1971. A point on the bull gear which showed very little change in height since installations was selected. The probable error r of a single observation was computed using the formula

$$r = 0.6745\,(n-1)^{-1/2}\left[\sum_{1}^{n} h_1^2\right]^{1/2}$$

Here n is the number of observations and h the heights above the gravity level reference plane. The probable error of a single observation based upon the 11 surveys was computed to be 0.023 mm (±0.0009 in.). This tolerance includes the accumulation of the individual incremental tolerances.

The probable error of the incremental observations was similarly determined to be 0.005 mm (+0.0002 in.). A comparison with 15 surveys taken at Goldstone over the same period of time indicates that at Goldstone the probable error of a single height observation is 0.020 mm (+0.0008 in.) and of the incremental observations 0.00025 mm (+0.00001 in.).

The diameter of the measurement circle on the top of the bull gear is 21.2 m (835 in.). A tolerance of 0.023 mm (0.0009 in.) at this diameter represents +0.22 arc-sec. Therefore, the probable error in the determination of the pedestal tilt is approximately +1/4 arc-sec.

V. Effects of Tilt

The major effect of the tilt is upon the hydrostatic bearing instrument (HBI). Since the HBI reference plane is determined from the top of the bull gear and the top of the bull gear tilts as the pedestal tilts, new corrections must be fed into the HBI every three to six months. It takes a crew of four men 8 to 10 hours to make a complete bull gear/HBI survey and program change. Frequent surveys will cause high maintenance cost.

The instrument tower, located in the center of the pedestal, is totally isolated from and independent of the pedestal. Observations made with a theodolite located at the top of the instrument tower looking at a gravity mirror located in the base of the tower indicate that the instrument tower has not tilted since placement of the Master Equatorial. There has not been any effect upon the pointing accuracy of the antenna.

Another area of concern is the effect upon the clearances between the windshield and instrument tower. Neither the insulation on the instrument tower nor the windshield is perfectly round, and some interferences were corrected during construction. The pedestal tilt affects the alignment of the windshield but is such that the tilt will improve the clearance at the closest point. The total clearance at the closest point between the floor of the ME room and the windshield now is in excess of 2.54 cm (1 in.). The rate of change at this elevation due to the pedestal tilt is only 0.66 mm (0.026 in.) per year.

The pedestal tilt will change the preload on the radial bearing by approximately the vertical component of the weight of the rotating structure or 4528 N (1018 lb), which is negligible compared to the 1.468×10^6 N (330-kip) preload The tilt will also change the elevations of the truck trace on the wearstrip by 0.79 mm (0.031 in.), where 1.27 cm (0.5 in.) can be tolerated before the radial bearing trucks would have to be readjusted.

VI. Risk Assessment

Table 1 summarizes the amount of the change at DSS 43 to date and the rate of change per year at the critical areas on the antenna caused by the pedestal tilt. The maximum change before corrective action must be taken is shown, and the time before corrective action is estimated based on the current rate

of change. There is no effect upon the antenna pointing accuracy.

VII. Conclusion

DSN Engineering is of the opinion that the tilt (differential settlement) of the pedestal is due to the nonuniform loading on the pedestal. The unbalanced load thesis can be tested by simply parking the heavier Pad 3 on the "high" or northern side of the pedestal when the antenna is not tracking and monitoring the tilt to determine if the tilt lessens proportionally to the amount of time the nonuniform load condition is reversed. The tilt does not affect the operation or the expected life of the antenna.

Table 1. Summary of antenna pedestal tilt at DSS 43

Location	Change since installation	Change per year	Maximum change allowable	Time before corrective action
Bull gear HBI reference	35 $\widehat{\text{sec}}$ 3.6 mm (.142")	3.6 $\widehat{\text{sec}}$ 0.381 mm (.015")	0.381 mm (.015")	1 year[a] requires update of HBI digital cam program
Cables between instrument tower and windshield	35 $\widehat{\text{sec}}$ 5 mm @ 30 5M (.195 @ 1200)	3.6 $\widehat{\text{sec}}$ 0.533 mm (.021")	12.7 mm (.500")	14.5 yrs
ME room floor joint	3.5 $\widehat{\text{sec}}$ 6.5 mm (.255")	3.6 $\widehat{\text{sec}}$ 0.66 mm (.026")	63.5 mm (2.5")	86 yrs
Radial bearing	3.5 $\widehat{\text{sec}}$ ±0.79 mm (±.031")	3.6 $\widehat{\text{sec}}$ 0.076 mm (.003")	12.7 mm (.5") ±6.35 mm (±.25")	150+ yrs

[a]The periodic corrective action to the hydrostatic bearing instrumentation digital cam program is minor. It takes approximately 8 hours to survey the level of the top surface of the bull gear and enter the corrective data into the digital cam computer program.

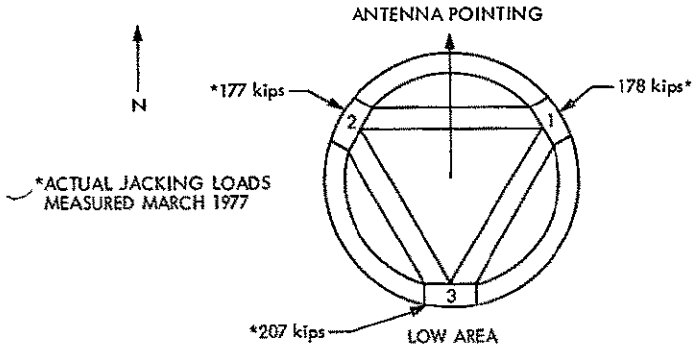

Fig. 1. DSS 43 bearing pad load

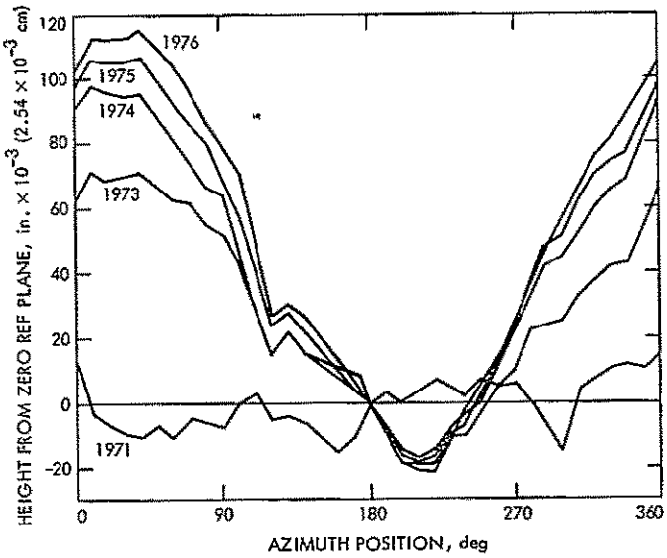

Fig. 2. Change in bull gear elevation since 1971

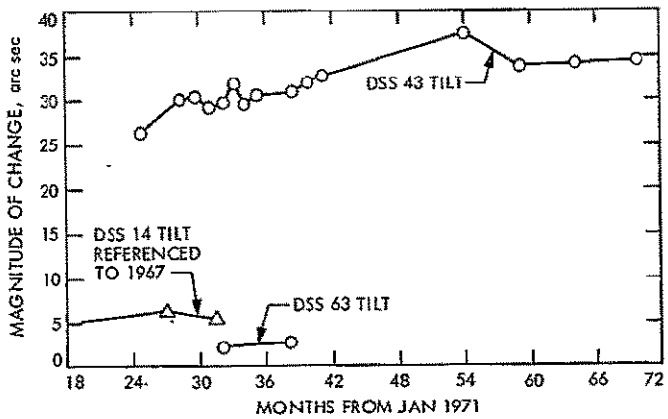

Fig. 3. DSS 43 bull gear plane tilt

Radio Frequency Interference Effects of Continuous Sinewave Signals on Telemetry Data

P. W. Low
Network Operations Office

This report presents the results of an investigation of continuous sinewave interference effects on telemetry data based on testing at the Goldstone Deep Space Station (DSS 11) in 1976. To analyze the effects, the continuous sinewave interference is treated as an extraneous noise. Empirical telemetry data degradation and drop-lock models are then developed based on test data and certain physical characteristics of the telemetry data processing system. These models will be used as a portion of the radio frequency interference detection tools in the first version of the Deep Space Interference Prediction software.

I. Introduction

There has been an increasing number of radio frequency interference (RFI) incidents occurring throughout the Deep Space Network (DSN) during spacecraft tracking operations in recent years. In many of these incidents the desired signal and the telemetry data processing performance were degraded, and in some severe cases the receiver and telemetry were knocked out of lock. Other than the basic observation and reporting of the RFI phenomenon, little could be done to avoid or minimize the impacts. From the DSN spacecraft tracking operations standpoint, a thorough investigation of the RFI effects was needed in order to develop a capability for:

(1) Prediction of possible RFI occurrence from a set of known sources, so that action could be taken to avoid or minimize the impacts and data loss.

(2) Prediction of possible RFI occurrence for future planning of DSN critical mission phases, and spectrum utilization of future missions.

There was very little material available either based on theoretical approach or experimental results that was applicable in analyzing the performance of the DSN spacecraft tracking and telemetry processing system in the presence of interfering signals. Therefore, an experimental approach was used. RFI tests were formulated and conducted with standard Deep Space Station (DSS) equipment to investigate continuous sinewave (CW) interference effects on the bit signal-to-noise ratio (SNR) and bit error rate (BER) of a telemetry signal. This article describes these tests and presents the empirical telemetry SNR and BER degradation and drop-lock models derived from the test data based on certain physical characteristics of the telemetry data processing system used.

II. Test Setup

A block diagram of the test configuration is shown in Fig. 1. The carrier tracking and telemetry data processing system is the standard DSS equipment. The Simulation Conversion Assembly was used to generate two binary data

streams; each data stream bi-phase-modulated a squarewave subcarrier. The two composite (data plus subcarrier) signals were then mixed and phase-modulated a continuous sinewave carrier. Operations support softwares were used in the Telemetry and Command Processor (TCP) and the Digital Instrumentation Subsystem (DIS) to provide the telemetry data BER and SNR and carrier tracking doppler phase jitter statistics respectively.

III. Pilot Study and Results

A preliminary quick-look test was performed to isolate the frequency spectrum regions where the CW interfering signal could cause "problems" to the desired signal. The results showed that:

(1) There were severe telemetry bit SNR and BER degradations when the CW interfering signal was near or on the subcarrier odd harmonics of the desired downlink signal.

(2) There was no observable degradation on telemetry data when the CW interfering signal was near or on the subcarrier even harmonics of the desired downlink signal.

(3) There were severe tracking doppler phase jitter degradation and telemetry bit SNR and BER degradations when the CW interfering signal was within 1000 Hertz of the desired downlink carrier.

(4) There was no observable degradation on tracking doppler phase jitter when the CW interfering signal was near or on any subcarrier harmonic of the desired downlink signal.

These results clearly indicated that the CW interfering signal causes two types of effect. They are:

(1) *Telemetry interference:* when the CW interfering signal is in the subcarrier or subcarrier odd harmonic spectra of the desired downlink signal.

(2) *Receiver interference:* when the CW interfering signal is within the receiver's theoretical carrier capture range ($\approx$ 1000 Hertz).

The frequency region for telemetry interference is much wider than the region for receiver interference. Thus, the probability of having telemetry interference during an RFI incident is much higher. Therefore, the characteristics of telemetry interference were first investigated by means of the following series of tests.

IV. Telemetry Interference Test

A. Test Objective

The test objective was to characterize the telemetry data bit SNR and BER degradations and the telemetry drop-lock conditions in the presence of a CW interfering signal.

B. Desired Downlink Signal Configuration

The desired downlink signal used for the test was a typical Viking spacecraft dual-subcarrier downlink signal. However, only the effects on the high rate subcarrier were investigated. Table 1 summarizes the exact desired downlink signal configuration.

C. Test Cases

Forty-two RFI cases were tested. They may be categorized into four different sets:

(1) *CW signal coincident with subcarrier:* The CW signal was placed coincident with the lower and upper subcarriers.

(2) *Subcarrier sweep:* The CW signal was swept across the subcarrier.

(3) *Subcarrier third harmonic sweep:* The CW signal was swept across the subcarrier third harmonic.

(4) *Subcarrier fifth harmonic sweep:* The CW signal was swept across the subcarrier fifth harmonic.

Tables 2 through 5 suminarize the test cases performed.

V. Bit Signal-to-Noise Ratio Degradation Analysis (Non-Drop-Lock Cases)

A. Method of Approach

In analyzing the bit signal-to-noise ratio (SNR) degradation, the CW interfering signal is treated as an extraneous noise.

The presence of this CW interfering signal causes an increase in the system's noise which in turn causes an increase in the effective system noise temperature. The increased system noise temperature is then derived from the test data. Finally, a SNR degradation model is constructed based on the physical characteristics of the telemetry data processing system used.

B. SNR Degradation Model

Let Fig. 2 be the simplified system configuration used for the test. Thus, when the RFI signal is not present, the received bit SNR is:

$$SNR_I = 10 \log \left(\frac{P_D T_B}{N_S} \right)$$

where

P_D = total high rate data power

BR = bit (symbol) rate

T_B = bit (symbol) time ($1/BR$)

N_S = noise spectral density when RFI is not present

When the RFI signal is present, the received bit SNR is:

$$SNR_{IR} = 10 \log \left(\frac{P_D T_B}{N_{SR}} \right)$$

where

N_{SR} = noise spectral density when RFI is present

Then, the received bit SNR degradation is:

$$\Delta SNR_I = SNR_I - SNR_{IR}$$

or

$$\Delta SNR_I = 10 \log \left(\frac{P_D T_B}{N_S} \right) - 10 \log \left(\frac{P_D T_B}{N_{SR}} \right)$$

$$\Delta SNR_I = 10 \log \left(\frac{N_{SR}}{N_S} \right)$$

Substituting $N_S = KT_S$ and $N_{SR} = KT_{SR}$, the above equation becomes

$$\Delta SNR_I = 10 \log \left(\frac{KT_{SR}}{KT_S} \right)$$

$$\Delta SNR_I = 10 \log \left(\frac{T_{SR}}{T_S} \right)$$

where

T_S = effective system noise temperature when RFI is not present (It is also referred to as SNT)

T_{SR} = effective system noise temperature when RFI is present

K = Boltzmann's constant

Let T_R = increased system noise temperature induced by the CW interfering signal

Then,

$$T_{SR} = (T_S + T_R)$$

Therefore,

$$SNR_I = 10 \log \left(\frac{T_S + T_R}{T_S} \right) \quad (1)$$

Also, when the RFI signal is not present, the SSA bit SNR is:

$$SNR_O = SNR_I - L_S$$

When the RFI signal is present, the SSA bit SNR is:

$$SNR_{OR} = SNR_{IR} - L_{SR}$$

where L_S and L_{SR} are system losses. These include waveform distortion loss, receiver (radio) loss, subcarrier demodulator loss, and bit sync/detection loss; they are assumed to be strictly a function of the received bit SNR for a given system and configuration. Therefore, the SSA bit SNR degradation is:

$$\Delta SNR_O = SNR_O - SNR_{OR}$$

or

$$\Delta SNR_O = \Delta SNR_I - (L_S - L_{SR}) \quad (2)$$

Having Eqs. (1) and (2) established, the next step is to determine the functional relationship of the CW interfering signal and the increased system noise temperature it induces.

C. Interfering Signal Coincident with Subcarrier

The functional relationship of the CW interfering signal and the increased system noise temperature for the interfering signal coincident with the subcarrier is to be determined in this subsection. Let us examine Eq. (1) again.

$$\Delta SNR_I = 10 \log \left(\frac{T_S + T_R}{T_S} \right)$$

Solving for T_R, then:

$$T_R = T_S \left[10^{\frac{\Delta SNR_I}{10}} - 1 \right]$$

Substituting

$$\Delta SNR_I = \Delta SNR_O + (L_S - L_{SR}),$$

then:

$$T_R = T_S \left[10^{\frac{\Delta SNR_O + (L_S - L_{SR})}{10}} - 1 \right] \qquad (3)$$

From Eq. (3), T_R for each test case (1A through 1Z) is calculated. Note:

ΔSNR_O = data obtained from test cases 1A through 1Z.

L_S and L_{SR} = estimated from the Telemetry Analysis Program (TAP) by using an iterative method. See Fig. 3 for a plot of the system loss vs received bit SNR generated by the TAP for the configuration used for the test.

Then, using a trial and error method, T_R is curve fitted. The result is

$$T_R \Big|_{\Delta f_{1sc}=0, BR=2K} = \left[\left(10^{8.21 e^{-.0421 P_{RFI}}} \right)^2 + (40)^2 \right]^{1/2} - 39.5 \qquad (4)$$

where

Δf_{1sc} = frequency separation between the CW interfering signal and the subcarrier

P_{RFI} = RFI signal level

Using Eqs. (1) and (4), the curve fitted values are plotted against the observed values (ΔSNR_I vs P_{RFI}) as shown in Figs. 4 and 5.

D. Interfering Signal at Various Frequency Offsets from Subcarrier or Subcarrier Harmonics

The RFI effect with the CW interfering signal at various frequency offsets from the subcarrier or subcarrier harmonics will be investigated in this subsection, but let us first examine the frequency response of the telemetry system used for the test.

The telemetry system used for the test must be able to pass the antipodal binary-valued data signal in the subcarrier harmonic spectra. Therefore, it must have an impulse response:

$$h(\tau) = \begin{cases} \frac{h}{n} & 0 \leq \tau \leq T_B \\ 0 & \tau < 0, \tau > T_B \end{cases}$$

where

h = gain

n = subcarrier harmonic number, $n = 1, 3, 5$, etc.

T_B = bit time ($1/BR$)

Then, its frequency response is

$$H(n, \Delta f_{nsc}) = \int_0^\infty h(\tau) \left[e^{-j2\pi \Delta f_{nsc} \tau} \right] d\tau$$

$$= \frac{h}{n} \int_0^{T_B} \left[e^{-j2\pi \Delta f_{nsc} \tau} \right] d\tau$$

$$= \frac{h}{n} \left[\frac{e^{-j2\pi \Delta f_{nsc} \tau}}{-j2\pi \Delta f_{nsc}} \right]_0^{T_B}$$

$$= \frac{h}{n} \left[\frac{e^{-j2\pi \Delta f_{nsc} T_B} - 1}{-j2\pi \Delta f_{nsc}} \right]$$

$$= \frac{h}{n\pi\Delta f_{nsc}}$$

$$\cdot\left[\frac{e^{-j\pi\Delta f_{nsc}T_B} - e^{j\pi\Delta f_{nsc}T_B}}{-j2}\right] e^{-j\pi\Delta f_{nsc}T_B}$$

where

$$\Delta f_{nsc} = \begin{cases} |(f_c + f_{nsc}) - f_{RFI}| & \text{if } f_{RFI} > f_c \\ |(f_c - f_{nsc}) - f_{RFI}| & \text{if } f_{RFI} < f_c \end{cases}$$

where $n = 1, 3, 5$, etc.

f_{nsc} = nth harmonic of subcarrier, where $n = 1, 3, 5$, etc. $(n \cdot f_{sc1})$ (1st harmonic is also referred to as subcarrier)

f_{RFI} = RFI signal frequency

Using the Euler's identity:

$$\sin\theta = \frac{e^{j\theta} - e^{-j\theta}}{j2}$$

$$H(n, \Delta f_{nsc}) = \frac{h}{n\pi\Delta f_{nsc}} (\sin\pi\Delta f_{nsc}T_B)\left(e^{-j\pi\Delta f_{nsc}T_B}\right)$$

$$= \frac{h\,T_B}{n}\left(\frac{\sin\pi\Delta f_{nsc}T_B}{\pi\Delta f_{nsc}T_B}\right)\left(e^{-j\pi\Delta f_{nsc}T_B}\right)$$

Thus:

$$|H(n, \Delta f_{nsc})|^2 = \left[\frac{h\,T_B}{n}\left(\frac{\sin\pi\Delta f_{nsc}T_B}{\pi\Delta f_{nsc}T_B}\right)\left(e^{-j\pi\Delta f_{nsc}T_B}\right)\right]$$

$$\cdot\left[\frac{h\,T_B}{n}\left(\frac{\sin\pi\Delta f_{nsc}T_B}{\pi\Delta f_{nsc}T_B}\right)\left(e^{j\pi\Delta f_{nsc}T_B}\right)\right]$$

$$|H(n, \Delta f_{nsc})|^2 = \left(\frac{h\,T_B}{n}\right)^2\left(\frac{\sin\pi\Delta f_{nsc}T_B}{\pi\Delta f_{nsc}T_B}\right)^2$$

For a CW signal with power (P) and one-sided power spectral density function $\{G(\Delta f_{nsc}) = (P/2)\,[\delta(\Delta f_{nsc} - \Delta f^{\star}_{nsc})]\}$ input into this telemetry system, the output power response is

$$P(n, \Delta f^{\star}_{nsc}) = \int_{-\infty}^{\infty} |H(n, \Delta f_{nsc})|^2\, G(\Delta f_{nsc})\, d(\Delta f_{nsc})$$

Using the sampling property of impulses, that is

$$\int_b^c f(\lambda)\, U_0(\lambda - a)\, d\lambda = f(\lambda) \quad \text{for } b < a < c$$

$$P(n, \Delta f^{\star}_{nsc}) = (P)\left(\frac{h\,T_B}{n}\right)^2\left(\frac{\sin\pi\Delta f^{\star}_{nsc}T_B}{\pi\Delta f^{\star}_{nsc}T_B}\right)^2$$

Therefore, the output power response function of the telemetry system for any CW signal with power (P) is

$$P(n, \Delta f_{nsc}) = (P)\left(\frac{h\,T_B}{n}\right)^2\left(\frac{\sin\pi\Delta f_{nsc}T_B}{\pi\Delta f_{nsc}T_B}\right)^2$$

Let

$$n = 1,$$

and

$$\Delta f_{nsc} = 0,$$

then

$$P(1,0) = (P)(h\,T_B)^2$$

Thus,

$$\left.\frac{P(n, \Delta f_{nsc})}{P(1,0)}\right|_{BR=2K} = \left(\frac{1}{n^2}\right)\left(\frac{\sin\pi\Delta f_{nsc}T_B}{\pi\Delta f_{nsc}T_B}\right)^2$$

or (expressed in decibel format)

$$P(n, \Delta f_{nsc}) = P(1,0) - 20\log n + 10\log\left(\frac{\sin\pi\Delta f_{nsc}T_B}{\pi\Delta f_{nsc}T_B}\right)^2$$

(The above result appears to be suitable for modelling SNR degradation for any bit rate. However, without test data to substantiate this claim, the scope of this model is limited to two thousand (2K) bits per second data in this analysis.)

$P(n, \Delta f_{nsc})$ is the system's power response to the CW interfering signal at any frequency offset (Δf_{nsc}), and $P(1, 0)$ is the system's power response to the CW interfering signal with Δf_{1sc} equal to zero. Also, remember that Eq. (4) obtained in the preceding subsection is based on the interfering signal level (P_{RFI}) with Δf_{1sc} equal to zero. Thus, Eq. (4) may be generalized as

$$T_R\Big|_{BR=2K} = \left[\left(10^{.821e^{.0421 P_I}}\right)^2 + (40)^2\right]^{1/2} - 39.5 \qquad (5)$$

where

$$P_I = P_{RFI} - 20 \log n + 10 \log \left[\frac{\sin \Delta f_{nsc} \left(\frac{\pi}{BR}\right)}{\Delta f_{nsc} \left(\frac{\pi}{BR}\right)}\right]^2$$

n = number of the subcarrier harmonic which the interfering signal is affecting.

Using Eqs. (1) and (5), the modeled values are compared with test data. The results show that the model's bit SNR degradation predictions are slightly but consistently less than the degradation indicated by the test data. Two "adjustment factors" are then introduced into Eq. (5) to compensate for this disparity. Thus, the model becomes:

$$P_I = P_{RFI} - (0.94)(20 \log n) + (0.90) \cdot \left[10 \log \left(\frac{\sin \left(\Delta f_{nsc} \left(\frac{\pi}{BR}\right)\right)}{\Delta f_{nsc} \left(\frac{\pi}{BR}\right)}\right)^2\right] \qquad (6)$$

$$T_R\Big|_{BR=2K} = \left[\left(10^{.821e^{.0421 P_I}}\right)^2 + (40)^2\right]^{1/2} - 39.5 \qquad (7)$$

$$SNR_I = 10 \log \left(\frac{T_S + T_R}{T_S}\right) \qquad (1)$$

$$SNR_O = \Delta SNR_I - (L_S - L_{SR}) \qquad (2)$$

(The observed disparity is probably caused by the "impurity" of the CW interfering signal. Because of this "impurity", the interfering signal does not have a perfect line spectrum; consequently, the resulting integral evaluation of the power response function, $P(n, \Delta f_{nsc})$, is only a close approximation. Therefore, the "adjustment factors" are needed in Eq. (6).)

The refined model (Eqs. (1), (2), (6) and (7)) predictions are compared with the test data for the eight telemetry non-drop-lock cases (2F, 3C through 3E, and 4B through 4E). The results are plotted on Figs. 6 through 13.

VI. Bit Error Rate Degradation Analysis

With no RFI, bit errors for uncoded data transmitted over a gaussian channel and detected in white additive noise are statistically independent of each other, and the BER (error probability) is

$$BER = P_E = 1/2 \; erfc \; \sqrt{\lambda}$$

where $\lambda = SNR_O$. The corresponding BER and λ values are tabulated in Table 6, and will be referred to as the "theoretical curve"

When a CW interfering signal is present, the bit errors may not be independent of each other; they may come in bursts. Consequently, the BER_R and SNR_{OR} relationship may not be the same as prescribed by the "theoretical curve." In fact, the test data show that

$$BER_R = 1/2 \; erfc \; \sqrt{\lambda}$$

where

$$\lambda = SNR_O - k(\Delta SNR_O)$$

$$k < 1$$

The coefficient k appears to be a function of SNR_O and ΔSNR_O. However, because it varies over a very small range, for practical purposes, a first-order approximation is used in this analysis. Thus, k is chosen to be 0.79 and the result is

$$BER_R = 1/2 \; erfc \; \sqrt{\lambda} \qquad (8)$$

where

$$\lambda = SNR_O - 0.79 (\Delta SNR_O)$$

$$= SNR_O (0.21) + SNR_{OR} (0.79)$$

(If k were 1, then Eq. (8) would become:

$$BER_R = 1/2\ erfc\ \sqrt{SNR_O - \Delta SNR_O}$$

$$= 1/2\ erfc\ \sqrt{SNR_{OR}} = P_E$$

That is: BER_R function behaves as the "theoretical curve.")

Using Eq. (8) and Table 6, calculated BER_R values are plotted against the test data and the "Theoretical Curve" on Figs. 14 through 17 for the test cases of interfering signal coincident with the subcarrier.

The RFI-BER model (Eqs. (1), (2), (6), (7), and (8)) predictions are compared with the test data for seven frequency-sweep telemetry non-drop-lock cases as shown on Figs. 18 through 24. (For the frequency-sweep test, the BER_R test data have a resolution of only 10^{-4}. Therefore, Test case 4E, which has BER_R's considerably less than 10^{-4}, is not plotted for comparison. Also, other data points which have BER_R's less than 10^{-4} are arithmetically averaged over a longer sample (time, or Δf_{nsc}) base.)

VII. Telemetry Drop-Lock Analysis

When an interfering signal is present in a communication system, it may not only degrade the desired signal, but may also, in some severe cases, cause the communication system to drop lock. In fact, during the performance of this RFI test, eight telemetry (SDA) drop-lock cases were observed. These drop-lock cases will be discussed in this section.

Normally, it is assumed that the major cause for a telemetry system to drop lock is that the bit SNR is below threshold. However, by comparing the SNR_R predicted by the degradation model obtained in the preceding sections with test data (RFI signal level and Δf_{nsc} at which drop-lock occurs) it is found that this is not so. It is because the SNR_R predicted by the model at the observed drop-lock frequency offset is above the SDA/SSA SNR threshold for each of the nine drop-lock cases. While the actual mechanism causing the telemetry system (SDA) to drop lock is not yet understood, it is believed to be similar in nature to the "jump phenomenon" (Ref. 2) as observed in some phase lock loop receiver systems. That is, when two signals are simultaneously present in a PLL receiver, and if the two signals are within the PLL receiver's frequency capture range, the receiver's tracking loop tends to track the stronger signal. (This occurs even when the PLL receiver is initially locked to the weaker signal.) Regardless of the specific cause, for this analysis, let us assume that the telemetry system (SDA) will drop lock when the following condition is satisfied: (in algebraic format)

$$\left(R\,\frac{P_{ID}}{P_D}\right)^U \geqslant \left(\frac{\Delta f_{nsc}}{BR}\right)$$

Expressing the above relationship in decibel format:

$$U\left[P_{ID} - P_D + 10\log(R)\right] \geqslant \left[10\log\left(\frac{\Delta f_{nsc}}{BR}\right)\right]$$

where

$$P_{ID} = P_{RFI} - (.94)(20\log n)$$

P_D = data power in dBm

$$\Delta f_{nsc} \geqslant BR$$

By fitting the eight drop-lock data points to the above relationship, it is found that the drop-lock condition is:

$$0.65\,(P_{ID} - P_D - 3) \geqslant \left[10\log\left(\frac{\Delta f_{nsc}}{BR}\right)\right]$$

Also, for $\Delta f_{nsc} < BR$, it is expected that the drop-lock condition is

$$(P_{ID} - P_D - 3) \geqslant 0$$

Thus, the telemetry drop-lock model becomes:

For $\Delta f_{nsc} \geqslant BR$,

$$0.65\,(P_{ID} - P_D - 3) \geqslant \left[10\log\left(\frac{\Delta f_{nsc}}{BR}\right)\right]$$

For $\Delta f_{nsc} < BR$,

$$(P_{ID} - P_D - 3) \geqslant 0 \qquad (9)$$

where

$$P_{ID} = P_{RFI} - (.94)(20 \log n)$$

Using Eq. (9), a telemetry drop-lock profile is plotted against the test data on Fig. 25.

VIII. Summary of Analysis Results

When an interfering signal is present in addition to white Gaussian system noise, the telemetry signal is degraded. For CW signal interference, the following was observed:

(1) There is no observable degradation on telemetry data when the interfering signal is placed on any even subcarrier harmonic.

(2) There is observable degradation on telemetry data when the interfering signal is placed on an odd subcarrier harmonic.

Treating the CW interfering signal as a noise source to the telemetry system, the bit SNR degradation is modeled:

$$\Delta SNR_O = SNR_I - (L_S - L_{SR})$$

$$\Delta SNR_I = 10 \log \left(\frac{T_S + T_R}{T_S} \right)$$

where:

$$T_R \Big|_{BR=2K} = \left[\left(10^{.821 e^{-.0421 P_I}} \right)^2 + (40)^2 \right]^{1/2} - 39.5$$

$$P_I = P_{RFI} - (0.94)(20 \log n)$$

$$+ (0.90) \left(10 \log \left\{ \frac{\sin \left[\Delta f_{nsc} \left(\frac{\pi}{BR} \right) \right]}{\Delta f_{nsc} \left(\frac{\pi}{BR} \right)} \right\}^2 \right)$$

$$n = 1, 3, 5, \text{etc.}$$

The BER is found to be:

$$BER_R = 1/2 \; erfc \; \sqrt{\lambda}$$

where

$$\lambda = SNR_O - (0.79)(\Delta SNR_O)$$

In some severe cases, a CW interfering signal will cause the telemetry (SDA) system to drop lock. The drop-lock condition is

For

$$\Delta f_{nsc} \geqslant BR,$$

$$0.65 (P_{ID} - P_D - 3) \geqslant \left[10 \log \left(\frac{\Delta f_{nsc}}{BR} \right) \right]$$

For

$$\Delta f_{nsc} < BR,$$

$$(P_{ID} - P_D - 3) \geqslant 0$$

where

$$P_{ID} = P_{RFI} - (0.94)(20 \log n)$$

IX. Conclusions

The test configuration and procedures used for this investigation provided a very effective and efficient way of RFI generation, control, and data collection. Forty-two CW signal interference cases were tested. Empirical telemetry bit SNR and BER degradation and drop-lock models were developed based on the test data and certain physical characteristics of the telemetry system. Although the test used a 2000-bps data rate configuration, and the telemetry bit SNR degradation model derived was for 2000 bps data rate only, the results showed some very interesting and vital characteristics of the CW interfering signal's effects on the telemetry signal (system).

Additional tests and analysis are needed to better understand RFI effects on telemetry signal. Some major tasks will include further development of models to characterize:

(1) CW interfering signal's effect on telemetry signal as a function of various telemetry parameters (e.g., data rate).

(2) Continuous spectrum interference effects on telemetry signal.

References

1. Edelson, R. E., *Telecommunications System Design Techniques Handbook,* Technical Memorandum 33-571, Jet Propulsion Laboratory, Pasadena, California, July 15, 1972.
2. Kliger, I. E., and Olenberger, C. F., "PLL Jump Phenomenon in the Presence of Two Signals," *IEEE Trans. Aerospace Electron. Systems,* Vol. AES-12, Jan. 1976.

Table 1. Desired downlink signal configuration

Carrier frequency, (f_c)	2293.148160 MHz
Carrier power (P_c)	See Tables 2 – 5
High rate data	
Subcarrier frequency (f_{sc1})	240 kHz
Data format	Uncoded
Bit rate (BR)	2000 bps
Modulation index	66.54 deg
Data power (P_D)	See Tables 2 – 5
Low rate data	
Subcarrier frequency	24 kHz
Data format	Uncoded
Bit rate	33-1/3 bps
Modulation index	19.25 deg
Data power	(P_c – 9.1) dBm

Table 2. Test cases of interfering signal coincident with subcarrier

Test number	P_C, dBm	P_D, dBm	SNT, °K	P_{RFI}, dBm	f_{RFI}
1A	–145.7	–138.5	28	–138.2	$f_c - f_{sc1}$
1B	–145.7	–138.5	28	–141.0	
1C	–145.7	–138.5	28	–144.0	
1D	–145.7	–138.5	28	–147.0	
1E	–145.7	–138.5	28	–150.0	
1F	–147.7	–138.5	28	–154.0	
1G	–145.7	–138.5	28	–164.0	
1H	–148.7	–141.5	28	–144.0	$f_c - f_{sc1}$
1I	–148.7	–141.5	28	–149.0	
1J	–148.7	–141.5	28	–153.7	
1K	–148.7	–141.5	28	–159.6	
1L	–148.7	–141.5	28	–168.0	
1M	–146.6	–139.4	26	–137.4	$f_c + f_{sc1}$
1N	–146.6	–139.4	26	–141.2	
1O	–146.6	–139.4	26	–146.2	
1P	–146.6	–139.4	26	–150.0	
1Q	–146.6	–139.4	26	–154.5	
1R	–146.6	–139.4	26	–158.0	
1S	–146.6	–139.4	26	–162.4	
1T	–146.6	–139.4	26	–164.6	
1U	–149.6	–142.4	26	–144.3	$f_c + f_{sc1}$
1V	–149.6	–142.4	26	–147.0	
1W	–149.6	–142.4	26	–150.0	
1X	–149.6	–142.4	26	–155.0	
1Y	–149.6	–142.4	26	–160.2	
1Z	–149.6	–142.4	26	–164.5	

Table 3. Test cases of subcarrier sweep

Test Number	P_C, dBm	P_D, dBm	SNT, °K	P_{RFI}, dBm	Sweep rate, Hz/sec
2A	−147.0	−139.8	35.9	−120.0	30
2B	−147.0	−139.8	35.9	−123.0	↓
2C	−147.0	−139.8	35.9	−125.0	
2D	−147.0	−139.8	35.9	−130.0	
2E	−147.0	−139.8	35.9	−135.0	
2F	−147.0	−139.8	35.9	−140.0	

Table 4. Test cases of subcarrier 3rd harmonic sweep

Test Number	P_C, dBm	P_D, dBm	SNT, °K	P_{RFI}, dBm	Sweep rate, Hz/sec
3A	−147.0	−139.8	35.9	−120.0	30
3B	−147.0	−139.8	35.9	−125.0	↓
3C	−147.0	−139.8	35.9	−130.0	
3D	−147.0	−139.8	35.9	−135.0	
3E	−147.0	−139.8	35.9	−140.0	

Table 5. Test cases of subcarrier 5th harmonic sweep

Test Number	P_C, dBm	P_D, dBm	SNT, °K	P_{RFI}, dBm	Sweep rate, Hz/sec
4A	−147.0	−139.8	35.9	−120.0	30
4B	−147.0	−139.8	35.9	−125.0	↓
4C	−147.0	−139.8	35.9	−130.0	
4D	−147.0	−139.8	35.9	−135.0	
4E	−147.0	−139 8	35.9	−140.0	

Table 6. BER vs λ for an uncoded channel

λ		BER	λ		BER
Ratio	dB		Ratio	dB	
0.080	−10.969	.34458	3.125	4.948	.00621
0.125	−9.031	.30854	3.380	5.289	.00466
0.180	−7.447	.27425	3.645	5.617	.00347
0.245	−6.108	.24196	3.920	5.933	.00256
0.320	−4.948	.21185	4.205	6.238	.00187
0.405	−3.925	.18406	4.500	6.532	.00135
0.500	−3.010	.15865	4.805	6.817	.0009689
0.605	−2.182	.13566	5.120	7.093	.0006882
0.720	−1.427	.11507	5.445	7.360	.0004843
0.845	−0.731	.09680	5.780	7.619	.0003377
0.980	−0.088	.08056	6.125	7.871	.0002333
1.125	9.512	.06681	6.480	8.116	.0001597
1.280	1.072	.05480	6.845	8.354	.0001082
1.445	1.599	.04457	7.220	8.585	.0000727
1.620	2.095	.03593	7.605	8.811	.0000484
1.805	2.565	.02872	8.405	9.245	.0000209
2.000	3.010	.02275	9.245	9.659	.0000087
2.205	3.434	.01787	10.125	10.045	.0000036
2.420	3.838	.01391	11.045	10.432	.0000015
2.645	4.224	.01073	12.005	10.792	.0000006
2.880	4.594	.00820			

[a]Source: Ref. 1, p. 143.

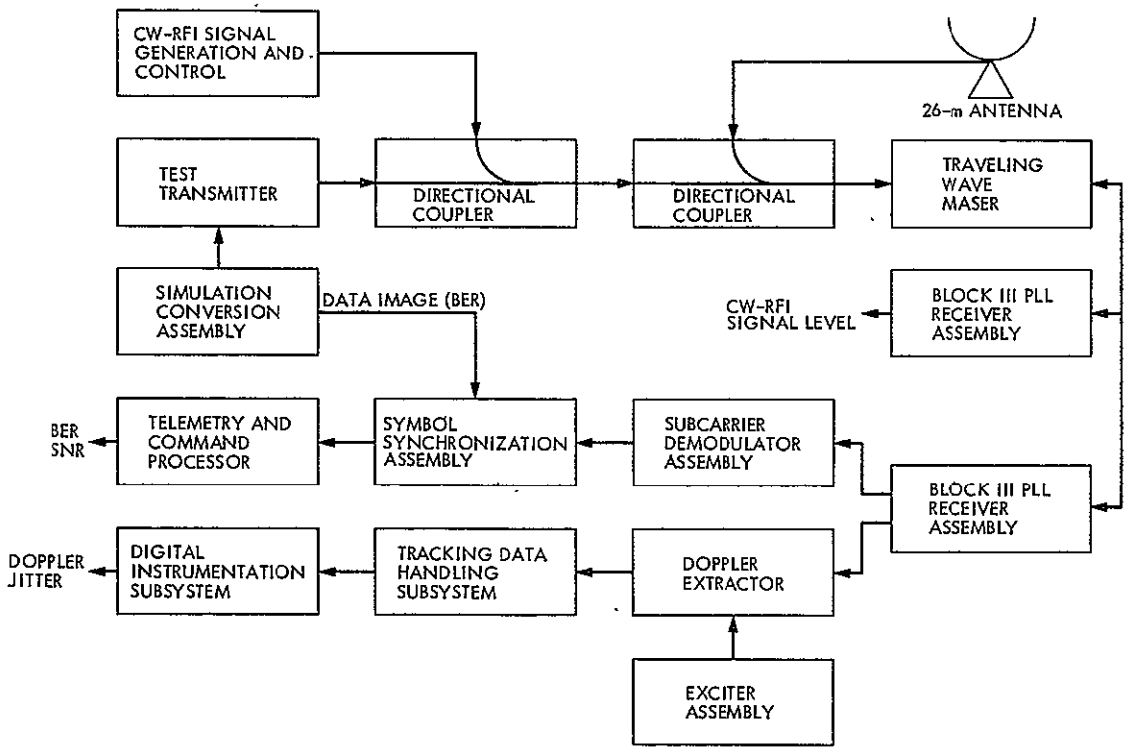

Fig. 1. Test configuration

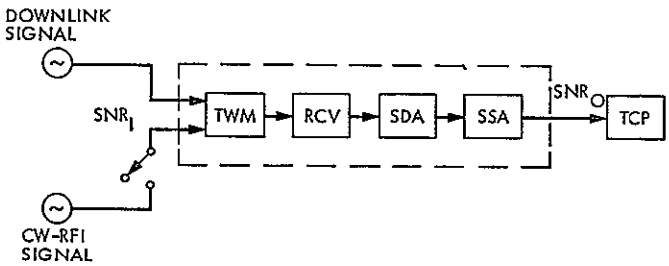

Fig. 2. Simplified carrier tracking and telemetry processing system

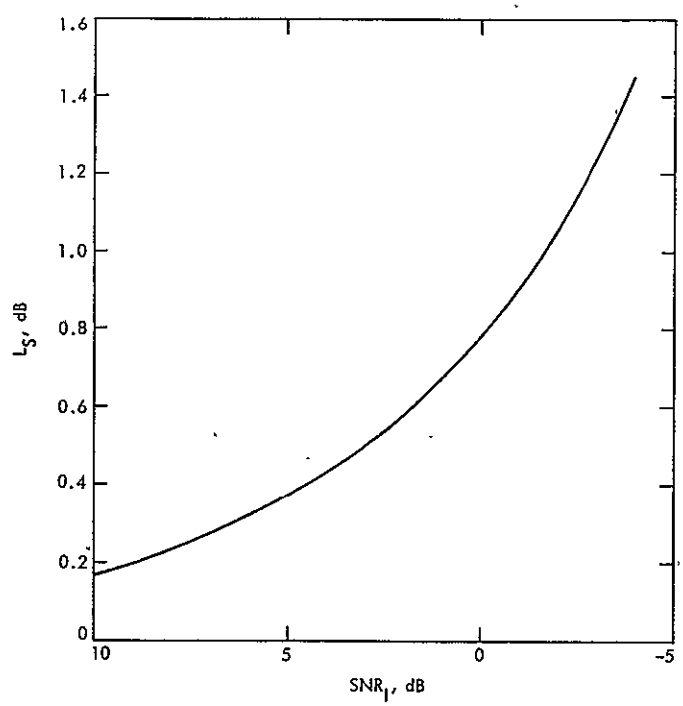

Fig. 3. Theoretical system loss curve (for test configuration)

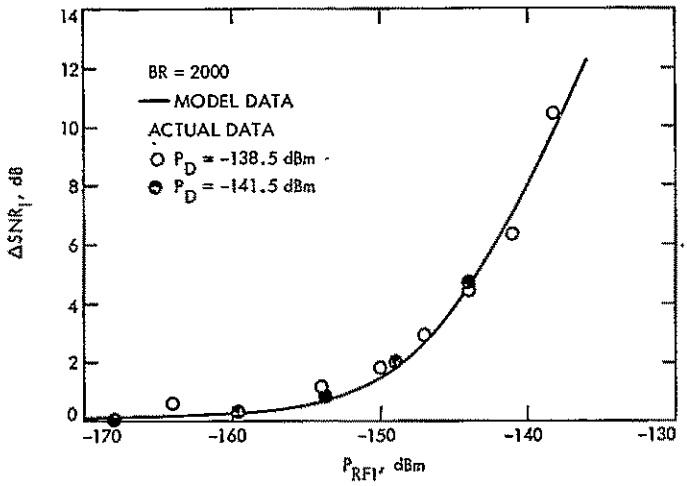

Fig. 4. Received telemetry bit SNR degradation (ΔSNR_I) vs CW interfering signal level (P_{RFI}) for $\Delta f_{1sc} = 0$ at SNT = 28°K

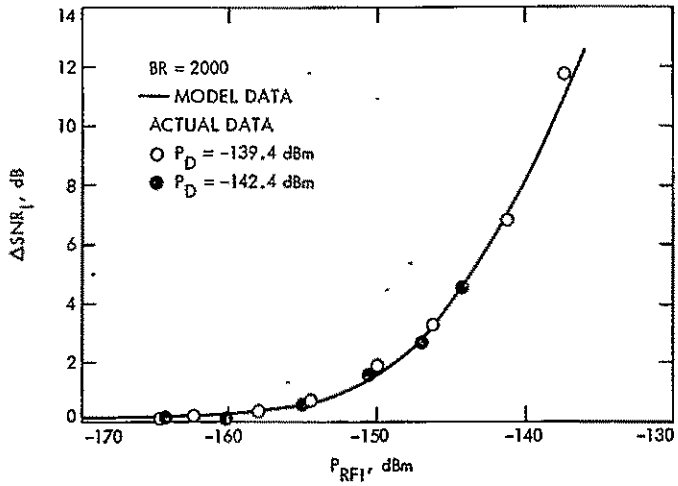

Fig. 5. Received telemetry bit SNR degradation (ΔSNR_I) vs CW interfering signal level (P_{RFI}) for $\Delta f_{1sc} = 0$ at SNT = 26°K

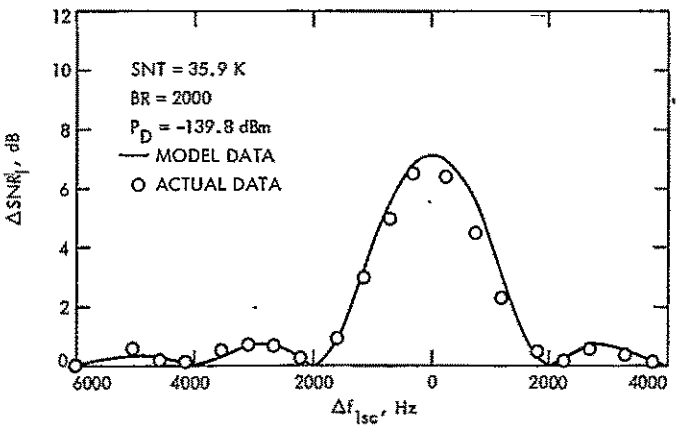

Fig. 6. Received telemetry bit SNR degradation (ΔSNR_I) vs frequency offset between subcarrier and CW interfering signal (Δf_{1sc}) for P_{RFI} = −140 dBm

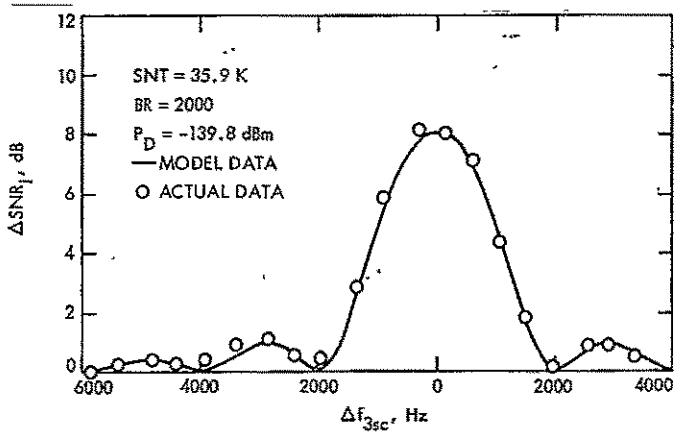

Fig. 7. Received telemetry bit SNR degradation (ΔSNR_I) vs frequency offset between subcarrier third harmonic and CW interfering signal (Δf_{3sc}) for P_{RFI} = −130 dBm

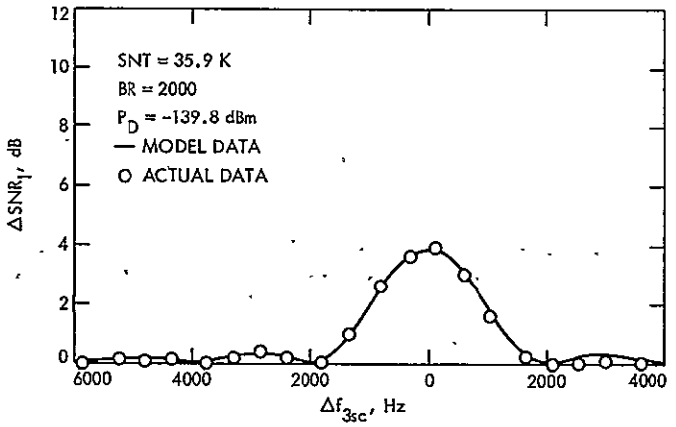

Fig. 8. Received telemetry bit SNR degradation (ΔSNR_I) vs frequency offset between subcarrier third harmonic and CW interfering signal (Δf_{3sc}) for P_{RFI} = −135 dBm

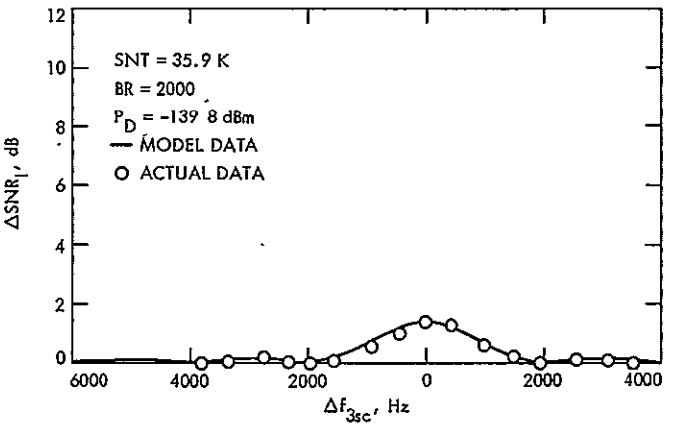

Fig. 9. Received telemetry bit SNR degradation (ΔSNR_I) vs frequency offset between subcarrier third harmonic and CW interfering signal (Δf_{3sc}) for P_{RFI} = −140 dBm

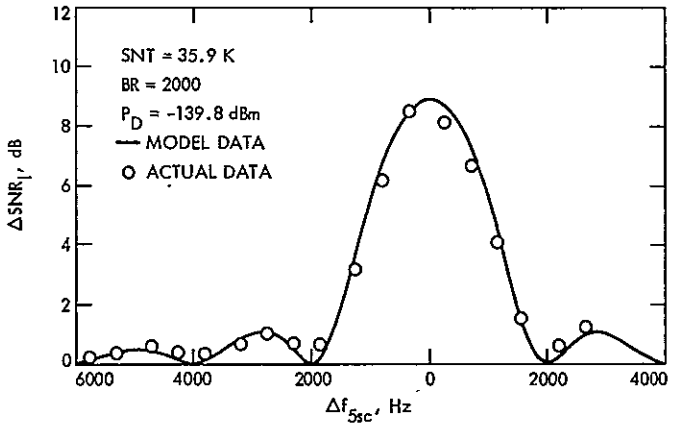

Fig. 10. Received telemetry bit SNR degradation (ΔSNR_I) vs frequency offset between subcarrier fifth harmonic and CW interfering signal (Δf_{5sc}) for P_{RFI} = −125 dBm

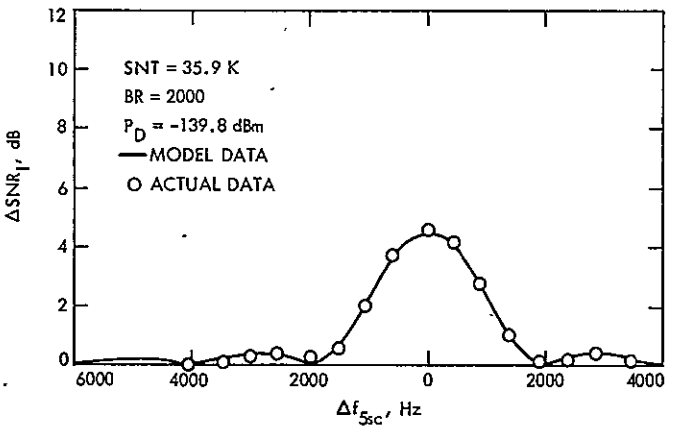

Fig. 11. Received telemetry bit SNR degradation (ΔSNR_I) vs frequency offset between subcarrier fifth harmonic and CW interfering signal (Δf_{5sc}) for P_{RFI} = −130 dBm

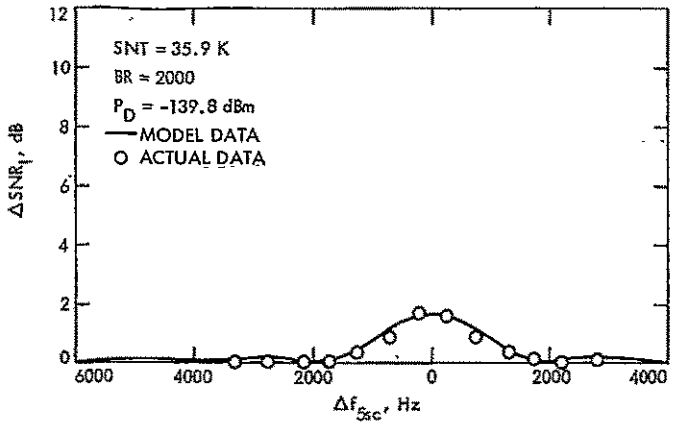

Fig. 12. Received telemetry bit SNR degradation (ΔSNR_I) vs frequency offset between subcarrier fifth harmonic and CW interfering signal (Δf_{5sc}) for P_{RFI} = −135 dBm

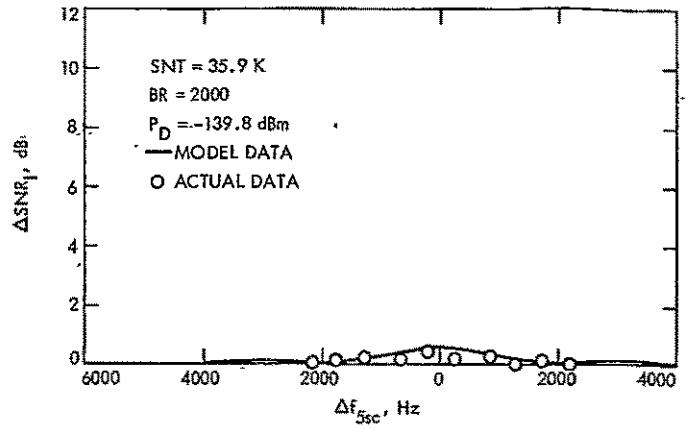

Fig. 13. Received telemetry bit SNR degradation (ΔSNR_I) vs frequency offset between subcarrier fifth harmonic and CW interfering signal (Δf_{5sc}) for P_{RFI} = −140 dBm

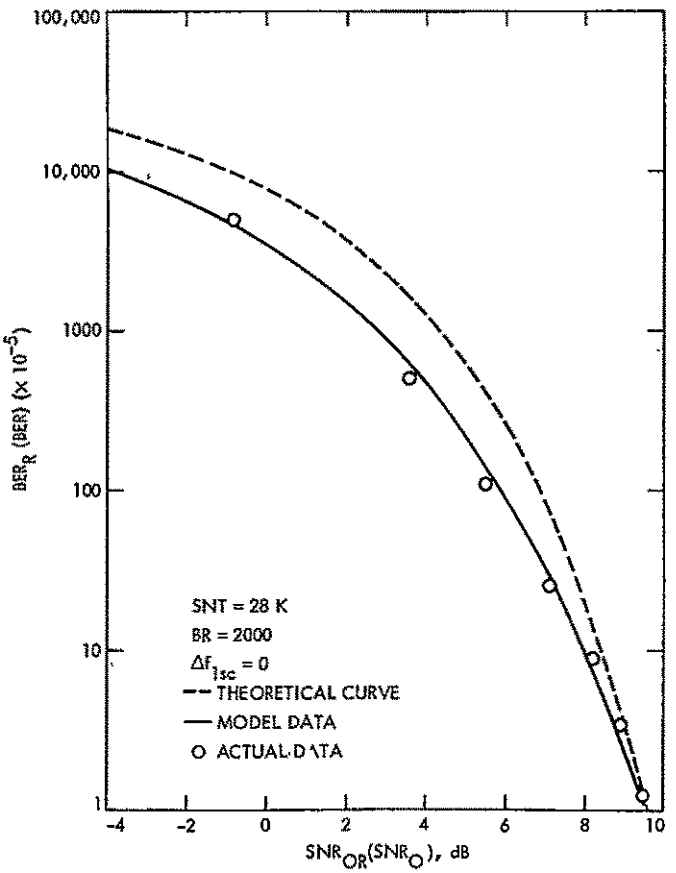

Fig. 14. Theoretical BER curve (*BER* vs *SNR*) and BER in the presence of CW interference (BER_R vs SNR_{OR}) for the case of P_D = −138.5 dBm

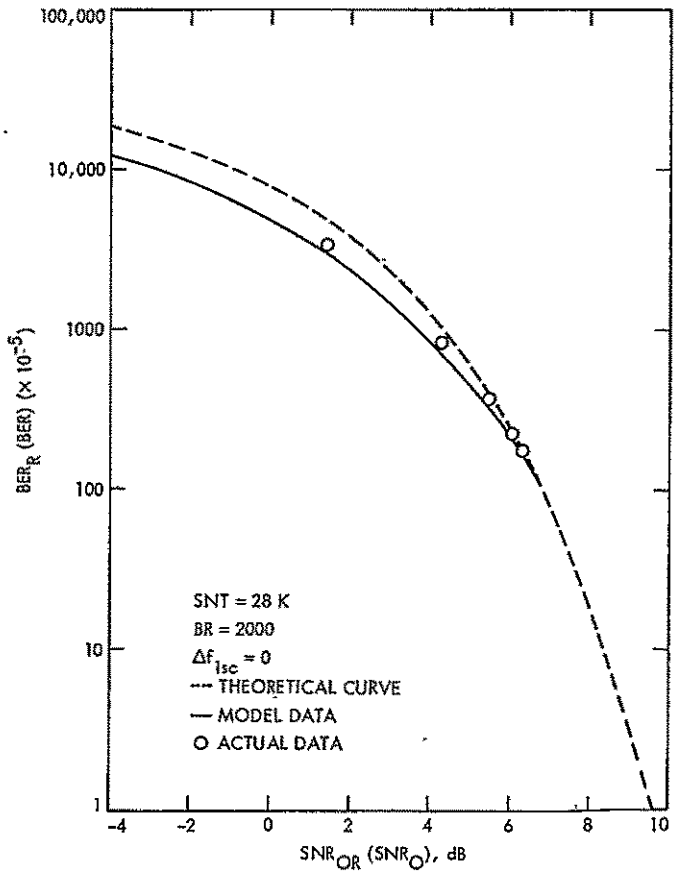

Fig. 15. Theoretical BER curve (*BER* vs SNR_O) and BER in the presence of CW interference (BER_R vs SNR_{OR}) for the case of P_D = −141.5 dBm

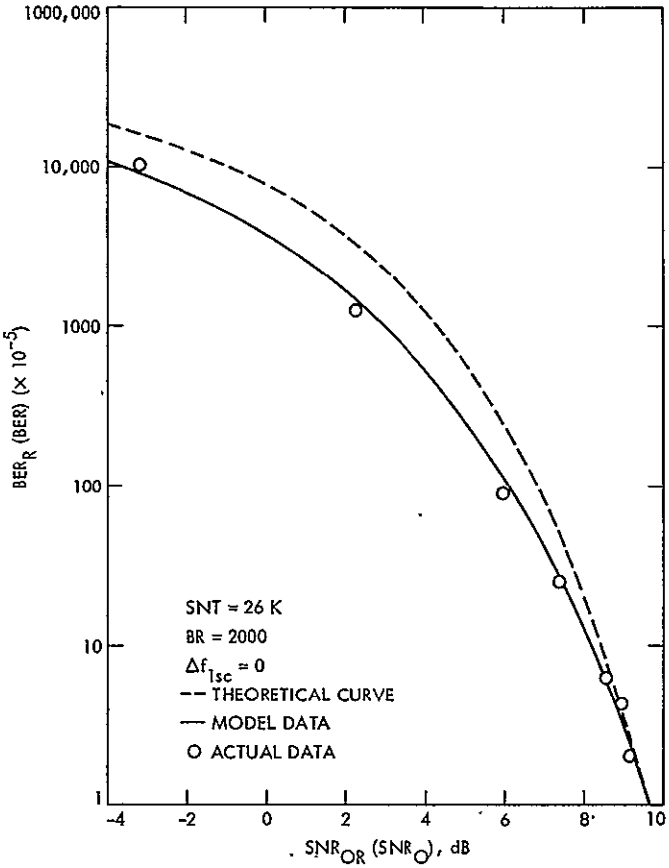

Fig. 16. Theoretical BER curve (*BER* vs SNR_O) and BER in the presence of CW interference (BER_R vs SNR_{OR}) for the case of P_D = −139.4 dBm

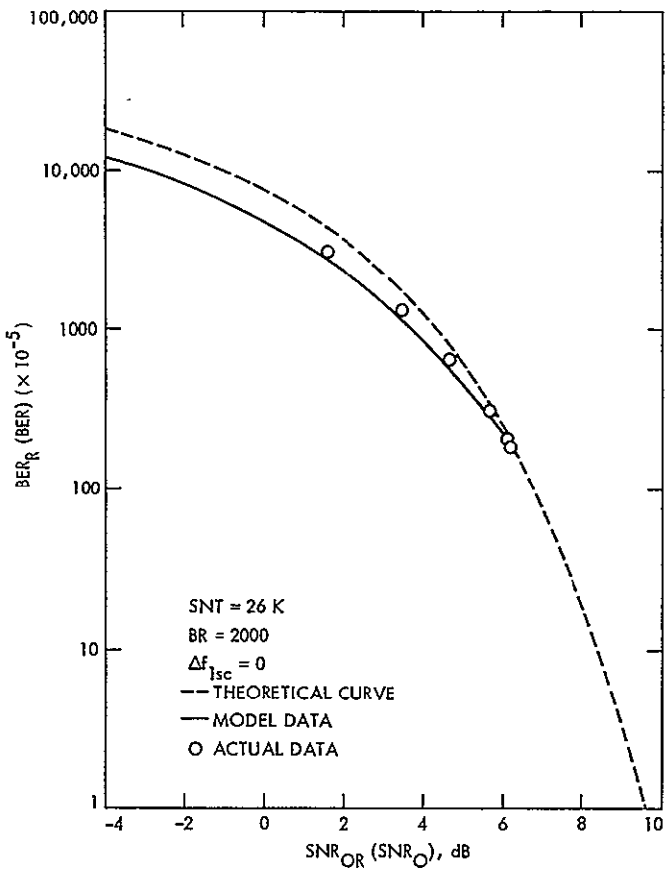

Fig. 17. Theoretical BER curve (*BER* vs SNR_O) and BER in the presence of CW interference (BER_R vs SNR_{QR}) for the case of P_D = −142.4 dBm

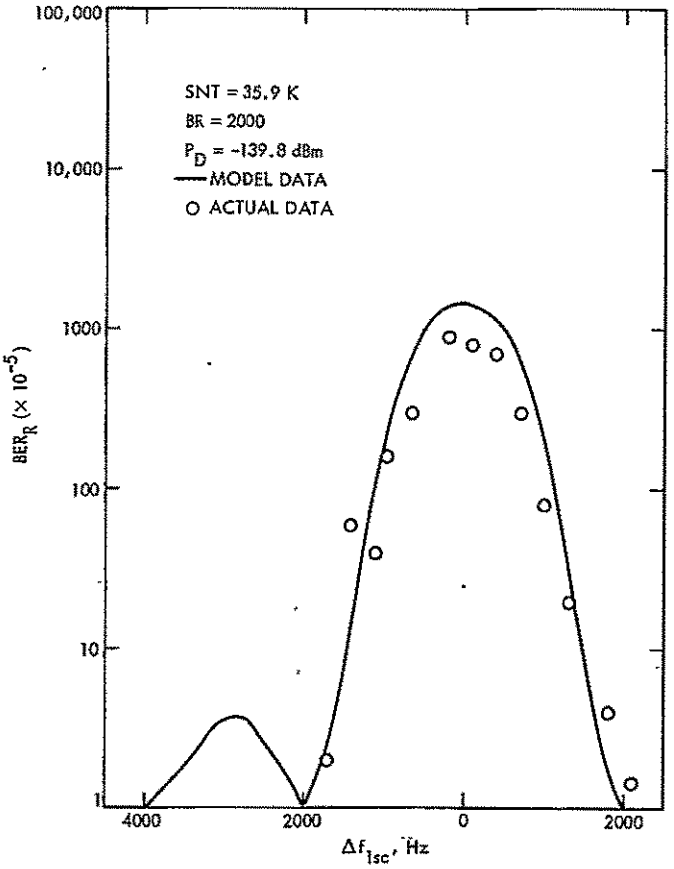

Fig. 18. Telemetry BER degradation (BER_R) vs frequency offset between subcarrier and CW interfering signal (Δf_{1sc}) for P_{RFI} = −140 dBm

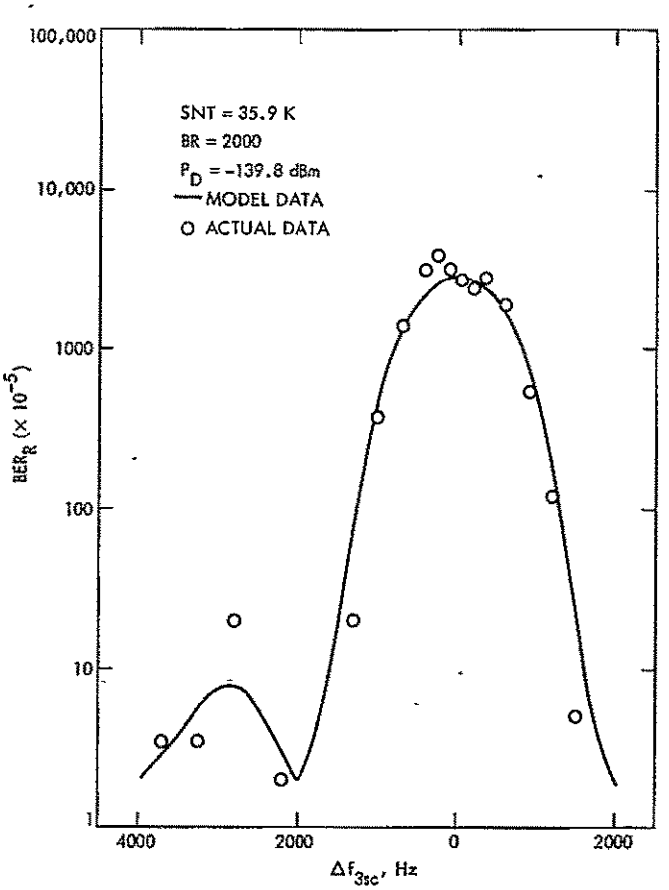

Fig. 19. Telemetry BER degradation (BER_R) vs frequency offset between subcarrier third harmonic and CW interfering signal (Δf_{3sc}) for P_{RFI} = −130 dBm

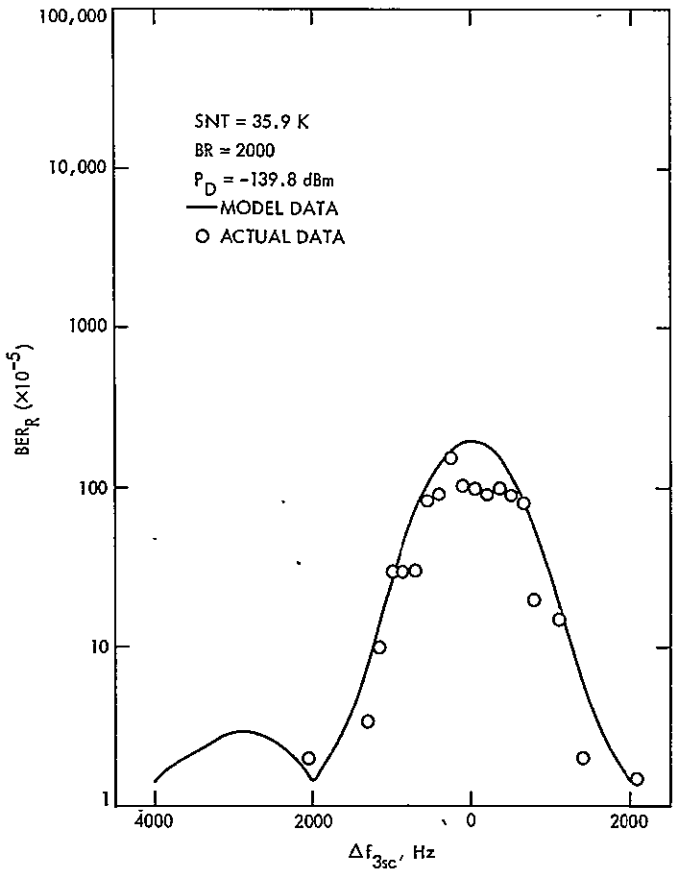

Fig. 20: Telemetry BER degradation (BER_R) vs frequency offset between subcarrier third harmonic and CW interfering signal (Δf_{3sc}) for P_{RFI} = −135 dBm

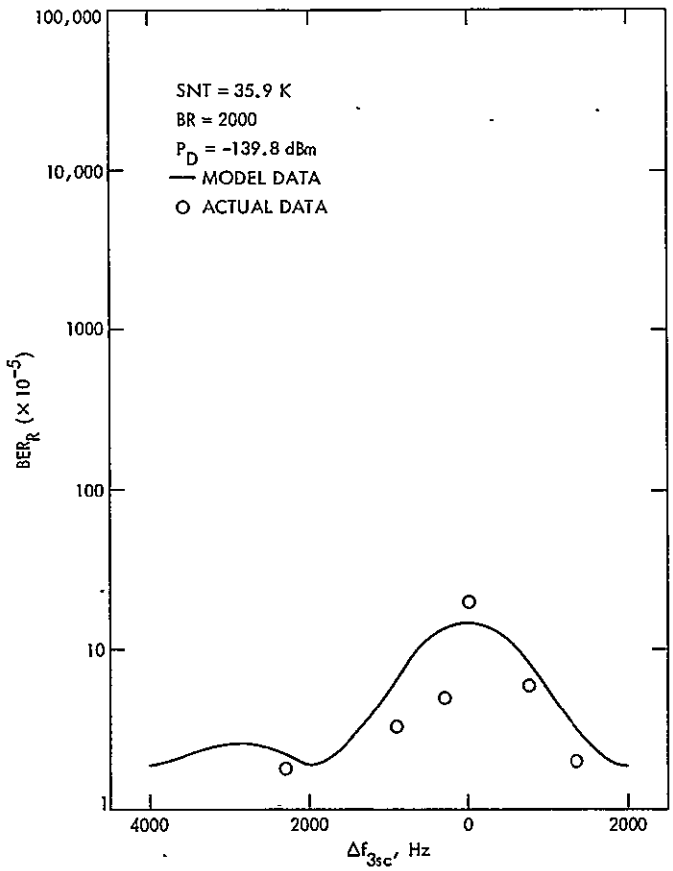

Fig. 21. Telemetry BER degradation (BER_R) vs frequency offset between subcarrier third harmonic and CW interfering signal (Δf_{3sc}) for P_{RFI} = −140 dBm

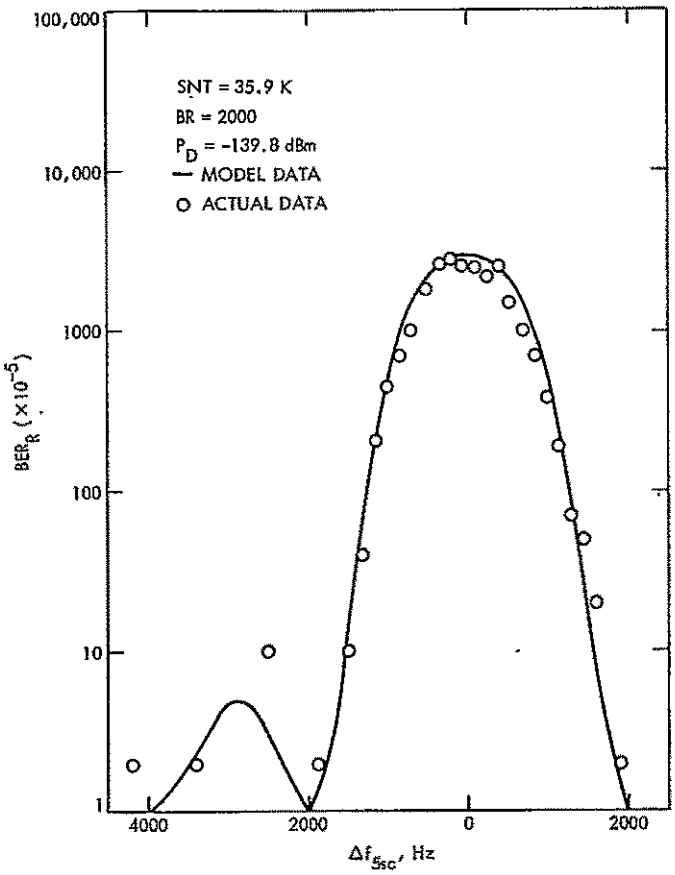

Fig. 22. Telemetry BER degradation (BER_R) vs frequency offset between subcarrier fifth harmonic and CW interfering signal (Δf_{5sc}) for $P_{RFI} = -125$ dBm

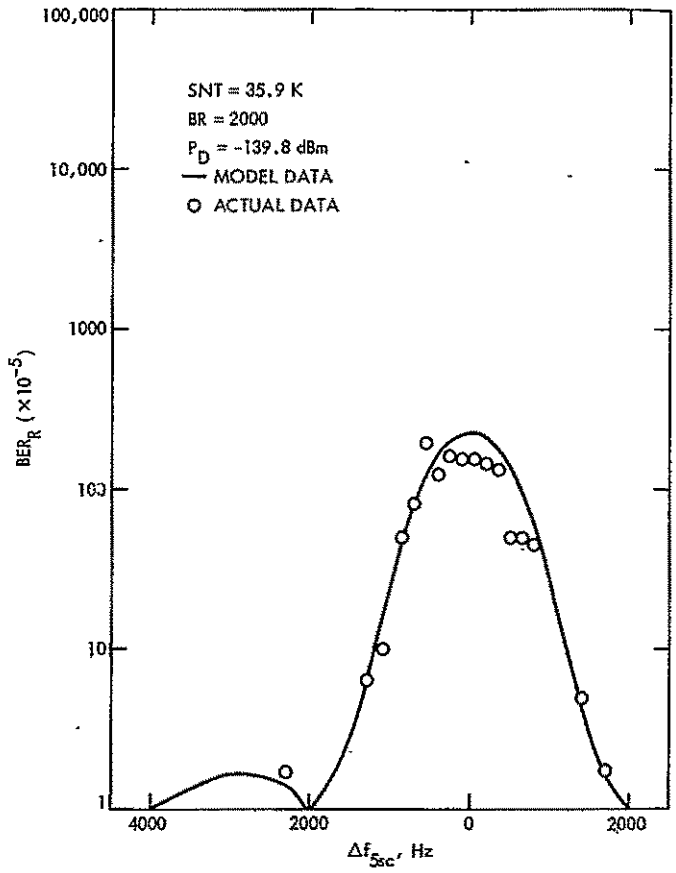

Fig. 23. Telemetry BER degradation (BER_R) vs frequency offset between subcarrier fifth harmonic and CW interfering signal (Δf_{5sc}) for $P_{RFI} = -130$ dBm

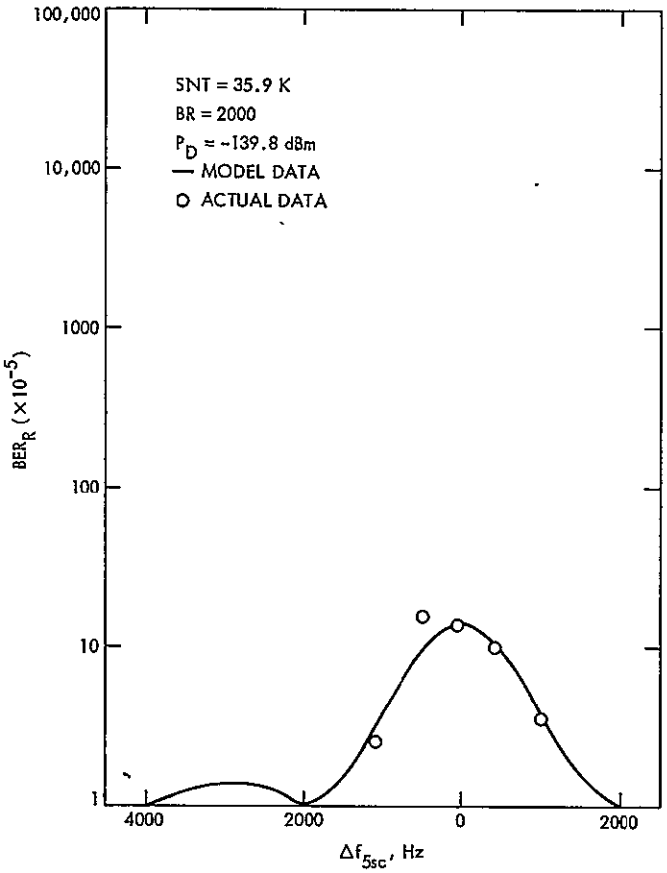

Fig. 24. Telemetry BER degradation (BER_R) vs frequency offset between subcarrier fifth harmonic and CW interfering signal (Δf_{5sc}) for P_{RFI} = −135 dBm

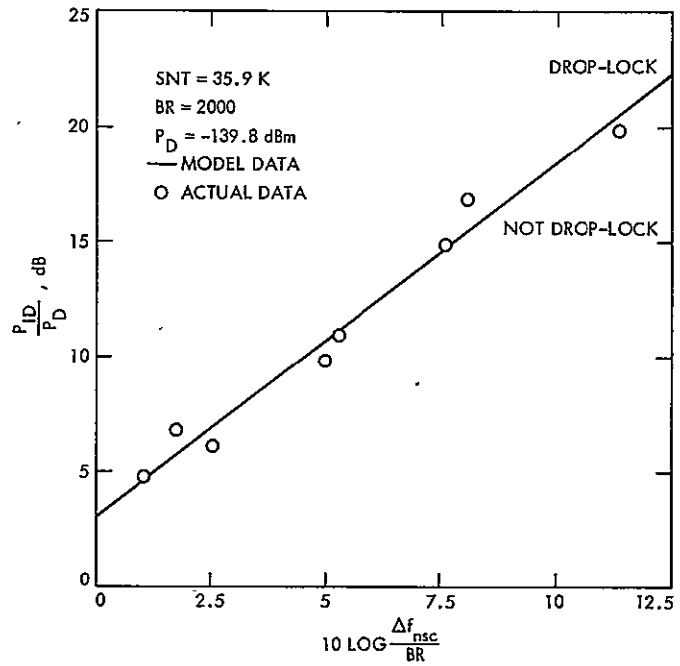

Fig. 25. Telemetry drop-lock profile

D24

Tracking System Performance Tests in the MDS Era

B. J. Buckles
DSN Network Operations Section

This article describes tracking system performance tests as developed to support DSN Mark III Data Subsystem implementation project and prepass readiness tests. Tracking SPT software and test configurations are described. Future test software requirements and areas of current development are noted.

I. Introduction

The DSN Tracking System (DTK) is currently being updated to the Mark III-77 configuration (Refs. 1 and 2). The first phase of this update is the DSN Mark III Data Subsystem (MDS) Implementation Project, which replaces at each Deep Space Station (DSS) the Tracking Data Handling (TDH) Subsystem and those functions of the Digital Instrumentation Subsystem (DIS) which formerly collected and formatted radio metric data into a form suitable for transmission by the Ground Communications Facility (GCF) with the Metric Data Assembly (MDA), a MODCOMP II minicomputer. In the new configuration, all tracking system data is collected and formatted by the MDA. Data that is to be transmitted via the GCF to the user is formatted into a high-speed data (HSD) block and "embedded" into a subsystem block (SSB), then transmitted by the MDA to the Communications Monitor and Formatter (CMF) via the DIS Monitor and Interface Assembly (DMI) star switch controllers (SSC). The CMF strips the HSD block from the SSB and inserts the proper error polynominal and then transmits the data. Data that is to be displayed by the DSS Monitor and Control Subsystem (DMC) is formatted into SSBs and transmitted to the DMC via the DMI.

Prior to the MDS implementation, Tracking System Performance Test (SPT) software was resident in the DIS and collected radio metric data for analysis purposes at the DIS -TDH interface in real-time. Obviously, a new tracking SPT test program would be necessary to support SPTs after MDS implementation, to support future mission configuration tests (MCT) and for operational support of prepass readiness tests. This article describes the system test design and rationale chosen for implementation and the inevitable compromises imposed by schedule constraints and resources.

II. Test Design

The functional requirements for the tracking system SPT program are listed in Table 1. The program design was to include all of the listed functions, with implementation carried out in a phased manner as necessary to deal with the realities of the hardware implementation schedule and the planned several different phases of the MDA operational software implementation. The requirements are separated into two groups: those functions that had to be available immediately upon MDS implementation and those that would be necessary to meet future DTK capabilities, as well as MCT and PRT requirements. In addition, the functional requirements are listed in order of priority within the two groups.

Table 2 lists those capabilities and features the new tracking system SPT software design would have to include in order to satisfy these requirements. All of these desired features were incorporated into the new test program, but due to the necessity of meeting the operational schedule of the MDS project, some compromises were necessary.

The first feature dictated that the test software would reside in the spare CMF (see Fig. 1), hereafter referred to as the System Performance Test Assembly (SPTA), as this was the only logical location from which to monitor DSS outgoing data. HSD output of the operational CMF is looped back via GCF data sets as input to the SPTA. DSS system performance is monitored at the DSS output port and data analysis is a true reflection of DSS system performance.

Reduction of necessary test time (Feature 2) was considered to be of only slightly less importance than Feature 1, but implementation was considerably more involved As the Deep Space Stations have become more and more complex to meet the requirements of the ever-increasing sophistication of new projects, system test requirements have also become more complex and stringent. Sophisticated and complex systems require sophisticated and complex testing, and this obviously requires more time to accomplish. Therefore, in order to reduce system test impact on tracking time, it was necessary to design test software that would allow as many different tests to be run simultaneously as possible.

Computerized semiautomatic test procedures and centralized operator control of both the test software and operational software were a second facet of this effort to reduce test time. This entailed designing the test program so that it could read the test procedure from a disc file and provide the test conductors with necessary prompting for equipment setup. This technique eliminates the need for the majority of operator type-ins, which reduces test setup time considerably. Manual testing capability with centralized operator control input was retained to allow special test configurations and troubleshooting to be performed with the test software.

The third goal was to provide certain new system test capabilities that were not available in the old test software. This was necessary to meet new system capabilities introduced with the MDS implementation and to correct some deficiencies in the old test program. These new capabilities include a predict system test, a HSD/SSB data dump and monitoring capability, a Block IV receiver frequency ramp test and a Meteorological Monitoring Assembly (MMA) test.

As a fourth goal it was desired to expand the doppler system noise model so that it predicted valid results at loop SNRs of less than 10 dB. In addition, the range noise model was modified to reflect the DSS stand-alone test configuration.

III. Implementation Status

Figure 2 shows the data flow path for the Tracking System Performance Test as it has been developed to support MDS implementation SPTs at DSS 14. It in effect represents a snapshot of functional test capabilities presently (June 1977) available in the test program. Once all of the operational and test software has been loaded and initialized and the necessary hardware configuration completed, then all test functions can be controlled from the DST. Test directives and/or operational directives are routed from the DST to the host computer (shown in the CMF in Fig. 2), which in turn routes it to the proper subsystem computer via the SSC. Status messages, acknowledgments and alarms are routed along the same path back to the DST for display.

A typical test mode would be for the DTK to generate radio metric SSBs from data received from, say, the PRA or the doppler system. These SSBs consist of "embedded" HSD blocks with a proper SSB header added. They are transmitted via the SSC to the CMF, which strips the SSB header and adds an error polynominal to the HSD block. The CMF sends the HSD to the HSD communications output buffer, where it is normally then transmitted to the project user; however, for the purposes of system testing the data is now looped back into the incoming HSD communications buffer, which routes it to the SPTA where it is analyzed.

At the SPTA the Test Executive Program is the resident communications handler for all SPT programs. It accepts directives that activate the proper SPT task. In this case it is the tracking test program. It can accept HSD or SSBs via the SSC; thus SPTs can be run in a "short loop" mode if necessary, obviating the need for the operational CMF to run a tracking test. The test executive routes the requested HSD/SSB data to the tracking test program, which analyzes the data and generates a test report which is output at either the printer/plotter or the local terminet.

The tracking test program validates the HSD headers as the data is received and generates alarm messages if something is amiss. The doppler and ranging analysis programs calculate theoretical noise values based on known or measured signal-to-noise ratios and compare these values to the measured noise. System specifications are used to determine "test passed" or "test failed" criteria. Any number of tests may be run simultaneously; for instance, at a 64-m DSS an S/X-band ranging performance test and S/X-band doppler performance can be run concurrently, resulting in an approximate 75% saving of test time, a matter of great importance for Prepass Readiness Tests. In addition, the tracking test program can generate and transmit test predict HSD blocks for testing the predict data handling capability.

IV. The Future

Although the MDS Implementation Project SPT support requirements have been met, much work remains to be done. The RF and antenna test functions were postponed because those systems could be supported using old test software. However, as these systems are automated and brought under software control, it will become more desirable to automate these tests, and preliminary work has begun in this area. Completely automated countdown procedures and tests are other capabilities currently being developed. Also, major modifications of the SPT software will be necessary in order to meet the new tracking HSD interface (TRK 2-14) to be introduced into the DSN in February 1978.

References

1. "Deep Space Network General Requirements and Plans," 820-20, Jet Propulsion Laboratory, Pasadena, Calif. (an internal document).
2. "Deep Space Station Subsystem Requirements – Tracking Subsystem 1974-1978," 824-2, Jet Propulsion Laboratory, Pasadena, Calif. (an internal document).

Table 1. Tracking SPT program functional requirements

Immediate requirements
Receive/verify DTK HSD/SSB blocks
Dump DTK HSD/SSB blocks
Evaluate doppler system performance
Evaluate ranging system performance
Display tracking system test results
Generate and transmit test predicts
Validate tracking ODR/TODR data
Maintain test log
Future requirements
Send control and configuration Msg's to DTK
Evaluate RF system performance
Calibrate RF system characteristics
Evaluate antenna system performance
Calibrate antenna characteristics
Generate simulated TRK system/data
Meet TRK 2-14 HSD interface

Table 2. New test program design features vs old program capabilities

New program design features	Old program comparable features
True system test that would analyze data as it left the station as HSD	Actually was a subsystem test that looked at the data at the TDH/DIS interface
Reduce test time by	None
(a) Simultaneous testing	
(b) Computerized procedures	
Provide new test capability for	None
(a) Predict system test	
(b) HSD/SSB data dumps and monitoring	
(c) POCA ramp test	
(d) MMA test	
Improved theoretical noise models for doppler and ranging	Modeled Block III receivers only. Doppler noise model valid for signal margin $\geq$ 10 dB only. Range noise model incorrect for DSS stand alone testing

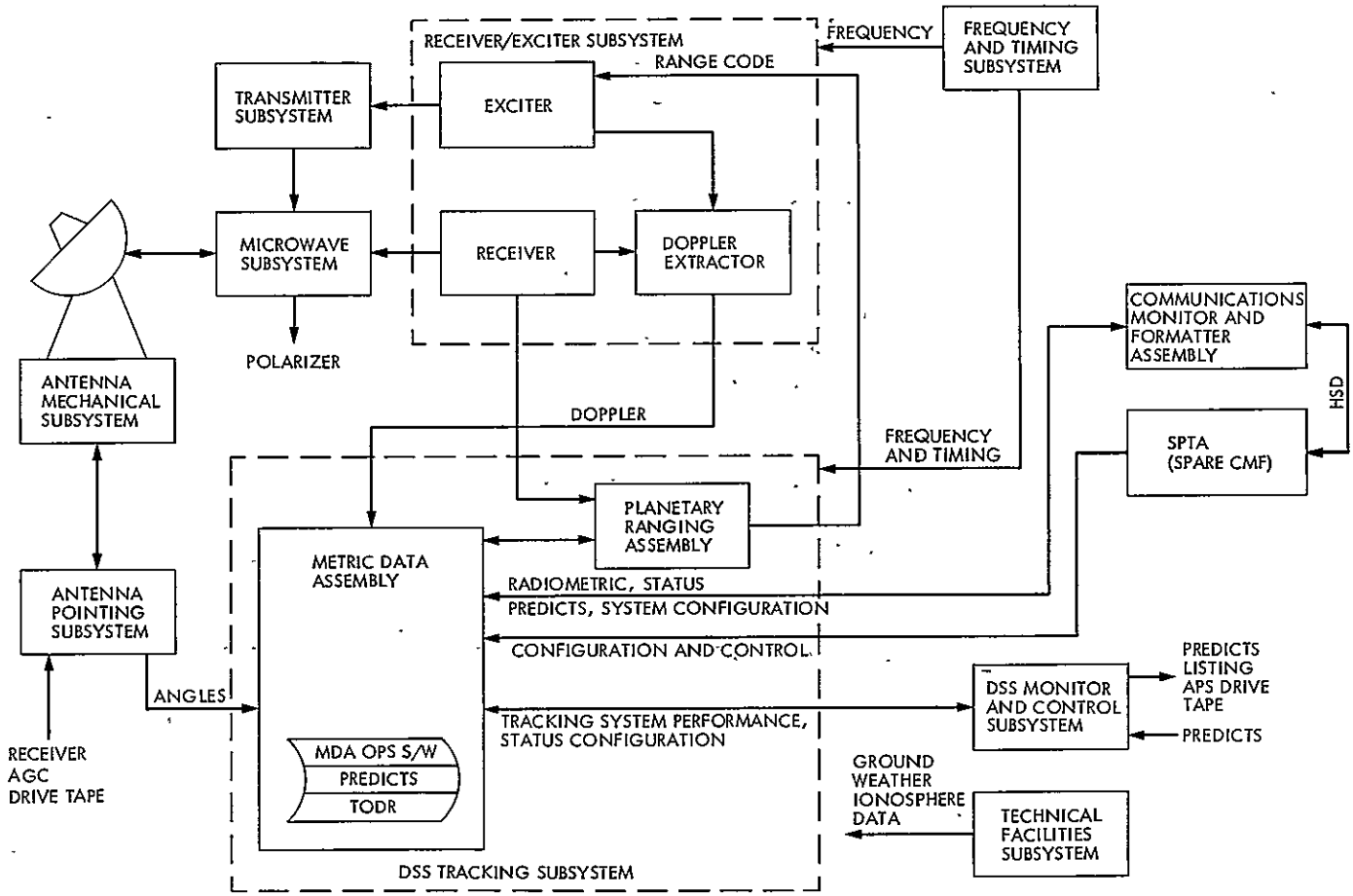

Fig. 1. Block diagram of the DSS tracking system configured for SPTS

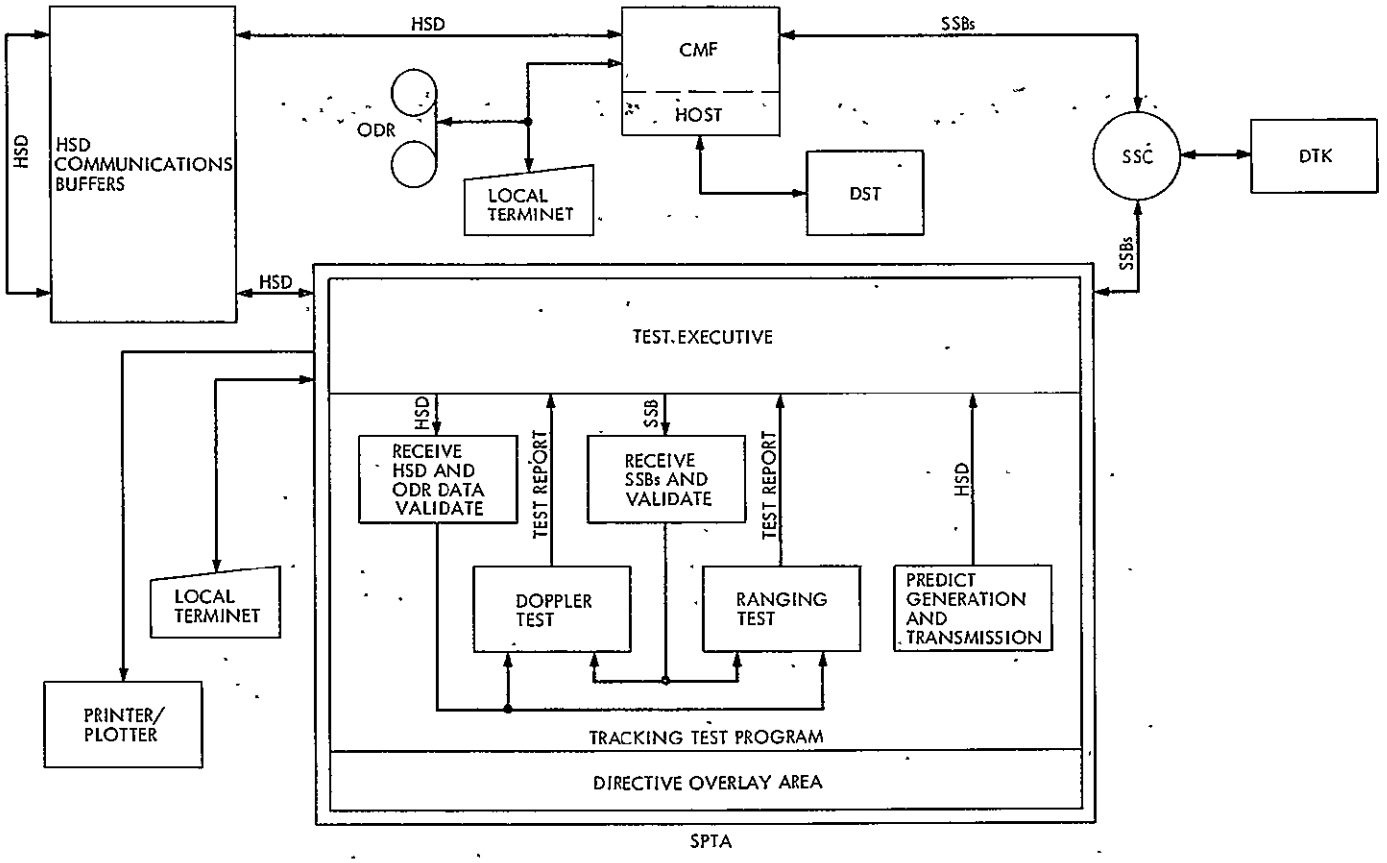

Fig. 2. Tracking system performance test data flow

D25

DSN Research and Technology Support

E. B. Jackson
Radio Frequency and Microwave Subsystems Section

The ongoing activities at the Venus Station (DSS 13) and the Microwave Test Facility (MTF) during the period February 14 through June 5, 1977, are discussed and progress noted.

Completion of phase one equipment implementation for unattended operation at DSS 13 is noted and operation demonstrated with several "hands off" spacecraft downlink acquisitions, using either locally (DSS 13) directed or remotely (JPL) directed computer control. Salvaging of a 20-kW klystron, at a cost savings of several thousand dollars, was accomplished by the DSN High Power Transmitter Facility, along with its more routine activities of testing and repairing high power transmitter components.

Extensive tracking activities with the 26-m antenna are discussed, including DSN Platform Parameters, Multistation Planetary Radar, Helios II Spectrum Broadening Analysis, VLBI Validation, Planetary Radio Astronomy, and Pulsar Rotation Constancy, for a total time of 219-1/4 observing hours.

Clock synchronization transmissions from the DSS 13 master clock to the overseas 64-m antenna complexes are reported and special implementation activities in support of PV-78 are discussed.

Implementation of a Hydrogen Maser Frequency Standard and the "pathfinder" installation of a Utility Control System (UCS) are reported, and significant station modification and maintenance activity are noted.

I. Introduction

The activities of the Development Support Group, in operating the Venus Station (DSS 13) and the Microwave Test Facility (MTF) during the period February 14 through June 5, 1977, are discussed.

II. Unattended Operation, DSS 13

A. Receiver and Microwave Subsystem Automation

An automatic acquisition module has been added with which control and indicator functions on the receiver may be

operated. This module, when an acquisition is confirmed, also stops the frequency search process, and the receiver then operates as a normal phase-locked receiver. A modem has been installed with which a CRT controller can be remotely operated, e.g., from JPL in Pasadena, and several completely automatic acquisitions have been successfully performed, using either local or remote control inputs. These test acquisitions verified the receiver subsystem configuration, including frequency sweep, and phase locking of the receiver and Subcarrier Demodulator Assembly (SDA).

B. Transmitter Subsystem Automation

The remote control cabinet (RCC) was temporarily removed from the Operations and Data Processing Building (G-51) and has been modified as necessary for interfacing with the transmitter microprocessor controller.

C. Antenna Subsystem Automation

The MODCOMP Computer has been interfaced with the 26-m antenna servo system and can start up the hydraulic system, select high or low speed on either axis, apply and release brakes on either axis, and move the antenna under controlled acceleration and velocity to point at either a fixed position or track. Program development is continuing and the capability to insert position offsets will be provided in the near future. The azimuth position transducer failed and was disassembled on-site, cleaned, bearings replaced, realigned, and reinstalled. The failures were probably due to the entrance of water from local rain storms. The pointing accuracy was then evaluated by tracking with an automatic boresighting computer program called SCOUR (Scan and COrrect Using Receiver) and was found usable. Optical alignment of the antenna is scheduled in the next several months.

III. Deep Space Network High Power Transmitter Maintenance Facility (DSN HPTMF)

A 20-kW klystron (Varian 5K70SG), which, except for tunability, was a fully functioning klystron, was repaired for operational use by replacing a stripped cavity tuning screw. Additionally, extensive measurements were made on the DSN waveguide arc detector "time to perform" under fault conditions.

Repairs effected included high power crowbar photon generators, body current, and collector current sensors. These were repaired and returned to DSS 14.

An engineering model and prototype directional coupler for near-Earth Voyager ranging calibration were tested at 400 kW. This testing was performed at 2388 MHz and verified that the couplers will handle the radio frequency power to which they will be subjected in the 64-m antenna stations.

IV. Observing Activity, 26-m Antenna

A. DSN Platform Parameters

Characterization of a suitably positioned net of compact radio sources is essential to operational use of Very Long Baseline Interferometry (VLBI) for navigation purposes. Examination of candidate sources and determination of their flux density and position is a task which is supported by DSS 13 with VLBI observations. During this reporting period, DSS 13 provided 53-1/2 hours of observation, during which 379 sources were observed. The cooperating VLBI stations in this Advanced Systems Experiment were either DSS 43 or DSS 63.

B. Three-Station Planetary Radar

This is an Advanced System experiment in which the planet Venus is illuminated by the high power transmitter at DSS 14 for a period of time equal to round-trip light time to the target. The transmitter is then turned off, and reflected signals are received by three stations in an interferometric mode, DSS 11, DSS 13, and DSS 14. The received signals from DSS 11 and DSS 13 were microwaved to DSS 14 for processing. Multistation data were collected for a total of 49-1/2 hours over a several week period. New technology demonstrated were hydrogen maser references at each station and wide band recording (80 MHz) for increased mapping information.

C. Helios II Spectrum Analysis

In mid-May 1977, the Helios II spacecraft's orbit was such that it slowly moved close to and then behind the sun, thus affording an excellent opportunity to examine the effect of the sun on the signal as received on Earth. High resolution spectrum analyzers were used to examine the signal in detail, and DSS 13 provided 10-3/4 hours of data collection for such spectrum analysis, using a prediction controlled receiver local oscillator to track the arriving signal. This effort was supported under the Helios SIRD/NSP.

D. VLBI Validation

This effort provides support of the VLBI validation effort under the DSN Implementation Program. Several formal demonstrations of short and long baseline length determination are planned. Experiment Series 1 has already been completed, and preliminary observation in preparation for Experiment Series 2 has commenced. DSS 13 provided 1-3/4

hours of observation for equipment checkout and also provided 2-1/2 hours of station verification observation in conjunction with the Caltech-Owens Valley Radio Observatory (OVRO) and the ARIES antenna positioned at San Francisco, CA. This observation was in preparation for the Sea Slope portion of the baseline determination task, and verified that the DSS 13 OVRO pair was functioning correctly; however, the DSS 13 ARIES pair did not produce fringes. Troubleshooting and repair of the ARIES station is now underway.

E. Planetary Radio Astronomy

On a time available basis, DSS 13 provides support to this experiment as defined under the Ground Based Radio Science Plan. The radiation received, at 2295 MHz, from Jupiter is measured and its variability determined. A number of radio sources are also used as calibrators for this program. During this period, a total of 51 hours of observation were accomplished, using the 26-m antenna adjusted to receive both right- and left-handed circular polarization, and using the Noise Adding Radiometer (NAR) to collect the data.

F. Pulsar Rotation Constancy

Also on a time available basis, DSS 13 observes pulsars in support of this experiment from the Ground Based Radio Science Plan. The data collected include pulse rate, pulse-to-pulse spacing, pulse power, and pulse shape. These measurements are made at 2388 MHz, with the 26-m antenna adjusted to receive left-handed circular polarization. During this period, 50-1/4 hours of observation were performed and data recorded.

V. Clock Synchronization System

During several of the transmissions, the system was troubled by transmitter problems. A comprehensive transmitter performance evaluation and maintenance effort is being undertaken to correct this deficiency. DSS 13 made 18 inter-DSN complex transmissions for a total of 18-1/2 hours, as scheduled by DSN Scheduling. Of these transmissions, 10 were made to the DSS 43 complex and 8 were made to the DSS 63 complex.

VI. Radiometer Performance Evaluation

As part of the work being performed under RTOP 66 "Radio Systems Development," DSS 13 provides long-term testing and performance evaluation of an S-band Noise Adding Radiometer (NAR) installed onto the 26-m antenna. These evaluation data are collected on a noninterference basis during the weekend periods. This NAR is also used operationally for system temperature measurement. During this period, 82 hours of performance evaluation was performed.

VII. PV-78 Probe Data Handling

As part of the data handling task on Pioneer Venus 1978 (PV-78), a fifth Block III receiver, to operate in the closed-loop mode, must be provided to DSS 14 and DSS 43. Integration, testing, and delivery of these receivers is being performed at DSS 13 by DSS 13 personnel. The two receivers have been installed in a test area, all modules have been tested and certified by the DSN Complex Maintenance Facility and inter-rack cabling has been fabricated. These receivers have been tested and performance verified. These are modified versions of equipment obtained as surplus from the Manned Space Flight Network. Final testing and shipment is planned to be completed by October 1977.

VIII. Station Modification and Maintenance

A. Hydrogen Maser

To support the observations requiring highly stable frequency references, such as Multistation Planetary Radar and VLBI observations, a Hydrogen Maser, Goddard Spaceflight Center (GSFC) Model NP2, has been borrowed from GSFC and installed at DSS 13. A 4-inch (10.16-cm) diameter conduit has been installed underground between Building G-60, in which the maser is installed, and Building G-51, in which the frequency references are required. Coaxial cables, both semi-flexible and flexible, have been installed in this conduit, and the maser has been used to support a number of observing missions.

B. Utility Control System (UCS)

The pathfinder installation of a Utility Control System (UCS) planned for DSN implementation has been made at DSS 13. The UCS has control of lights and heating, ventilation, and air conditioning (HVAC) in Buildings G-51 and G-60. It also has control of eight selected electronic racks in Building G-51. Initially, the station's operating schedule will be provided to the control computer (an INTEL 8080 based microcomputer) and power control modes provided accordingly. Other modes and functions will be added as the need arises. Manual control is provided for emergencies or schedule changes. The entire Goldstone complex suffered an extended outage of commercial power for 7-1/2 hours. This required all stations, which had such capability, to switch to standby power sources. At DSS 13, the delay in bringing up standby diesel electric alternators (the outage occurred during non-manned hours) resulted in partial warmup of the S-band maser. Associated voltage surges caused failure of the 60- to 400-Hz frequency converter which supplies 400 Hz for station needs. This points out the need for adequate power control and automatic switchover for unattended station operation configuration in order to maximize station availability to the user.

NASA—JPL—Coml., L.A., Calif

best sellers

NTIS

from NATIONAL TECHNICAL INFORMATION SERVICE

Product Liability: Industry Study. Volumes I and II
PB-265 542/PSK 886 p PC$21.25/MF$3.00

An Atlas of Radiation Histopathology
TID-26676/PSK 234 p PC$7.60/MF$3.00

The Medical School Admissions Process. A Review of the Literature, 1955-76
PB-263 962/PSK 193 p PC$7.50/MF$3.00

Integrated Energy Vocabulary
PB-259 000/PSK 459 p PC$22.50/MF$3.00

Nuclear Air Cleaning Handbook. Design, Construction, and Testing of High-Efficiency Air Cleaning Systems for Nuclear Application
ERDA-76/21/PSK 300 p PC$9.75/MF$3.00

Evaluation of the Air-To-Air Heat Pump for Residential Space Conditioning
PB-255 652/PSK 293 p PC$9.25/MF$3.00

Federal Information Processing Standards Register: Guidelines for Documentation of Computer Programs and Automated Data Systems. Category: Software. Subcategory: Documentation
FIPS-PUB38/PSK 55 p PC$4.50/MF$3.00

Life Cycle Costing Emphasizing Energy Conservation: Guidelines for Investment Analysis
ERDA-76/130/PSK 117 p PC$5.50/MF$3.00

Analysis of Projected Vs. Actual Costs for Nuclear and Coal-Fired Power Plants
FE-2453-2/PSK 38 p PC$4.00/MF$3.00

Quality Criteria for Water
PB-263 943/PSK 537 p PC$13.00/MF$3.00

Passive Solar Heating and Cooling Conference and Workshop Proceedings May 18-19, 1976, University of New Mexico, Albuquerque, New Mexico
LA-6637-C/PSK 352 p PC$10.50/MF$3.00

Predicting the Performance of Solar Energy Systems
AD-A035 608/PSK 45 p PC$4.00/MF$3.00

NIOSH Analysis Methods for Set J
PB-263 959/PSK 128 p PC$6.00/MF$3.00

Flat-Plate Solar Collector Handbook: A Survey of Principles, Technical Data and Evaluation Results
UCID-17086/PSK 96 p PC$5.00/MF$3.00

How to Order

When you indicate this method of payment, please note if a purchase order is not accompanied by payment, you will be billed an additional $5.00 *ship and bill* charge. And please include the card expiration date when using American Express.

Normal delivery time takes three to five weeks. It is vital that you order by number or your order will be manually filled, insuring a delay. You can opt for *priority mail* for $3.00 outside North American continent charge per item. Just check the *priority mail* box. If you're really pressed for time, call the NTIS Rush Handling Service (703) 557-4700 For a $10.00 charge per item, your order will be sent *priority mail* within 48 hours. Or, you can pick up your order in the Washington Information Center & Bookstore or at our Springfield Operations Center within 24 hours for a $6.00 per item charge.

You may also place your order by telephone or if you have an NTIS Deposit Account or an American Express card order through TELEX. The order desk number is (703) 557-4650 and the TELEX number is 89-9405.

Thank you for your interest in NTIS We appreciate your order.

METHOD OF PAYMENT

- ☐ Charge my NTIS deposit account no. _____
- ☐ Purchase order no. _____
- ☐ Check enclosed for $ _____
- ☐ Bill me. Add $5.00 per order and sign below. (Not available outside North American continent.)
- ☐ Charge to my American Express Card account number

Card expiration date _____.

Signature _____

☐ Priority mail requested

NAME _____

ADDRESS _____

CITY, STATE, ZIP _____

Item Number	Quantity		Unit price*	Total Price*
	Paper Copy (PC)	Microfiche (MF)		

All prices subject to change. The prices above are accurate as of 3/31/78
Foreign Prices on Request.

Sub Total	
Additional Charge	
Enter Grand Total	

Clip and mail to:

NTIS

National Technical Information Service
U.S. DEPARTMENT OF COMMERCE
Springfield, Va. 22161
(703) 557-4650 TELEX 89-9405